Photophysics of Soret-excited Metallated Tetrapyrroles in Solution: Experimental and Theoretical Studies

A Thesis Submitted to
The College of Graduate Studies and Research
In Partial Fulfillment of the Requirements
For the Degree of Doctor of Philosophy
In the Department of Chemistry
University of Saskatchewan

by

Xia Liu

Department of Chemistry
University of Saskatchewan

Permission to Use

In presenting this thesis in partial fulfilment of the requirements for a Postgraduate degree from the University of Saskatchewan, I agree that the Libraries of this University may make it freely available for inspection. I further agree that permission for copying of this thesis in any manner, in whole or in part, for scholarly purposes may be granted by the professor Ronald P. Steer who supervised my thesis work or, in his absence, by the Head of the Department or the Dean of the College in which my thesis work was done. It is understood that any copying or publication or use of this thesis or parts thereof for financial gain shall not be allowed without my written permission. It is also understood that due recognition shall be given to me and to the University of Saskatchewan in any scholarly use which may be made of any material in my thesis.

Requests for permission to copy or to make other use of material in this thesis in whole or part should be addressed to:

The Head
Department of Chemistry
University of Saskatchewan
Saskatoon, Saskatchewan S7N 5C9
Canada

Abstract

The photophysics of highly electronically excited states of a set of d^0 and d^{10} metallated tetrapyrroles, which have different peripheral substituents and central metal atoms, macrocycle substitution patterns and macrocycle conformations, have been investigated both theoretically and experimentally. Theoretically, the energies of ground state molecular orbitals and the energies and rank in energy of the excited states have been calculated using density functional theory and time-dependent density functional theory methods. Experimentally, the steady-state absorption and fluorescence spectra have been measured. Temporal fluorescence profiles have been measured using a time correlated single photon counting system for the S_1 state and a fluorescence upconversion system for the S_2 state.

The DFT and TDDFT calculations show that the ground state geometries are not significantly altered by substitutions on the porphyrin macrocycle. However, they do affect the orbital energies, and the energy and the rank in energy of the excited states accessible in the near uv-region of the spectrum of the metalloporphyrins studied. The TDDFT calculations of the excited states predict that a number of singlet and triplet excited states lie in the vicinity of the 2^1E_u state. One or more of them may contribute to the fast relaxation of the S_2 state of the metalloporphyrins.

The $S_2 - S_1$ energy gap, $\Delta E(S_2 - S_1)$, is controlled by both solvent and porphyrin polarizabilities for a given metalloporphyrin. A good linear correlation between $\Delta E(S_2 - S_1)$ and the Lorenz-Lorentz solvent polarizability function, f_1, is obtained for ZnTPP, MgTPP and ZnTBP metalloporphyrins in the set of solvents employed. Extrapolation of such plots to $f_1 = 0$ gives the $\Delta E(S_2 - S_1)$ of the bare molecules observed in a supersonic expansion. In addition, the slope of such plot for ZnTBP is different from those of ZnTPP and MgTPP because of different porphyrin polarizabilities.

The S_2 depopulation rates have been calculated based on the S_2 fluorescence lifetimes obtained. For a given metalloporphyrin in several fluid solvents, the logarithms of the radiationless decay rates of the S_2 states decrease linearly with the increase of $\Delta E(S_2 - S_1)$. However, the slopes of such energy gap law plots of ZnTPP and ZnTBP are dif-

ferent from that of MgTPP. The internal conversion efficiency is close to 1.0, except for CdTPP, where it is only 0.69. The fact and the equality of the S_2 decay and S_1 rise times indicate that the only important relaxation pathway of the S_2 state is $S_2 - S_1$ internal conversion. Further analysis indicates that there is no evidence of significant contributions from heavy-atom induced $S_2 - T_n$ ($n > 2$) intersystem crossing or of the existence of a dark or S_2' state and its participation in the nonradiative decay processes of the S_2 state.

The decay mechanisms of highly electronically excited states are governed by the nonradiative $S_2 - S_1$ internal conversion. The ultrafast $S_2 - S_1$ internal conversion rates are determined by two factors; The magnitude of the Franck-Condon factor and the $S_2 - S_1$ interstate electronic coupling energy, β_{el}^2, according to the Fermi Golden Rule. For MgTPP, the change in k_{nr} with ΔE is determined exclusively by the magnitude of F, which varies inverse exponentially with ΔE, and thus strictly follows the predictions of the energy gap law for the weak coupling, statistical limit case. However, the other metalloporphyrins investigated have $S_2 - S_1$ electronic coupling energies falling within the intermediate to strong coupling range. The difference of k_{nr} relative to the weak coupling limit can be rationalized by the different magnitudes of β_{el}. Thus β_{el} is the major factor in determining the radiationless depopulation rate constants of the S_2 states in metallated tetrapyrroles which have $S_2 - S_1$ interstate electronic coupling energies exceeding the weak coupling limit. In some cases, such as ZnOEP, the magnitude of F has only minor effect.

The photophysics of Soret-excited metallated corroles have also been investigated in this study. Primary work has shown that two metallated corroles examined have similar $S_2 - S_1$ interstate electronic coupling energies to that of CdTPP and thus the radiationless decay rates of Soret-excited S_2 state are also determined by the magnitude of β_{el}.

Acknowledgements

First of all, I would like to sincerely acknowledge my supervisor, Professor Ronald P. Steer, to give me this opportunity to get involved in this exciting project. I greatly appreciate his consistent support, excellent guidance and faith in me throughout the course of this program. His integrity and enthusiasm as a scientist and supervisor will benefit me not only for my research career but all my later life.

I would like to thank the members of my advisory committee: Professor M. Paige, Professor S. Urquhart and Professor J.S. Lee for their suggestions and advice to help me to complete this program.

I am very grateful to Dr. E. Yeow, Dr. S. Velate, Dr. U. Tripathy and Dr. D. Kowalska for the opportunity to work and collaborate with them. The discussions and suggestions with them are invaluable and very helpful. I am also grateful to the members of Professor Ronald P. Steer group: Shamus Blair, Sunish K. Sugunan, Jaclyn O'Brien and Dr. M. Maiti for having a good time during my stay in Saskatoon.

I greatly appreciate the help of Dr. S. Brunet in the training and maintaining the TCSPC instruments.

I am grateful to Professor S. Langford group for supplying samples of ZnTBP and deuterated porphyrin samples, and Professor Z. Gross group for supplying corroles samples.

Thanks to NSERC, University of Saskatchewan and Department of Chemistry of the consistent financial support. Thanks to the Saskatchewan Structure Science Centre for the use of TCSPC and fluorescence upconversion instruments.

Finally, I sincerely express my deepest gratitude to my husband Hengmin Zhao for his support, encouragement and faith in me, to my parents and father-in-law for their love and support and taking care of my daughter for me so that I can focus on my work. My deepest gratitude is also going to my sweetheart, Angela, for so much joy her bringing to me in the life.

Table of Contents

List of Figures

List of Tables

List of Charts

List of Abbreviations

A	Absorption
a.u.	Arbitrary units
ABO	Adiabatic Born-Oppenheimer approximation
Abs	Absorption
Al(tpfc)(py)	Aluminum metallated corrole
AlClOEP	Aluminum-octaethyl-porphyrin chloride
AlClTPP	Aluminum tetraphenyl-porphyrin chloride
B3LYP	Becker three-parameter Lee-Yang-Parr functional
BBO	Beta barium borate (β-bariumborate, BBO or β-BaB_2O_4)
BS	Beam splitter
CAM-B3LYP	Coulomb-attenuating method of B3LYP functional
CASSCF	Complete active space multiconfiguration self-consistent field method
CdTPP	Cadmium tetraphenyl-porphyrin
CFD	Constant fraction discriminator
CH_2Cl_2	Dichloromethane
CH_3CN	Acetonitrile
$CHCl_3$	Chloroform
Corr	Corrected
DFT	Density functional theory
DMF	Dimethylformide
DMSO	Dimethyl sulfoxide
EGL	Energy gap law
EtOH	Ethanol
F	Fluorescence
EPA	Mixture of ether : isopentane : ethyl alcohol in the ratio 2:2:5
fs	Femtoseconds
FWHM	Full width at half maximum of the spectrum
Ga(tpfc)(py)	Gallium metallated corrole
H_2OEP	31,33-H-β-octaethyl-porphyrin
H_2TPP	5,10,15,20-tetraphenyl-31,33-H-porphryin
HOMO	Highest occupied molecular orbital
HPLC	High performance liquid chromatography
IC	Internal conversion
INDO	Intermediate neglect of differential overlap
IRF	Instrument response function
ISC	Intersystem crossing
IVR	Intramolecular vibrational redistribution
LBO	Lithium triborate (LiB_3O_5)
LDA	Local density approximation
LUMO	Lowest unoccupied molecular orbital
M	Mirror
MCA	Multiple channel analyzer
MCP	Microchannel plate
MgTPP	Magnesium tetraphenyl-porphyrin
MRCI	Multireference configuration interaction
MRMP	Multireference MØller-plessert perturbation theory
Norm.	Normalized
ns	Nanoseconds
Obs	Observation
P	Phosphorescence
PbOEP	Lead β-

	octaethylporphyrin
PMT	Photomultiplier tube
ps	Picoseconds
PTI	Photon technology international
RegA	Regenerative amplifier
S	Singlet state
SAOP	Statistical averaging of different orbital-dependent model potentials
SHG	Second harmonic generator
SS	Stokes shift
T	Triplet state
TAC	Time-to-amplitude converter
TCSPC	Time correlated single photon counting
TDDFT	Time-dependent density functional theory
TDHF	Time-dependent hartree-fock theory
$Ti:Al_2O_3$	Titanium sapphire crystal
TLC	Thin layer chromatography
VD	Variable delay
VR	Intermolecular vibrational redistribution
ZnDPP	Zinc *meso*-diphenyl-porphyrin
ZnOEP	Zinc β-octaethyl porphyrin
ZnP	Zinc porphyrin
ZnTBP	Zinc tetrabenzoporphyrin
ZnTPP	Zinc tetraphenylporphyrin
$ZnTPP(Cl_8)$	Zinc *meso*-(o-dichloro phenyl) porphyrin
$ZnTPP(F_{20})$	Zinc *meso*-(pentafluoro-phenyl)porphyrin
ZnTPTBP	Zinc *meso*-tetraphenyl-tetrabenzoporphyrin
ZnTTP	Zinc 5,10,15,20-tetrakis(4-methyl phenyl)porphyrin
ZnEMBPP	Zinc 2,8,12,18-tetraethyl-3,7,13,17-tetramethyl-5,15-di(3,5-di-t-butyl phenyl)-porphyrin

List of Symbols and Mathematical Terms

A	Absorbance
a	Constant
c	Concentration or speed of light or expansion coefficient
d	Thickness of the absorbing media in cm
d_M	Degeneracy of specific vibrational modes
e	Electron charge or as subscript to indicate electronic states
E_n	Energy of the electronic state
E_v	Vibronic coupling energy
f	Oscillator strength or integrated intensity of the Soret or Q band of the spectrum or functions of the dielectric constant and refractive index of the solvents
Δf, f_A, f_B, f_C, f_D	functions of the dielectric constant and refractive index of the solvents
f_1	Lorenz-Lorentz solvent polarizability function
F	Inner filter correction factor
g	Gerade symmetry
h	Planck constant
I	Light intensity
J_N	Nuclear kinetic energy operator
k_{IC}	$S_2 - S_1$ internal conversion rate constant
k_{nr}	Rate constants of radiationless processes
k_q	Rate constant of quenching
k_r	Radiative rate constant
m_e	Mass of electron
M_Q	Molar concentration of the quencher
n	Refractive index of the solvent or channel number
N_A	Avogadro's constant
p	Number of variable parameters in the fitting function
$P_s(t)$	Probability of find the excited molecule in its initial state ϕ_s at time t
q	Electron coordinates
Q	Nuclei configuration
Q_0	Nuclei configuration near the equilibrium position of the potential energy surface
R	Dipole integral or ratio of integrated intensity of the spectrum
$R(t_i)$	Weighted residual
S	Total electron spin quantum number
V_{sl}	Interstate interaction energy
$Y(t_i)$	Calculated fitting function
Z	Atomic number
ν	Frequency in Hertz
η	Efficiency of the $S_2 - S_1$ internal conversion or a function of the relative number of vibrational modes
ε	Molar extinction coefficient or dielectric constant of the solvent
ϵ	average energy level spacing of $\{\phi_l\}$
Ψ	Total molecular wavefunctions or molecular eigenstates
χ	Vibrational wavefunction
υ	Indicates vibrational states or quanta number of vibrational level
ξ^2	Spin-orbital coupling energy
τ_r	Resonance time or Poincare resonance time
τ_d	relaxation time of $\{\phi_l\}$ states
Δ_M	Reduced displacements of vibrational mode
H'	Time-independent Hamiltonian

ε_0	Vacuum permittivity
$\bar{\nu}$	Frequency in wavenumber
τ_f	Fluorescence lifetime
ϕ_f	Fluorescence quantum yield
χ_r^2	Goodness-of-fit parameter or reduced "chi-square"
$\hbar\omega_M$	Vibrational energy of specific vibrational mode
u	Ungerade symmetry
Γ	Molecular symmetry representation
δE	Energy difference between two ($^1a_{2u}{}^1e_g$) and ($^1a_{1u}{}^1e_g$) excited electron configurations
μ	Electric dipole moment operator
ϕ	Zeroth-order Born-Oppenheimer molecular electronic states
ρ	Density of states
$\Delta\bar{\nu}$	FWHM of spectrum
ΔE	Energy gap between two coupled electronic states
β_{el}	Electronic coupling energy matrix element
γ	A function of the dimensionless reduced displacement parameter, Δ_M, degeneracy d_M and vibrational energy $\hbar\omega_M$
λ	Wavelength in nm
$\lambda/2$	Half wave plate
τ_0	Intrinsic radiative lifetime

Chapter 1: Introduction and Literature Review

1.1 Introduction

Many electronically excited polyatomic molecules emit fluorescence. For many years, it was believed that molecules with closed shell singlet ground states emitted fluorescence only from the lowest excited singlet state (Kasha's Rule).[1] In addition, the emission spectrum and quantum yield were thought to be independent of excitation wavelength within the uv-visible region of the absorption spectrum. This extension of the Kasha's Rule was named Vavilov's Law.[2]

The observation of emission from the second excited singlet state of azulene and its derivatives is considered to be the first known violation of Kasha's Rule. Later, researchers found that thiones and their derivatives can also emit fluorescence from higher excited states. These exceptional molecules have attracted considerable attention because the "abnormal" fluorescence provides an experimental measurable not found in most compounds. The photochemical and photophysical properties of highly excited states of azulenes and thiones have now been extensively investigated and their decay dynamics are well-understood. Comprehensive information can be found in references 2 and 3.[2,3] In addition to the azulenes and thiones, since the 1970s a large number of tetrapyrrolic compounds have been found to emit fluorescence from highly excited electronic states with very small but measurable fluorescence quantum yields (ϕ_f (S_2) is $\leq 10^{-3}$).[4] The lifetimes of these fluorescent highly excited molecules were estimated to be several picoseconds (ps) or hundreds of femtoseconds, based on the integration of the absorption spectra in solution or the linewidths of resolved vibrational bands of the isolated molecule in supersonic jet. Such short lifetimes were beyond the time resolution of fluorescence lifetime experimental setup in these early days.[5,6]

The tetrapyrroles are promising candidates for use in photo-actuated optoelectronic devices, such as molecular logic gates,[7,8] and in dye-sensitized solar cells.[9-12] Further research regarding the photochemical and photophysical properties of the highly excited states of these compounds is needed to improve the efficiency of these solar cells. Thanks to the invention and application of femtosecond pulsed lasers, ultrafast time

resolution and excellent photon detection sensitivity are now available to make direct measurements of the ultra-short fluorescence lifetimes of tetrapyrroles. More accurate information with respect to the relaxation dynamics of the more highly excited states of the tetrapyrroles can now be obtained.

In the following paragraphs, some theories are briefly introduced that are essential in understanding and interpreting the experimental phenomena and results presented in this thesis. Some recent developments concerning the decay dynamics of the highly excited states of tetrapyrroles and their derivatives are also reviewed as a follow-up to recent previous reviews. Finally, the motivation of the present work is explained.

1.2 Molecular and electronic structures of the metalloporphyrins studied

Molecular structures of the porphyrins and related compounds studied in this thesis are shown in Chart 1.1: zinc(II) porphyrin (ZnP), zinc(II) *β*-octaethylporphyrin (ZnOEP), zinc(II) *meso*-tetraphenylporphyrin (ZnTPP), magnesium(II) *meso*-tetraphenylporphyrin (MgTPP), cadmium(II) *meso*-tetraphenylporphyrin (CdTPP), zinc(II) *meso*-pentafluorophenylporphyrin (ZnTPP(F_{20})), zinc(II) *meso*-(o-dichlorophenyl) porphyrin (ZnTPP(Cl_8)), zinc(II) *meso*-diphenylporphyrin (ZnDPP), zinc(II) tetrabenzoporphyrin (ZnTBP), and zinc(II) *meso*-tetraphenyl-tetrabenzoporphyrin (ZnTPTBP). The parent compound ZnP acts as a reference. The other compounds were obtained by substitution either on the *meso*- or C_m position or on the pyrrolic C_β position of the porphyrin macrocycle, or by substitution of the central metal atom. The common feature of these compounds is that they have a porphyrin macrocycle, with conjugated π-electron system. More details of the effects of the substitutions on their molecular structures, which are characterized by structural parameters such as bond distances, bond angles and dihedral angles, will be discussed later in Chapter 3.

Without external perturbation, all electrons of the molecule occupy orbitals of the lowest total energy and the corresponding electron configuration is called the ground state. Perturbation by means such as photon absorption will move one or more electrons from the ground state to the excited state. When the details of the electronic structure of states are unknown or not necessary, each electronic state is given a shorthand notation

by their electron spin multiplicities, S (singlet) or T (triplet). In most organic molecules, the ground singlet electronic state is denoted as S_0, and higher excited states as S_1, S_2,…S_n and T_1, T_2,….T_n increasing in energy relative to the ground state.[13] Thus S_1 is the first electronically excited singlet state above S_0, and the S_2 is the one next to it with higher energy, while T_1 is the first excited triplet state above S_0, but lower in energy than S_1, as shown in Fig. 1.1.

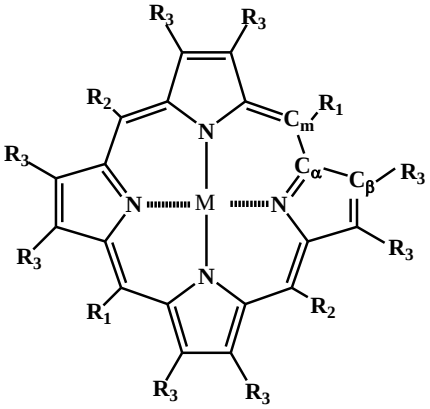

ZnP: M = Zn, $R_1 = R_2 = R_3 = H$
ZnDPP: M = Zn, R_1= Ph, $R_2 = R_3 = H$
H_2TPP: M = 2H, $R_1 = R_2$ = Ph, $R_3 = H$
TPP-d_{30}: M = 2H, $R_1 = R_2 = C_6D_5$, $R_3 = D$
MTPP: M = Zn, Mg, Cd, $R_1 = R_2$ = Ph, $R_3 = H$
ZnTPP-d_{28}: M = Zn, $R_1 = R_2 = C_6D_5$, $R_3 = D$
ZnOEP: M = Zn, $R_1 = R_2 = H$, R_3 = Et
ZnTPP(F_{20}): M = Zn, $R_1 = R_2 = C_6F_5$, $R_3 = H$
ZnTPP(Cl_8): M =Zn, $R_3 = H$, $R_1 = R_2$ =

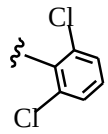

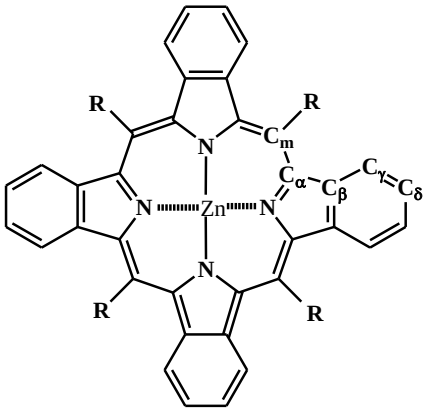

ZnTBP: M = Zn, R = H
ZnTPTBP: M = Zn, R = Ph

Chart 1.1 Molecular structures and corresponding abbreviations of compounds investigated in this project.

To characterize the energy states of a polyatomic molecule, on the basis of molecular symmetry, molecular term symbol was adopted as a shorthand expression of the group representation and angular momentum of the molecule. The general form of the molecular term symbol for nonlinear large polyatomic molecules is $^{2S+1}\Gamma$. Here, S is the total electron spin quantum number, and 2S+1 is the electron spin multiplicity of the

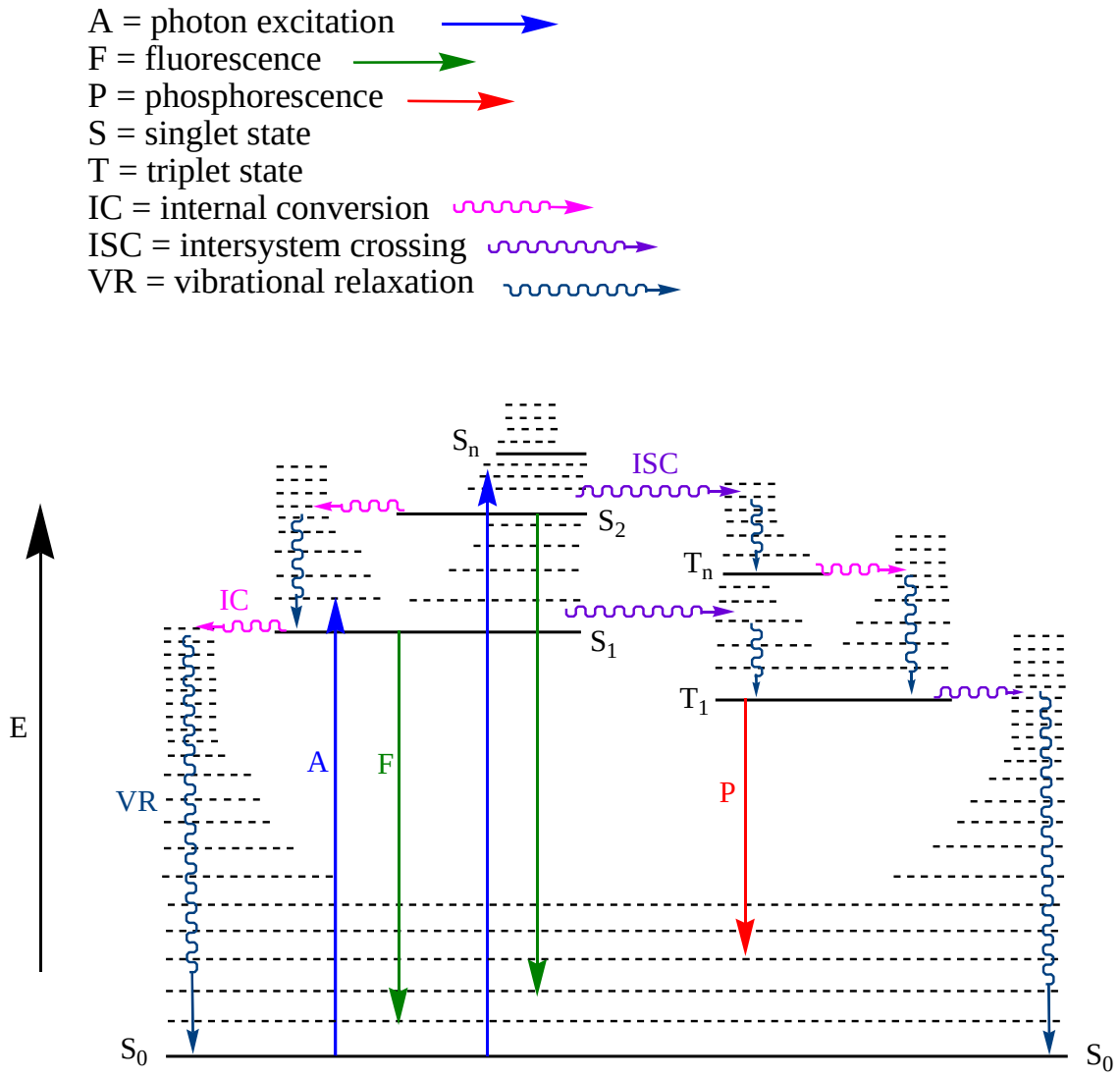

Fig. 1.1 A modified Jabłoński diagram for a typical polyatomic molecule with a singlet ground state. Only photophysical processes are concerned, where a solid line indicates a radiative transition and a wavy line represents a radiationless transition. The vertical energy scale has no particular meaning. Dashed horizontal lines schematically represent vibrational energy levels of each electronic state, and the rotational states of each vibrational state are not shown.

state. Γ is a general representation of the irreducible representation of a point group, to which a molecule belongs.[14] In group theory, for a centrosymmetric molecule with D_{4h} symmetry, according to the D_{4h} point group character table, the electron-paired singlet ground state (S_0) has A_{1g} symmetry, and is a $^1A_{1g}$ state. The first singlet excited electronic state (S_1) has E_u symmetry and is a 1^1E_u state. Similarly, 2^1E_u is for S_2 and 1^3E_u is for T_1, respectively.

For a single polyatomic molecule, each electronic state is associated with a number of vibrational states (shown in Fig. 1.1), each of which is in turn associated with a substantial number of rotational states (not shown in Fig. 1.1). Because electronic spectra of many polyatomic molecules are obtained in solution, the rotational structure of the bands is blurred; the vibrational structure may be present in weakly interacting solvents such as hydrocarbons, but most of the details have disappeared. Thus rotational states will not be concerned in this thesis.

Nonlinear, polyatomic molecules such as tetrapyrroles composed of N atoms possesses 3N-6 normal modes of vibration, each of which can be assigned to a particular symmetry species according to the character table of the molecular point group. For a molecule belonging to D_{4h} point group, the vibrations can be assigned to one of six possible symmetry species A_{1g}, A_{2g}, B_{1g}, B_{2g}, A_{1u}, A_{2u}, B_{1u}, B_{2u}, E_g, E_u appropriate to the D_{4h} character table. The total vibrational energy of the system is spread over all vibrations associated with the electronic state, resulting in different vibrational states associated with particular quantum numbers υ_i (υ= 0, 1, 2 … j; i = 1 to 3N-6). The number of vibrational states is thus large and increase rapidly with size and vibrational energy of the system. Population distributions of the molecules in vibrational states at thermal equilibrium follow the Boltzmann distribution. Under thermal equilibrium at room temperature without external perturbation, almost all molecules occupy the lowest energy vibrational level of the ground electronic state. Perturbation by photon absorption will populate the higher vibrational states associated with the excited electronic states by the choice of the photon energy absorbed (Fig. 1.1).

1.3 Unimolecular photophysical processes in polyatomic molecules

The external perturbation such as photon absorption may promote a molecule in the ground state to higher excited electronic states upon energy absorption. Electronically excited polyatomic molecules may undergo a number of possible processes to dissipate the excess electronic or vibrational energies. These processes are classified into two categories, photochemical processes and photophysical processes. Photochemical processes, such as decomposition, isomerization, ionization and excited state reaction, lead molecules to the final products that are different from those of photon absorbers.

On the other hand, electronically excited molecules can return back to their initial ground state by dissipating the excess energy to the surroundings either as heat via non-radiative means such as vibrational relaxation, internal conversion and intersystem crossing, or by the emission of photons via radiative pathways. These photophysical decay processes generally are associated with and strongly influence photochemical decay processes, and often decide the photochemical behavior of a molecule and reduce the quantum yield of a photochemical reaction to much less than unity. Therefore, for a complete understanding of a photochemical reaction, considerable interest resides in the study of photophysical processes.[1,13] This thesis only focuses on the photophysical processes of monomeric polyatomic molecules.

Transitions between two energy states of a molecule are either optically allowed or forbidden and are governed by transition selection rules. The general requirement of an electronic transition to be observed in an electronic spectrum is that the dipole integral, R, should not be zero.[14]

$$R = \int \psi'^{*} \mu \psi'' \, d\upsilon \neq 0 \qquad (1.1)$$

Here, μ is the electric dipole transition moment operator, ψ' and ψ'' represent the total wavefunctions of the upper and the lower electronic states, respectively. If the effects of the interaction with rotational states and the dependence of ψ_e on the nuclear coordinates (Born-Oppenheimer approximation) are neglected, eq 1.1 becomes

$$R_{e'e''\upsilon'\upsilon''} = \int \psi_e'^{*}(q, Q_0)\, \mu_e\, \psi_e''(q, Q_0)\, dV_e \int \psi_\upsilon'^{*}\, \psi_\upsilon''\, dV_\upsilon \neq 0 \qquad (1.2)$$

Here, q stands for all the electronic coordinates and Q_0 corresponds to a fixed molecular nuclei configuration near the equilibrium position of one of the two electronic states, ψ_e and ψ_υ represent the electronic wavefunctions and vibrational wavefunctions, respectively, μ_e is the electronic dipole moment operator. Subscripts e, υ represent electronic and vibrational states, respectively.[14]

When applying this general selection rule to a polyatomic molecule, the effects of the electron spin multiplicity, symmetry and parity of the molecule should be taken into account. Thus the following specific selection rules were developed in basis of the

above general selection rule: (i) The electron spin conservation rule ($\Delta S = 0$). Transitions between states of the different electron spin multiplicities are forbidden, but allowed for the same electron spin multiplicity. Forbidden transitions $S \nleftrightarrow T$ become possible in the presence of the perturbation of spin-orbit coupling, which introduces a weak interaction between two coupled states by removing their "pure" electron spin character. Thus $S \leftrightarrow T$ radiative phosphorescence emission can be observed. However, this kind of transition is usually too weak to be seen in the spectra of light molecules in solution. (ii) Parity (or Laporte) restriction. In a centrosymmetric molecule, electronic dipole transitions are allowed between electronic states of the different parity, $g \leftrightarrow u$ allowed, and $g \nleftrightarrow g$ and $u \nleftrightarrow u$ forbidden. However, transitions of $g \leftrightarrow g$ and $u \leftrightarrow u$ may be induced by vibronic coupling, in which non-totally symmetric vibrations mix electronic states of the same parity, or due to release of the inversion centre by instantaneous vibrations. As a consequence, parity-forbidden transitions can then be observed experimentally but with very weak intensity. (iii) Symmetry properties of the stationary states must be conserved. An electronic electric dipole transition is allowed only if the product of $\Gamma(\Psi_e') \times \Gamma(\mu_e) \times \Gamma(\Psi_e'')$ contains the totally symmetric irreducible representation of the molecular point group. Here Ψ_e' refers to the upper electronic wavefunctions and Ψ_e'' of the lower state. μ_e is the electronic electric dipole moment operator. However, symmetry forbidden transitions would occur via vibronic coupling to the vibrations with appropriate symmetry, if the overall symmetry of the vibronic state is able to produce a totally symmetric representation in the integrand of eq. 1.2.[14]

For those radiationless electronic transitions, which can occur but not be observed in the optical spectra, the electron spin, parity and symmetry selection rules are all applicable. Here the electric dipole operator μ_e in eq.1.2 is replaced by the nuclear kinetic energy operator or J_N for transitions between two electronic states of the same spin multiplicity. If radiationless electronic transition occurs between two electronic states with different spin multiplicity, both nuclear kinetic energy operator and spin-orbital coupling should be considered. In addition to these rules, there are some other requirements.[15-17] These requirements will be further explained in the radiationless transition theory in the later sections.

According to these selection rules, some possible electronic transitions involving the population and decay of higher electronically excited states, which are the subject of this thesis, in a polyatomic molecule are shown in Fig. 1.1 by a modified Jabłoński diagram. The initial act of absorption may promote a molecule in the lowest energy vibrational level of the ground state to higher excited states S_2, S_3 etc, or to higher vibrational levels of the S_1 state by the choice of the photon energy absorbed. The absorption is completed in a time period of 10^{-15} s. Electronically excited molecules can quickly lose the electronic energy of the S_2, and S_3 states on a time scale of picosecond (ps) or even less via internal conversion (IC) to the higher vibrational levels of the S_1 state. The rate constants of internal conversion *i.e.* $S_2 - S_1$ IC are *ca.* $10^{13} - 10^{12}$ s^{-1} the same as vibrational frequencies. Alternatively, in parallel with $S_2 - S_1$ IC, the electronic energy of the S_2 and S_3 states can be dissipated partly by emission of photons in violation of Kasha's rule in azulenes, thiones and some tetrapyrroles as mentioned at the beginning of this chapter. The following relaxation processes are associated with the depopulation of the S_1 state. Vibrational thermalization will carry the molecules from an initial distribution of higher energy vibrational levels to the zero vibrational level of the S_1 state via intramolecular vibrational redistribution (IVR) and intermolecular vibrational relaxation (VR). Once in the zero vibrational level of the S_1 state, the molecule may return to the ground state via several possible photophysical means. In absence of photochemical processes these are $S_1 - S_0$ radiative fluorescence emission, radiationless $S_1 - S_0$ IC and $S_1 - T_1$ intersystem crossing (ISC). These three processes are all possible, but typically one or two of them are dominant depending on their rate constants. The rate constants of the $S_1 - S_0$ IC is much smaller than that of the $S_2 - S_1$ IC because of the different energy gaps between two coupled electronic states. The rate constant of $S_1 - T_1$ ISC varies from 10^{11} to 10^{7} s^{-1} due to effects of spin restriction factor.[1] Relaxation dynamics of the first triplet states of molecules have been thoroughly studied[18] and will not be reported in this thesis.

In the following paragraphs, radiative and radiationless transition theories will be briefly introduced, emphasizing those materials that are essential in understanding and interpreting the vast difference among electronic transition rate constants.

1.3.1 Radiative transitions

Electronic transitions accompanied by photon absorption or emission are called radiative transitions. In Fig. 1.1 the blue solid arrows represent one-photon absorptions by molecules in the lowest energy vibrational level in the ground state that populate the higher energy vibrational levels of electronically excited states. The deep green solid arrows indicate the emission of a photon as fluorescence (if the states are of the same electron spin multiplicity), or as phosphorescence (if the two coupled states are of different spin multiplicity) as indicated by red solid arrow.

Franck-Condon principle and mirror image rule

Vibronic transitions result in the excitation of several vibrational states of an electronically excited state. The relative intensity of the vibrational bands in either absorption or emission spectra is determined by the Franck-Condon factor (F) of the individual vibronic transitions, which is the square of the overlap of the vibrational wavefunctions of the upper and lower states involved. The evaluation of the F is based on the Franck-Condon principle, which follows from the Born-Oppenheimer approximation and states that radiative electronic transitions occur without a change in the position or velocity of the nuclei in the molecule.[19] Thus, the Franck-Condon factors are evaluated for molecules in which nuclei are in fixed positions and thus the radiative electronic transition is also called a “vertical transition”.

In the case of little or almost no relative displacement between two potential energy surfaces of the ground state and the excited state, the most intense vibronic transition occurs from the lowest vibrational level ($\upsilon'' = 0$) of the ground state to the same vibrational level of the final state ($\upsilon' = 0$) for absorption and vice versa for emission. The most intense vibronic transition is always accompanied by several less intense vibronic transitions. However, in most polyatomic molecules, one-photon absorption results in a shift of the potential energy curve of the excited state to the longer equilibrium bonding distances relative to the ground state. Thus the most intense vibronic transition is from $\upsilon'' = 0$ to $\upsilon' = n$ (n = 1, 2, ...n) for absorption and $\upsilon' = 0$ to $\upsilon'' = n$ (n = 1, 2, ...n) for emission depending on the extent of the relative displacement of two potential energy surfaces and the photon energy absorbed. As a consequence, the absorption spectrum

reflects the vibrational characteristics of the electronically excited state and similarly, the fluorescence emission spectrum reflects those of the electronic ground state. For aromatic molecules with rigid structure, *e.g.* metalloporphyrins because the vibrational levels of the excited state are similar to those of the ground state, the fluorescence emission spectrum is the mirror image of the corresponding absorption spectrum. Exceptions to the mirror image rule occur in the cases that (i) if the lifetime of the excited state is sufficiently long enough to allow geometric rearrangement following absorption; (ii) presence of excited state reaction or complex formation, etc.[20]

The energy difference between the maximum of the fluorescence emission spectrum and the maximum of the corresponding absorption spectrum is called Stokes shift. The magnitude of the Stokes shift is an experimental measure of the extent of potential energy surface displacement in the excited state.

Radiative transition theory

The purpose here is not to review details of the development of the radiative theory, which is well established,[14] but to briefly introduce some materials which are necessary to interpret the data derived from the experimental measurements of the relaxation rates of highly excited electronic states of polyatomic molecules presented in this thesis.

In practice, it is useful to evaluate transition probabilities in terms of experimental measurable such as absorption intensities. The efficiency of one-photon light absorption follows the Beer-Lambert Law, eq. 1.3.[21]

$$A(\bar{\nu}) = \log_{10}(\frac{I_0}{I_d}) = \varepsilon(\bar{\nu})dc \qquad (1.3)$$

Here $A(\bar{\nu})$ is called the absorbance of the sample, the quantity $\varepsilon(\bar{\nu})$ (in $dm^3\ mol^{-1}cm^{-1}$) is the molar extinction coefficient, as a function of $\bar{\nu}$ in wavenumber, I_0 is the incident light intensity at d = 0, d is the thickness of the absorbing media in cm, while I_d is the transmitted light intensity at d = d, c (in mol dm^{-3}) is the concentration of a single absorbing species contained in the sample. A linear relationship between the absorbance and the molar concentration of the absorbing species is established. The presence of multiple absorbing species can be accommodated via

$$A(\bar{\nu}) = d \sum \varepsilon_i(\bar{\nu}) c_i \tag{1.4}$$

For electric dipole allowed electronic transitions, the magnitude of typical extinction coefficients, $\varepsilon(\bar{\nu})$, measured at the absorption maxima falls in the range of $10^4 - 10^5$ $dm^3\ mol^{-1}\ cm^{-1}$, while $10^2 - 10^3$ $dm^3\ mol^{-1}\ cm^{-1}$ for electric dipole forbidden electronic transitions.

The integrated absorption coefficient ($\int \varepsilon(\bar{\nu}) d(\bar{\nu})$) of a band in the uv-visible absorption spectrum is directly linked to the square of transition electric dipole ment, $|\mu_{fi}|^2$, so it is useful to introduce a quantity of dimensionless oscillator strength, f, of a transition, expressed in eq. 1.5.[19]

$$f = \left(\frac{4\pi m_e}{3e^2\hbar}\right)\nu_{fi}|\mu_{fi}|^2 = \left(\frac{4m_e c\varepsilon_0}{N_A e^2}\right)\int \varepsilon(\bar{\nu}) d(\bar{\nu}) \tag{1.5}$$

Here m_e is the electron mass and e is the electron charge, υ_{fi} is the frequency of the transition, the integral $\int \varepsilon(\bar{\nu}) d(\bar{\nu})$ is over the entire absorption bandwidth, $\hbar = h/2\pi$, where h is Planck's constant, c is speed of light, ε_0 is vacuum permittivity, N_A is Avogadro's constant. The quantity f has a maximum value of unity for an allowed transition of a free electron.

The radiative rate constant can be determined either by deconvolution of the experimental fluorescence decay profile or theoretically using the integrated areas of steady-state absorption and emission spectra according to the Strickler-Berg equation, eq 1.6.[22] If we assume that fluorescence emission is the only relaxation process of an electronic excited state, the reciprocal of the radiative rate constant is defined as the intrinsic radiative lifetime, τ_0, of the electronic excited state.

$$k_r = \frac{1}{\tau_0} = 2.88 \times 10^{-9} n^2 \langle \bar{\nu}_f^{-3} \rangle_{av}^{-1} \int \varepsilon(\bar{\nu}) d\ln\bar{\nu} \tag{1.6}$$

Here,

$$\langle \bar{\nu}_f^{-3} \rangle_{av} = \frac{\int \bar{\nu}^{-3} I(\bar{\nu}) d\bar{\nu}}{\int I(\bar{\nu})\, d\bar{\nu}}$$

and $I(\bar{\nu})$ is the fluorescence intensity in units of relative numbers of quanta, n is the refractive index of the solvent, and $\varepsilon(\bar{\nu})$ is the same as defined previously. $\langle \bar{\nu}_f^{-3} \rangle_{av}$ is the mean value of $\bar{\nu}_f^{-3}$ in the fluorescence spectra. Eq. 1.6 strictly applies only to strongly electric dipole allowed electronic transitions and the relative displacement of the two potential energy surfaces involved in the electronic transitions is small.[2] These two requirements are easily met for the metalloporphyrins studied in this thesis.

The fluorescence quantum yield, ϕ_f, which is the ratio of photons emitted to photons absorbed, describes the fractional probability that the excited state decays by emission of fluorescence. The value of ϕ_f can be related to important photophysical quantities using eq 1.7 in terms of lifetimes and eq 1.8 in terms of rate constants.

$$\phi_f = \frac{\tau_f}{\tau_0} \tag{1.7}$$

$$\phi_f = \frac{k_r}{k_r + \sum k_{nr}} \tag{1.8}$$

Here, τ_f is fluorescence lifetime, k_r is the rate constant of radiative decay and $\sum k_{nr}$ is sum of the rate constants of all radiationless processes by which the excited state decays. In practice, the absolute fluorescence quantum yield of compounds is hard to measure especially under the circumstances encountered in the present work described later in this thesis. Thus fluorescence quantum yields are measured relative to a carefully determined fluorescence standard. Details of measurements and calculations of the relative fluorescence quantum yields presented in this thesis will be described in Chapter 2.

Fluorescence lifetime of an electronic excited state, τ_f, which is an average value of the time spent by molecules in the excited state can be obtained directly by analysis of the time-resolved fluorescence decay profiles and is affected by both radiative and radiationless rate constants.

$$\tau_f = \frac{1}{k_r + \sum k_{nr}} \tag{1.9}$$

Eq. 1.9 can be derived by combination of equations 1.6 to 1.8. Substitution of 1.9 into 1.8 gives 1.10 and substitution of 1.10 into 1.8 gives 1.11.

$$k_r = \frac{\phi_f}{\tau_f} \tag{1.10}$$

$$\sum k_{nr} = \frac{1 - \phi_f}{\tau_f} \tag{1.11}$$

It is obvious that when $\phi_f << 1$, eq. 1.11 can be simplified to

$$\tau_f = \frac{1}{\sum k_{nr}} \tag{1.12}$$

Thus when the fluorescence quantum yield of an excited state is very small, the lifetime of the excited state is primarily determined by rates of its radiationless decay processes.

If a fluorescence quencher is present in solution, bimolecular fluorescence quenching processes can be competitive with the unimolecular emissive and radiationless decay processes mentioned above, resulting in an accelerated relaxation rate of the excited state and decreased fluorescence quantum yield.[23] If the rate constant of quenching is k_q, and the molar concentration of the quencher is M_Q, eqs. 1.8 and 1.9 should be modified to include the contribution of the quenching processes, as is shown in the following two equations.

$$\phi_f = \frac{k_r}{k_r + \sum k_{nr} + k_q M_Q} \tag{1.13}$$

and

$$\tau_f = \frac{1}{k_r + \sum k_{nr} + k_q M_Q} \tag{1.14}$$

Eqs. 1.10 to 1.12 are used to calculate the radiative and radiationless decay rate constants of the S_2 excited states of the tetrapyrroles examined in the present study, because, except for solvent, no quencher is present with high enough concentration to affect their ps decay rates.

1.3.2 Radiationless transitions

Transitions between electronic states that do not involve photon emission or absorption, but in which the electronic energy is converted into kinetic energy associated with nuclear motion are called radiationless transitions and are shown by wavy arrows in Fig. 1.1. Taking the possible relaxation passages of the S_2 state as an example, these include intramolecular vibrational redistribution (IVR) in the S_2 state, (intermolecular) vibrational relaxation (VR) to the surroundings, $S_2 - S_1$ internal conversion (IC) and $S_2 - T_n$ intersystem crossing (ISC). Each of them will be explained below.

Intramolecular vibrational redistribution and intermolecular vibrational relaxation

According to the symmetry selection rule and Franck-Condon principle described previously, only a few vibrational modes with large Franck-Condon factors are optically active in bridging electronic transitions. Upon light excitation, the deposited vibrational energy is initially concentrated in only these optically active vibrational modes and then rapidly redistribute among all vibrational modes available following the excitation at constant total energy of the excited molecule. This process is called intramolecular vibrational redistribution and is typically complete within a few ps or 100s of fs.

The excess energy of the excited molecule can be transferred to the vibrational modes of the surrounding medium via collisions or other interaction means between the excited solute and solvent molecules or the container. This process is called intermolecular vibrational relaxation. The efficiency of this energy transfer, because it involves the perturbation and mixing of the states of the two systems, depends how closely the energy separations of the excited molecules match those of the surroundings. As a consequence, the lifetime of an excited state may depend on the initial deposited vibrational energy and be affected considerably by varying of the solvents. In general the time scale of intermolecular vibrational relaxation taking to complete ranges from a few ps to tens of ps for polyatomic molecules in solution at room temperature conditions similar to those used in this thesis.[1,13]

Internal conversion and intersystem crossing

Radiationless relaxation processes of IVR and VR lead to vibrational relaxation of an electronically excited state. However, the fact that the fluorescence quantum yield of polyatomic molecules in solution is very small, $\phi_f < 1$, or even $\phi_f \ll 1$ for higher electronically excited states indicates that the electronically excited molecules also relax nonradiatively back to the ground state. Such radiationless processes include internal conversion and intersystem crossing.

Internal conversion is "a radiationless passage between two different electronic states of the same spin multiplicity".[18] Transitions such as from S_n ($n \geq 2$) to S_1, T_n ($n \geq 2$) to T_1 and S_1 to S_0 etc. are called internal conversion. Of particular interest in this thesis is the transition from highly excited singlet electronic states (S_n ($n \geq 2$)) to the lowest singlet excited state (S_1). Such radiationless transition between two "pure" electronic states consists of several possible steps. Taking the $S_2 - S_1$ internal conversion for an example, first is the rapid IVR to populate the thermalized S_2 state; following is the energy transfer between two equienergetic locations of two potential energy surfaces of the S_2 and S_1 states, which is followed by rapid VR processes in the S_1 state to dissipate the excess vibrational energy.[18] During the internal conversion processes, specific vibrations with the largest Franck-Condon factor in the lower state must act as acceptors of the energy difference between the two electronic states involved in the transition because of energy conservation restriction.[13] However, the rate at which molecules can accept large amount of vibrational energy is limited, thus the efficiency of IC is limited by energy separation between two electronic states involved. As will be discussed in the following text, this efficiency decreases with increasing the energy spacing of the two potential energy surfaces of the upper and lower electronic states.

Intersystem crossing is a radiationless passage occurring between two electronic states of the different spin multiplicity. These include radiationless transitions from S_2 to T_n, S_1 to T_1, T_1 to S_0 etc. Transitions between electronic states of the different spin multiplicity are highly forbidden because of spin prohibition, according to the transition selection rules introduced previously. However, this forbiddenness is relaxed by involvement of spin-orbital coupling, but the necessity of spin reorientation still retards (by up to *ca.* 10^6) the rate constants of the intersystem crossing processes, for transitions between two electronic states with identical conditions except spin multiplicity. Fur-

thermore, the intersystem crossing rate constant highly depends on the energy gap of two coupled electronic states.[18]

For polyatomic molecules in solution, the S_1 and T_1 states often are far separated from the ground state, thus radiationless transitions of $S_1 - S_0$ IC and $T_1 - S_0$ ISC is relatively slow.[15] Thus the rate of $S_1 - S_0$ fluorescence can be competitive, resulting in a relatively high fluorescence quantum yield. However, higher excited electronic states are almost always much more closely spaced with energy spacing *ca.* 1 eV or less, consequently, radiationless relaxation rates (10^{11}~10^{14} s^{-1} for $S_2 - S_1$ IC) of higher excited electronic states are usually much higher than the radiative rate and results in a low fluorescence quantum yield.[18]

Radiationless transition theory

Radiationless transition theory, which has been validated in a large number of molecular systems,[16,17] is briefly introduced here to provide those materials which are necessary to understand and interpret the radiationless relaxation processes of highly excited electronic states in polyatomic molecules. The model shown in Fig. 1.2 is used to discuss radiationless relaxation processes in polyatomic molecules.[16]

In this model, ϕ_0 is zeroth-order Born-Oppenheimer molecular ground state. ϕ_s and $\{\phi_l\}$ are zeroth-order Born-Oppenheimer molecular excited states, of which $\{\phi_l\}$ are dense manifold states lower in energy than ϕ_s. It assumes that the transition from ϕ_0 to ϕ_s is electric dipole allowed, *i.e.* $\mu_{0s} \neq 0$, while it is forbidden for the transition from ϕ_0 to $\{\phi_l\}$, *i.e.* $\mu_{0l} = 0$. Thus upon absorption of light with energy of $E(\phi_s)$–$E(\phi_0)$, only state ϕ_s is populated at time t = 0, while the dense manifold states $\{\phi_l\}$ are not. This is the case for intersystem crossing occurring from a singlet state ϕ_s to a manifold of triplet states $\{\phi_l\}$. However, $\mu_{0l} = 0$ is not a necessity for unpopulation of states $\{\phi_l\}$ at time t = 0. In the case of internal conversion, the radiationless transition occurs between two electronic states of the same multiplicity, and even though $\mu_{0l} \neq 0$, still only state ϕ_s is populated at time t = 0 upon absorption of light with energy of $E(\phi_s)$–$E(\phi_0)$ because of energy conservation and the degree of "forbiddenness" associated with populating a high vibrational state in $\{\phi_l\}$.

The molecules in ϕ_s state can either return back to the ground state associated with fluorescence, or nonradiatively "cross over" to isoenergetic levels of $\{\phi_l\}$. For an isolated molecule in the gas phase, a molecule in $\{\phi_l\}$ states can "resonate" back and forth

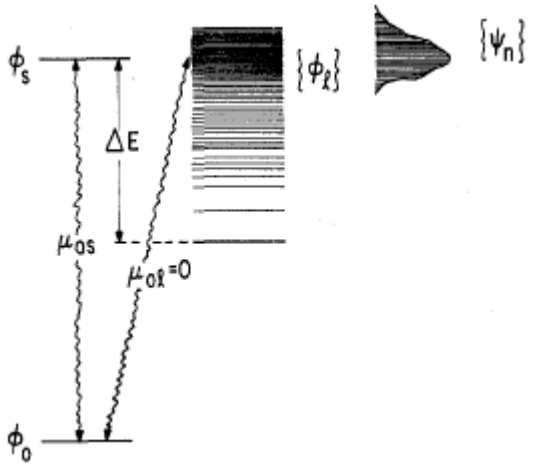

Fig. 1.2 The molecular energy level model used to discuss radiationless relaxation processes in polyatomic molecules (reproduced from reference 16).[16] ϕ_0 is the zeroth-order Born-Oppenheimer (BO) molecular state of the thermally populated ground electronic state vibrational levels. $\phi_s$is the zeroth-order BO molecular state of a vibronic component of an excited electronic state, with a nonzero dipole transition moment, $\mu_{0s} \neq 0$ connecting ϕ_0 and ϕ_s. $\{\phi_l\}$ is the zeroth-order BO molecular state corresponding to a dense manifold of excited vibronic levels whose electronic origin is below that of $\phi_s$and with the dipole transition moment connecting ϕ_0 and ϕ_l being zero, $\mu_{0l} = 0$. $\{\psi_n\}$ corresponds to the molecular eigenstates, ψ_n.[16,17]

between isoenergetic states of $\{\phi_l\}$ and ϕ_s state. Once back to the ϕ_s state, it will take the chance to fluorescent back to the ground state. These resonance processes continue until molecules decay back to the ground state resulting in $\phi_f = 1$. Here the time that it takes as the molecule resonates from $\{\phi_l\}$ back to ϕ_s is called the resonance time or Poincare recurrence time (τ_r).[16] The efficiency of resonance back to the ϕ_s state is determined by the relative density of vibrational states in the two coupled electronic states. For polyatomic molecules in condensed media, as the case studied in this thesis, the dense manifold states $\{\phi_l\}$ act as an energy sink, where excess vibrational energy is dissipated rapidly via vibrational relaxation carrying the molecule to lower $\{\phi_l\}$ levels from which it can no longer resonate back to ϕ_s because of insufficient energy,[16,17] and the low probability that the vibrational energy will be found again in the accepting modes.

The initially populated ϕ_s state is a nonstationary state, but it can be expressed as a superposition of the molecular eigenstates $\{\psi_n\}$ at t = 0 using (time-independent) expansion coefficients, C_n^s.[16]

$$\phi_s = \sum_n C_n^s \psi_n \tag{1.15}$$

Because each ψ_n with energy E_n evolves separately in time, a nonstationary state at time t is thus described by eq. 1.16.

$$\Psi(t) = \sum_n C_n^s \exp(-iE_n t/\hbar)\psi_n \tag{1.16}$$

The probability, $P_s(t)$, of find the excited molecule in its initial state ϕ_s at time t is

$$P_s(t) = |\langle\phi_s|\Psi(t)\rangle|^2 = \left|\sum_n C_n^s \exp(-iE_n t/\hbar)\right|^2 \tag{1.17}$$

If ϵ is the average energy level spacing of $\{\phi_l\}$, and the interstate interaction energy $V_{sl} = \langle\phi_s|H'|\phi_l\rangle$, when the conditions of $V_{sl} >> \epsilon$ and $\tau_d \ll \hbar/\epsilon$ (τ_d is the relaxation time of $\{\phi_l\}$ states) are satisfied, $P_s(t)$ shows an exponential decay as expressed in eq. 1.18.[24] Both conditions are easily fulfilled in typical, moderately large polyatomic molecules (statistical limit) such as those concerned in this thesis, thus ϕ_s state decays single-exponentially and irreversibly.

$$P_s(t) = \exp(-k_{nr} t) \tag{1.18}$$

The radiationless relaxation rate constant k_{nr} is given by the Fermi Golden Rule shown in eq. 1.19.[16]

$$k_{nr} = \frac{2\pi}{\hbar}\rho_l V_{sl}^2 \tag{1.19}$$

Here $\rho_l = 1/\epsilon$ is defined as the density of states of $\{\phi_l\}$, Eq. 1.19 can be further simplified as follows by separating V_{sl}^2 into an electronic coupling term (β_{el}^2) and a Franck-

Condon factor (F) on the basis of the Born-Oppenheimer approximation. Then the square of the energy of interaction between the two electronic states becomes

$$V_{sl}^2 = \beta_{el}^2 F \tag{1.20}$$

Thus k_{nr} can be expressed in terms of β_{el}^2 and F, as shown in eq. 1.21, which is the most popular form of the Fermi Golden Rule.

$$k_{nr} = \frac{2\pi}{\hbar}\rho_l \beta_{el}^2 F \tag{1.21}$$

Here the electronic coupling matrix element, β_{el}, depends only parametrically on the nuclear coordinates (Q_0), and q stands for electron coordinates.

$$\beta_{el} = \langle \psi_e'^*(q, Q_0) | H' | \psi_e''(q, Q_0) \rangle \tag{1.22}$$

To first order, the time-independent Hamiltonian H' contains only J_N, the nuclear kinetic energy operator in the case of internal conversion, while it also contains a spin-orbital coupling term in the case of intersystem crossing.[2]

In the weak coupling, statistical limit case, because the density of states and the electronic coupling matrix elements are insensitive to small variations in electronic energy spacings, the value of k_{nr} is mainly determined by the magnitude of F according to the Fermi Golden Rule (eq. 1.21).[25] The following discussion of F is restricted to the weak coupling, statistical limit case of radiationless transition theory.

The Franck-Condon factor, F asexpressed in eq. 1.23, is a squared vibrational overlap taken as averages over all interacting vibronic states.

$$F = \sum_a \sum_{j=1}^{3N-6} \langle \chi_i(Q_{ij}) | \chi_l(Q_{lj}) \rangle^2 \tag{1.23}$$

Here $\chi_i(Q_{ij})$ is the vibrational wavefunction of the higher of the two coupled vibronic states, and $\chi_l(Q_{lj})$ is that of the lower of the two coupled vibronic states. The magnitude of the F depends on several factors, including the relative displacement of the potential energy surfaces of the two electronic states, the number of quanta of vibrational energy

of a given mode needed to bridge the electronic energy gap and the frequencies of the vibrations. The vibrational overlap varies significantly with the number of quanta of vibrational energy in the accepting state, because the amplitude of a vibrational wave-function with large quantum number is relatively large near the turning points of the potential energy curve, but small otherwise as shown in Fig. 1.3. When the energy spacing is large and the relative displacement of the two coupled potential energy surfaces is small, *e.g.* between the S_0 and S_1 states, the vibrational overlap which occurs between

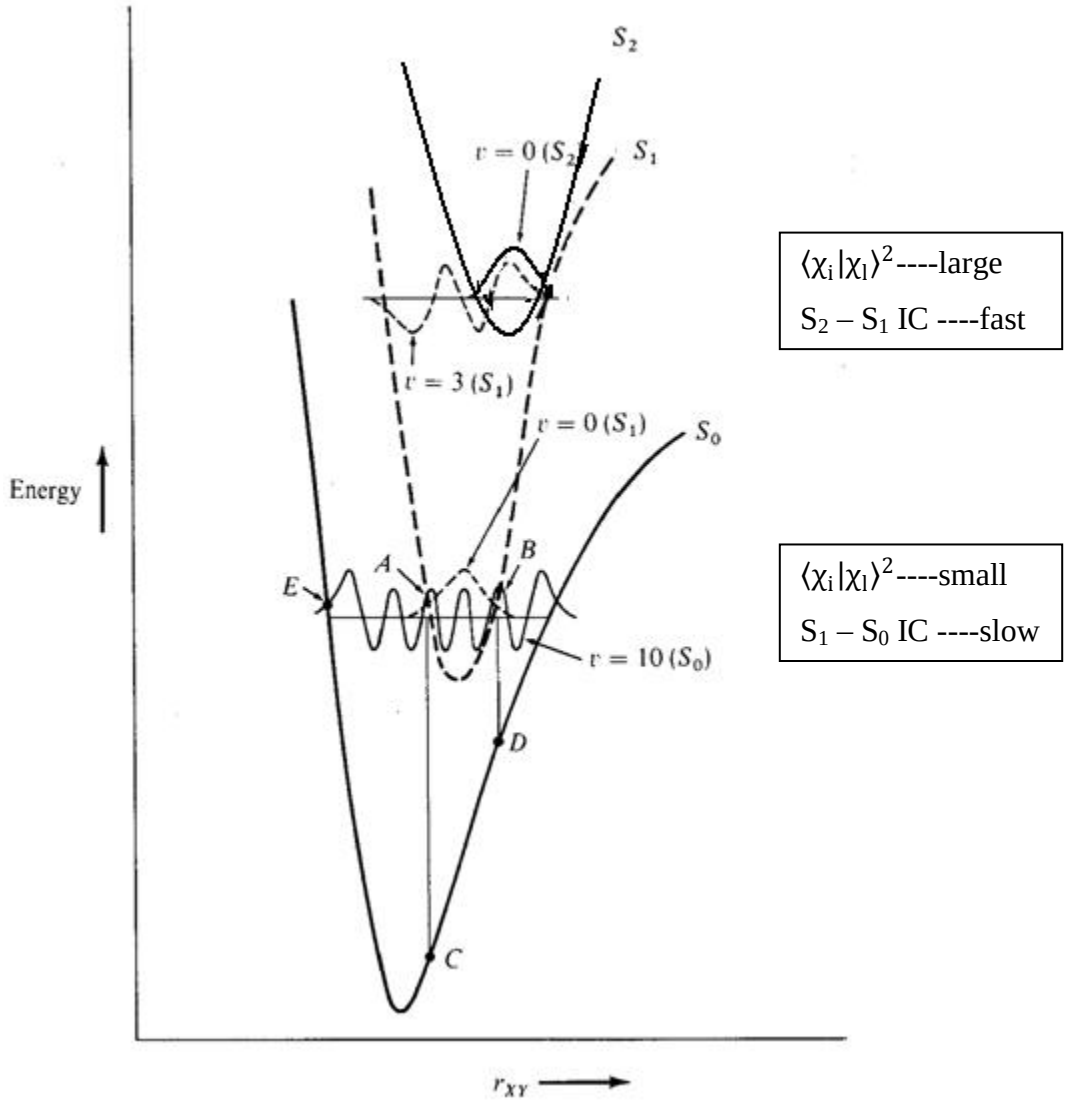

Fig. 1.3 Representation of change in Franck-Condon factor for $S_2 - S_1$ internal conversion when $\Delta E(S_2 - S_1)$ is small, and for $S_1 - S_0$ internal conversion where $\Delta E(S_1 - S_0)$ is large. Modified from reference 13.[13]

the centre of the vibrational wavefunction of S_1 state and that of the ground state is small, resulting in a relatively small Franck-Condon factor and thus slow $S_1 - S_0$ IC. However, for the S_2 and S_1 vibronic states, as shown in Fig. 1.3, the two potential energy surfaces are close to each other and the energy spacing $\Delta E(S_2 - S_1)$ is relatively small. As a consequence, the vibrational wavefunctions of the S_1 state which have smaller quantum numbers ($\upsilon = 3$ in the figure) have considerable overlap with the zero point vibrational wavefunction of the S_2 state, leading to a relatively large Franck-Condon factor and thus fast $S_2 - S_1$ IC.[13]

The magnitude of the Franck-Condon factors also depends on the frequencies of the vibrations involved in bridging the vibronic transitions. For a given energy gap between two coupled electronic states, due to conservation of energy, the vibrational state built from high frequency vibrations has the smallest quantum number. Thus the largest Franck-Condon factors are obtained for energy accepting modes with the highest frequencies, such as C–H stretching vibrations. For aromatic hydrocarbons, for example, a considerable deuterium isotope effect on the nonradiative transition probabilities would be expected due to the significant decrease in the Franck-Condon factors as a result of replacing C–H by C–D. This isotope effect on k_{nr} of $S_1 - T_1$ ISC has also been verified experimentally in many aromatic compounds.[18]

The quantitative correlation between the Franck-Condon factors and the quantum numbers of vibrational energy has been investigated by Siebrand.[25] For sufficiently large electronic energy spacing between two coupled electronic states, the Franck-Condon factors decrease exponentially with increasing vibrational quantum number of the accepting mode(s). Thus an inverse exponential dependence of k_{nr} on ΔE is expected, according to the Fermi Golden Rule (eq. 1.21).

In the case of internal conversion, the electronic coupling energy which depends parametrically on the nuclear coordinates can be affected by the relative displacement of the potential energy surfaces of the two coupled electronic states of the same electron spin multiplicity. As displayed in figure 1.3, if the relative displacement is substantial and two potential energy surfaces are close or even “cross”, as is the case between the S_2 and S_1 states, it leads to an intermediate to strong interstate electronic coupling.[13] On the other hand, as illustrated in Fig. 1.3 by the S_1 and S_0 states, if the two potential ener-

gy surfaces are almost parallel to each other, the electronic coupling energy between these two states is expected to be small. Calculations of the electronic coupling energy of weak coupling cases of radiationless transition theory will be described in the following section.

Energy gap law of radiationless transition theory in the weak coupling limit

Based on the approach of the Fermi Golden Rule, a correlation named the energy gap law (EGL) of radiationless transition theory was proposed by Englman *et al*.[15] It describes the relationships between k_{nr} and the electronic energy gap between the two coupled electronic states. At low temperature in the weak coupling limit, the EGL is expressed using an analytical form for F as eq. 1.24.

$$k_{nr} = \{\sqrt{2\pi}\beta_{el}^2/\hbar(\hbar\omega_M \Delta E)^{1/2}\}\exp\{-(\gamma/\hbar\omega_M)\Delta E\} \qquad (1.24)$$

where,

$$\gamma = \ln\{2\Delta E/d_M \hbar\omega_M \Delta_M^2\} - 1 \qquad (1.25)$$

The parameter β_{el} is the same as defined previously, γ is a function of the dimensionless reduced displacement parameter, Δ_M, and $\hbar\omega_M$ is the energy of the accepting vibrational modes with degeneracy d_M, and ΔE is the energy gap between the two coupled electronic states. The transformed relationship expressed in eq. 1.26 is derived by differentiation of the logarithm of the nonradiative rate constant from eq. 1.24. The values of $\sum k_{nr}$ can be calculated by measuring the fluorescence lifetimes, using eq. 1.11 or 1.12. Based on accurate measurements of steady-state absorption and emission spectra, the value of ΔE can be obtained. (The details of how to get this value will be explained in Chapter 2.). For a single radiationless decay process $\sum k_{nr}$ can be identified with k_{nr} in eq. 1.26.

$$\frac{d(\log_{10} \sum k_{nr})}{d(\Delta E)} = -\frac{1}{4.6\Delta E} - \frac{\gamma + 1}{2.3\hbar\omega_M} \qquad (1.26)$$

Graphs of the logarithm of the sum of nonradiative rate constants ($\sum k_{nr}$) versus the energy gap (ΔE) are called energy gap law plots. A straight line with a negative slope is expected if the experimental data conform to the weak coupling statistical limit of radiationless transition theory. Based on the value of the slope, the value of γ can be calculated for a given energy gap ΔE and a vibrational mode with a specific frequency. Thus the strength of the interstate electronic coupling energy can be evaluated by substituting the appropriate values of γ, ΔE, k_{nr} and $\hbar\omega_M$ into eq. 1.27, which is derived by rearrangement of eq. 1.26.

$$\beta_{el}^2 = \frac{k_{nr}\hbar(\hbar\omega_M \Delta E)^{1/2}}{\sqrt{2\pi}} \exp(\gamma \Delta E/\hbar\omega_M) \qquad (1.27)$$

As will be seen in later chapters, the values of the interstate electronic coupling energy are very important in the interpretation of the radiationless decay dynamics of the metallated tetrapyrroles studied in this thesis.

The deuterium isotope effect on k_{nr} can also be evaluated quantitatively using eq. 1.28, which is derived based on eq. 1.26. The frequency of an aromatic C–H stretching vibration is *ca.* 3000 cm^{-1}, while the C–D stretch is only *ca.* 2300 cm^{-1}. The ratio of the nonradiative rate constants of $S_2 - S_1$ internal conversion between the perhydro and the perdeuterated azulenes is thus estimated to be *ca.* 30 with a $\Delta E(S_2 - S_1)$ as 14000 cm^{-1}.[15] However, the ratio is rapidly decreased to *ca.* 2 for an energy gap of *ca.* 6800 cm^{-1}, typical of the metalloporphyrins.

$$\frac{k_{nr}^H}{k_{nr}^D} = \left(\frac{\hbar\omega_M^D}{\hbar\omega_M^H}\right)^{\frac{1}{2}} \exp\left(\Delta E\left(\frac{\gamma_D}{\hbar\omega_M^D} - \frac{\gamma_H}{\hbar\omega_M^H}\right)\right) \qquad (1.28)$$

Any factors, such as substitution, solvation and distortion of geometry in the excited state relative to the ground state can influence the nonradiatively decay rate indirectly via changing the energy gap and thus the magnitude of F and β_{el} between the two coupled electronic states. The energy gap law has been used successfully to explain the variation in the radiationless rate constants of the S_2 state of azulene and its derivatives,

and of the S_2 state of the aromatic thiones, where the $\Delta E(S_2 - S_1)$ energy gap has been modified by attachment of different substituents or by the use of solvents with different polarizability.[2,26,27]

In the following section, research regarding the photophysical properties of highly excited electronic states of tetrapyrroles will be reviewed. The experimental decay dynamics of their highly excited states have been rationalized using the theories introduced above. The work in this thesis mainly focuses on tetrapyrroles, in particular, metalloporphyrins and metallated corroles.

1.5 Literature review of the photophysical properties of higher excited states of tetrapyrrolic compounds

Porphyrins and related compounds are tetrapyrrolic compounds that help make the natural world a colorfully beautiful place to live. Because of their importance in nature and their widespread practical and proposed potential applications they have been, for many years, the subject of intense experimental spectroscopic and theoretical studies.[28,29] Applications, including use as catalysts, photosensitizers in photodynamic therapy, electrochemical sensors and receptors in donor-acceptor electron or energy transfer systems, have attracted considerable attention. Metalloporphyrins in particular, because of their high degree of photochemical stability, have been widely used as chemical and biological sensors,[30] and fluorescent probes.[31] They are also promising candidates for use in photo-actuated optoelectronic devices,[7,8] and solar energy harvesting systema.[9-12] More exciting and amazing examples of practical and potential applications of the porphyrins and related molecules can be found in references 20, 21, 28.[20,21,28]

For many years, information regarding the photophysical properties of highly excited electronic states of the metalloporphyrins and their participation in energy or electron transfer processes was lacking.[7] Motivated by the amazing applications of the metalloporphyrins, considerable efforts have been made recently to remedy this deficiency. To avoid the complexity due to the participation of intramolecular charge transfer states, the present study has been confined to the intramolecular relaxation dynamics of excited states of diamagnetic metalloporphyrins, where the d orbitals of the metal ion are either empty (d^0) or full (d^{10}). Metalloporphyrins containing open-shell metal ions have been

excluded. Excitation in the Soret absorption bands of such d^0 and d^{10} metalloporphyrins therefore cause transitions from the ground singlet state (S_0) to the second excited singlet state (S_2).

Before ps excited state lifetimes could be measured experimentally, the S_2 fluorescence lifetimes of the metalloporphyrins were estimated indirectly using integration of the Soret absorption band and measured emission quantum yields or by measuring the widths of homogeneously-broadened single vibrational bands in the isolated molecule. Thanks to the invention and application of femtosecond pulsed lasers, the time resolution and photon detection sensitivity necessary to directly measure ultra-short fluorescence lifetimes are now available. Direct experimental measurements thus now provide accurate data concerning the relaxation dynamics of the S_2 excited states of the metalloporphyrins. Two techniques, transient absorption and fluorescence upconversion, based on femtosecond laser sources are now routinely utilized. (Details of these techniques will be explained in chapter 2.) The following paragraphs review recent developments regarding the decay dynamics of highly excited electronic states of the tetrapyrroles and related molecules.

1.5.1 Intramolecular photophysical relaxation of highly excited electronic states of ZnTPP

ZnTPP has been adopted as a model metalloporphyrin by researchers. The lowest energy transition in the visible region is the $1^1E_u \leftarrow {}^1A_{1g}$ band spectrum often referred to as the Q bands in the metalloporphyrins. The most prominent feature of the near uv-visible absorption spectrum in solution is the intense Soret (B) band ($2^1E_u \leftarrow {}^1A_{1g}$) with a main peak at 420 nm and a shoulder centered at 400 nm. The positions of both the main Soret band and its shoulder and the ratio of the relative intensities of these two bands vary with the polarizability of the solvent. There is some controversy among experimentalists and theorists regarding the assignment of the transitions occurring to the excitation in the Soret band and its shoulder.[23]

The dynamics of its S_2 state has now been extensively studied. Even *et al.*[5,32,33] estimated an S_2 lifetime of ZnTPP of 1.0 ps by measuring the width of the homogenously-broadened vibrational bands in the $S_2 \leftarrow S_0$ fluorescence excitation spectra in a su-

personic expansion. These experiments also provided the most accurate value of the $S_2 - S_1$ energy gap ($\Delta E(S_2 - S_1)$), 7763 cm^{-1} in the bare molecule. Later Chosrowjan *et al.*[34] studied the decay dynamics of the S_2 state of ZnTPP in CH_3CN and CH_2Cl_2. By using both fluorescence upconversion and transient absorption technologies, they were able to directly measure the ultra-short S_2 lifetime, which exhibited single exponential decay kinetics with τ = 3.5 ps (λ_{ex} = 380 nm, λ_{em} = 428 nm) in CH_3CN, and a much shorter lifetime of 0.75 ps ((λ_{ex} = 380 nm, λ_{em} = 425 nm) in CH_2Cl_2. The shorter S_2 lifetime in CH_2Cl_2 was attributed to the participation of fast intermolecular electron transfer from the S_2 excited state to the solvent molecules. In both solvents, intramolecular decay of the S_2 state is governed by $S_2 - S_1$ IC. Later, Gurzadyan *et al.*[35] further investigated the relaxation dynamics of the S_2 state of ZnTPP in ethanol and other solvents by measuring both the S_2 decay and S_1 rise fluorescence lifetimes using fluorescence upconversion techniques. The S_2 lifetime in ethanol was measured to be 2.35 ps (λ_{em} = 430 nm) which was the same as the S_1 rise time (λ_{em} = 600 nm) when both were excited at 394 nm. Equal S_2 decay (1.7 ps) and S_1 rise (1.7 ps) time were confirmed by their later experiments of ZnTPP in DMSO, by using the same techniques.[36] A measured short S_2 rise time component of *ca.* 60 to 90 fs was ascribed to IVR in the S_2 state. They inferred that a similar IVR processes should occur in the S_1 excited state, but its time constant was too fast to be distinguished from the S_1 rise time. Mataga *et al.*,[37,38] also observed a single exponential decay of the S_2 state of ZnTPP in ethanol, with a time constant *ca.* 2.3 ps (λ_{ex} = 405 nm, λ_{em} = 430 nm,), identical to the S_1 rise lifetime (λ_{ex} = 405 nm, λ_{em} = 600 nm,). Their results are in excellent agreement with those previously obtained by Gurzadyan *et al.*[35] and Shibata *et al.*[38] In addition, Enescu *et al.*[39] also detected the S_2 lifetime of 2 $\pm$ 0.2 ps (λ_{ex} = 404 nm) for ZnTPP in ethanol, but measured an IVR time within the S_2 state of 150 fs, slightly longer than 60 to 90 fs obtained by Gurzadyan *et al.*[35] Besides, Yoon *et al.*[40] using femtosecond coherence spectroscopy examined the decay dynamics and potential curvatures of excited states of ZnTPP. For ZnTPP in toluene, upon excitation at 406 nm, they detected an ultrafast initial rise time of 89 fs for the S_2 state, followed by subsequent $S_2 - S_1$ IC with a decay time of 1.2 ps. The S_2 decay of 1.2 ps is slightly shorter than 1.58 ps obtained by Gurzadyan *et al.*,[36]

but the 89 fs rise time is consistent with the 60 to 90 fs components obtained by them for ZnTPP in ethanol.

One should note that, in the experiments described above, the authors used solutions with high ZnTPP concentrations without examining the possible effects of (i) solute aggregation and fluorescence reabsorption, and (ii) the intensity of the excitation laser pulse, which, at high peak power, can easily induce two-photon absorption. Nevertheless, based on the identity of the S_2 decay and S_1 rise times observed for ZnTPP in ethanol, these experiments rule out the existence of any additional long-lived electronic states lying between the S_2 and S_1 states, that could contribute to the radiationless depopulation of the S_2 excited state, via processes bypassing $S_2 - S_1$ IC. The decay dynamics of the S_2 state can be pictured as follows up to this stage. First, the initially populated S_2 vibrational states quickly dissipate the total vibrational energy via IVR within 100 fs. Secondly, the S_2 state decays through a highly efficient nonradiative $S_2 - S_1$ IC (with efficiency close to unity) to produce vibrationally excited levels within the S_1 state. This is immediately followed by the rapid IVR and VR in the S_1 state, yielding a thermalized series of S_1 vibrational states. The susequent decay passages are associated with the depopulation of the S_1 electronic state. The parallel $S_2 \rightarrow S_0$ emission process has a very small fluorescence quantum yield, *ca.* 10^{-3}, and is slow compared to $S_2 - S_1$ IC. Whether other possible decay pathways such as $S_2 - T_n$ as found in azulene and its derivatives are presented in ZnTPP is not reported yet.

More recently, Yu *et al.* have conducted detailed, systematic experiments to study the relaxation dynamics of the S_2 excited state of ZnTPP in benzene and CH_2Cl_2, using both transient absorption and fluorescence upconversion techniques.[41] In their experiments, concentrations of solutions are low enough to minimize the effect of fluorescence self-quenching due to the presence of solute aggregates, and any effects due to fluorescence reabsorption. They also found that high laser powers can induce multiple photon absorption when ZnTPP is excited in the Soret band. They therefore used low laser power to avoid this problem. Yu *et al.* measured the S_2 fluorescence lifetime of ZnTPP in CH_2Cl_2 and obtained a single exponential decay lifetime of 1.9 ps, which is in agreement with value of 2.0 ps previously reported by Gurzadyan *et al.*[36] These two lifetimes, for ZnTPP in CH_2Cl_2, are much longer than 0.75 ps previously reported by

Chosrowjan *et al.*[34] However, on the basis of transient absorption measurements Yu *et al.* agreed with the previous interpretation of the existence of fast electron transfer from the S_2 state of ZnTPP to electron accepting solvent molecules, but they emphasized the importance of the orientation between the solute and solvent molecules in order to facilitate electron transfer. Gurzadyan *et al.*[36] attribute the short lifetime 0.75 ps of ZnTPP in CH_2Cl_2 obtained by Chosrowjan *et al.*[34] to a contribution from the Raman scattering of the solvent or of scattered excitation light, *i.e.* the previous observation was misinterpreted. The real lifetime of *ca.* 2.0 ps, which is slight shorter than that of ZnTPP in ethanol, can be ascribed to the effect of the solvent-induced differences in the $\Delta E(S_2 - S_1)$.

However, the decay dynamics of the S_2 state of ZnTPP in benzene reported by Yu *et al.* is even more complicated.[41] They observed that the S_2 population decay time of 1.45 ps (λ_{em} = 430 nm) is different from the corresponding S_1 (λ_{em} = 560 ~ 650 or 680 nm) population rise time (1.15 ps,) upon one-photon excitation at 397 nm for both cases, but the S_2 population decays biexponentially with two time constants, 200 fs and 1.0 ps, upon two-photon, one-color absorption at 550 nm. However, they didn't observe the ultra-short IVR time of 150 fs reported by Enescu *et al.*[35] and Gurzadyan *et al.*[39] The difference between S_2 decay and S_1 rise times is contrary to their identity as reported previously by Gurzadyan[35] and Mataga[37] groups. To interpret this difference for the first time, Yu *et al.* proposed the existence of an excited state designated as S_2', with an energy slightly above the S_2 state. They thus concluded that the Soret band contains contributions from two different excited electronic states (S_2 and S_2').

Evidence supporting the existence of the S_2' state was later found by Karolcazk *et al.*[42] and Lukaszewicz *et al.*[43] who reported that the S_1 fluorescence quantum yields of ZnTPP in ethanol depend somewhat on the excitation wavelength when varying it from the blue to the red edge of the Soret band. Although they agreed with the existence of the S_2' state, they proposed that the S_2' state was nearly degenerate with or lower in energy than the S_2 state, and that it's decay channels include both $S_2' - S_1$ IC to populate S_1 and ISC to the T_n state or nonradiative $S_2' - S_0$ IC to the ground state. They also found that this S_2' state is nonfluorescent and they designated it as a "dark" state. However, the dependence of the S_1 fluorescence quantum yields on the excitation wave-

lengths is in disagreement with the conclusion drawn by Kubayashi *et al.*,[4] who concluded that the S_1 fluorescence quantum yields are independent on the excitation wavelengths ranging within the entire absorption spectrum.

More evidence supporting the existence of another electronic state in the vicinity of the S_2 state was provided by Tobita *et al.*,[44] who investigated the formation the S_2 state of ZnTPP in EPA using two-photon absorption techniques. They found that the S_2 state is produced subsequent to stepwise one-color, two-photon absorption via the S_1 state, and obtained a large absorption cross section for the $S_n \leftarrow S_1$ transition, comparable to that of the $S_2 \leftarrow S_0$ transition. To interpret the large $S_n \leftarrow S_1$ cross section obtained experimentally, they conducted ab initio molecular orbital calculations. Despite the poor accuracy of their calculations, their results and those of previous screened potential calculations[45] did reveal the presence of singlet and triplet excited states of A_{1g}, A_{2g}, B_{1g}, and B_{2g} symmetry at energies higher than the 2^1E_u state. Surprisingly, however, they found no states lying between the 1^1E_u and 2^1E_u states. Thus they proposed that a $^1A_{2g}$ state, populated via a strongly electric dipole allowed transition from the 1^1E_u (S_1) state, was responsible for the large absorption cross section of the $S_n \leftarrow S_1$ transition.

The latest calculations done by the Baerends[46] and Ziegler[47] groups using an improved TDDFT/SAOP method, provide more accurate information about the properties of the excited states of metalloporphyrins and phthalocyanines. For example for ZnP, their calculations predict that the 2^1E_u state at 3.24 eV, is almost degenerate with the 3^1E_u state at 3.32 eV, and that the one-photon transitions to these two states have comparable oscillator strength. Thus they suggest that two transitions (to the 2^1E_u and 3^1E_u states) contribute to the main Soret band in the spectra observed in solution. However, Nguyen *et al.*[48,49] and Parcel *et al.*,[50] using the TDDFT/B3LYP method predicted that the 3^1E_u state has a higher energy and assigned it as the shoulder to the blue side of the main Soret band. The very recent calculations reported by Solheim *et al.*[51] confirm that the 3^1E_u state, with a significantly higher energy, is well separated from the 2^1E_u state, and conclude that 2^1E_u is the only excited state that contributes to the Soret bands in the absorption spectra observed in solution. Experimentally, based on the laser-induced fluorescence excitation spectra of ZnTBP obtained in seeded pulsed supersonic expansion

experiments, Even *et al.*[52] considered the shoulder to the blue side of the main Soret band to a vibronic feature, instead of a distinct electronic excited state.

Considerable uncertainty regarding the assignments of the Soret and higher energy electronic transitions exists at the time this thesis was written.

1.5.2 Intramolecular photophysical relaxation of highly excited electronic states of tetrapyrrolic compounds other than ZnTPP

The intramolecular photophysics of the Soret-excited states of some metalloporphyrins other than of zinc porphyrins with different substituents and of tetrapyrroles with different macrocycles have also been studied. The initial report of weak emission from the S_2 excited states of metalloporphyrins was made by Bajema *et al.* in the 1970s,[53] for zinc tetrabenzoporphyrin (ZnTBP) in octane containing 0.5% pyridine. Its S_2 fluorescence quantum yield was measured to be 1.6×10^{-3} and its S_2 lifetime was estimated to be *ca.* 2.4 ps using the Strickler-Berg equation. A decade later, using a similar method, Tsvirko *et al.*[54] estimated the S_2 decay times for a series of lanthanide tetra-para-tolylporphyrin complexes, and found that the lifetimes fell in the range of 0.2 to 5.4 ps. Despite the error that may be introduced in this kind of estimation, they nevertheless, proved that the S_2 lifetimes of these metalloporphyrins were no more than few ps, comparable to that of ZnTPP.

Later, Even *et al.*,[5,6,32,33] conducted a series of studies of the spectroscopic properties of metalloporphyrins, using the technique of laser-induced fluorescence spectroscopy in seeded pulsed supersonic expansions, where the molecules are ultra-cold and isolated. They obtained S_2 lifetimes of 4 ps for ZnTBP and ~ 1 ps for MgTPP, by examining the widths of the homogenously-broadened vibrational bands in the $S_0 \leftarrow S_2$ fluorescence excitation spectra. Unfortunately, they didn't observe S_2 emission from ZnOEP due to detection limitations at that stage. However, the available results are in good agreement with the order-of-magnitude estimates of the S_2 lifetimes initially reported from steady-state measurements. These spectroscopy experiments obtained under supersonic expansion conditions also provided the most accurate values of the $\Delta E(S_2 - S_1)$ energy gaps by obtaining the exact energies of the $S_2 - S_0$ and $S_1 - S_0$ band origins. The $\Delta E(S_2 - S_1)$ energy gap for ZnTBP was determined to be *ca.* 8953 cm^{-1} for ZnTBP which is larger

than that of other metalloporphyrins. As mentioned in section 1.3, the probability of radiationless transition between the S_2 and S_1 electronic states in the metalloporphyrins is related to the $\Delta E(S_2 - S_1)$ energy gap. As will be seen in later chapters, this information is crucial in any discussion of the correlation between the electronic structure and the relaxation dynamics of the excited states of the metalloporphyrins considered in this thesis.

Of particular interest is the result for H_2TPP reported by Even *et al.*[32] The presence of the proton-proton axis in H_2TPP leads to a lower symmetry of D_{2h} rather than the D_{4h} of ZnTPP. This lower symmetry effect results in the appearance of two $S_1^x \leftarrow S_0$ and $S_1^y \leftarrow S_0$ transitions, and the degeneracy of the S_1 state is lifted in H_2TPP. They proposed that the S_2 state of H_2TPP consists of two closely lying states, S_2^x and S_2^y, but only evidence of the transition $S_2^x \leftarrow S_0$ (the B_x band) was observed in its gas-phase fluorescence excitation spectrum, which has features similar to those of $S_1^x \leftarrow S_0$. Evidence of the transition $S_2^y \leftarrow S_0$ was, unfortunately, not observed. Based on the widths of the homogenously-broadened vibrational bands of the fluorescence excitation spectrum, the best estimate of the lifetime of the S_2^x state was at least 5 ps. Very recently, Baskin *et al.*[55] conducted a detailed study of the S_2 decay dynamics of H_2TPP in benzene using both fluorescence upconversion and transient absorption techniques with femtosecond time resolution. They determined that the S_2 state of H_2TPP decays in less than 50 fs to the S_1^y state via $S_2 - S_1^y$ IC, followed by ultrafast intramolecular vibrational energy redistribution to populate S_1^x, and then via intra- and intermolecular vibrational relaxation leading to a thermal equilibrium in the S_1^x state. This result is consistent with previous reports of an S_2 excited state lifetime of tens of femtoseconds obtained in $CHCl_3$,[56] and is also in agreement with its extremely low S_2 fluorescence intensity, which is usually hard to observe in solution using steady-state spectroscopy method.[57]

Gurzadyan *et al.*[36] conducted a systematic study of the S_2 decay of MgTPP in several solvents and measured S_2 lifetimes of 3.25 ps in ethanol, 2.85 ps in CH_2Cl_2, and 2.40 ps in DMSO. They have explained the solvent-induced differences of the S_2 lifetimes on the basis of the energy gap law. However, these lifetimes are much longer than *ca.* 1 ps obtained by Even *et al.*[52] using homogeneous-broadening method.[6] This lifetime is

much shorter than that obtained by Mataga *et al.*[37] who investigated the relaxation dynamics of the S_2 excited state of zinc 5,15-diphenylporphyrin (ZnDPP), and obtained similar results to ZnTPP. Kurabayashi *et al.*[4] examined the effect of the central metal ion on the decay dynamics of the S_2 state of various metalloporphyrins. They measured the S_2 fluorescence quantum yields for AlClTPP and CdTPP (TPP = tetraphenylporphyrin) in acetonitrile at room temperature, and estimated the radiative and nonradiative rate constants of the S_2 state using the Strickler-Berg equation. Comparing to ZnTPP, the S_2 fluorescence quantum yields are in the order, AlClTPP > ZnTPP > CdTPP. They also found that the $S_1 \rightarrow S_0$ fluorescence quantum yield does not depend on whether the excitation wavelength is in the Q band or the Soret band, and they thus concluded that the dominant nonradiative relaxation channel of the S_2 states in these metalloporphyrins is $S_2 - S_1$ IC. They proposed that the absence of S_2 emission in the free base H_2TPP, and in most β–octaethylporphyrin (OEP) complexes such as H_2OEP, AlClOEP and ZnOEP, is due to much more rapid $S_2 - S_1$ IC compared with ZnTPP.

More detailed and systematic studies of the effects of substituents and central metal ion on the S_2 relaxation dynamics of diamagnetic metalloporphyrins have been made by Ohno *et al.*[58] and Kobayashi *et al.*,[57] using steady-state spectroscopy. Based on study of a wide set of diamagnetic metalloporphyrins, they found that the $\Delta E(S_2 - S_1)$ energy gap and the S_2 fluorescence quantum yields are dependent on the nature and pattern of substitution and on the nature of the central metal ion. However, for the same porphyrin macrocycle substitution pattern, variation of the central metal ions didn't greatly influence the S_2 fluorescence quantum yields. They thus concluded that the $S_2 - T_n$ ISC is not important in the nonradiative relaxation of the S_2 state of diamagnetic metalloporphyrins. Consistent with previous reports, the S_2 fluorescence from ZnOEP in benzene was not observed, but it was observed for PbOEP. Thus they proposed that one reason for the absence of S_2 fluorescence in most OEP complexes except PbOEP is due to the presence of a substantial number of high frequency C–H vibrations, which act as energy accepting modes in the $S_2 - S_1$ radiationless decay.

Using femtosecond coherence spectroscopy techniques, Yoon *et al.*[40] examined the decay dynamics and potential surface curvatures of the excited states of ZnOEP. Due to the limitation of the time resolution of the technique, they were unable to detect the S_2

lifetime of ZnOEP in toluene, but inferred from its resonance Raman spectra that the lifetime should be less than 20 fs. They attribute the ultrafast relaxation of the S_2 state in ZnOEP to the conical intersection of the potential energy surfaces of the S_2 and S_1 states. A similar mechanism previously reported by Zhong *et al.*[56] was used to interpret the absence of S_2 emission from H_2TPP in $CHCl_3$ solution. However, this mechanism cannot be inferred to ZnOEP, because in ZnOEP, the two interacting states S_2 and S_1 have the same symmetry and thus conical interactions between two coupled potential energy surfaces are avoidable.

LeGourriérec *et al.*[59] have measured a lifetime of 1.6 ps for the S_2 state of zinc 5,10,15,20-tetrakis(4-methylphenyl)porphyrin (ZnTTP) in DMF by using pump-probe spectroscopy. In another experiment, Akimoto *et al.*[60] using a femtosecond fluorescence upconversion method, made precise measurements of the decay dynamics of the S_2 state of zinc 2,8,12,18-tetraethyl-3,7,13,17-tetramethyl-5,15-di (3,5-di-t-butylphenyl) porphyrin (ZnEMBPP) and its free base in benzene. In the zinc derivative, they measured an S_2 population decay of 150 fs as the same as S_1 population rise time. The S_2 lifetime of the free base was too short to be detected under their experimental conditions, and was inferred to be less than the resolution limit of 40 fs. Comparing to ZnTPP, the relaxation rates of the S_2 states of these two molecules are very fast.

Maiti *et al.*[61] found that a series of zinc basket-handle porphyrins exhibit red shifts of both the S_1 and S_2 emission spectra and decreased fluorescence quantum yields compared to similar planar derivatives. They concluded that the deformation of the porphyrin ring enhances $S_2 - S_1$ IC, due to a reduced $\Delta E(S_2 - S_1)$ energy gap. Gupta *et al.*[62] studied the spectroscopic properties of a series of *meso*-tetrathienylporphyrins with heteroatom substituted porphyrin cores and found that modification of the porphyrin core significantly alters the electronic structure and decreases the lifetime and fluorescence quantum yields of the S_1 state.

Porphyrin variants, with expanded, contracted or heteroatom-substituted porphyrin macrocycles, constitute special families of tetrapyrrolic compounds.[63] Of particular interest here are the porphyrinoids with contracted cavities, which constitute a family named corroles, since they have a macrocycle skeleton identical with the cobalt-chelating corrin of vitamin B_{12}. It was found recently that corroles, especially their me-

tallated derivatives, show remarkable electronic and photophysical properties that have suggested their applications as catalysts and sensors, and offer promise for use in dye-sensitized solar cells and some medical applications.[64]

The concern in this thesis focuses on the potential applications of corroles in the design of dye-sensitized solar cells. Such applications involving energy and/or electron transfer between the excited corroles and other components in the solar cell. To date, no attention has been paid to the photophysical properties of their highly excited electronic states, even though these states may be involved in electron and/or energy transfer processes in their photo-actuated applications. The initial research into their participation in dye-sensitized solar cells shows that some corroles with particular substituents have high electron transfer efficiencies, while some others have very low such efficiency. Thus it is worthwhile to study the photophysical properties of their highly excited electronic states in order to make more efficient applications.[64] The relevant literature will be reviewed in chapter 6.

1.5.3 Correlation between radiationless relaxation of high excited states and the energy gap law

The correlation between electronic structure and nonradiative rate constant predicted by the energy gap law has been successfully used to interpret the photophysical properties and relaxation dynamic behavior of the S_2 states of azulene and its derivatives,[26,27] and of the aromatic thiones.[65]

To examine whether or not this correlation can be applied to tetrapyrroles and their derivatives, a systematic study of the photophysics of the S_2 excited state of metalloporphyrins was conducted by Kurabayashi *et al.*[4] In their experiments, several metalloporphyrins (AlClTPP, ZnTPP and CdTPP) have been investigated in acetonitrile at room temperature. The S_2 fluorescence quantum yields were measured and the radiative and nonradiative rate constants of S_2 state were estimated based on these measured quantum yields. Plots of the natural logarithm of the nonradiative rate constants versus the $S_2 - S_1$ energy gap (ΔE ($S_2 - S_1$)) showed a good linear relationship. It seems that the nonradiative $S_2 - S_1$ relaxation of the S_2 state follows the predictions of the energy gap law of radiationless transition theory in the weak coupling limit. However, based on the slope

of this energy gap law plot, they estimated the value of the $S_2 - S_1$ interstate electronic coupling energy, which was much too large to be assigned as the electronic coupling energy between the S_2 and S_1 states in the weak coupling limit. This value though not further explained by Kurabayashi *et al.*[4] indicates that the interaction between S_2 and S_1 states might be different from the weak coupling case in the metalloporphyrins.

More detailed and systematic studies of a set of metalloporphyrins with different substituents or central metal ions have been carried out by Ohno *et al.*[58] using steady-state spectroscopy. Later their work, together with other work regarding the S_2 emission of metalloporphyrins not of concern here, was comprehensively reviewed by Kobayashi et al,[57] who calculated the $S_2 - S_1$ energy gap and S_2 quantum yields of all the molecules under study. Based on their results, they agreed that the nonradiative $S_2 - S_1$ IC process entirely dominates the relaxation of the S_2 states of the porphyrins and metalloporphyrins. They proposed that the absence of S_2 fluorescence in most OEP complexes and free-base porphyrins is due to strong interstate coupling between the S_1 and S_2 states. In order to evaluate the extent of coupling in different porphyrins, they correlated the intensity ratios $\varepsilon(0,0)/\varepsilon(1,0)$ of the Q(0,0) and Q(1,0) bands, which they suggested reflects the extent of vibronic coupling between the S_2 and S_1 states, to the $\Delta E(S_2 - S_1)$ energy gap. They found that the $\Delta E(S_2 - S_1)$ energy gap of ZnOEP (7210 cm^{-1}, in benzene) is greater than ZnTPP (6690 cm^{-1}, in benzene), and noted that this is consistent with the intensity ratios of the $\varepsilon(0,0)/\varepsilon(1,0)$, ZnOEP (1.81) > ZnTPP (0.16). Thus they concluded that "an increase of $\Delta E(S_2 - S_1)$ in ZnOEP enhances admixing of the Q and B states and thus the $S_2 - S_1$ internal conversion is promoted in ZnOEP much more than in ZnTPP".[58] In fact, according to the energy gap law of radiationless transition theory (weak coupling, statistical limit case), a large ΔE results in a slow $S_2 - S_1$ IC and a long-lived S_2 fluorescence. Kobayashi *et al.* proposed that potential energy surfaces of the S_2 and S_1 states were not perfect parallel leading to a big Franck-Condon overlap and promoting nonradiative $S_2 - S_1$ IC. As will be discussed in later chapters, strong $S_2 - S_1$ interstate coupling does occur in ZnOEP, but this is definitely not due to the large $\Delta E(S_2 - S_1)$ energy gap. It will be shown that the changes in the Franck-Condon factor are also insufficient to account for the ultrafast relaxation of the S_2 state in ZnOEP.

Using a femtosecond fluorescence upconversion method, Akimoto *et al.*[60] have precisely examined the decay dynamics of the S_2 state of ZnEMBPP and its free base in benzene. The population decay of the S_2 state of the zinc derivative is 150 fs, which correlates with its S_1 rise time. However in the free base the S_2 lifetime is too short to be detected under their experimental conditions and is inferred to be less than the resolution limit of 40 fs. Based on their spectroscopic data, they found that the two molecules have almost the same $\Delta E(S_2 - S_1)$ energy gap as ZnTPP, but the S_2 lifetimes are much shorter than that of ZnTPP. They simply ascribed these differences to the effect of different substituents on the porphyrin macrocycle, but didn't give further explanation of this effect.

Based on the results discussed above, it seems that the energy gap law is invalid or at least insufficient to interpret the radiationless decay of the S_2 states of various metalloporphyrins. Gurzadyan *et al.*[36] extensively investigated the correlation between the depopulation dynamics of the S_2 state and the $\Delta E(S_2 - S_1)$ energy gap. They found that plots of natural logarithms of nonradiative rate constants $\ln(k_{nr}(S_2))$ *vs.* $\Delta E(S_2 - S_1)$ are linear for both MTPP (M= Zn, Mg) and MTBP (M= Lu, Zn, Cd) in various solvents. However, the data used in their plots are highly scatted. Nevertheless, the slopes of their plots are similar to the slope of the EGL plots obtained for azulene and its derivatives previously reported by Wagner *et al.*[26] Based on the value of the slope, the general $S_2 - S_1$ interstate electronic coupling energies for MTPP and MTBP were estimated to be *ca.* 10^3 cm^{-1}, which is actually much larger than the values of the azulenes, where it is only 100 cm^{-1} for the $S_2 - S_1$ transitions. According to radiationless transition theory of large molecules in the weak coupling case, the value of electronic coupling energy is expected to be less than 10^3 cm^{-1}. Therefore, the value they calculated lies at the upper limit of the weak coupling cases.

1.6 Motivation of the present work

The above review has focused on the unimolecular photophysical relaxation dynamics of highly electronically excited metallated tetrapyrroles. Previously reported results show some discrepancies among the several individual experiments done to date and their interpretations. Some open questions have been identified. In particular, the li-

mited numbers of both experimental and theoretical results concerning metallated tetrapyrroles other than ZnTPP are insufficient to obtain a complete understanding of the relaxation mechanisms of the higher excited states of the entire set of compounds in solution. More extensive reliable experiments and more accurate theoretical calcuations are necessary.

The S_2 relaxation mechanisms of the model metalloporphyrin, ZnTPP, have been extensively studied by both experimentalists and theorists. However, some discrepancies exist among the reported results. Chosrowjan *et al.*[34] measured an S_2 lifetime of 0.75 ps for ZnTPP in CH_2Cl_2, which is much faster than that in CH_3CN (3.5 ps), and thus they proposed the existence of fast electron transfer from the S_2 state of ZnTPP to the CH_2Cl_2 solvent molecules. However, both Gurzadyan *et al.*[35] and Yu *et al.*[41] have examined effect of CH_2Cl_2 on the S_2 relaxation of ZnTPP and obtained the lifetimes are 2.0 ps and 1.9 ps, respectively. Even though Yu *et al.* agree with the interpretation reported by Chosrowjan *et al.*, Gurzadyan *et al.* disagree and propose that the difference of lifetimes obtained in CH_2Cl_2 and ethanol is due to the difference in the $\Delta E(S_2 - S_1)$ induced by solvation. In addition, Yu *et al.* recently reported a difference in the S_2 decay and S_1 rise times of ZnTPP in benzene, which they attributed to parallel decay processes bypassing $S_2 - S_1$ IC due to the participations of excited states (S_2') other than S_2. However, neither they nor other experimentalists have confirmed these results by doing similar work on ZnTPP in other solvents. In addition, Yu *et al.*[41] proposed that the S_2' state is fluorescent, but a "dark" S_2' state by others.[42] The nature of either the S_2' state or some other "dark" state and its participation in the relaxation of the S_2 state are not yet established.

Previous reports also indicate that the S_2 lifetimes of ZnTPP are dependent on the solvent and vary in a range from hundreds of femtoseconds to several picoseconds. Even for the same solvent, some researchers have obtained different S_2 lifetimes using different experimental techniques. Three groups[35,42,66] have examined the solvation effect on S_2 fluorescence quantum yields or lifetimes of ZnTPP in a small set of solvents. However, no one has carried out systematic studies of the effect of solvent on the S_2 relaxation of ZnTPP by making both quantum yield and lifetime measurements. All these questions motivate us to conduct systematic and detailed studies of solvation ef-

fects in order to obtain a better understanding of the relaxation mechanisms of the S_2 state of ZnTPP.

Measurements of steady-state absorption, excitation and emission spectra of ZnTPP in a set of solvents with a wide range of polarizabilities would provide information about the solvation effect on spectroscopic properties. By using femtosecond fluorescence upconversion techniques, direct measurements of the S_2 decay and S_1 rise times in a wide set of solvents could provide direct information convincing the effect of solvent on relaxation rate constants of the S_2 state of ZnTPP. Also whether or not the S_2 decay and S_1 rise times are identical would provide direct experimental evidence about the involvement of any excited states (such as S_2' or "dark" states) in the $S_2 - S_1$ relaxation mechanism. Based on a set of spectroscopic properties and accurate S_2 lifetimes, possible correlations between the nonradiative rate constants and the $S_2 - S_1$ energy gaps could be analyzed to determine if the weak coupling model is applicable to metalloporphyrins such as ZnTPP. The S_1 decay mechanism of ZnTPP is well known, and is dominated by $S_1 - T_1$ ISC, which is significantly enhanced by heavy atoms. A similar study of the effect of heavy atoms on the nonradiative rate constants of the S_2 state has not been reported. In addition, the effect of deuteration of H_2TPP and ZnTPP relative to the corresponding perhydro compounds would identify the role played by C–H(D) vibrations in the nonradiative decay of the S_2 states of the tetrapyrroles.

Limited available experimental results indicate that the S_2 lifetime is strongly dependent on the nature of the substituents and central metal ions, and is also greatly affected by the macrocycle substitution pattern in tetrapyrroles. Gurzadyan *et al.*[35] and Kobayashi *et al.*[57] found that, for the same macrocycle substitution pattern, the S_2 fluorescence quantum yields do vary with different central metal ions, but the change is not large. However, S_2 lifetimes ranging from tens of femtoseconds to several picoseconds have been measured for tetrapyrroles with different substituents or different macrocycle substitution patterns. This implies that the effects of substituents and of deformation of the tetrapyrrole ring could be considerable, but the mechanism is still unknown. Compared to the metalloporphyrins, not much attention has been paid to the photophysical properties of the S_2 states of other tetrapyrroles even though these porphyrin analogues are very important in nature.[28] Thus it would be worthwhile to conduct a systematic

study of the effect of changing the tetrapyrrole macrocycle, using both steady-state and pulsed excitation methods.

Researchers also have tried to find some clues regarding the remarkable aspects of the S_2 nonradiative decay rate constants of the tetrapyrroles using theoretical calculations, and by correlating the calculated electronic transitions to the observed spectroscopic transitions. The discrepancy in the assignment of the shoulder to the blue side of the main Soret band observed in tetrapyrrole spectra is an important issue of ongoing interest. Our objective regarding this issue is to make systematic calculations of different tetrapyrroles to study the effect of different substituents on the electronic structure and excitation energy and the rank in energy of the excited states. Analysis of the differences among the calculated results may provide some clues about the unusual nonradiative rate constants and possible different relaxation mechanisms of the excited states involved.

The contribution of this thesis is to study the potential relationships between the molecular electronic structures of sets of d^0 and d^{10} metallated tetrapyrroles and their spectroscopic properties, and to use the results to interpret the differences in the decay dynamics of their higher excited states. A set of metallated tetrapyrroles has been investigated using both steady-state and advanced time-resolved technologies, together with theoretical calculations. The aim of this thesis is to study systematically the photophysical properties of highly electronically excited metallated tetrapyrroles and to determine the effects of the nature and pattern of substitution and of macrocycle deformation on the relaxation dynamics and mechanisms of highly excited electronic states. The applicability of the energy gap law in correlating the S_2 decay rates of the metallated tetrapyrroles with $S_2 - S_1$ energy gap and other factors could be assessed by such a study.

Chapter 2: Experimental and Computational Methods

2.1 Materials investigated and sample preparation

A set of metallated tetrapyrroles with a wide range of structures has been the subject of the study in this thesis. Their molecular structures with corresponding abbreviations are shown in Chart 1.1 in Chapter 1. Of these compounds, H_2TPP, ZnP, ZnDPP MgTPP, ZnTPP, CdTPP, ZnTPP(F_{20}), ZnTPP(Cl_8) and ZnTPTBP were purchased commercially from Frontier Scientific Inc. All samples were checked for purity before taking any data used for further analysis, and found no impurities that fluoresced significantly in the Soret region, and thus were used as received. TPP-d_{30} and ZnTPP-d_{28} were synthesized and purified to remove persistent fluorescent impurities by collaborating colleagues from the group of Professor Langford at Monash University in Australia, who provided them for photophysical measurements.

The $S_2 \rightarrow S_0$ fluorescence of ZnTBP was first observed in the 1970s.[53] However, since then experimentalists have found it hard to synthesize this compound without contamination by fluorescent impurities that have an absorption near 460 nm.[67] Efforts by us and others to remove these impurities in commercially purchased ZnTBP (from both Sigma Aldrich and Frontier Scientific Inc.), using methods such as TLC, HPLC, etc., all have failed. Nevertheless, the larger ΔE ($S_2 - S_1$) energy gap and the potentially long S_2 lifetime of this compound make it highly valuable to obtain a purified sample. Fortunately, Professor Steven Langford provided us with a sample of good purity. It also shows a small absorption in the 450 ~ 470 nm region due to impurity, but fortunately this impurity is nonfluorescent.

All solvents were obtained from Sigma-Aldrich and Commercial Alcohol, Inc. (ethanol), and were of the highest purity available. They were used as received if they exhibited no fluorescent impurities. Further care was taken by using molecular sieves to keep some water sensitive solvents moisture free, *e.g.* benzene.

All experiments were done using air saturated solutions at room temperature, except when otherwise specified.

2.2 Uv-visible absorption spectroscopy

Steady-state uv-visible absorption spectra of all compounds were recorded with a Varian-Cary 500 spectrophotometer using the double-beam mode. A matched pair of 10 mm x 10 mm standard quartz cuvettes was used for all measurements of absorption spectra. Pure solvent was used as a reference. Spectra were recorded with a spectral band width of 2.0 nm, the same as that used to record fluorescence excitation spectra. A scan rate of 0.25 nm/s was used, typically. The scanning range of the absorption spectra varies with samples and solvents.

To accurately measure the molar extinction coefficient of a sample at the wave-number of its maximum absorbance, (ε_{max} (?)), a series of solutions with different, carefully measured concentrations were prepared, and the corresponding absorbances were recorded at the stated spectral bandwidths. According to eq. 1.2, ε_{max} (?) was obtained from the slope of the linear plot of absorbance *vs.* concentration.

2.3 Steady-state fluorescence spectroscopy

The steady-state fluorescence emission and fluorescence excitation spectra were measured with either a Jobin-Yvon Spex Fluorolog instrument or a Photon Technology International QuantaMaster spectrofluorometer fitted with double monochromators on both the excitation and emission arms. Both instruments used a calibrated photodiode which scattered the excitation light for correcting the wavelength dependence of the exciting light intensities. Care was taken to calibrate these instruments and to use them only in their regions of linear response.

2.3.1 Fluorescence spectrometer

The optical layout of the PTI instrument is shown in Fig. 2.1. A high-pressure xenon arc lamp was used to provide a continuous excitation light source. This lamp produces broadband output ranging from the infrared to the ultraviolet. Selection of the excitation and emission wavelengths is computer-controlled through scanning excitation and emission monochromators, which are filtered with automatically operated continuously variable slits. The bandwidth of both the excitation and emission monochromators was

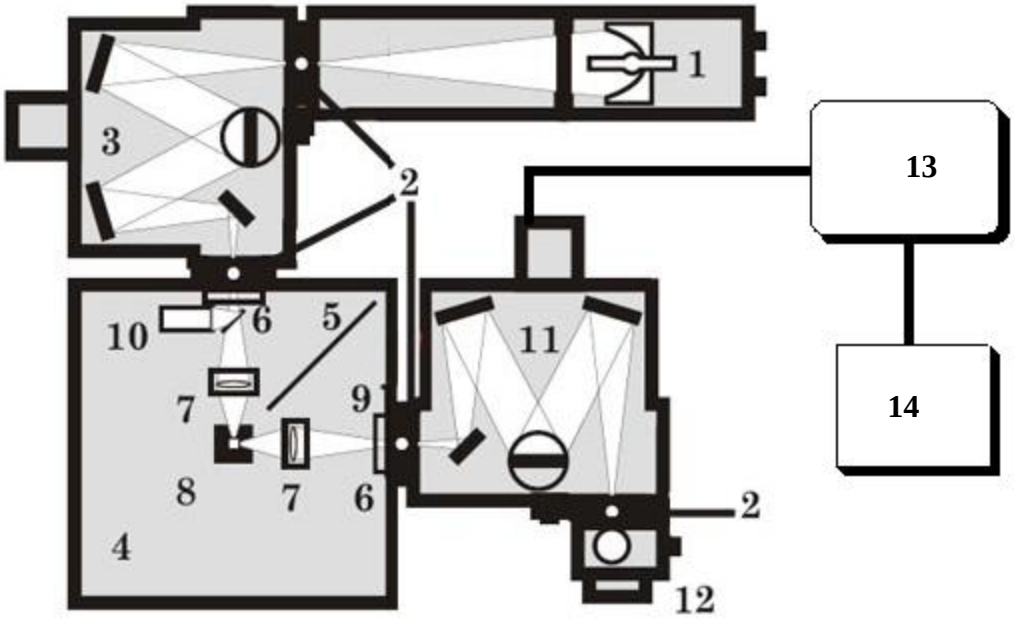

Fig. 2.1 Optical layout of the PTI spectrophotometers, adapted from the operation manual of the QuantaMaster™ UV VIS spectrofluorometer [68] 1 Arc lamp housing, 2 Adjustable slits, 3 Excitation monochromator, 4 Sample compartment, 5 Baffle, 6 Filter holder, 7 Excitation/emission optics, 8 Sample holder, 9 Emission port shutter, 10 Excitation correction Photodiode, 11 Emission monochromator, 12 PMT detector, 13 Electronics control, 14 Computer.

set to be 2.0 nm (1 mm slit width). Before entering the sample, a small fraction of the excitation light is directed toward a preinstalled calibrated photodiode to correct for the variation of the wavelength-dependent excitation light intensity. Emission was collected at 90° to the excitation axis and was detected using a single photon counting photomultiplier tube (PMT) detector, which provides high detection sensitivity. Spectra were recorded as photon counts per second versus wavelength to give fluorescence spectra. For the measurements of ZnOEP, most of which were done using a Jobin-Yvon Spex Fluorolog instrument, due to the extremely low S_2 fluorescence intensity, a high concentration solution is necessary. In this case, a triangular cuvette and front face collecting configuration was using to minimize the inner filter effect, which will be introduced in the following section.

Fluorescence spectra were corrected synchronously using detector/monochromator sensitivity files supplied by the manufacturers. Particular care was needed to obtain ful-

ly corrected $S_2 - S_0$ emission spectra when the emission quantum yields were very small. First, the solvent background, predominately Raman scatter, was corrected before subtraction from the measured fluorescence (plus background) spectrum by multiplying it by the constant correction factor $F = (1 - 10^{-A_{ex}(\lambda)})/2.303A_{ex}(\lambda)$, where $A_{ex}(\lambda)$ is the absorbance of the sample solution in the same solvent at the sample excitation wavelength.[42] This serves to correct the measured background for the reduced intensity of incident light traversing the cell when it contains the sample solution as compared with pure solvent. Correction for reabsorption of the S_2 fluorescence by the strong Soret absorption band was minimized by employing dilute sample solutions and sample cells with short emission path lengths (*e.g.*, 10 mm × 2 mm with emission viewed along the short path). When comparing fluorescence excitation and absorption spectra, care was taken to ensure that both were measured with the same excitation and emission bandwidths (typically 2.0 nm). The excitation spectra were corrected by viewing the sampled excitation light with a calibrated photodiode and dividing the raw excitation intensity by the photodiode signal. Artifacts resulting from changes in the excitation intensity at the viewed emissive volume due to the finite absorbance of the solution (especially important when scanning through the strong Soret absorption band) were minimized by using cells with short excitation paths (*i.e.* 2 mm × 10 mm with emission viewed along the long path).

2.3.2 Correction of inner filter effect on fluorescence intensity

Fluorescence spectroscopy has proven to be a sensitive technique. However fluorescence spectroscopy is limited by some experimental difficulties due to the inner filter effect, particularly when applied to porphyrins and metalloporphyrins. This effect consists of two components. One is caused by the attenuation of the incident light in the sample before it reaches the point at which the fluorescence of molecules that are excited is collected for measurement of the emission intensity (the primary inner filter effect). The other is called the secondary inner filter effect or fluorescence reabsorption effect which results from the overlap of the absorption and emission spectra so that, in the region of overlap, some of the fluorescence is reabsorbed by the molecules in the ground state before being collected for detection.

For metalloporphyrins, it is challenging to get accurate fluorescence spectra and quantum yields because of the strong influence of the inner filter effects particularly in the Soret region. One reason is that the overlap between the strongly allowed absorption spectrum and the corresponding fluorescence spectrum in the Soret region is large because of the small Stokes shift. Another reason is that the solubility of most metalloporphyrins is very low in most organic solvents. Care must therefore be taken to avoid aggregation since aggregates can quench the fluorescence from highly excited electronic states and will also result in displaced or distorted emission spectra. A linear relationship between fluorescence intensity and absorbance at the excitation wavelength can only be found when the inner filter effect is corrected. More details can be found in Appendix II.

Many efforts have been made to correct the inner filter effect on fluorescence spectra and quantum yield measurements. Kubista *et al.*[69] developed an equation, which can be used to correct the primary inner filter effect. Benefiting from Kubista's and other previous approaches,[8,20,70] eq. 2.1 was used to correct both attenuation and reabsorption inner filter effects.

$$I_{corr} = I_{obs} \times 10^{(A_{ex} l_{ex} + A_{em} l_{em})} \quad (2.1)$$

Here I_{corr} is the corrected fluorescence intensity; I_{obs} is the observed fluorescence intensity. A_{ex} and A_{em} are absorbance at the excitation and emission wavelengths, respectively. l_{ex} and l_{em} represent the distances between the entry and exit walls, respectively, of the cell and the fluorescence emitted point inside the cell. The details of how to get the effective light paths, l_{ex} and l_{em}, can be found in Appendix II.

The difference between the observed and corrected Soret band of fluorescence spectra of ZnTPP observed in ethanol is shown in Fig 2.2. At the Soret band maximum, the difference between the corrected and uncorrected intensities lies between 5 and 10% when the absorbance is no more than 0.07 at the excitation wavelength of 400 nm for ZnTPP in ethanol. It is important to note that a linear correlation between I_{obs} and A_{ex} is maintained well when the absorbance at the excitation wavelength is ≤ 0.05, and the difference of the emission intensity caused by the inner filter effect is less than 5%, which is of the same order as the absolute error (*ca.* 5%) obtained with the instrumenta-

tion used for the present measurements. Thus in the present work, for most measurements, the absorbance at the excitation wavelength were kept at 0.05 or less to eliminate the inner filter effect.

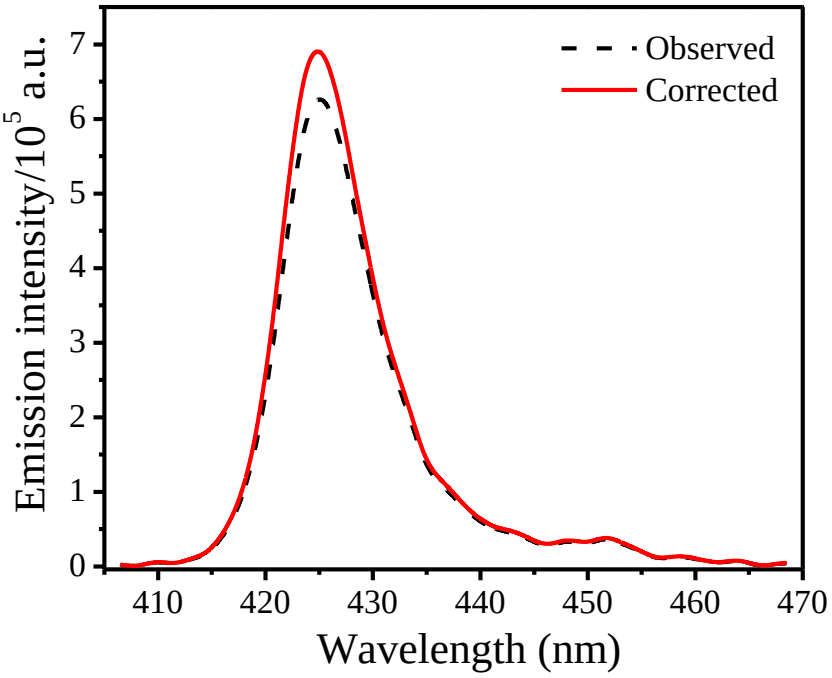

Fig. 2.2 Comparison of the observed and corrected Soret band fluorescence spectra of ZnTPP in ethanol with absorbance of 0.07 at the excitation wavelength of 400 nm.

2.3.3 Fluorescence quantum yields

The fluorescence quantum yield is important because it is involved in calculations of some important dynamic parameters, such as electron transfer, energy transfer, radiative and radiationless rate constants, which characterize the photophysical properties of the higher excited states of the metalloporphyrins.[71]

The absolute fluorescence quantum yield of a compound is hard to measure, and this is especially true for the metalloporphyrins studied in this thesis because of unavoidable inner filter effects. Thus, it is calculated by referring to the absolute quantum yield of a fluorescent standard using eq. 2.2.

$$\phi_{f_s} = \frac{I_s}{I_r} \times \frac{n_s^2}{n_r^2} \times \frac{(1-10^{-A_{ex}})_s}{(1-10^{-A_{ex}})_r} \times \phi_{f_r} \qquad (2.2)$$

Here I is the integrated area under the corrected fluorescence spectrum, s denotes the sample, r the reference (or standard) compound with a known quantum yield, n is the refractive index of the solvent, A_{ex} is the absorbance at the excitation wavelength, and the third term in the equation is to correct for any difference in absorbance at the excitation wavelength between the sample and reference solutions.

The quantum yields of the metalloporphyrins were calculated in this thesis by using ZnTPP in ethanol as a secondary standard (c = 1~2 x 10^{-6} M, ϕ_f = 1.42 x 10^{-3} at λ_{ex} = 400 nm).[42] If the solvents used for the sample and reference are different, the differences in solvent refractive indexes are also corrected. When possible, the same excitation wavelength and identical absorbance at the excitation wavelength were used for both sample solutions and reference solutions to minimize the inner filter effect and ensure equal excitation intensities. In a few cases (*e.g.* ZnP and ZnOEP) the same excitation wavelength could not be used for the sample and reference, and in these cases the measured quantum yields were corrected to equal excitation photon flux by using a calibrated photodiode that sampled the incident intensities at the two excitation wavelengths.

2.4 Fluorescence lifetime measurements

Fluorescence lifetime measurements receive considerable attention because the temporal fluorescence intensity decay profiles contain more and complementary information than is available through analysis of the steady-state fluorescence spectra. Fluorescence lifetime measurements can directly monitor the decay dynamics of the electronically excited molecules. In particular, it is very useful in distinguishing the presence of multiple fluorescent species which have similar steady-state fluorescence spectra by analyzing the fluorescence decay profile in terms of multiple exponential decay times.[20] The two most popular techniques used for fluorescence lifetime measurements are time-correlated single photon counting (TCSPC) technology for relatively longer-lived electronically excited molecules (longer than 100s of picoseconds), and fluorescence upconversion technique is used to measure ultrashort-lived electronically excited molecules (less than tens of picoseconds). In the present work, the S_1 lifetimes of metallated tetrapyrroles were studied, which is on the order of a few nanoseconds (ns) have

been measured using the TCSPC technique, and the S_2 lifetimes which fall in the range of tens of femtoseconds to a few picoseconds have been measured using fluorescence upconversion technology. Details will be explained in following sections.

2.4.1 TCSPC technology and S_1 lifetime measurements

Preparation of picosecond laser pulses

A Coherent diode pumped solid state laser (Verdi V-10) was used to produce continuous wave (cw) laser light with a frequency-doubled output at 532 nm. The output power is greater than 10W with low optical noise (<0.03% rms). Then this cw laser was used to pump a Coherent Mira Model 900-D titanium-sapphire ($Ti:Al_2O_3$) laser to produce tunable (700 nm to 1000 nm) mode-locked ultrafast laser pulses. The output beam of the Mira 900 with a 76 MHz repetition rate was directed to a high efficiency acousto-optic modulator (Bragg cell) in a Coherent Model 9200 pulse picker. The acousto-optic modulator provides a controllable pulse repetition rate over the widest range available by integer division of the fundamental 76 MHz repetition rate. When the laser beam travels through the acousto-optic modulator, a single pulse with relatively high intensity and particular bandwidth is extracted from the input Mira pulse train. The output beam of the pulse picker is then divided into two fractions, one directed to a photodiode to generate stop pulses by a time to amplitude converter (TAC) device via a photodiode, and the remaining major fraction of the beam is directed to an angle-tuned second harmonic generator 9300 (SHG) system to produce frequency-doubled sample excitation pulses in the 360 nm to 500 nm range. Thus the tunable excitation wavelength range was extended to short wavelengths, generated when the beam at the fundamental wavelengths travels through a 1.5 mm thick, nonlinear LBO (Lithium triborate (LiB_3O_5)**)** optical crystal. The frequency-doubled ultrashort laser pulses were used to excite fluorescence in the samples studied. In the present work, the excitation wavelength was set at 400 nm for most measurements (Soret-band excitation) and 495 nm otherwise (Q band excitation).

Time-correlated single photon counting (TCSPC) technology

The S_1 fluorescence lifetimes of molecules under consideration were measured

using TCSPC technology. A schematic diagram of the TCSPC experimental setup is given in Fig. 2.3. With reference to this diagram, the initial ultrafast light beam was split into two beams. The beam containing major fraction, after frequency-doubling, was directed to excite fluorescence in the sample. The fluorescence signal, after travelling through a Carl Zeiss prism monochromator (M4 QIIId), was detected by a cooled (-30 ^{0}C) amplified Hamamatsu microchannel plate photomultiplier tube (MCP-PMT) (R3809-50U), which is placed just after the monochromator. A slit with an adjustable entrance was placed before MCP-PMT to adjust the fluorescence count rate and insure that only single photon events were detected. The PMT output was further amplified by a preamplifier (HP Model 6216A) and then fed into a Tennelec TC 454 Quad constant fraction discriminator (CFD). The output pulses of the MCP-PMT have been greatly amplified and contain considerable contributions from electronic noise and minor multiple photon events. The CFD establishes a threshold to eliminate pulses due to background noise, thus improving the signal-to-noise ratio. Then the output signal of the CFD is fed into a time-to-amplitude converter (TAC).[72]

As indicated in Fig. 2.4, when a high repetition rate of exciting pulses was employed, the TAC was operated in a reverse way. The detected fluorescence single photon voltage pulse from the CFD acts as a "start" pulse to activate the voltage sweep in the TAC, and the "stop" pulse is provided by the laser excitation pulse detected by a Spectra-Physics photodiode (model 403), delayed by a certain fixed time by a TC 412A delay line. The TAC generates an analog pulse, the amplitude of which is proportional to the charge accumulated in the TAC's capacitor and hence correlated to the time interval between the start and stop pulses. The TAC signal was further amplified via a biased amplifier (BA, TC864 TAC/Biased Amplifier) and then fed into an analog to digital converter (ADC). Each "count" is assigned to the digital channel number of the ADC corresponding to the pulse amplitude received from the TAC. Upon receiving this specific channel number, the data acquisition board (TRUMP-8k/2k, Perkin-Elmer) of a multichannel analyzer (MCA) incorporated into the computer adds this event to an address of its memory corresponding to that channel number. Thus, the digital channel number, in fact a memory address of the photon, is correlated to the time

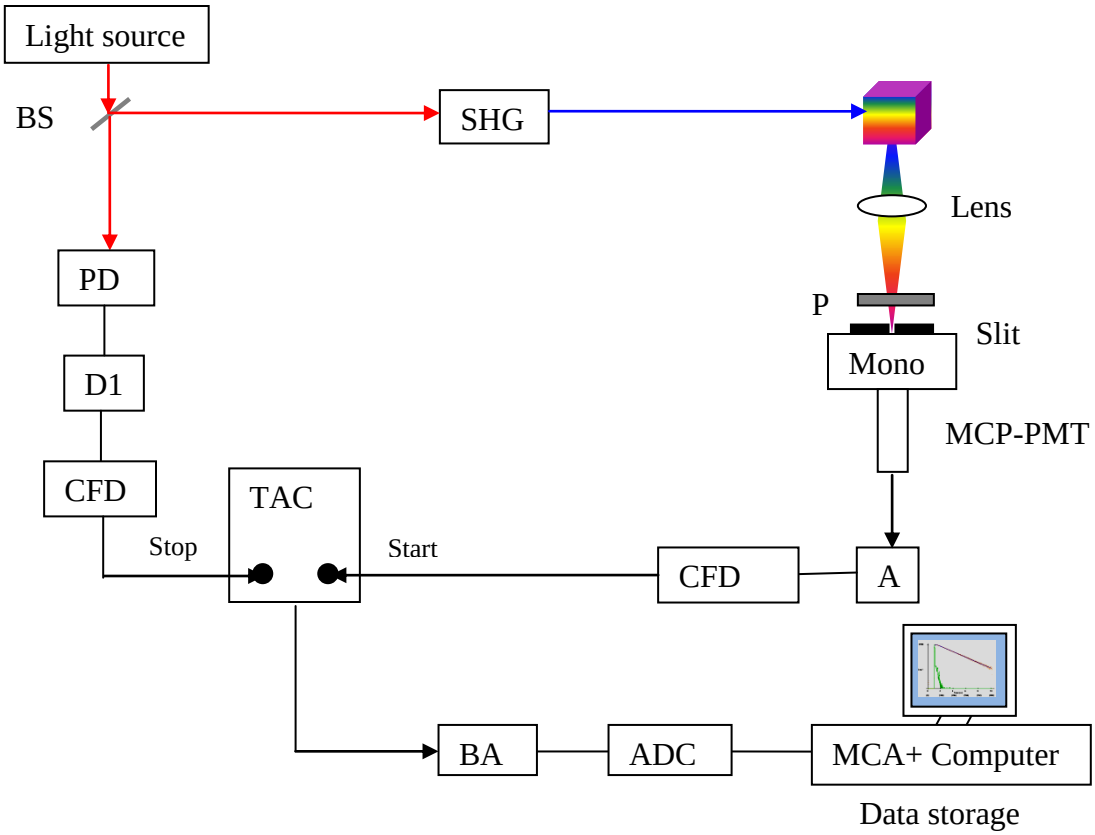

Fig. 2.3 Simplified the block diagram of TCSPC instrument. A, amplifier; ADC, analog to digital converter; BA, biased amplifier; CFTD, constant fraction timing discriminator; D, delay; Mono, monochromator; MCP-PMT, microchannel plate photomultiplier tube; MCA, multiple channel analyzer; PD, photodiode; P, polarizer; TAC, time to amplitude converter.

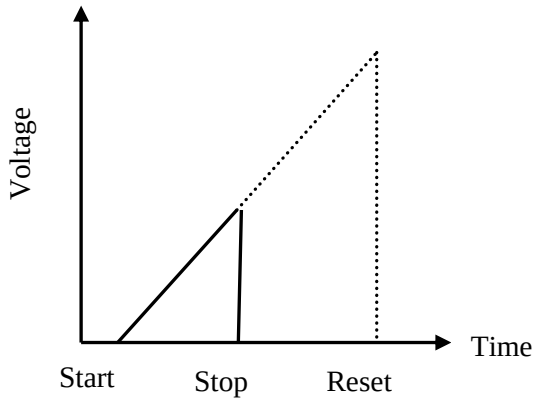

Fig. 2.4 Schematic diagram of TAC operation (modified from reference 72).[72]

interval at which the photon is detected. One cycle of this single photon detection and counting takes only a few nanoseconds. This process is then repeated over and over again until a histogram of the numbers of counts against channel number represents the time profile of the detected emission. Counting is continued until the desired statistical precision is obtained.

The time resolution of the TCSPC system is governed not only by the pulse width of the excitation light, but also the time resolution and precision of the detection electronics. The time resolution of the TCSPC system is mostly determined by the width and stability of the instrument response function (IRF) (refer to the next section) – which is in turn is determined primarily by the PMT's electron optics and photoelectron path differences. The most critical component of the electronics is the TAC. In the present work, the TAC was operated in a reverse mode using emitted photon signal as the start pulse, as shown in Fig. 2.3. Operation in this way greatly decreases the repetition rate of the TAC and avoids overload due to the high repetition rate of the excitation light. It is important to note that only one photon should be detected for one TAC operation cycle. If more than one photon arrives at the MCP-PMT within one TAC cycle, the resultant counting statistics of the MCA will be distorted, and the final decay curve will be biased toward shorter times. The effect of multiple photon detection by MCA within one TAC cycle is called pulse pile-up. In order to avoid this effect, the fluorescence count rate is set to be below 2% of the excitation pulse repetition rate by limiting the entrance of light to the PMT using a small slit width and setting a higher threshold in the CFD. Under these conditions, the probability of detecting only one photon during each TAC operation cycle is very high. A time resolution of *ca.* 50 ps is achieved for the TCSPC instrument used for the measurements presented in this thesis.

S_1 lifetime measurements and data analysis

Data collection was based on a computer controlled Maestro-32 Program. Before recording the instrument response and fluorescence decay profiles, the proper time window for the measurement was chosen and the time scale per channel of the MCA was calibrated. The S_1 lifetimes of the tetrapyrroles studied can be estimated based on their steady-state absorption and emission spectra using eq. 1.6. Thus the time window of the

MCA (and the time scale per channel) required for the measurements can be estimated before making any measurements. The accurate time calibration was done as follows. Either a LUDOX (colloidal silica) or a dilute milk solution was used to obtain the instrument response function (IRF) by scattering a small fraction of the excitation light used as the "start pulse". The observation wavelength was chosen to be the same as the excitation wavelength for these IRF measurements. The channel number corresponding to the maximum of the IRF profile was adjusted to be in the range of 900 to 920 out of a total of 1024 channels. The delay of the stop pulse was set to be zero for the first IRF profile. Then, delays of 2, 4, 6, 8 ns were applied to the stop pulses respectively, and a series of IRF profiles were lined up on the analyzer screen. The channel numbers corresponding to the maxima of the IRF profiles were recorded. A plot of the difference in channel numbers between two neighboring IRF profiles *vs.* the corresponding time delay gives a straight line, the slope of which is the time increment per channel.

The effect of scattered excitation light on fluorescence decay profiles can be minimized by setting the observation wavelength as far as possible away from the excitation wavelength. However, due to the short lifetimes (a few nanoseconds) of the S_1 states of the molecules investigated in this thesis, the collected experimental data contain contributions from the excitation laser pulses and detection systems. Deconvolution is required even if scattered light is not present when the IRF has a width that is a significant fraction of the sample fluorescence lifetime. The scattered light portion was eliminated by deconvolution of the measured decay profile from the IRF, to obtain the true fluorescent decay.

First, the IRF was measured by replacing the sample with a light scatterer, and observing the scattered light at the excitation wavelength (usually 400 nm). The S_1 fluorescence decay of the sample was then recorded by setting the observation wavelength to the maximum of the Q band fluorescence spectrum obtained by steady-state measurement for each sample. Decay profiles of each sample were recorded for at least three trials; the final S_1 lifetime reported is the average value of three trials. As a representative, Fig. 2.5 shows a typical single exponential fluorescence decay profile plotted in logarithm of counts *vs.* time.

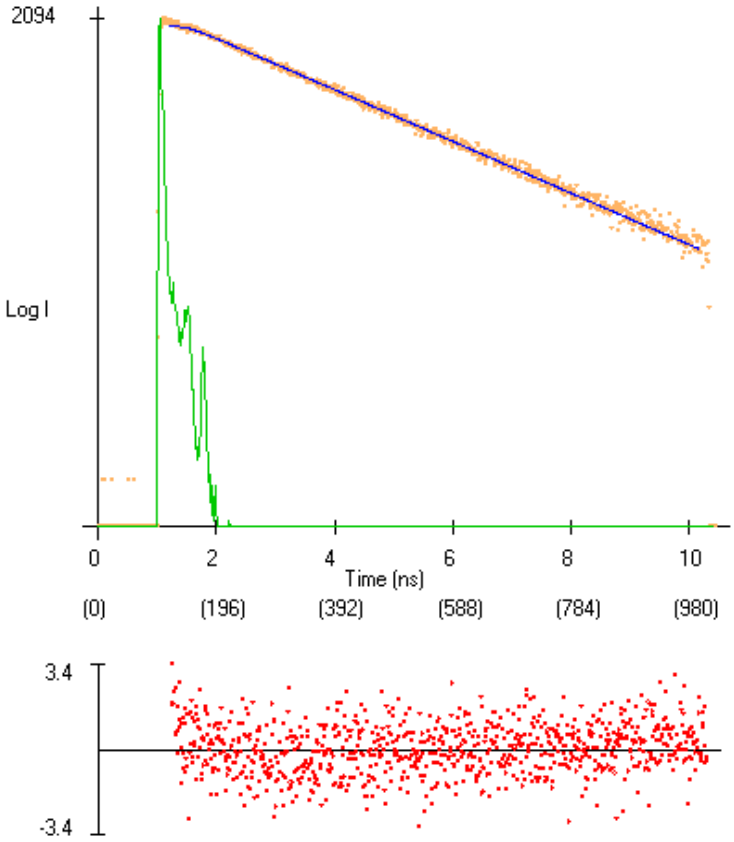

Fig. 2.5 A typical single exponential fluorescence decay profile (scattered dots) logarithm of counts *vs.* time **(**or channel number**)** and the fitting line (blue) and instrument response function (green) (Top)**,** and a representative residual plot of a good fit to a single exponential decay function (bottom). This profile was obtained for ZnP in methanol using dilute solution of 1 x 10^{-6} M. The excitation wavelength is at 495 nm and the fluorescence intensity was recorded at 625 nm. The deconvolution gives a time constant of 2.57 ns, when χ_r^2 = 1.00.

The experimental data are affected by electronic dark noise and stray room light, which result in a constant background. This can be corrected by subtraction of the background counts from both the experimental fluorescence profiles and the instrument response function prior to deconvolution. Within a time period t_e, the sum over the range of any time t_i preceding t_e, gives the observed decay curve, $I_0(t_e)$ at time t_e, eq. 2.3, where the subscript '0" represents the intensity after background correction.[72]

$$I_0(t_e) = \int_0^{t_e} P_0(t_i) G(t_e - t_i)\, dt_i \qquad (2.3)$$

Here the $G(t_e - t_i)$ is the true decay profile of the sample, $P_0(t_i)$ is the instrument response function which contains effects of the distortion from the ideal δ-pulse response of both excitation pulse and the detection system. Thus all observed decay curves have to be deconvoluted to get the correct lifetime of the sample.

There are a number of methods based on the above theories which can be used for the deconvolution of the observed decay data in TCSPC. Non-linear least squares curve fitting is the most widely used technique and its validity has been proved.[72] Data analysis of the S_1 lifetime measurements presented in this thesis was performed using in-house software, Psdecay 2000. This program performs a deconvolution of the instrument response function from the observed fluorescence decay profile via an iterative reconvolution procedure that minimizes the deviations between the fitting data and the observed fluorescence decay data. Some adjustable parameters in this program can be initially set up and "fixed", while other parameters such as the fraction of each component in a multiple exponential decay are optimized during the reconvolution procedure. The goodness of this non-linear least squares fit of the observed data to a trial function, consisting of one of a single, double or triple exponential decay, was assessed by examining the value of the reduced "chi-square", χ_r^2, eq. 2.4, and the distribution of the weighted residuals, eq. 2.5.

$$\chi_r^2 = \sum_{i=n_1}^{n_2} \frac{[I_0(t_i) - Y(t_i)]^2}{I(t_i)} \Big/ (n_2 - n_1 + 1 - p) \qquad (2.4)$$

Here values of $I_0(t_i)$ and $I(t_i)$ are the corrected and uncorrected number of counts in channel i, respectively, $Y(t_i)$ is the calculated fitting function, n_1 and n_2 are the first and the last channels of the region chosen for lifetime analysis, p is the number of variable parameters in the fitting function. The ideal value of χ_r^2 should be close to unity, since the distribution of the data in each channel follows a Poisson distribution. In practice, the values of χ_r^2 in the range of 0.9 to 1.1 are considered to be "good" enough to provide a precise fit. Sometimes, this value could be larger depending on the extent of scatter of the experimental data.[72] According to eq. 2.5, the weighted residuals, $R(t_i)$, of a suc-

cessful fit when plotted against channel number should be randomly distributed about zero, as shown at the bottom of Fig. 2.5.

$$R(t_i) = \frac{I_0(t_i) - Y(t_i)}{\sqrt{I(t_i)}} \tag{2.5}$$

All experimental results related to S_1 lifetimes discussed in later chapters were analyzed as described above.

2.4.2 Femtosecond fluorescence upconversion technology and S_2 lifetime measurements

The TCSPC technique is very sensitive because of single photon counting, and works very well with low emission yield materials. However, its time resolution is limited by pulse to pulse jitter and the width of the IRF of the detection system. The best time resolution (*ca.* 50 ps) for standard TCSPC technique has been achieved by using MCP-PMT detectors.[72] However, this is insufficient to detect the ultrashort fluorescence lifetimes which lie in the range of tens of femtoseconds to a few picoseconds.

Recently developed fluorescence upconversion technology, in which an ultrafast femtosecond laser is used as the light source, provides the time resolution and photon detection sensitivity necessary for direct ultrashort fluorescence lifetime measurements. The basic idea of this technique is based on the use of two synchronized femtosecond laser pulses. One pulse is used to excite fluorescence of the sample. The initial fluorescence signal is collected and focused onto a BBO upconversion crystal. The fs gating pulse is optically mixed with the fluorescence signal at a variable delay to generate the "sum frequency". Thus the time resolution relies primarily on the width of the excitation and gate pulses available with modern femtosecond lasers, and is not severely limited by the time resolution of the detection system.[20] As shown in Fig. 2.6, the simultaneous presence of the fluorescence and gate pulses in the non-linear BBO crystal yields an upconversion signal at the gate plus fluorescence sum frequency when the two pulses are matched in phase. The frequencies of the upconversion signal and of the two incoming pulses are related via eq. 2.6.

$$\bar{\nu}_{sum} = \bar{\nu}_{em} + \bar{\nu}_{gate} \quad (2.6)$$

Here, $\bar{\nu}_{sum}$ is the sum-frequency of the upconversion signal, $\bar{\nu}_{em}$ is the fluorescence at user-selected frequency, and $\bar{\nu}_{gate}$ is the frequency of the gate pulse. The intensity of the upconversion signal is proportional to the intensity of the fluorescence from the sample at the moment of the arrival of the gating pulse.

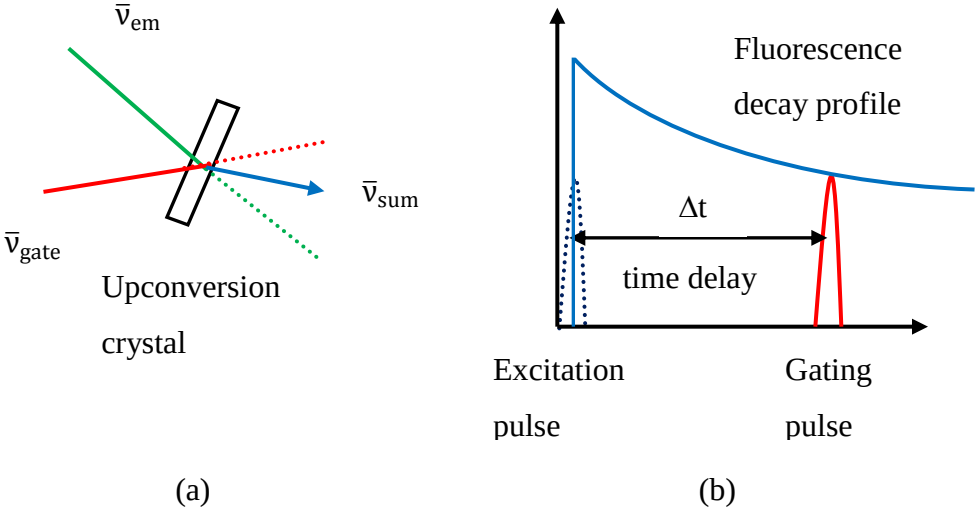

Fig. 2.6 Schematic illustration shows the (a) principle of upconversion and (b) the fluorescence signal gated by the delayed gating pulse.

Femtosecond fluorescence upconversion technology

The home-build fluorescence upconversion setup which was constructed by Dr. Suresh Velate and coworkers using commercially available components is schematically shown in Fig. 2.7. The femtosecond laser source is a diode-pumped solid state Ti:Al_2O_3 laser (Coherent, Vitesse Duo), which is amplified by a regenerative amplifier (Coherent, RegA 9000). The output of the RegA has an average power of *ca.* 400 mW at 800 nm when it is operated at 100 kHz repetition rate and the pulse width is *ca.* 160 fs (measured using a cross correlation method).[73]

The output light beam of the RegA is split into two fractions (80/20 in power) through a beam-splitter. The larger fraction with wavelength of 800 nm (λ_{gate}) consist-

ing of a fs pulse train at a repetition rate of 100 KHz is directed through a motor-controlled variable delay line (Newport, ILS150PP controlled by an ESP 300 motion controller), and then focused onto the fluorescence upconversion crystal (0.5 mm thick Type I BBO crystal, Photop, UTO8201), and serves as the gate pulse. The time resolution of each step of the motor controlled delay line can be as short as *ca.* 3.3 fs, by setting the step size $\Delta d \geq 0.001$ mm.

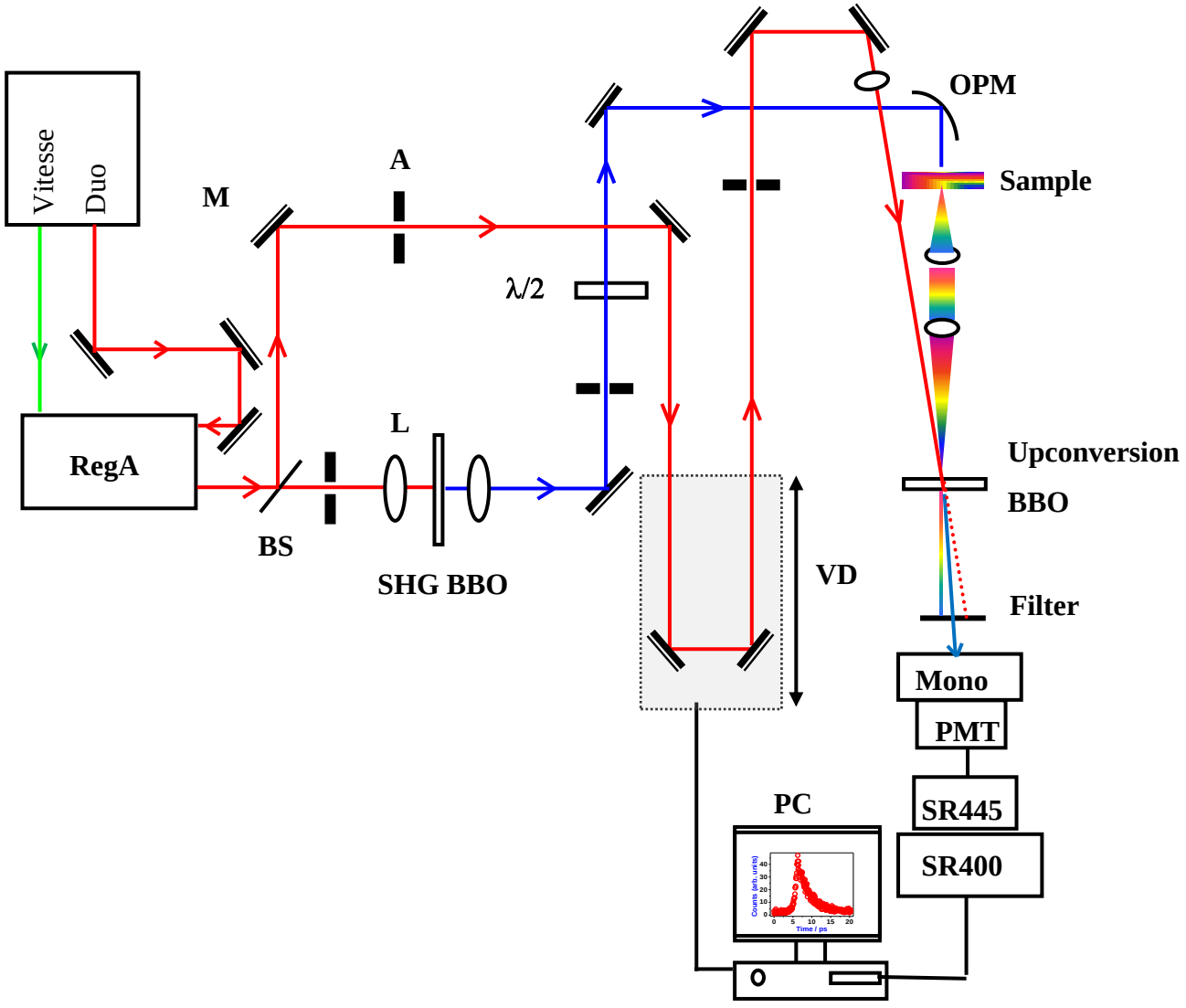

Fig. 2.7 Schematic diagram of the fluorescence upconversion setup. Reproduced from reference 74.[74] M, mirror; A, aperture; BS, beam splitter; L, plano convex lens; VD, variable delay; OPM, off axis parabolic mirror; Mono., monochromator; SR445, amplifier and SR400 single photon counter; PMT, photomultiplier tube; SHG, second harmonic generator, λ/2 half wave plate.

The smaller fraction of the 800 nm beam is directed to pass through a second harmonic generator (0.5 mm thick Type I BBO crystal, UTO8201, 29.5°) to generate the excitation beam with a wavelength of 400 nm. The 400 nm excitation pulse train is passed through a halfwave (λ/2) plate to rotate its plane of polarization by 90º, and is then focused by a first surface Al-coated 90º off-axis parabolic mirror (Edmund Optics, effective focal length = 101 mm) into the sample. (To keep the sample fresh, the sample solution was continuously flowed through a 200 μm thick quartz flowcell (Starna), the flow rate of which was controlled by an HPLC pump (Millipore, Model 510).) The resultant fluorescence was collected with a combination of two plano-convex lenses (each of 50 mm focal length) and was focused into the fluorescence upconversion crystal (BBO) together with the gate pulse to generate the sum-frequency. The gate and fluorescence beams have to be matched temporally and spatially in the BBO crystal to obtain the best efficiency of the sum-frequency generation. Thus the crystal is cut at a phase-matching angle of 37º to mix the beam with a wavelength of 800 nm and another beam with a wavelength in the range of 400 to 700 nm. The angle between the gate and pump beams was held at *ca.* 10° to achieve maximum spatial overlap of two beams in the BBO upconversion crystal. The intensity of the upconverted signal at the user-selected observation wavelength was maximized by tuning the angle of the upconversion crystal.

The upconverted light was passed through a filter to eliminate the scattered pump and gate light, and was focused (with a 50 mm focal length plano-convex lens) onto the entrance slit of a double monochromator (CM112, Spectral Products). Finally, the upconversion signal at the sum frequency was detected by a photomultiplier (PMT, Hamamatsu, H7732P-01 module with C7169 power supply). The output of the PMT was amplified using a preamplifier (Stanford Research, model SR445) and then detected by a photon counter (Stanford Research, model SR400). A computer controlled program written (by Dr. Suresh Velate) in Labview (version 7.0) was used to control the data acquisition and monochromator systems, and a stepping motor-driven optical delay stage was used to control the variable delay time of the gating pulse. The fluorescence upconversion setup was tested by measuring the pump-gate cross-correlation profile,

and was well described by Gaussian function with a full width at half-maximum (FWHM) of *ca.* 170 ~ 230 fs.[74]

S_2 lifetime measurements and data analysis

All the results of the measurements of the S_2 fluorescence lifetimes presented in this thesis were obtained in collaboration with Dr. Suresh Velate and Dr. Umakanta Tripathy.

The lifetimes of the S_2 excited states of the tetrapyrroles measured in this thesis lie in the range of tens of fs to a few ps, which is comparable to or shorter than the FWHM of the IRF, which has a wider FWHM than the cross-correlation function due to broadening by the fluorescence collection optics. The measured up-converted fluorescence decay is a convolution of the real decay of the fluorescence with the instrument response function. Under these circumstances, deconvolution of the observed fluorescence profiles is crucial and measurements of the instrument response function are required.

The IRF can be measured by obtaining the sum frequency of the scattered Raman light arising from the C–H stretching vibrations of the solvent (*i.e.* benzene) with the gate pulse. However, in the present work the observed S_2 emission decay profile of ZnOEP in benzene at the wavelength of the maximum Soret fluorescence intensity was used as the IRF. The fluorescence decay profile of the S_2 state of ZnOEP in benzene can be well-modeled by a Gaussian function with a FWHM of *ca.* 470 fs resulting from the symmetric broadening of the emission profile by the fluorescence collection optics employed and convoluted with a fast exponential decay of *ca.* 30 fs. The latter decay time is consistent with the lifetime of the S_2 state of ZnOEP calculated using the Strickler-Berg equation based on its measured $S_2 - S_0$ fluorescence quantum yield of *ca.* 1×10^{-6} (refer to results presented in chapter 4 and 5). This method is also justified by the result obtained for H_2TPP, whose S_2 lifetime of *ca.* 50 fs was obtained by convolution of its observed fluorescence decay profile and the IRF described above. It reproduces the value of *ca.* 50 fs reported by Baskin *et al.*[55] for H_2TPP in benzene measured under similar conditions using a fluorescence upconversion system.

It has been reported that, for ZnTPP and other metalloporphyrins excited to the Soret band, ultrafast intramolecular vibrational redistribution occurs within the first 200 fs, a process that is superimposed on the population decay of the S_2 state.[35,39,40] For those samples with S_2 decay times longer than 1.0 ps, fits of the temporal emission decay profiles were made for $t > 200$ fs in order to assess complications due to this intramolecular vibrational relaxation process within the S_2 state. The decay parameters obtained this way showed no significant difference, when compared with those obtained by full deconvolution over the entire decay profile.

The temporal profiles of the S_1 fluorescence rise were measured using the same experimental setup, but changing the observation wavelength to the maximum of the Q band of the steady-state fluorescence spectra in solution. For efficient upconversion, the angle of the upconversion crystal was also changed to produce optimum phase matching. The S_1 rise temporal profiles were deconvoluted by fitting with a triple exponential function, consisting of one fast exponential rise and two longer exponential decays. In all cases the ultrafast rise time constant of the S_1 state was found to be identical to the corresponding decay time constant of the S_2 state within an experimental error of *ca.* 50 fs. One of the two longer exponential decays, of the order of 10 ~ 20 ps, corresponds to intermolecular vibrational relaxation of the S_1 state, and the other is associated with the S_1 population decay, which is the order of several ns.[74]

To make accurate measurements of S_2 lifetimes shorter than 500 fs, the smallest delay line step size of 0.001 mm, which corresponds to the shortest available time delay of $\Delta t = 3.3$ fs was used to increase the number of data points. Thus, both the instrument response function and the temporal fluorescence profiles of the short-lived states were accumulated by using a larger and more statistically significant number of data points. For the S_2 emission decay of molecules with S_2 lifetimes shorter than 1.0 ps, the decay parameters were obtained solely by deconvolution of the observed upconversion signal decay profile and the instrument response function by obtaining the parameters of the convoluted function that minimized the sum of the squares of the deviations between fitting data and the measured decay as described previously. We estimate that the uncertainty in the measurement of the Soret-excited (S_2) fluorescence lifetimes is *ca.* $\pm$ 30 fs with this improvement.[75]

2.5 DFT calculations

All DFT calculations were carried out using the Becke-Lee-Yang three-parameter hybrid functional (B3LYP) model.[76,77] Since the effect of using different basis sets is known to be rather small[76], the 6-31G(d) basis set was used for all computations, unless otherwise specified. All molecular structures were optimized using a D_{4h} symmetry constraint for the porphyrin framework, except for ZnDPP and ZnTPTBP, and were followed by analytical vibrational frequency computations to confirm the minimum energy structures. Although the imposition of D_{4h} symmetry ignores the non-planar distortions caused by substitution on the macrocycle, DiMagno *et al.*[78] have shown that such "ruffled" and "saddled" distortions are not the source of the shifts in the electronic spectra of several model porphyrins, induced by substitution. Based on optimized structures, the excitation energies and oscillator strengths were calculated using time-dependent density functional theory (TDDFT) at the B3LYP/6-31G(d) level,[79,80] unless otherwise specified. All calculations were carried out using the Gaussian 03W program.[81]

Chapter 3: DFT and TDDFT Calculations

3.1 Introduction to density functional theory (DFT) and time-dependent density functional theory (TDDFT)

Since the 1960s, DFT and TDDFT have gained considerable attention because they are very important tools in exploring the electronic structures of atoms, molecules and crystals and predicting their electronic properties. To date, research areas related to the development and improvement of DFT and TDDFT are still interesting subjects.[82] The following paragraphs will give a brief introduction of the development of DFT and TDDFT. For a comprehensive and detailed review of the theoretical background, the mathematical formalisms that have been derived and the development of these theories, interested readers can refer to recent reviews[82,83] and some books.[84,85]

The predecessor to the DFT is the electron density concept introduced by Thomas and Fermi in the 1920s.[84] The energy of an atom can be expressed in terms of electron density, rather than the many-body wave functions previously employed. Distinct from a function, a functional is a function that takes another function as its input and produces a scalar quantity. Hence in this thesis the functional of interest is the one that minimizes the energy of the molecules when expressed in terms of electron densities. Electron density describes and determines the probability of finding the N electrons in a particular position in a unit volume with arbitrary spin while the positions and spin of the remaining N-1 electrons in the system are arbitrary. By ignoring electron spin, this model completely neglects the effects of exchange and correlation energies between electrons.[84] After these early developments, further efforts were dedicated to modeling exchange and correlation energies by taking the electron spin into account to improve the Thomas-Fermi model.

By adopting the local density approximation (LDA), Kohn and Sham developed the famous Kohn-Sham equation,[86] which gives quite satisfactory results of energy calculations. Further efforts to seek better approximations of exchange-correlation energy by scientists,[76,77,83,85] such as Parr, Yang, Lee, and Becke resulted in the local density approximation, the local spin-density approximation and the hybrid functional approximation etc. Currently, the most popular hybrid functional approximation is Becke's three-

parameter Lee-Yang-Parr formulation (B3LYP),[83,85] as demonstrated by Stephens *et al.* in 1994.[87] It gives good performance in many applications, and more new functionals with quite good performance have been developed since. However, none of the new functionals have gained the same popularity as the B3LYP hybrid functional for chemical applications.[84]

The DFT shows good performance in the treatment of the electronic ground states and properties of molecules, but encounters difficulties when dealing with excitation energies and properties of excited states. However, excited states are important and relevant to many areas of chemistry, including photochemistry, electronic spectroscopy and many other photo-initiated processes. Thus considerable effort has been made to develop and improve the time-dependent local density approximation within the framework of DFT. Some new theories[88-91] have been proposed to calculate the electronic excitation energies. Notable is the TDDFT, which was introduced by Runge *et al.*[89] in 1984 to treat such time-dependent problems. Since then, most but not all time-dependent problems, such as excitation energies and properties of excited states can be solved. Detailed information of the development of the TDDFT can be found in a recent review.[82]

Very recently, Imamura *et al.*[90] revealed that the TDDFT is able to accurately predict interstate excitation energies generated by the promotion of valence electrons, but it fails for core-excited states. Van Faassen *et al.*[91] found a new challenge to the TDDFT to deal with those transitions involved in d Rydberg states. The other limitations of TDDFT method were found due to poor asymptotic potential,[79,92] which can be corrected by combining the asymptotic tail of the potential with the LDA potential. Double excitations are missed by the TDDFT due to adoption of the adiabatic approximation, and this has been corrected by applying a frequency-dependent exchange-correlation kernel. Limitations regarding charge-transfer excitation or long range spatially separated excitation still remain problematic.[91,93,94] In very recent studies, the Baerends and Ziegler groups made great progress in the treatment of the excitation energies by using TDDFT and an improved Kohn-Sham exchange-correlation potential, named statistical averaging of orbital dependent mode potentials (SAOP).[46,47] Nevertheless, further improvement in the application theory appears desirable.

Despite the limitations that still remain, the DFT and TDDFT have proved to be effective and successful in exploring electronic structures and predicting many molecular properties, with less computing time cost but accuracy comparable to Moller-Plesset perturbation theory (MP) methods.[95] Due to their advantages in being able to handle large numbers of electrons, they have gained wide application in the calculation of electronic structures, the prediction of the electronic spectra and other electronic properties of relatively large molecules, including tetrapyrroles and metallated tetrapyrroles etc.[46,49,96] In the present study, the DFT and TDDFT methods at the B3LYP level were used for all calculations. The following paragraphs will show the calculated electronic structures of the ground state together with excitation energies and properties of the excited states and their aid in understanding and interpreting the features of the electronic spectra.

3.2 Interpretation of the electronic spectra of metalloporphyrins

The typical electronic absorption spectra of porphyrin-type complexes are characterized by one weak Q band in the visible region and one intense Soret band in the uv-visible region accompanied by several weak bands lying still further to higher energies, as shown in Fig. 3.1. The Soret and Q band features have for many years been interpreted in terms of Gouterman's four-orbital model (Fig. 3.1).[97] Under D_{4h} molecular symmetry, the two nearly degenerate highest occupied molecular orbitals (HOMO and HOMO-1, a_{2u} and a_{1u}, not necessary respectively), and the two strictly degenerate lowest unoccupied molecular orbitals (LUMO, e_g) are well-separated in energy from the remaining orbitals. The major contributions to the Q and B bands arise from linear combinations of the wavefunctions resulting from one-electron promotions involving these four frontier molecular orbitals. Due to the near degeneracy of the HOMO and HOMO-1 orbitals, a strong interaction occurs between the two lowest energy excited electron configurations, $^1a_{1u}{}^1e_g$ and $^1a_{2u}{}^1e_g$. For the $S_1 - S_0$ transition, the transition dipole moments of the two excited electron configurations $^1a_{1u}{}^1e_g$ and $^1a_{2u}{}^1e_g$ are anti-parallel, with intensities that nearly cancel, giving rise to a weak absorption, the Q band in the visible region. The two transition dipole moments are parallel for the $S_2 - S_0$ transition, with intensities

reinforced, leading to a strong absorption, known as the B (or Soret) band in near uv-visible region of the absorption spectrum.

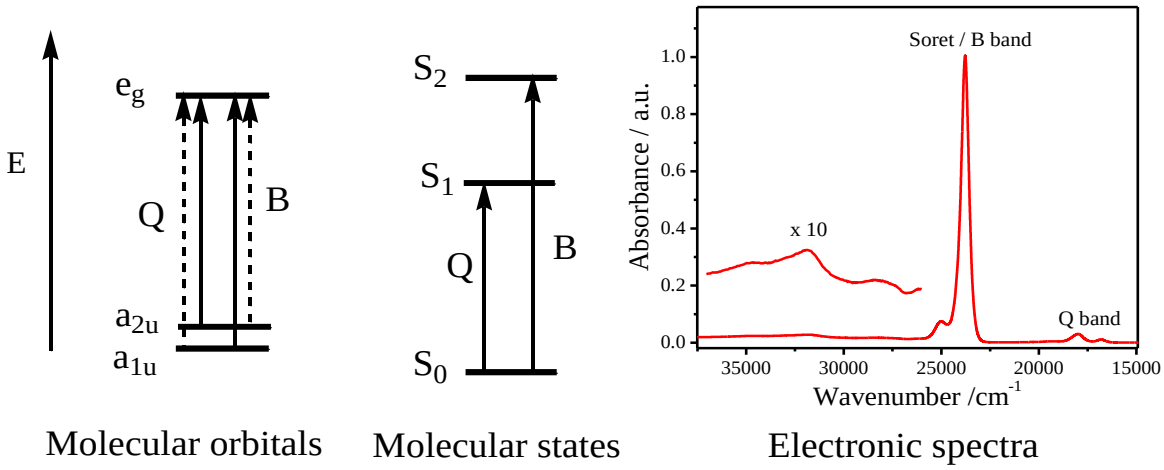

Fig. 3.1 Gouterman's four-orbital model and a typical electronic spectrum of metalloporphyrins.

The common features of the near uv-visible spectra of the diamagnetic metallated tetrapyrroles can be rationalized qualitatively or semi-quantitatively on the basis of the four-orbital model. The relative intensities of the Q and B bands are traceable to the extent of the degeneracy of the HOMO and HOMO–1 orbitals. However, those bands on the blue side of the Soret band with higher energies are beyond the scope of Gouterman's model. In addition, a large body of previous computational work has been published, notably by Weiss *et al.*,[98] Nguyen *et al.*,[48,99-101] Baerends *et al.*[46] and Peralta *et al.*[47] All these calculations have shown that the four-orbital model provides neither a full nor an adequate description of the nature of the higher energy Soret band in the absorption spectra of porphyrins and phthalocyanines. Calculations on closed-shell ground state metalloporphyrins using several DFT methods (including DFT/SCI,[102] DFT/MRCI[50] and several variants of TDDFT[46,103]), time-dependent Hartree-Fock theory with the INDO/S approximation (TDHF/INDO/S[48]), and multi-reference methods (MRMP/CASSCF[104]) have revealed that the energies of electronic states higher than the 1^1E_u state are particularly sensitive to the methods used to account for the effect of electron exchange-correlation and excited electron configuration interaction. In a recent review, Baerends *et al.*[46] have shown that the Q band can be fully explained in

terms of the lowest energy spin and electric dipole allowed transition in Gouterman's four-orbital model. However, Gouterman's model is inadequate in describing the B or Soret band and provides no insight into the composition of higher energy bands on the blue side of the Soret band, labeled as N, L, M, etc. By using the TDDFT/SAOP method, their calculations predict that the Soret band in ZnP and MgP is composed of transitions to both the 2^1E_u and 3^1E_u states, with the 2^1E_u state of slightly lower in energy reached by an electric dipole allowed transition (f = 0.45) of $e_g \leftarrow b_{2u}$ character and the 3^1E_u state corresponding to the strong (f = 1.01) transition. Similar suggestions were proposed by Peralta *et al.*[47] By using the same TDDFT/SAOP method, they found that the 2^1E_u state is coupled strongly to the near degenerate 3^1E_u and both contribute to the Soret band. Weiss *et al.*[98] also found that the four-orbital model was adequate for the Q band, but was less successful in predicting the composition of the B band, especially, for porphyrin-type compounds where one needs to consider the higher lying excited states to interpret the B band characteristics. Several other TDDFT, TDHF and DFT/MRCI calculations[48,50,99,102] find no state in the vicinity of the Soret band that consists of transitions with a high oscillator strength comparable to the transition to the 2^1E_u state. However, none of their calculations reproduce the energies of the more highly excited valence states particularly well, when comparing with the values obtained from gas-phase absorption spectra.

In order to clarify the controversy in the interpretation of the electronic spectra of metalloporphyrins and seek further understanding of the potential connections between electronic structure and electronic spectra of metalloporphyrins, a set of metalloporphyrins with different substituents has been studied in this thesis. The electronic structures of the ground states and the excitation energies and oscillator strengths of transitions to the excited states have been calculated using DFT and TDDFT methods. The potential relationships between the electronic structures and the observable spectroscopic properties of the metalloporphyrins under consideration will be discussed.

3.3 Computational methods

All the DFT and TDDFT calculations were carried out using the Becke-Lee-Yang three-parameter hybrid functional (B3LYP)[76,77] with the 6-31G(d) basis set, unless oth-

erwise specified. The basis set is defined as "the mathematical description of the orbitals within a system used to perform the theoretical calculation".[95] There is a big library of basis sets and one can select any of them according to the requirements of the calculation. Details may be found in the documentation of commercial software.[95] For molecules, such as metallated tetrapyrroles with a large number of atoms, it has been proven that the 6-31G(d) and 6-31G+(d,P) basis sets provide satisfactory accuracy but with acceptable computing time for atoms from H to Cl. The effect of using different basis sets, 6-31G(d) and 6-31G + (d,P), has been shown to be rather small.[105] Therefore, a typical 6-31G(d) basis set was used for all computations when otherwise specified.

Atoms heavier than Cl are treated by adoption of a core efficient potential (CEP), which considers relativistic effects. Of the many special basis sets designed for heavy metal atoms, the lanl2dz and Steven's basis sets (CEP-31G) have been used by most chemists and have been proven to be accurate and reliable, but the computation takes a relatively long time compared to the 6-31G(d) basis set. Several authors[106,107] have tested the accuracy of applying the 6-31G(d) basis set to atoms from K to Zn, and have obtained results as reliable as those using lanl2dz and Steven's basis sets. Here, geometry optimizations of MgTPP, CdTPP and ZnTPP were performed using three different basis sets, 6-31G(d), lanl2dz and CEP-31G to check the basis set-dependent differences. The data are collected in Table 3.1. Analysis of these data indicates that all geometrical parameters obtained using different basis set are consistent with the well-established experimental values for ZnTPP. The differences among basis sets are negligible, except for the M-N bond lengths. The results indicate that it is acceptable to use the 6-31G(d) basis set for all metalloporphyrins under consideration except CdTPP. The 6-31G(d) basis set is known to be the smallest basis set that can give satisfactory results in vibrational frequency calculations.[95] All ground state molecular structures except ZnDPP and ZnTPTBP were optimized using a D_{4h} symmetry constraint for the porphyrin framework, and were followed by analytical vibrational frequency computations to confirm that the optimized structure has the minimum energy. Unconstrained geometry optimizations show that the porphyrin macrocycle adopts a slightly non-planar saddle conformation in some *meso*-substituted ZnP derivatives and a ruffled conformation in others, but such "ruffled" and "saddled" distortions have a minimal impact on the elec-

tronic spectra of several model porphyrins.[78,108] Besides, the objective of the calculations of this thesis was to determine the influences of the energies and symmetries of all excited electronic states that might be involved in the relaxation of the S_2 state, thus such slightly stabilizing deformations were ignored here.

Table 3.1 Geometric parameters of MTPP metalloporphyrins calculated with different basis sets.

	MgTPP		ZnTPP					CdTPP	
	CEP-31G	6-31G(d)	CEP-31G	6-31G(d)	Lanl2dz	Ref[101].	Expt.	CEP-31G	Lanl2dz
M-N	2.073	2.062	2.052	2.043	2.066	2.055	2.037	2.152	2.144
N-C_a	1.375	1.375	1.376	1.377	1.375	-	1.376	1.367	1.376
C_a-C_b	1.448	1.447	1.446	1.446	1.447	-	1.438	1.455	1.464
C_a-C_m	1.412	1.409	1.407	1.406	1.410	1.408	1.400	1.424	1.418
C_b-C_b	1.363	1.363	1.362	1.363	1.363	1.361	1.349	1.367	1.369
M-N-C_a	126.3	-	126.5	-	126.4	126.4	126.3	124.9	-
C_a-N-C_a	107.4	107.1	106.9	106.5	107.3	-	106.6	110.1	110.2
N-C_a-C_m	125.7	125.7	125.8	125.8	125.8	125.9	126.3	125.9	126.1
N-C_a-C_b	109.2	109.4	109.5	109.8	109.3	-	109.4	107.4	107.1
C_a-C_b-C_b	107.1	107.1	107.1	107.0	107.1	-	107.3	107.5	107.8
C_a-C_m-C_a	125.9	125.6	125.2	124.9	125.7	-	124.8	128.4	128.0
C_m-C_a-C_b	125.0	124.9	124.7	124.4	124.9	124.7	125.0	126.7	126.8

- Not available.

The excitation energies and transition oscillator strengths of the excited states were calculated, based on the optimized ground state structures, using time-dependent density functional theory (TDDFT) at the B3LYP level with the same basis set.[79,80] All calculations were carried out using Gaussian 03W.[81]

3.4 Results and discussions

3.4.1 Ground state geometry optimization and electronic structure

Electronic structures are fundamental to the interpretation and understanding of the features of the electronic spectra. Because the accuracy of the computed electronic structure is dependent upon the structural parameters used in the calculations, it is important to establish the quality of the computed structures by comparing to the available experimental data. The structural parameters and electronic structures of the ground state of all the metalloporphyrins under study were optimized using the DFT method at

Table 3.2 Ground state geometric parameters of metalloporphyrins calculated by DFT (B3LYP/6-31G(d) (lanl2dz for Cd) (distances in Å and angles in degrees). Symmetry is in D_{4h} unless otherwise specified.

parameters	ZnP	ZnOEP	ZnTBP	ZnDPP(D_{2h})	ZnTPTBP(D_{2d})
	cal.	cal.	cal.	cal.	cal.
Zn-N	2.042	2.064	2.068	2.042	2.033
N-C_α	1.374	1.375	1.374	1.376	1.375
C_α-C_β	1.445	1.455	1.455	1.448	1.462
C_α-C_m	1.395	1.398	1.391	1.405	1.409
C_{β}–C_β	1.363	1.379	1.411	1.362	1.416
C_α-N-C_α	106.6	106.9	108.0	106.5	109.0
N-C_α-C_m	125.0	124.3	125.4	125.5	123.7
N-C_α-C_β	109.8	110.0	109.7	109.6	108.8
C_α-C_{β}–C_β	106.9	106.5	106.2	107.0	106.4
C_α-C_m-C_α	126.5	128.3	127.3	124.5	124.9
C_m-C_α-C_β	125.1	125.7	124.9	124.9	127.3

Table 3.2 (cont'd)

parameters	MgTPP	ZnTPP		CdTPP		ZnTPP (Cl_8)	ZnTPP (F_{20})	
	cal.	expt[a].	cal.	Expt.[b]	cal.	cal.	Expt.[c]	cal.
M-N	2.062	2.037	2.043	2.187	2.144	2.043	2.036	2.043
N-C_α	1.375	1.376	1.377	1.37	1.379	1.374	1.371	1.374
C_α-C_β	1.447	1.438	1.446	1.446	1.464	1.446	1.438	1.446
C_α-C_m	1.409	1.400	1.406	1.416	1.418	1.404	1.398	1.404
C_{β}–C_β	1.363	1.349	1.363	1.349	1.369	1.361	1.339	1.361
C_α-N-C_α	107.1	106.6	106.5	108.4	110.2	106.5	106.2	106.5
N-C_α-C_m	125.7	125.9	125.8	125.8	126.1	125.5	125.1	125.5
N-C_α-C_β	109.4	109.4	109.8	108.3	107.1	109.9	109.6	109.9
C_α-C_{β}–C_β	107.1	107.3	107.0	107.5	107.8	106.9	107.3	106.9
C_α-C_m-C_α	125.6	124.8	124.9	126.8	128.0	125.4	126.1	125.5
C_m-C_α-C_β	124.9	125.0	124.4	125.7	126.8	124.6	125.4	124.6

[a] from reference 109,[109] [b] from reference 110,[110] [c] from reference 111,[111] the experimental values are averaged to give D_{4h} symmetry.

the B3LYP level. The computed key structural parameters characterizing the geometry of the porphyrin frameworks are summarized in Table 3.2. When comparing with available experimental data for ZnTPP, CdTPP and ZnTPP(F_{20}) the calculated values are in good agreement with the experimental results,[109-111] but crystal structures for the other compounds of interest here are not available.

The slight changes of bond distances and angles among different molecules reflect the effect of substitutions either on the porphyrin macrocycle or of changes of the central metal atom. Comparing the metal to nitrogen bond lengths (M–N) in three MTPP (M = Mg, Zn, and Cd) metalloporphyrins, it is obvious that the Cd–N bond is 2.144 Å, which is longer than Zn–N (2.042 Å) and Mg–N (2.062 Å). The bond length of Cd–N in CdTPP reproduces the result of 2.14 Å reported by Rodesiler *et al.*[112] They found the crystal structure of CdTPP(dioxane)$_2$ to be nearly planar with Cd only 0.03 Å out of the plane of the nitrogens and a mean Cd–N distance of 2.14 Å. However, Hazell found a the non-planar porphyrin skeleton with a "floppy-hat" shaped structure, of which the pyrrole groups are not coplanar with the nitrogens but tilted out of the N_4 plane and Cd is being 0.578 Å out of N_4 plane with the mean Cd–N distance of 2.187 Å.[110] The differences among M–N bond lengths in three MTPP metalloporphyrins are in accord with the central metal ionic radii, where Mg^{2+} is 0.66 Å comparable to Zn^{2+} at 0.74 Å, while Cd^{2+} is significantly larger at 0.97 Å.[113] The size of the Zn^{2+} ion fits well into the cavity of the porphyrin macrocycle, and the Mg^{2+} is similar. However, when the Cd^{2+} ion with a larger diameter is incorporated, the cavity expands, making the interaction between the Cd^{2+} ion and the porphyrin macrocycle weaker. The effect of the central metal ion on the features of the porphyrin macrocycle can be also reflected by the comparison of the changes of bond lengths, such as C_α–N and C_α–C_β.

The characteristics of the porphyrin macrocycle also vary with the pattern and nature of substituents on the porphyrin framework. Ethyl-substitution or benzo-annulation of the four pyrrole rings slightly enlarges the cavity of the porphyrin macrocycle (the Zn–N bond length is *ca.* 0.02 Å longer in ZnOEP and ZnTBP than in other molecules calculated), and lengthens the C_β–C_β □bond (*ca.* 0.04 Å longer in ZnTBP than the others). However, substitution of phenyl groups and their halogenated derivatives at the four *meso*-positions does not significantly affect the geometry of the porphyrin framework when the D_{4h} symmetry constraint is applied.

Other than the slight changes in geometry, the effects of substitution are also reflected by energies and electron density distributions of the molecular orbitals of the ground state. A graphical representation of the orders of molecular orbitals and their symmetries is shown in Fig. 3.2. The corresponding energies of the molecular orbitals

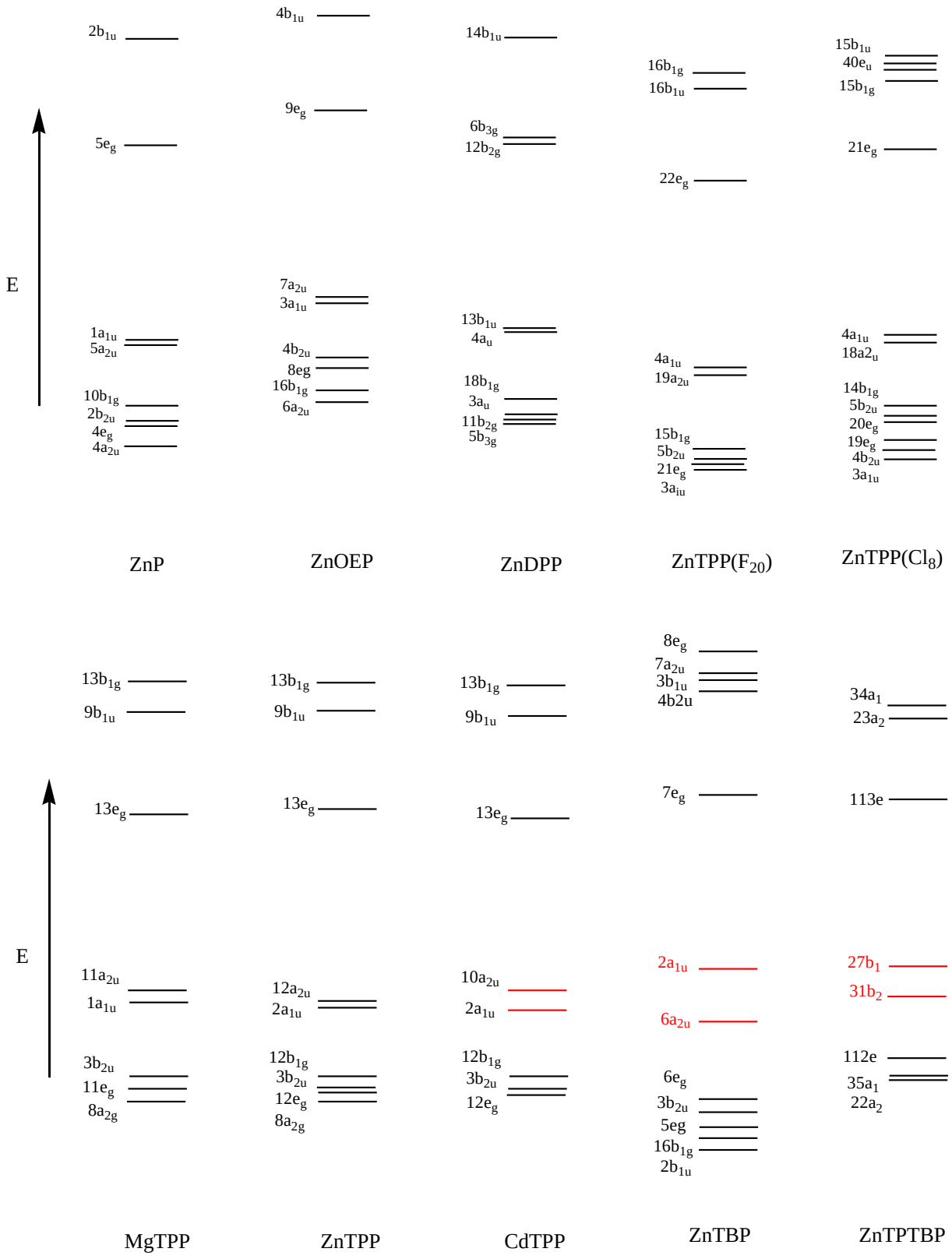

Fig. 3.2 Molecular orbital energy level diagrams for the molecules as shown.

are collected in table 3.3. These results are in good agreement with those values obtained by Nguyen *et al.*[49] using similar calculation methods. The energy levels of the two highest occupied orbitals HOMO and HOMO-1 and the two lowest unoccupied orbitals LUMO are of special interest because of their involvement in both Q and Soret

Table 3.3 TDDFT (B3LYP/6-31G(d)) orbital energies (in eV) at the DFT-calculated geometry of the ground state with a D_{4h}-symmetry constraint.

	ZnP		ZnOEP		ZnTPP(F_{20})		ZnTPP(Cl_8)		ZnDPP	
	Sym.	E	Sym.	E	Sym.	E	Sym.	E	Sym.	E
LUMO+2	$6a_{2u}$	0.86	$8a_{2u}$	1.12	$16b_{1g}$	-1.07	$40e_u$	-0.70	$14b_{1u}$	-0.51
LUMO+1	$2b_{1u}$	-0.54	$4b_{1u}$	-0.10	$16b_{1u}$	-1.32	$15b_{1g}$	-0.73	$6b_{3g}$	-2.11
LUMO	$5e_g$	-2.14	$9e_g$	-1.68	$22e_g$	-2.91	$21e_g$	-2.26	$12b_{2g}$	-2.12
HOMO	$1a_{1u}$	-5.21	$7a_{2u}$	-4.72	$4a_{1u}$	-5.87	$4a_{1u}$	-5.21	$13b_{1u}$	-5.13
HOMO-1	$5a_{2u}$	-5.22	$3a_{1u}$	-4.73	$19a_{2u}$	-5.95	$18a_{2u}$	-5.25	$4a_u$	-5.16
HOMO-2	$10b_{1g}$	-6.35	$4b_{2u}$	-5.74	$15b_{1g}$	-7.05	$14b_{1g}$	-6.41	$18b_{1g}$	-6.29
HOMO-3	$2b_{2u}$	-6.59	$8e_g$	-5.80	$5b_{2u}$	-7.14	$5b_{2u}$	-6.55	$3a_u$	-6.50
HOMO-4	$4e_g$	-6.60	$16b_{1g}$	-6.02	$21e_g$	-7.18	$20e_g$	-6.56	$11b_{2g}$	-6.51
HOMO-5	$4a_{2u}$	-7.00	$6a_{2u}$	-6.10	$3a_{1u}$	-7.21	$19e_g$	-6.78	$5b_{3g}$	-6.53

Table 3.3 (Cont'd)

	MgTPP		ZnTPP		CdTPP		ZnTBP		ZnTPTBP	
	Sym.	E	Sym.	E	Sym.	E	Sym.	E	Sym.	E
LUMO+2	$12b_{1g}$	-0.10	$13b_{1g}$	-0.11	$13b_{1g}$	-0.10	$3b_{1u}$	-0.53	$36a_1$	-0.53
LUMO+1	$9b_{1u}$	-0.52	$9b_{1u}$	-0.51	$9b_{1u}$	-0.64	$4b_{2u}$	-0.64	$23a_2$	-0.67
LUMO	$23e_g$	-2.11	$25e_g$	-2.11	$25e_g$	-2.18	$7e_g$	-2.09	113e	-2.04
HOMO	$10a_{2u}$	-4.97	$11a_{2u}$	-5.04	$11a_{2u}$	-5.02	$2a_{1u}$	-4.60	$27b_1$	-4.47
HOMO-1	$2a_{1u}$	-5.11	$2a_{1u}$	-5.13	$2a_{1u}$	-5.20	$6a_{2u}$	-5.33	$31b_2$	-5.00
HOMO-2	$3b_{2u}$	-6.38	$12b_{1g}$	-6.38	$12b_{1g}$	-5.75	$6e_g$	-6.39	112e	-6.04
HOMO-3	$22e_g$	-6.46	$3b_{2u}$	-6.42	$24e_g$	-6.41	$3b_{2u}$	-6.48	$35a_1$	-6.25
HOMO-4	$8a_{2g}$	-6.65	$24e_g$	-6.45	$3b_{2u}$	-6.43	$5e_g$	-6.59	$22a_2$	-6.27
HOMO-5	$58e_u$	-6.70	$8a_{2g}$	-6.67	$8a_{2g}$	-6.67	$16b_{1g}$	-6.63	110e	-6.32

transitions. Analyzing the data in Table 3.3 and the orders of the molecular orbitals shown in Fig. 3.2 indicates that in the metalloporphyrins examined, except ZnTBP, ZnTPTBP and CdTPP, the nearly degenerate two highest occupied orbitals HOMO and HOMO-1 and the strictly degenerate two lowest unoccupied orbitals LUMO are well-separated in energy from the remaining molecular orbitals as predicted in Gouterman's four-orbital model. However, the near-degeneracy of the HOMO and HOMO-1 molecular orbitals is lifted in ZnTBP and ZnTPTBP, and slightly lifted in CdTPP as shown in Fig. 3.2, while it remains in the other metalloporphyrins.

In addition, analyzing the differences of the electron density distributions among the orbitals (shown in Fig. 3.3) indicates that the a_{1u} orbital has nodes at the C_m atoms, but places considerable electron densities at the C_β atoms. Thus first order perturbation by substituents at the C_m position will be small; on the other hand, substituents on C_β atoms will contribute a lot to the changes of the porphine ring system. For the a_{2u} orbital, in contrast, a relatively smaller contribution has been placed on the C_β atoms but more on the C_m atoms and would be strongly influenced by substituents on C_m positions. As a result, the energy of the a_{1u} orbital is sensitive to substitution on C_β atoms, while that of the a_{2u} orbital is altered by substitution on C_m atoms. Therefore the orders of these two highest occupied orbitals can be altered by the substitutions on the porphyrin macrocycle, or the change of the central metal atom. [114]

In ZnTBP, benzo-annulation on the pyrroles expands the conjugation of the macrocycle from 26 to 42 π-electron system and thus delocalizes the electron density from the central porphyrin ring. As a result, the molecular orbital HOMO (a_{1u}) is relatively destabilized resulting in a higher (*ca.* 0.7 eV) energy than that of HOMO-1 (a_{2u}). This energy separation between the HOMO and HOMO-1 molecular orbitals is significant comparing to the differences in the other molecules which is less than 0.1 eV. As a consequence, a relatively weak interference between two excited electron configurations associated with the near-degeneracy of the two highest occupied molecular orbitals would be expected, and this is observed in ZnTBP.

However, in ZnOEP, all molecular orbital energies are globally increased due to the substitution of the ethyl groups on eight pyrrolic β–positions. This is consistent with the

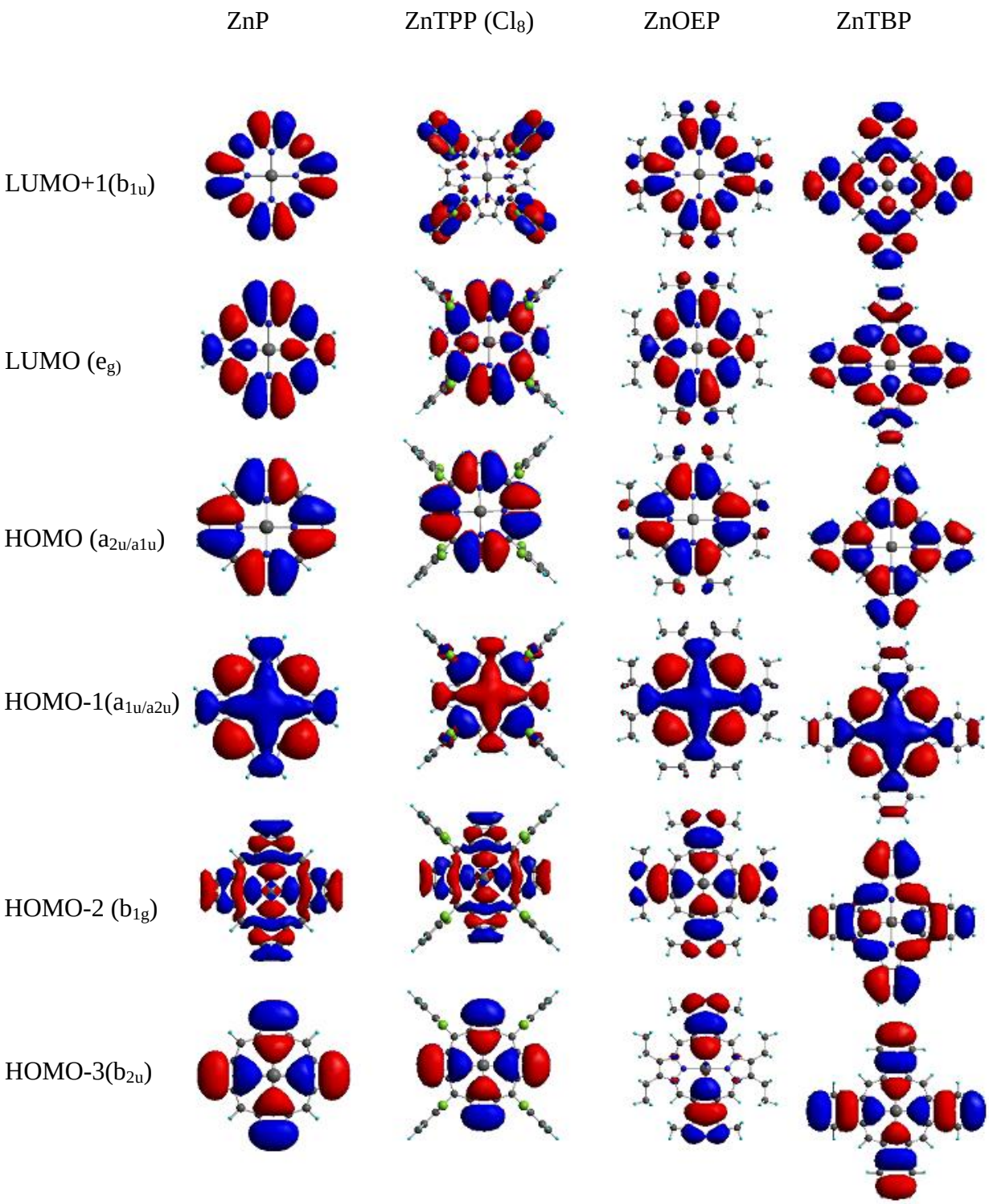

Fig. 3.3 Selected representative frontier molecular orbitals for ZnP, ZnTPP(Cl_8), ZnOEP and ZnTBP.

notion that the electron-donating substituents on the porphyrin ring would raise the orbital energies because of the electron repulsion.[115] Spellane *et al.*[116] also predicted that the change of the porphyrin ligand from P to OEP would raise the energy of the molecular orbitals. However, the electron-withdrawing substituents on the *meso*-substituted phenyl groups significantly stabilize molecular orbitals by lowing their energies in ZnTPP(F_{20}) and slightly in ZnTPP(Cl_8).

Another concern here is the differences of energy gaps between the HOMO and LUMO of each of the metalloporphyrins investigated, that can be calculated using the data in Table 3.2. There is no clear trend in these energy gaps for the whole set of compounds. In fact, these energy gaps are similar with the average about 3.0 eV and the differences less than 0.2 eV, but it is significantly smaller only *ca.* 2.5 eV in CdTPP and ZnTPTBP. In addition to the four frontier molecular orbitals involved in the Gouterman's model, the presence of more orbitals lying slightly in energy below the HOMO-1, especially the b_{2u} orbital, provides the possibility of one-electron transition such as $e_g \leftarrow b_{2u}$ leading to an excited electron configuration $b_{2u}^1e_g^1$ that mainly contributes to the 3^1E_u excited state, as can be seen in the following discussion.

In conclusion, substituents on the porphyrin macrocycle induce only slight changes in the molecular geometry of the ground state, but they do significantly affect the electron density distribution and orbital energies. In the following sections the ground state vibrations will be analyzed and the properties of the excited states will be discussed.

3.4.2 Ground state vibrations

DFT calculations can predict the frequencies of vibrational normal modes of the molecule and the intensities of their vibrational spectral bands. The changes in vibrational frequencies, particularly those in-plane skeletal vibrational modes would reflect the effects of substitutions on the porphyrin macrocycle.[95] Any substantial photoinduced change in the macrocycle conformation will result in a coordinate displacement of the ground and excited state potential energy surfaces. Such change is evidenced by two observable spectroscopic properties: one is the Stokes shift between the absorption and fluoresce maxima and the other is the FWHM of the absorption and emission spectra. The emission spectrum is even featureless when the displacement is large. However,

for the metalloporphyrins investigated in this thesis, the small Stokes shift and the similar FWHM of the emission spectra to that of the absorption spectra (refer to results presented in chapter 4 and 5) indicate that the displacement is minimal. Thus similar vibrational structures are expected between the ground and excited state potential energy surfaces. Thus it is reasonable to assume that the frequencies of the vibrational modes of the excited state are similar to those of the ground state.

Of particular interest here are the in-plane skeletal vibrations of the porphyrin macrocycle because of the possibility of their involvement in the S_2 radiationless transitions, and they have been selected for detailed analysis. For a model MTPP metalloporphyrin with D_{4h} symmetry, four phenyl rings of TPP are perpendicular to the planar porphyrin core with the metal being located in the center of the plane and with absence of the axial ligands. Such a planar porphyrin core has 71 in-plane skeletal vibrational modes that are combinations of C–C and C–N stretches of the porphyrin macrocycle. The aim of the vibration calculations concerns the differences in the vibrational frequencies among the metalloporphyrins under study, rather than assigning the calculated vibrational frequencies to specific vibrational normal modes. Detailed information regarding the assignments of vibrational normal modes may be found in references 117-119.[117-119]

In the present work, the vibrational frequencies of the set of metalloporphyrins under consideration have been calculated following geometry optimization using the same theoretical model and basis set. The vibrational spectrum can be produced according to the calculated vibrational frequencies and magnitudes. In table 3.4, those in-plane skeletal molecular vibrations with specific symmetries of ZnTPP, MgTPP, CdTPP and ZnOEP with frequencies falling within the range 1100 ~ 1600 cm^{-1} are summarized. The computed frequencies are usually scaled by an empirical factor that compensates for unavoidable systematic errors and that vary with the basis set used in the calculations. In the present study, all computed frequencies have been multiplied by a scaling factor of 0.9613 which is the optimal scaling factor for the 6-31G(d) basis set.[95] The vibrational spectra shown in Fig. 3.4 illustrate the differences of the vibrational intensities and frequencies of the four molecules compared.

Disregarding the differences in intensity and small shifts in wavenumbers of frequencies, all these four molecules have a similar number of vibrations with similar frequencies falling in the range from 1000 to 1600 cm^{-1}. The similar results have been found for all metalloporphyrins studied. The degeneracy of the vibrations with specific

Table 3.4 In-plane skeletal vibrations of the porphyrin macrocycle calculated using the DFT/B3LYP method (in cm^{-1}).

Symmetry	MgTPP	ZnTPP	CdTPP	ZnOEP
a_{1g}	1531	1543	1513	1525
	1426	1486	1407	1460
	1332	1437	1306	1354
	1213	1337	1213	1134
	1068	1215	1068	
		1070		
a_{2g}	1466	1322	1428	1552
	1314	1233	1254	1127
	1233		1297	1310
b_{1g}	1514	1536	1477	1498
	1485	1493	1460	1602
	1276	1269	1279	1225
	1072	1074	1068	1119
b_{2g}	1437	1453		
	1345	1351	1337	1133
	1246	1249	1150	1362
	1160	1165	1250	
		1164		
e_u	1511	1522	1495	1497
	1455	1473	1425	1547
	1410	1423	1218	1123
	1314	1318	1313	1342
	1279	1288	1057	1423
	1212	1215		1342
	1191	1195		1138
	1061	1064		

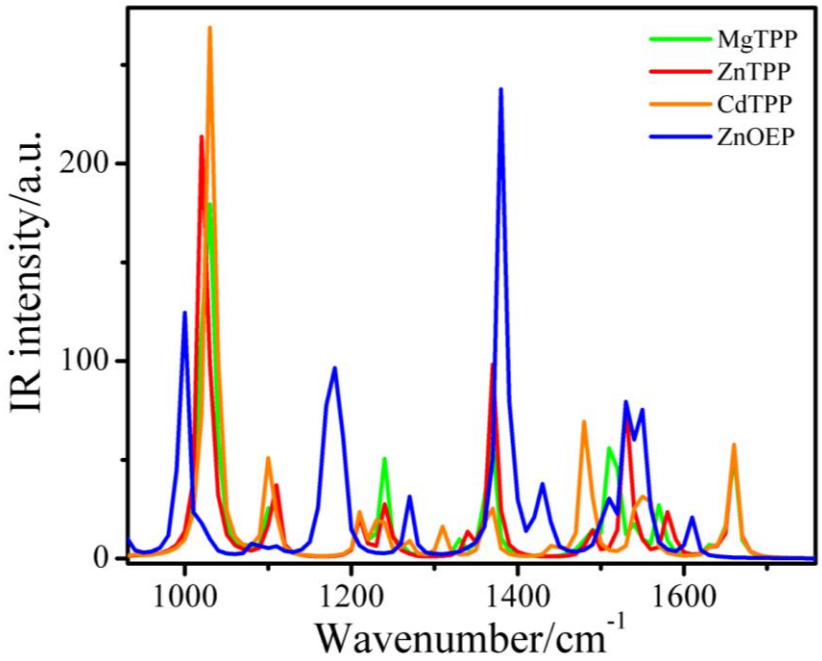

Fig. 3.4 Calculated IR spectra in the range of *ca.*1000 to 1600 cm^{-1} for MgTPP, ZnTPP, CdTPP and ZnOEP.

symmetries in this frequency range is between 20 and 30 for most metalloporphyrins studied here except for ZnTBP and ZnTPTBP which have more than 50 vibrations within this range, due to their expanded benzo-annulated macrocycles. Of importance, the average frequency of these vibrations is *ca.* 1350 cm^{-1} for all the metalloporphyrins considered. Together with the studies of the effects of deuteration, this information is needed to evaluate the role molecular vibrations play in the radiationless decay of the excited states of the metalloporphyrins, as will be discussed in the following chapters.

3.4.2 Excited states

In general, the optical spectra of metalloporphyrins are characterized by a weak Q band in the visible region with two vibronic bands referred to as Q (0,0) and Q(1,0); one intense B(0,0) band or Soret band in the uv-visible region with a small shoulder on its blue side and several bands with still higher energies. These spectroscopic features can be understood on the basis of the nature of the electronic transitions between the ground state and excited states. According to the electronic transition selection rules, for a

model metalloporphyrin ZnTPP, under D_{4h} molecular symmetry, only the spin and electric dipole allowed transitions from the ground state of the $^1A_{1g}$ symmetry to excited states of E_u and A_u symmetry are allowed.[47] Of these only those A_{1g} to E_u transitions, whose transition oscillator strengths are large enough, can be observed experimentally in absorption spectra, while the corresponding E_u to A_{1g} transitions are observed in the emission spectra. The lowest energy Q band is attributed to the transition $1^1E_u \leftarrow {}^1A_{1g}$. However, assignment of the Soret band to electronic transitions either $2^1E_u \leftarrow {}^1A_{1g}$, or $3^1E_u \leftarrow 1A_{1g}$, or both of them remains problematic. Higher energy bands on the blue side of the Soret band originate from the transitions to still higher energy n^1E_u states.

In the present work, sets of metalloporphyrins with different substituents at either *meso* or C_β positions or both have been selected to examine the potential relationship between their electronic structures and the photophysical properties of their Soret-excited states. The objective here is not to improve and develop the calculation methods to obtain the "best" calculation of either the ground state geometries or the excitation energies but rather to use a standard TDDFT (B3LYP/6-31G(d)) method to identify all of the electronic excited states in the vicinity of the 2^1E_u state that is initially populated by one photon excitation in Soret band region for all the molecules under consideration. All such states, including those that are "dark" because they are reached by electronically forbidden transitions, can potentially contribute to the radiationless decay of the initially populated Soret-excited states. Therefore, these calculations will provide clues to understand the nature of the radiationless decay processes involved in the relaxation of the short-lived upper excited states.

The calculated excitation energies, the one-electron promotion compositions of the transitions and the oscillator strengths of several singlet E_u excited states reached by one-photon, electric dipole allowed transitions are summarized in Table 3.5. According to the calculations (data in table 3.5), all the metalloporphyrins under study except ZnTBP and ZnTPTBP, exhibit common features of the transition to the first lowest energy singlet 1^1E_u excited state, which is assigned as the Q band by experimentalists. This transition has a very small oscillator strength ($f << 1$), and the one-electron promo tion compositions are near 50% $e_g \leftarrow a_{1u}$ and 50% $e_g \leftarrow a_{2u}$ in agreement with the interpretation of Gouterman's model.[97] Calculations regarding the transition to the 1^1E_u state

Table 3.5 One-electron promotion compositions, excitation energies (in eV) and oscillator strengths, f, of electric dipole allowed transitions to singlet E_u excited states in metalloporphyrins.

States	Compositions				TDDFT			Exp.
					E(eV)	f	Assign.	E(eV)
ZnP								
$1\ ^1E_u$	$1a_{1u}$-$5e_g$	49.46%	$5a_{2u}$-$5e_g$	48.66%	2.45	0.0024	Q	2.06[a]
$2\ ^1E_u$	$1a_{1u}$-$5e_g$	39.64%	$2b_{2u}$-$5e_g$	5.16%	3.55	0.9028	B	2.91[a]
	$5a_{2u}$-$5e_g$	41.53%	$4a_{2u}$-$5e_g$	5.51%				
$3\ ^1E_u$	$2b_{2u}$-$5e_g$	94.81%	$5a_{2u}$-$5e_g$	2.22%	3.85	0.0507		
$4\ ^1E_u$	$4a_{2u}$-$5e_g$	95.55%	$2b_{2u}$-$5e_g$	1.30%	4.31	0.1664		
ZnOEP								
$1\ ^1E_u$	$3a_{1u}$-$9e_g$	50.30%	$7a_{2u}$-$9e_g$	47.91%	2.41	0.0031	Q	2.17[b] 2.19[c]
$2\ ^1E_u$	$3a_{1u}$-$9e_g$	23.09%	$4b_{2u}$-$9e_g$	50.19%	3.42	0.64	B	3.19[b] 3.10[c]
	$7a_{2u}$-$9e_g$	18.69%						
$3\ ^1E_u$	$4b_{2u}$-$9e_g$	62.20%	$7a_{2u}$-$9e_g$	19.53%	3.53	0.55		
	$3a_{1u}$-$9e_g$	13.98%						
$4\ ^1E_u$	$7a_{2u}$-$9e_g$	95.54%	$4b_{2u}$-$9e_g$	2.10%	3.87	0.14		3.81[b] 3.75[c]
ZnTBP								
$1\ ^1E_u$	$2a_{1u}$-$7e_g$	71.21%	$6a_{2u}$-$7e_g$	28.20%	2.18	0.1754	Q	2.06[d] 1.98[e]
$2\ ^1E_u$	$6a_{2u}$-$7e_g$	71.29%	$2a_{1u}$-$8e_g$	3.59%	3.29	1.1166	B	3.18[d] 3.06[e]
	$2a_{1u}$-$7e_g$	13.55%	$1a_{1u}$-$7e_g$	1.81%				
	$3b_{2u}$-$7e_g$	1.65%						
$3\ ^1E_u$	$2a_{1u}$-$8e_g$	82.79%	$6a_{2u}$-$7e_g$	1.80%	3.76	0.1478		3.87[e]
	$3b_{2u}$-$7e_g$	12.83%						
$4\ ^1E_u$	$2b_{2u}$-$7e_g$	77.11%	$5a_{2u}$-$7e_g$	4.34%	3.87	0.0032		
	$2a_{1u}$-$8e_g$	13.15%	$2b_{1u}$-$7e_g$	3.77%				
ZnTPP								
$1\ ^1E_u$	$2a_{1u}$-$13e_g$	47.04%	$12a_{2u}$-$13e_g$	51.93%	2.35	0.0011	Q	2.09[f] 2.11[g]
$2\ ^1E_u$	$2a_{1u}$-$13e_g$	47.43%	$3b_{2u}$-$13e_g$	2.53%	3.35	1.3	B	3.05[f] 2.92[g]
	$12a_{2u}$-$13e_g$	38. 05%						
$3\ ^1E_u$	$3b_{2u}$-$13e_g$	95.90%	$12a_{2u}$-$13e_g$	1.21%	3.73	0.06		
$4\ ^1E_u$	$12a_{2u}$-$13e_g$	66.86%	$2a_{1u}$-$13e_g$	13.78%	4.18	0.069		
	$3b_{2u}$-$13e_g$	16.46%						
$ZnTPP(Cl_8)$								
$1\ ^1E_u$	$4a_{1u}$-$21e_g$	49.02%	$18a_{2u}$-$21e_g$	49.91%	2.35	0.0000	Q	1.92[h]
$2\ ^1E_u$	$4a_{1u}$-$21e_g$	43.65%	$5b_{2u}$-$21e_g$	3.01%	3.32	1.2498	B	2.72[h]
	$18a_{2u}$-$21e_g$	41.98%	$17a_{2u}$-$21e_g$	3.96%				
$3\ ^1E_u$	$5b_{2u}$-$21e_g$	95.90%	$18a_{2u}$-$21e_g$	1. 43%	3.69	0.0989		
$4\ ^1E_u$	$4b_{2u}$-$21e_g$	50.20%	$3a_{1u}$-$21e_g$	48.82%	4.01	0.0036		

Table 3.5 (cont'd)

States	Compositions				TDDFT			Exp.
					E(eV)	f	Assign	E(eV)
ZnTPP(F_{20})								
1 ^1E_u	$4a_{1u}$-$22e_g$	50.48%	$19a_{2u}$-$22e_g$	48.48%	2.37	0.0004	Q	2.11[i]
2 ^1E_u	$4a_{1u}$-$22e_g$	17.39%	$5b_{2u}$-$22e_g$	1.46%	3.37	1.2558	B	2.97[i]
	$19a_{2u}$-$22e_g$	18.16%	$18a_{2u}$-$22e_g$	2.04%				
3 ^1E_u	$5b_{2u}$-$22e_g$	78.07%	$4b_{2u}$-$22e_g$	17.51%	3.66	0.0989		
	$19a_{2u}$-$22e_g$	2.21%						
4 ^1E_u	$4a_{1u}$-$22e_g$	57.30%	$5b_{2u}$-$22e_g$	6.36%	3.78	0.0036		
	$4b_{2u}$-$22e_g$	34.76%						
MgTPP	CEP-31G basis set							
1 ^1E_u	$2a_{1u}$-$12e_g$	44.5%	$10a_{2u}$-$12e_g$	53.8%	2.30	0.0045	Q	2.07[j] 2.06[k]
2 ^1E_u	$2a_{1u}$-$12e_g$	31.4%	$10a_{2u}$-$12e_g$	39.7%	3.33	1.3106	B	3.05j 2.91[k]
	$9a_{2u}$-$23e_g$	3.7%	$10a_{2u}$-$24e_g$	8.7%				
3 ^1E_u	$3b_{2u}$-$12e_g$	90.8%			3.68	0.0844		
4 ^1E_u	$9a_{2u}$-$12e_g$	85.3%			4.11	0.1673		
CdTPP	CEP-31G basis set							
1 ^1E_u	$2a_{1u}$-$13e_g$	43.1%	$11a_{2u}$-$13e_g$	55.0%	2.31	0.0067	Q	2.03[l]
2 ^1E_u	$2a_{1u}$-$13e_g$	50.3%	$11a_{2u}$-$13e_g$	30.0%	3.28	1.2061	B	3.02[l]
	$10a_{2u}$-$13e_g$	4.6%						
3 ^1E_u	$3b_{2u}$-$13e_g$	94.4%	$11a_{2u}$-$13e_g$	1.5%	3.67	0.0937		
4 ^1E_u	$10a_{2u}$-$13e_g$	86.1%	$2b_{2u}$-$13e_g$	4.3%	4.05	0.1516		
ZnTPTBP								
1 ^1E	$31b_2$–$57e$	31.3%	$27b_1$-$57e$	67.2%	2.05	0.096	Q	1.90[m]
2 ^1E	$27b_1$–$57e$	17.8%	$31b_2$-$57e$	68.0%	2.95	1.2254	B	2.69[m]
1 $^1B2$	$27b_1$-$23a_2$	88.1%	$31b_2$–$36a_1$	2.5%	3.37	0.0299		
	56e–57e	4.6%						
3 ^1E	$30b_2$-57e	92.5%			3.52	0.0407		
4 ^1E	56e–57e	75.0%			3.56	0.0292		
ZnDPP								
1^1B_{2u}	$4a_u$–$12b_{2g}$	49.7%	$13b_{1u}$–$6b_{3g}$	50.3%	2.40	0.0012	Q	2.13[n]
1^1B_{3u}	$4a_u$–$6b_{3g}$	48.1%	$13b_{1u}$–$12b_{2g}$	51.8%	2.40	0.0005	Q	
2^1B_{3u}	$4a_u$–$6b_{3g}$	51.7%	$13b_{1u}$–$12b_{2g}$	43.6%	3.44	1.4975	B	3.02[n]
	$12b_{1u}$–$12b_{2g}$	4.6%						
2^1B_{2u}	$4a_u$–$12b_{2g}$	46.6%	$13b_{1u}$–$6b_{3g}$	41.9%	3.46	0.7716	B	
	$3a_u$–$12b_{2g}$	6.5%	$12b_{1u}$–$6b_{3g}$	5.0%				
3^1B_{2u}	$3a_u$–$12b_{2g}$	97.6%	$13b_{1u}$–$12b_{2g}$	2.3%	3.79	0.0541		
3^1B_{3u}	$3a_u$–$6b_{3g}$	100.0%			3.80	0.0458		

[a] Data taken in benzene at room temperature;[23] [b] Data taken in gas-phase;[23] [c] Data taken in benzene at room temperature;[23] [d] Data taken in a gas phase supersonic jet;[52] [e] Data taken in gas-phase;[49.] [f] Data taken in gas-phase;[23] [g] Data taken in benzene at room temperature;[23] [h] Data taken in chloroform;[48] [i] Data taken in ethanol at room temperature; [j] Data taken in gas-phase;[23] [k] Data taken in benzene at room temperature;[23] [l] Data taken in gas-phase;[23] [m] Data taken in ethanol at room temperature; [n] Data taken in ethanol at room temperature.

reproduce the results reported by Nguyen *et al.* for ZnP,[48,49,46] ZnTBP,[49] ZnTPP,[48,18] ZnTPP(Cl_8)[48] and MgTPP,[47] where given systematic calculation errors, the calculated values are in good agreement with available experimental values obtained either from the gas-phase or from solution. Some available representative experimental data are also included in Table 3.5 for comparison. All calculations mentioned above regarding the nature of the transition to the 1^1E_u state including the excitation energies, transition oscillator strength and one-electron promotion compositions are consistent and in good agreement with experimental results. However, the Soret band cannot be as simply pictured as the Q band. In the following paragraphs, our concerns focus on the nature of the Soret band.

Taking MgTPP as an example, according to the calculations, the second lowest energy electric dipole allowed electronic transition is to the 2^1E_u state. This transition includes major contributions from Gouterman's one-electron promotions and minor contributions from other one-electron promotions involving lower energy molecular orbitals. The transition to the 2^1E_u state has an exceedingly intense oscillator strength (f = 1.31) comparing to that to the 1^1E_u state (f = 0.0045). The ratio of the intensities of these two oscillator strengths is consistent with what is observed in the spectra obtained in solution. The predicted excitation energy (3.33 eV) is in reasonable agreement with available experimental values for the Soret band obtained in the gas-phase (3.05 eV) and in benzene at room temperature (2.91 eV).[23] The solvation effect is significant when comparing the values obtained in gas-phase and those obtained from solutions. In addition, it is of interest to see that the transition to the 3^1E_u state has a very weak oscillator strength (0.084) for MgTPP, and that the major contribution to the transition to the 3^1E_u state is from $e_g \leftarrow b_{2u}$, which is beyond the scope of Gouterman's four-orbital model. Moreover, the one-electron promotion compositions of transitions to other n^1E_u (n>3) excited states with higher energies involve contributions from lower energy molecular orbitals other than Gouterman's four orbitals.

As indicated by data in Table 3.5, the compositions of the one-electron promotions for electronic transitions to n^1E_u states vary with different compounds. Notable is that in ZnTBP, the composition of the transition to the 2^1E_u state is 71% $e_g \leftarrow a_{2u}$, 14% $e_g \leftarrow a_{1u}$ and some minor contributions from the lower energy molecular orbitals. The situa-

tion in ZnTPTBP is even more complicated, where transitions to n^1E_u states consist of contributions from even more one-electron promotions involving more molecular orbitals. These changes are traceable to the extent of the separation between two highest occupied orbitals in ZnTBP and ZnTPTBP, as discussed previously. The calculation results related to other metalloporphyrins studied in this project are also in good accord with available experimental values, and representative experimental values are also collected in Table 3.5. Thus the transition to the 2^1E_u state is assigned as the main Soret band near uv-visible region in spectra obtained in solution or the gas-phase.[23,48,49,120] The shoulder on the blue side of the main Soret band, denoted as B(1,0), is attributed to an envelope of vibronic transitions involving one quanta of skeletal vibrations in the S_2 excited state. The transition to the 3^1E_u state is assigned as the N band and the even higher energy bands are labeled as L and M bands etc.[23]

However, recent DFT calculations suggest that the main Soret band cannot be assigned as a single electronic transition to the 2^1E_u state, but also includes a transition to the 3^1E_u state. By using an improved TDDFT/SAOP method Baerends *et al.*[46] and Peralta *et al.*[47] have made great progress in improving the accuracy of excitation energy calculations. Their calculation results are in excellent agreement with gas-phase experimental values, with errors ≤ 0.2 eV. The TDDFT/SAOP method thus apparently performs better than the TDDFT/B3LYP method used here in the calculation of excitation energies. However, the most recent calculations conducted by Solheim *et al.*[51] challenge the results obtained by Baerends *et al.*[46] and Peralta *et al.*[47] who both use the same "Amsterdam TDDFT code". In particular, it is of interest to note that the Amsterdam group calculations predict that the oscillator strengths of the transitions to the 2^1E_u and 3^1E_u states are comparable to each other, which does not agree well with the results calculated using different calculation methods as mentioned above. Besides, in ZnP and MgP they found that the $e_g \leftarrow b_{2u}$ promotion is the main contributor to the electronic transition to the 2^1E_u state, while the Gouterman's transitions mainly contribute to the electronic transition to the 3^1E_u state. Moreover, the oscillator strength of the transition to the 2^1E_u state (0.4452) is less than that of the transition to the 3^1E_u state (1.0062), while the excitation energies corresponding to these two transitions are nearly degenerate in energy. However, in ZnTPP and MgTPP, the intensity ratio of the oscillator

strength of transitions to the 2^1E_u and 3^1E_u states is *ca.* 1:3 instead of >10:1 that is obtained in this work and other previous calculations.[48,49] Based on this information, the groups using Amsterdam code suggest that both electronic transitions to the 2^1E_u and 3^1E_u excited states contribute to the main Soret band observed in spectra, and attribute the transition to the 4^1E_u excited state to the shoulder on the blue side of the main Soret band.

TDDFT calculations presented in this thesis predict that the two transitions to the 2^1E_u and 3^1E_u excited states of ZnOEP are nearly degenerate in energy, and both have large transition oscillator strengths. This is similar to those of ZnP and MgP, reported by Baerends *et al.*[46] and Peralta *et al.*[47] However, the calculated energy gap between the 2^1E_u and 3^1E_u states in ZnOEP is only *ca.* 0.11 eV, but in other metalloporphyrins it is $\geq$ 0.9 eV. For molecules other than ZnOEP studied in this project, calculations provide no evidence of the existence of a transition to the ^1E_u state with such high oscillator strength in the vicinity of the 2^1E_u state. The very recent calculations reported by Solheim *et al.*[51] have confirmed our results that the two excited states 2^1E_u and 3^1E_u are well separated in energy, *ca.* 0.7 eV by their report, a value that is in good agreement with experimental findings, even though the excitation energy is overestimated about 0.5 eV by using the CAM-B3LYP method. In addition, several other TDDFT[47,98], TDHF[104], SAC-CI[121] and DFT/MRCI[50] calculations also found no state coupled to the ground state other than the 2^1E_u state. Solheim *et al.*[51] even argued that the SAOP functional used by Ziegler *et al.*[47] gave an incorrect description of the 3^1E_u state.

These most recent calculations are in agreement with both the experimental data and the calculations reported in this thesis that the Soret band is corresponding to a single, degenerate excited state, 2^1E_u. As will be shown in later chapters, the main Soret band of the spectrum obtained in solution is a single narrow band with FWHM *ca.* 300 cm^{-1} for ZnTPP. Therefore, if the main Soret band contains contributions from two separate electronic transitions, it must be only one of them that has a major contribution to the main Soret band intensity. The other one, if present, must make a minor contribution to the observed intensity and must be embedded under the main Soret band. If the transition to the 3^1E_u state is considered as the shoulder to the blue side of the main Soret band, the ratio of the 3^1E_u to 2^1E_u oscillator strengths obtained by Peralta *et al.*[47] might

be wrong, since their calculated oscillator strength do not agree with experimental spectroscopic observables, as will be shown in later chapters.

The computations mentioned above have focused on those n^1E_u excited states accessed by electric dipole allowed transitions. However, the calculations done here find a rather large number of additional states with symmetries other than E_u. Of particular interest are those states lying near or between the 1^1E_u and 2^1E_u excited states, *i.e.* those that might be accepting states in radiationless transitions. Typical TDDFT calculation results are illustrated in Fig. 3.5 to 3.7. The excitation energies and symmetries of all excited states that lie lower in energy than the 3^1E_u state include both singlet and triplet states, with both gerade and ungerade symmetry.

Note particularly (i) for ZnTPP(Cl_8) and ZnTPP(F_{20}) the 1^1E_g state lies just below the 2^1E_u state with almost the same energy. (ii) In CdTPP, this state is far below 2^1E_u state, and lies very close to the 1^1E_u state. (iii) In other metalloporphyrins, such as MgTPP, the 1^1E_g state has a higher energy and lies well above the 2^1E_u state. (iv) In ZnOEP the 2^1E_u state is accompanied by two nearly degenerate states, A_{1g} and B_{2g} with gerade symmetry, whereas these states lie above the 2^1E_u state (by 0.3 eV) in ZnTPP and its halogenated derivatives. (v) In ZnDPP, because the molecular symmetry decreases from D_{4h} to D_{2h}, the static Jahn-Teller effect lifts the degeneracy of the E_g and E_u states, yielding two nearly degenerate B_{2g} and B_{3g} and B_{2u} and B_{3u} states, respectively. Can this symmetry breaking significantly affect the interstate coupling energies between the S_2 and S_1 states and thus alter the relaxation dynamics of the S_2 excited states?

In ZnTBP, the energy of the 1^1E_u state is significantly stabilized by extension of the π-electron system, while the effect on the 2^1E_u state is insignificant, thus producing a large energy gap (*ca.* 1.11 eV) between the 1^1E_u and 2^1E_u states. As introduced in the chapter 1, this $S_2 - S_1$ energy gap is essential in the interpretation of the radiationless decay dynamics of the S_2 excited state when the energy gap law is applied. However, both the 1^1E and 2^1E states of ZnTPTBP have been stabilized substantially, resulting in the smallest $2^1E - 1^1E$ ($S_2 - S_1$) energy gap (*ca.* 0.9 eV) among the molecules examined here. In addition, the 1^1E and 2^1E states are well-separated from the remaining singlet excited states in ZnTPTBP, and are not accompanied by any of the singlet states as

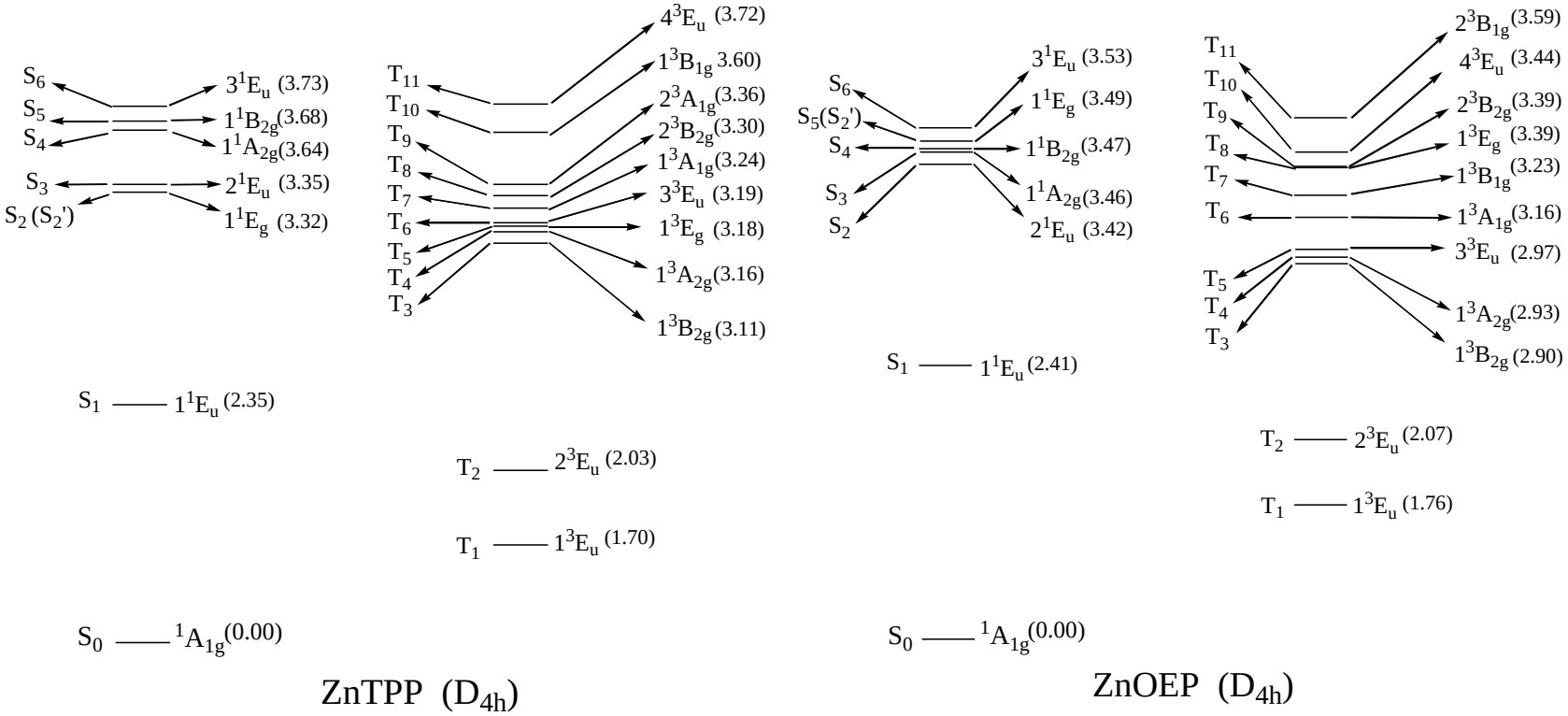

Fig. 3.5 Energy level diagram of ZnTPP and ZnOEP calculated by TDDFT (B3LYP/6-31G(d)) using a D_{4h} symmetry constraint. Energies are in eV.

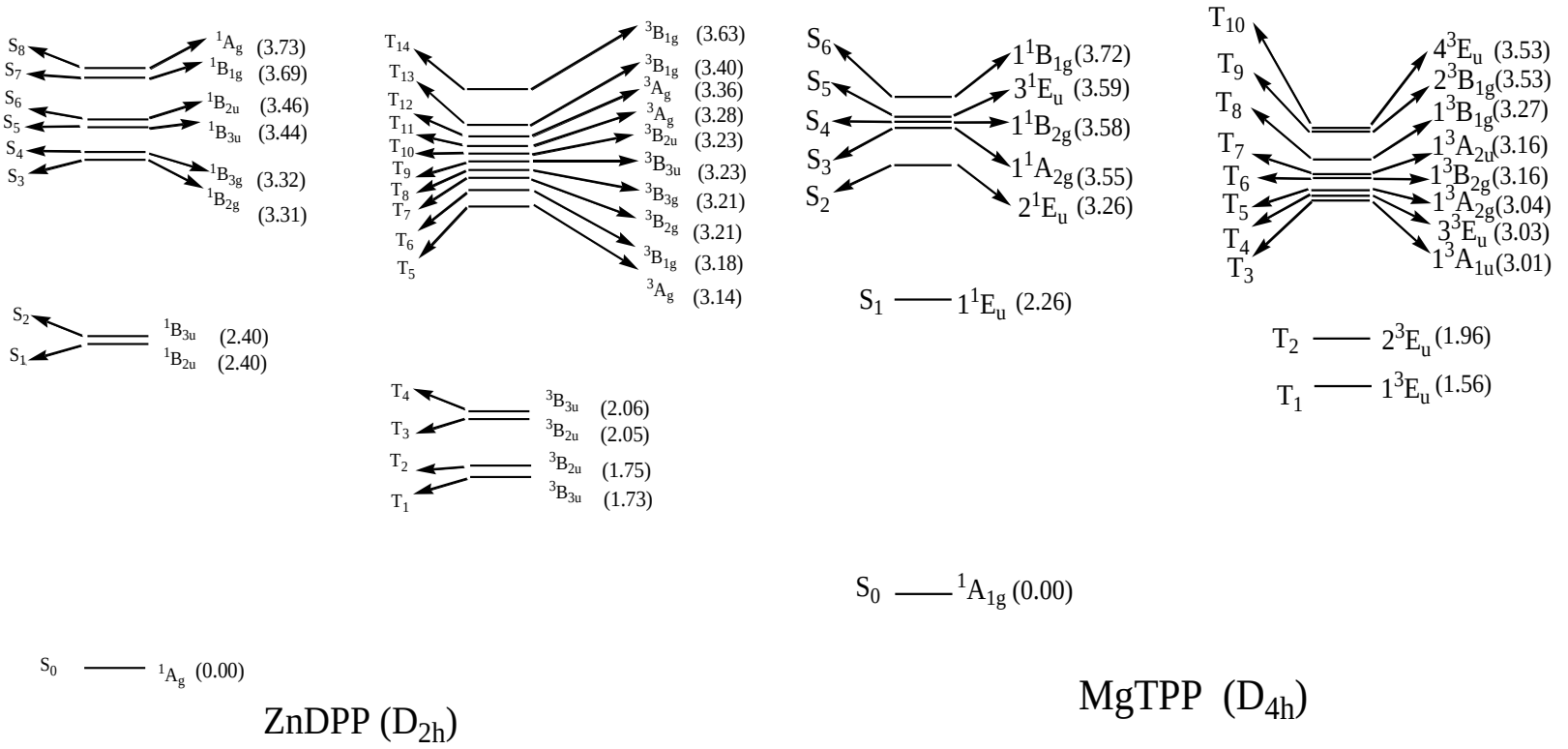

Fig. 3.6 Energy level diagram of ZnDPP (D_{2h}) and MgTPP (D_{4h}) calculated by the TDDFT (B3LYP/6-31G(d)) Energies are in eV.

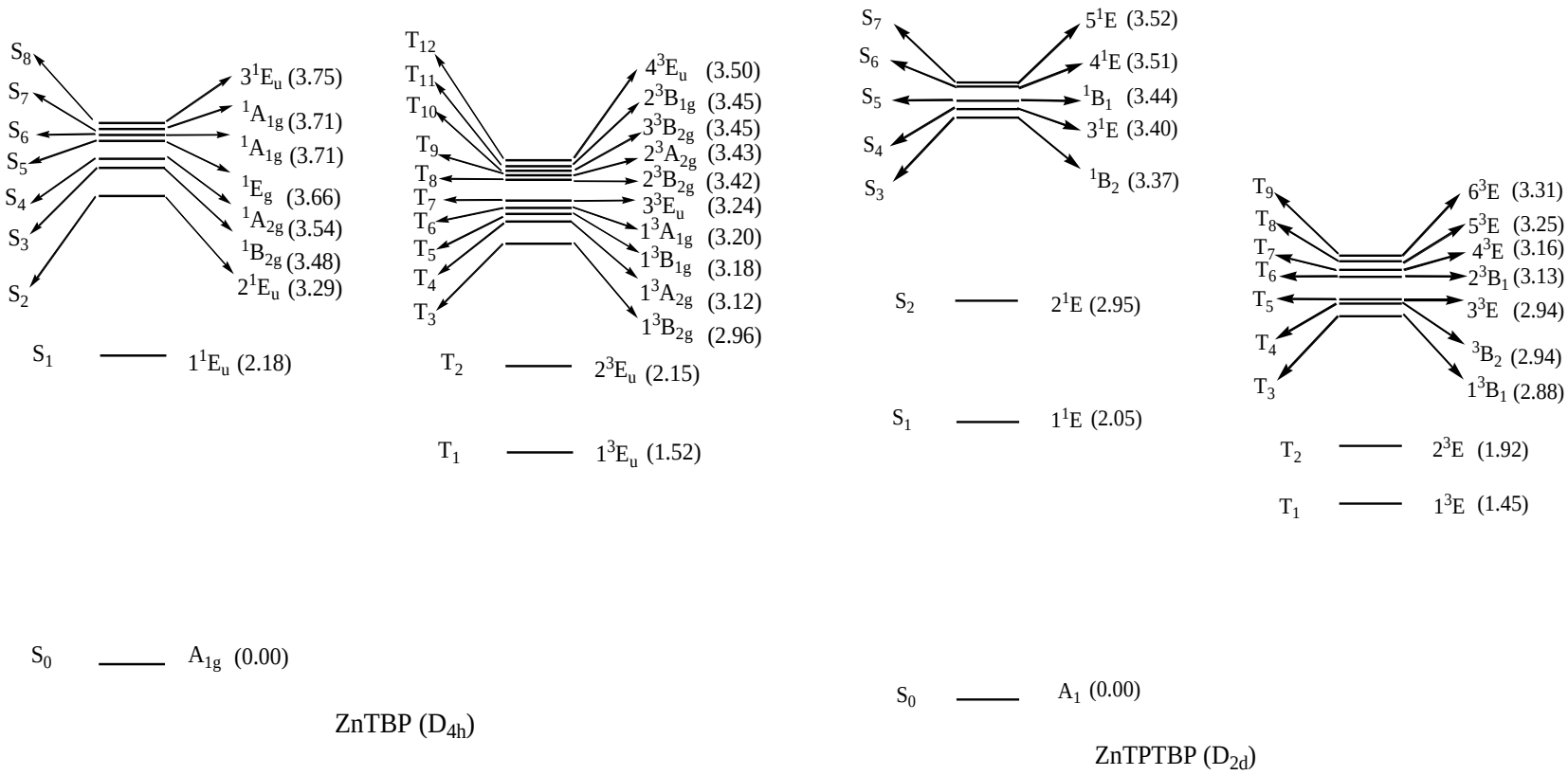

Fig. 3.7 Energy level diagram of ZnTBP calculated by TDDFT (B3LYP/6-31G(d)) using a D_{4h} symmetry constraint, and ZnTPTBP using a D_{2d} symmetry constraint. Energies are in eV.

found in the other metalloporphyrins. Nevertheless, the energy gaps between the first two excited singlet electronic states are very similar, *ca.* 0.9 to 1.1 eV, with an average of 1.0 eV, for the metalloporphyrins under consideration in this project. The difference does not exceed 0.2 eV.

In a model that ignores vibronic and spin-orbit coupling, all of these gerade states carry zero oscillator strength in transitions to and from ground state. However, any of them could be involved as accepting states in the radiationless decay of the 2^1E_u (or 3^1E_u) state populated by one-photon absorption in the near uv-visible region. In addition to gerade singlet states, the calculations also predict the existence of a number of triplet states lying between the S_2 and S_1 excited states in the metalloporphyrins studied. The role these triplet states might play in the relaxation of the singlet excited states is of interest. Are they able to accelerate the intersystem crossing between the Soret excited singlet states and the higher energy triplet excited states manifolds?

The existence of gerade electronic states at energies slightly higher than the 2^1E_u state has been confirmed experimentally in sequential two-photon, one-color absorption experiments.[42,44] Moreover, based on a careful analysis of the ultrafast dynamics of the S_2 state of ZnTPP in benzene, Yu, *et al.*[41] reported that one-photon absorption near 400 nm populates two independent and at most weakly coupled states (called S_2 and S_2' by them), both of which carry significant oscillator strength. This S_2' state was assigned as the 3^1E_u state by Baerends, *et al.*[46] However, no transition involving an n^1E_u ($n>2$) state near the 2^1E_u state with a large oscillator strength has been experimentally observed in the electronic spectra of ZnP, ZnTPP or ZnTBP at high temperature in the gas phase,[23,97,120] at low temperature in an inert matrix[53,122] or in a supersonic expansion.[32,33,52] Can either the 3^1E_u state or the gerade 1^1E_g state predicted by TDDFT calculations in ZnTPP that lies near the 2^1E_u state be responsible for the shoulder on the blue side of the Soret band observed in the absorption spectra in solution?

Up to date, how to assign the shoulder of the Soret band has remained an open question. Whether or not it participates in the radiationless decay of the S_2 and higher excited states is still unknown. Possible answers to these questions will be discussed in the following chapters with the aid of experimental results concerning the excited state relaxation dynamics.

3.5 Conclusions

The ground state geometries, vibrational frequencies, electronic structures and excited states energies of a set of metalloporphyrins have been calculated using DFT and TDDFT methods. The DFT and TDDFT methods used have proved to be sufficiently reliable to aid in interpretations of the experimental data to be presented in the following chapters. The following tentative conclusions can be drawn based on the analysis and discussions of the calculation results presented in this chapter. Substitutions on the porphyrin macrocycle do not significantly change the ground state geometry, however, they do affect the electronic structures by altering the energies and orders of the frontier molecular orbitals and the energy and the rank in energy of excited states in the metalloporphyrins under study. The biggest energy gap between the 2^1E_u and 1^1E_u states is found in ZnTBP, while the smallest one is found in ZnTPTBP. This energy gap is very similar among all other metalloporphyrins studied including ZnOEP. In addition, these calculations uncover some differences in the symmetries and relative energies of the frontier molecular orbitals and excited states among the metalloporphyrins, caused either by reduced molecular symmetry, or by the substitution of heavy atoms and other substituents.

The average frequency and the number of vibrations of the in-plane skeletal vibrations are almost the same in all the metalloporphyrins studied. ZnTBP and ZnTPTBP are exceptional due to their extended conjugated macrocycles. The role played by these vibrations in the relaxation of the 2^1E_u excited state will be discussed in later chapters.

The existence of a number of "dark" electronic excited states has been predicted by the TDDFT calculations, including both singlet and triplets with either gerade or ungerade symmetry, in the vicinity of the 2^1E_u state. The gerade state 1^1E_g, which is predicted to lie slightly lower than the 2^1E_u state in ZnTPP, lies far below the 2^1E_u state in CdTPP and lies higher than the 2^1E_u in MgTPP. In ZnOEP, different from other metalloporphyrins, there are several gerade and ungerade excited states near the 2^1E_u excited state. The roles these excited states, which are electric dipole forbidden in one photon transitions from the ground state, play in the radiationless decay dynamics of the excited molecules are as yet unknown. Based on these calculations and experimental results

presented in later chapters, the assignment of the observed transitions to excited state of known symmetry will be discussed in the following chapters.

Chapter 4: Solvatochromic Effects on the Photophysics of Higher Excited States of Zinc Metalloporphyrins

4.1 Introduction

The electronic spectroscopic properties of fluorophores observed in solution, such as band positions, intensities and shapes are dependent on the solvent and local microenvironment and may differ substantially from the corresponding gas phase spectra. The solvent-induced shift of band position is called the solvatochromic effect,[20,71,123,124] and this phenomenon can be used to determine important properties of the solute and solvent. For example, Zhou *et al.* have studied the binding and catalysis properties of solvent-responsive metalloporphyrins which were functionalized by eight cholate units at *meta* positions of the phenyl rings, and found that the solvent-dependent intramolecular aggregation of the cholate derivatives can be used to tune the catalytic activity of iron porphyrins.[125]

Nappa *et al.*[126] conducted a detailed study of solvatochromic effects on the positions of the absorption maxima of individual Soret and Q bands and also measured the effects of solvent on the relative intensities of two vibronic bands in the Q absorption region of ZnTPP. However the effects of solvent on the decay dynamics of the excited states of ZnTPP were not included in their study.

The limited existing information[35,42,57] regarding the effects of solvent on the S_2 fluorescence quantum yields and lifetimes of ZnTPP and other diamagnetic metalloporphyrins is insufficient to obtain a complete understanding of solvation effects on the S_2 relaxation mechanisms. In particular, no one has carried out systematic studies of the effect of solvent on the S_2 relaxation of the model compound, ZnTPP, by measuring both steady-state and time-resolved spectroscopy in a wide set of solvents. The objective of the present work is to conduct systematic and detailed studies of solvation effects in order to obtain a better understanding of the relaxation mechanisms of the S_2 state of ZnTPP, and hence other similar metalloporphyrins.

4.2 Results and discussion

4.2.1 Solvent dependence of steady state absorption and emission spectra of ZnTPP

The steady state absorption and emission spectra of ZnTPP in various solvents were carefully measured as described in sections 2.2 and 2.3 of chapter 2. Dilute solutions with concentration *ca.* 1 to 3 x 10^{-6} M or less were used to avoid the effects of aggregation and to eliminate inner filter effects. All emission spectra were corrected following the procedures presented in section 2.3, if necessary, before being used for analysis. Representative absorption spectra of ZnTPP in a set of solvents, plotted as molar extinction coefficient versus wavenumbers (linear in energy) are shown in Fig. 4.1.

In general, the solvation effects on the Soret bands cause a red shift with increasing polarizability (or refractive index) of the solvents from methanol to carbon disulfide. However, the shift of the Q band is relatively small compared to the bandwidth of the origin band and no clear trend observed. It is important to note that the Soret band is more sensitive than the Q band to the change of the solvent polarizability. As a consequence, the $S_2 - S_1$ energy spacing of ZnTPP becomes smaller with increasing polarizability of the solvent. In addition to the shift of the band maximum positions, Fig. 4.1 also shows the changes of the relative magnitudes of molar extinction coefficient due to solvation effects. The common trend is that the molar extinction coefficient of ZnTPP decreases with increasing the solvent polarizability. A similar trend of the spectral shift was observed in the emission spectra of ZnTPP in different solvents.

Fig. 4.2 illustrates a typical normalized corrected fluorescence spectrum of ZnTPP in benzene together with its corresponding absorption spectrum. A few features are important to note. (i) The fluorescence spectrum is a good mirror image of the corresponding absorption spectrum in both the Soret and Q bands, which implies that the vibrational levels in the excited state are very similar to those in the ground state. (ii) The Stokes shift is only 167 $\pm$ 20 cm^{-1} for the Soret band and 245 $\pm$ 20 cm^{-1} for the Q band (between two (0,0) vibronic bands). The Stokes shift of the Q band is larger than that of the Soret band, but both are very small compared to other chromophores, where it could be as large as 1000 cm^{-1} or more.

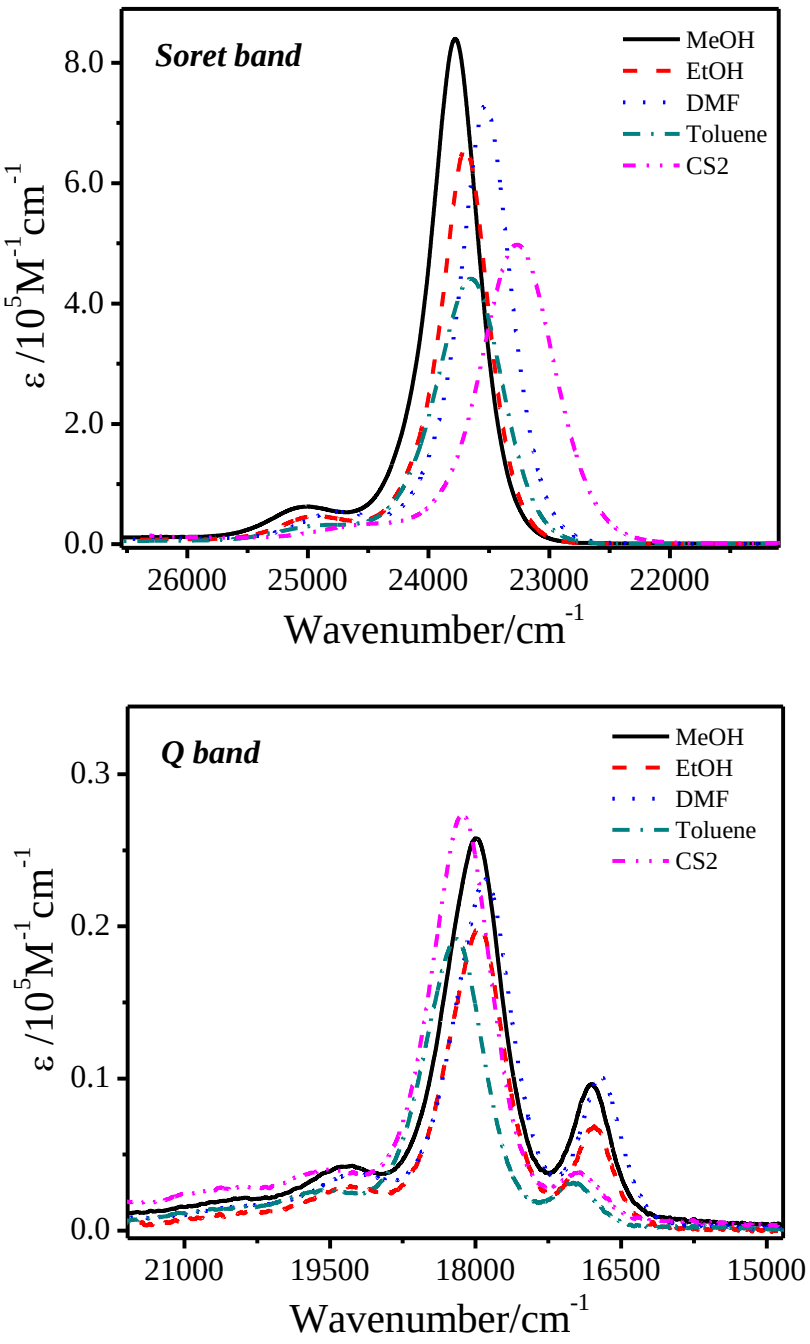

Fig. 4.1 Representative absorption spectra of the Soret bands (top) and Q bands (bottom) of ZnTPP in different solvents as shown. Solution concentrations are in the 1 to 2 x 10^{-6} M range.

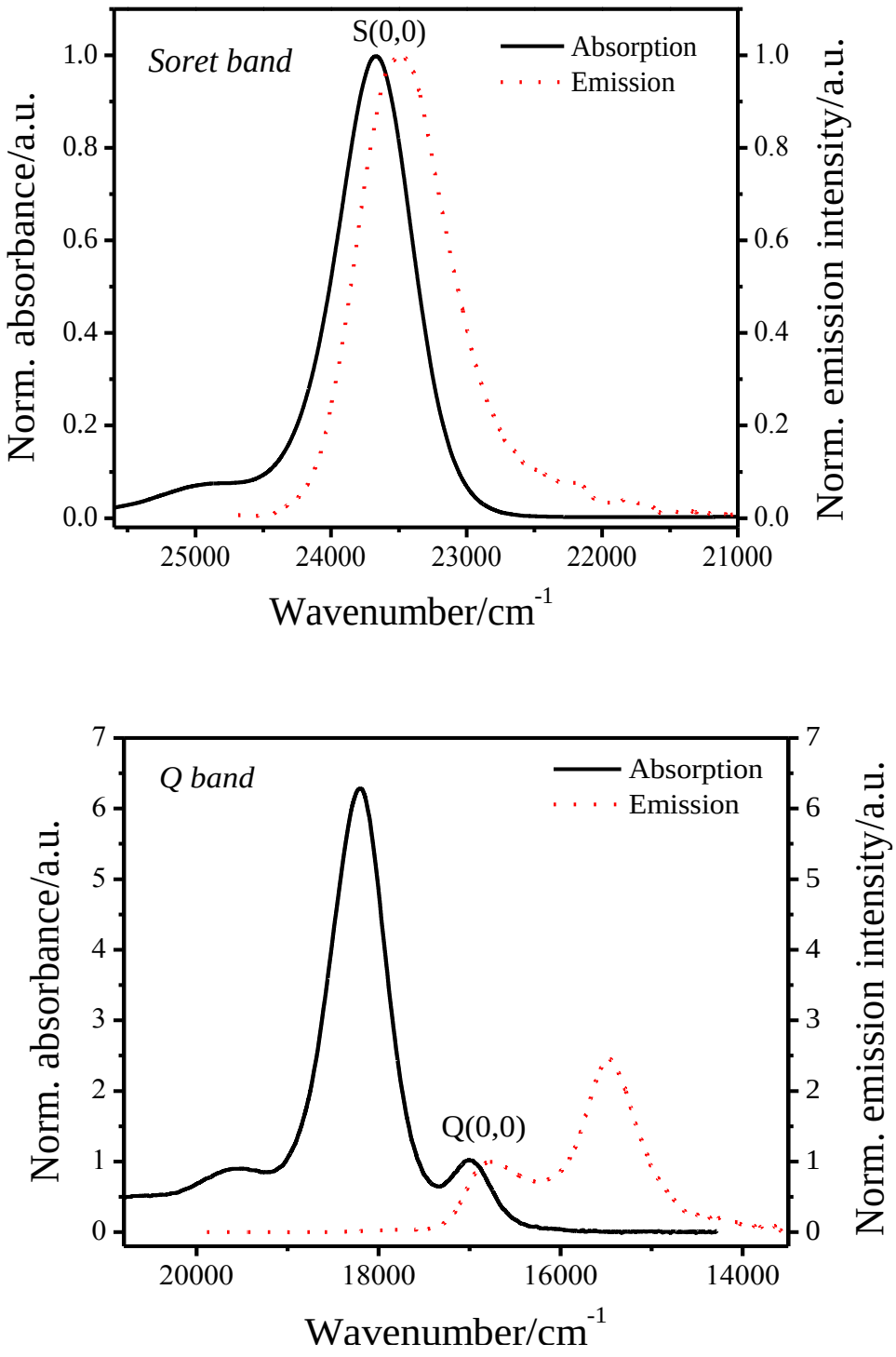

Fig. 4.2 Normalized absorption and emission spectra of ZnTPP in benzene. The emission was obtained with excitation at 400 nm. The crossing points Q(0,0) and S(0,0) are also shown.

When comparing the Stokes shift of the Soret band in different solvents, the maximum variation in the range from 180 $\pm$ 20 cm^{-1} in methanol to 235 $\pm$ 20 cm^{-1} in toluene is not significant given the great difference of the refractive indices of the wide range of solvents employed. The small Stokes shift is consistent with the rigid structure of the porphyrin macrocycle. As well, the rigidity of the macrocycle isn't significantly altered by phenyl substitution at least as shown by small changes in both the absorption and emission spectra when comparing ZnP with ZnTPP in solution at room temperature. (iii) The overlap between the absorption and the corresponding emission spectra in the Soret region is significant. This introduces a big challenge for experimentalists to obtain accurate measurements of the S_2 emission intensity and fluorescence quantum yields. Due to the large molar extinction coefficient of ZnTPP in this region, fluorescent photons emitted from the S_2 state will be reabsorbed by molecules in the ground state before exiting the sample solution. In order to obtain an accurate S_2 fluorescence spectrum, corrections for the inner filter effect including both attenuation and reabsorption effects should be made as described in section 2.3, when solutions with high concentrations are used.

The spectroscopic properties of ZnTPP obtained by analysis of the absorption and corrected emission spectra in various solvents are collected in Table 4.1. The fluorescence quantum yields of the ZnTPP in different solvents for both S_2 and S_1 states were calculated using the method described in section 2.3.3 of chapter 2. The data are also included in Table 4.1. Accurate measurements of the absorption and emission spectra provide data by which, the $S_2 - S_1$ energy gap, $\Delta E(S_2 - S_1)$, can be determined most accurately. The best procedure to calculate $\Delta E(S_2 - S_1)$ has not always been followed. Values previously calculated by taking the energy difference between the band maximum of the Soret band and the furthest red Q band of the absorption spectra observed in solution, ignore differential solvation effects on the electronic transition origins. To do a more accurate calculation in the present work, the wavenumber of the $S_2 - S_0$ electronic transition origin (S(0,0) was determined by taking the crossing point between the red edge of absorption spectrum and blue edge of the corrected, normalized corresponding emission spectrum, as shown in Fig. 4.2. The same method is used to get the value of the wavenumber of the $S_1 - S_0$ electronic transition origin Q(0,0), and the wavenumber of the $\Delta E(S_2 - S_1)$ spacing is then calculated by subtracting the Q band Q(0,0) value

from value of the S(0,0) of the Soret band. The data are collected in Table 4.1. In particular, the $\Delta E(S_2 - S_1)$ of ZnTPP ranges from 6998 $\pm$ 30 cm^{-1} to 6460 $\pm$ 30 cm^{-1} when increasing the solvent polarizability from methanol to CS_2. The changes in $\Delta E(S_2 - S_1)$ are not large, even though in the present work a set of solvents with a wide range of Lorenz-Lorentz polarizabilities ($f_1 = (n^2 - 1)/(n^2 + 2)$ from 0.205 in methanol to 0.354 in CS_2) have been selected in order to induce the largest possible range in $\Delta E(S_2 - S_1)$.

Interpretation of solvent-dependent spectroscopic properties is a very complicated topic, because of the complexity of the interactions between solvent and solute molecules and the influence of these interactions on both the ground state and excited states of the solute.[20] Nicol has extensively studied solvent effects on electronic spectra, and classified the effects into two major groups according to the nature of the solvent-solute interactions. One is due to specific effects, such as presence of hydrogen-bonding, formation of non-covalently bound intermediate states or metal-ligand complexes, charge transfer states, etc. The others result from physical interactions between solvent and solute molecules, and have been further divided into four types according to the properties of the solvents and solutes: (a) interaction between polar solute and polar solvent, (b) interaction between polar solute and induced dipole of solvent, (c) interaction between induced dipole of solute and polar solvent, and (d) interaction between mutually induced dipoles of solute and solvent.[71,127] In the present work, the set of metalloporphyrins are large symmetric non-polar molecules, so physical interaction of either type (c) or (d) or both would be most important here. The nature of the interactions between the excited metalloporphyrin solutes and different solvents would be explored by studies of the solvatochromic effects on the steady-state spectroscopy and dynamic relaxation of the highly excited electronic states.

The physical interactions between solute and solvent molecules, for each of two coupled electronic states with different polarizabilities, results in different alterations of the energy of each state. As a consequence, the energy spacing between the two electronic states will depend on the polarizability of the solvent. Eq. 4.1, which was derived by Nicol,[71] shows a correlation between the spacing of two electronic states and the dielectric constants and refractive indexes of the solvents.

$$\Delta E(S_1 - S_0) = (A + C)\left[\frac{n^2 - 1}{2n^2 + 1}\right] + B\left[\frac{(\varepsilon - n^2)(2\varepsilon + n^2)}{\varepsilon(n + 2)^2}\right] + D\left[\frac{\varepsilon - 1}{\varepsilon + 2} - \frac{n^2 - 1}{n^2 + 1}\right] \quad (4.1)$$

$\Delta E(S_1 - S_0)$ is the energy gap between the first excited singlet state and the ground state, A, B, C, D are parameters related to the electric dipole moments of the solute and solvent corresponding to the solute-solvent physical interaction types throughout (a) to (d), respectively, n stands for the refractive index and ε is dielectric constant of the solvent.

For convenience the parameters f_A, f_B, f_C and f_D are defined in eq. 4.2 to eq. 4.4, to represent functions of the dielectric constant and refractive index of the solvents based on eq. 4.1.

$$f_A = f_C = \frac{n^2 - 1}{2n^2 + 1} \quad (4.2)$$

$$f_B = \frac{(\varepsilon - n^2)(2\varepsilon + n^2)}{\varepsilon(n + 2)^2} \quad (4.3)$$

$$f_D = \frac{\varepsilon - 1}{\varepsilon + 2} - \frac{n^2 - 1}{n^2 + 1} \quad (4.4)$$

In addition to parameters extracted from Nicol's equation, another two parameters Δf (eq. 4.5) and f_1 (eq. 4.6) are defined as follows.

$$\Delta f = \frac{\varepsilon - 1}{2\varepsilon + 1} - \frac{n^2 - 1}{2n^2 + 1} \quad (4.5)$$

and

$$f_1 = \frac{n^2 - 1}{n^2 + 2} \quad (4.6)$$

These two parameters are extracted from the Lippert equation,[20] and also proposed to interpret the dependence of $\Delta E(S_1 - S_0)$ on the property of the refractive index (n) and/or dielectric constants (ε) of the solvent. Note particular that f_1 is the Lorenz-Lorentz polarizability function, which is a function of solvent refractive index only and measures the polarizability of the solvent. When trying to correlate particular spectroscopic properties with the nature of the solvent or the structural properties of the

Table 4.1 Near uv-vis spectroscopic properties of ZnTPP in various solvents at room temperature.

Solvents	Methanol	Acetonitrile	Ethanol	1-Propanol	1-Butanol	THF
$f_1=(n^2-1)/(n^2+2)$	0.205	0.212	0.222	0.234	0.242	0.245
$E^{abs,0-0}$(Soret)/cm^{-1}	23780	23753	23694	23645	23607	23640
ε_{max}(Soret) /$10^5 M^{-1}cm^{-1}$	8.46	-	6.58	6.75	6.70	7.56
FWHM $\Delta\bar{\nu}^{abs}$(Soret)/cm^{-1}	314	340	274	312	314	306
E^{em} B(0,0)/cm^{-1}	23600	23585	23550	23470	23446	23529
FWHM $\Delta\bar{\nu}^{em}$(Soret)/cm^{-1}	388	393	319	385	388	391
Shift(SS_2)/cm^{-1}	180	168	144	175	161	111
Soret (0,0)/cm^{-1}	23692	23675	23619	23556	23525	23601
Q (0,0)/cm^{-1}	16694	16714	16689	16664	16659	16735
ΔE (S_2 - S_1)/cm^{-1}	6998	6961	6930	6892	6866	6866
$E^{abs,0-0}$(Q)/cm^{-1}	16788	16807	16786	16773	16764	16835
ε^{max}(Q) /$10^4 M^{-1}cm^{-1}$	2.57	-	2.17	2.16	2.18	2.51
FWHM $\Delta\bar{\nu}^{abs}$(Q)/cm^{-1}	326	359	398	389	381	346
E^{em} Q(0,0)/cm^{-1}	16593	16610	16590	16561	16552	16625
FWHM $\Delta\bar{\nu}^{em}$(Q)/cm^{-1}	374	433	360	378	370	306
Shift(SS_1)/cm^{-1}	195	197	196	212	212	210

Table 4.1 (cont'd).

Solvents	DMF	c-hexane	Toluene	Benzene	CS_2
$f_1=(n^2-1)/(n^2+2)$	0.257	0.258	0.296	0.295	0.354
$E^{abs,0-0}$(Soret)/cm^{-1}	23529	24038	23641	23641	23263
ε^{max}(Soret) /$10^5 M^{-1}cm^{-1}$	7.29	-	4.42	5.87	5.00
FWHM $\Delta\bar{\nu}^{abs}$(Soret)/cm^{-1}	423	352	385	590	440
E^{em} B(0,0)/cm^{-1}	23406	23753	23406	23474	22988
FWHM $\Delta\bar{\nu}^{em}$(Soret)/cm^{-1}	472	545	477	660	542
Shift(SS_2)/cm^{-1}	123	285	235	167	283
Soret (0,0)/cm^{-1}	23469	23958	23536	23561	23124
Q(0,0)/cm^{-1}	16637	17062	16875	16866	16764
ΔE (S_2 - S_1)/cm^{-1}	6832	6896	6661	6695	6460
$E^{abs,0-0}$(Q)/cm^{-1}	16736	17097	16983	16975	16936
ε^{max}(Q) /$10^4 M^{-1}cm^{-1}$	2.36	-	2.45	2.54	2.17
FWHM $\Delta\bar{\nu}^{abs}$(Q)/cm^{-1}	411	577	366	458	395
E^{em} Q(0,0)/cm^{-1}	16556	16731	16764	16729	16598
FWHM $\Delta\bar{\nu}^{em}$(Q) /cm^{-1}	416	607	564	656	554
Shift(SS_1)/cm^{-1}	180	366	219	246	338

- not available

metalloporphyrins, it was found that some but not all spectroscopic parameters can be correlated with the nature of the solvent. Of particular interest here is the correlation between the $S_2 - S_1$ energy spacing, $\Delta E(S_2 - S_1)$, and these parameters defined in eq. 4.2 to 4.6. Fig. 4.3 shows a series of graphs of $\Delta E(S_2 - S_1)$ of ZnTPP in different solvents against the four parameters f_B, f_1, Δf, and f_A (f_C). A good linear relationship is

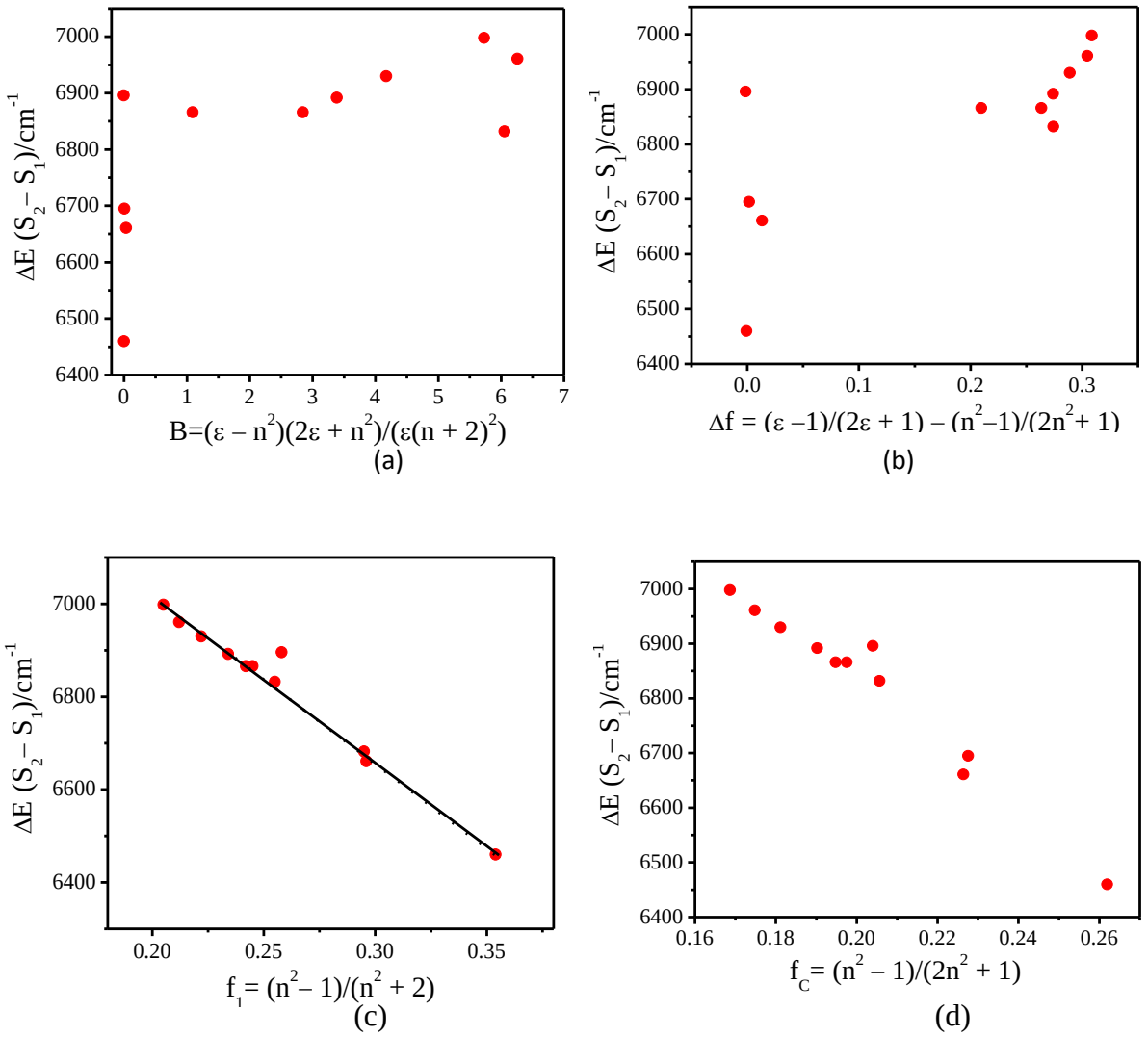

Fig. 4.3 Plots of the $S_2 - S_1$ energy gaps, $\Delta E(S_2 - S_1)$, of ZnTPP versus several functions of the dielectric constants and refractive indices of the solvents

obtained for plots of the $\Delta E(S_2 - S_1)$ of ZnTPP against the Lorenz-Lorentz solvent polarizability function, f_1, and function, f_A (f_C), respectively. However, similar plots for the other three parameters, f_B, f_D and Δf, don't exhibit such a linear relationship. A similar correlation was obtained in an investigation of solvatochromic effects on the individual Soret and Q band absorptions of ZnTPP, as reported previously by Nappa *et al.*[126]

It is important to note that both f_1 and f_A (f_C) only depend on the refractive index of the solvent, and therefore, each of these two parameters is a measure of the influence of only solvent polarizability. Note particularly when the straight line of the plot of $\Delta E(S_2 - S_1)$ *vs.* f_1 is extrapolated to $f_1 = 0$ (n=1), the intercept gives the electronic energy gap between the Q and Soret absorption bands of the bare molecule observed in a supersonic expansion. But this value can not be obtained from the extrapolation of the straight lines of the plots of $\Delta E(S_2 - S_1)$ *vs.* f_A (f_c) to $f_A = 0$. Thus the parameter f_1 is more precise in measuring the solvent polarizability and was chosen for the following discussion of the correlations between $\Delta E(S_2 - S_1)$ and solvent polarizability.

As shown in Fig. 4.4, extrapolation of the straight line of ZnTPP to $f_1 = 0$ results in an intercept of 7746 $\pm$ 10 cm^{-1} which agrees with 7752 cm^{-1} observed in a supersonic expansion.[32] Here, the points at $f_1 = 0$ are introduced for the purposes of obtaining an

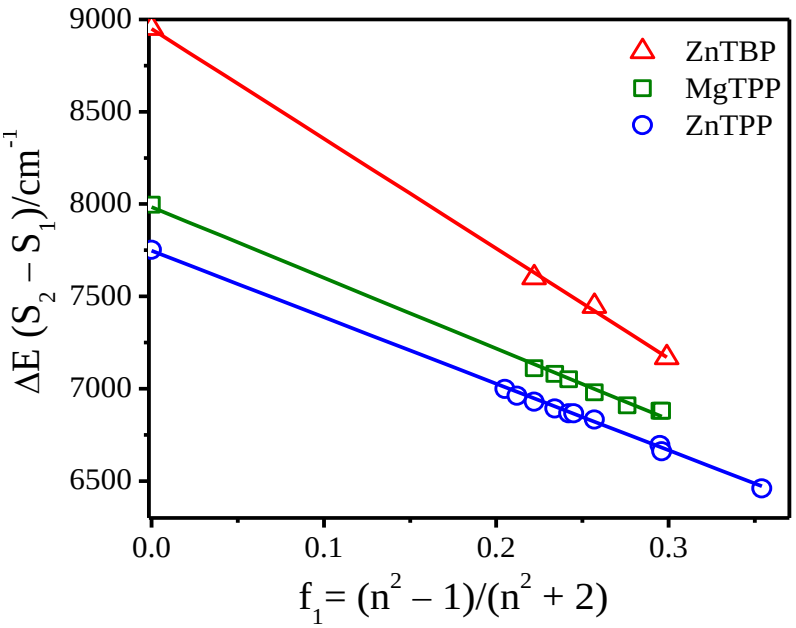

Fig. 4.4 Plots of $\Delta E(S_2 - S_1)$ versus the solvent polarizability function f_1 for ZnTBP, MgTPP and ZnTPP. The values of $\Delta E(S_2 - S_1)$ for the isolated molecules ($f_1 = 0$) from supersonic jet spectroscopy are also plotted.[5,6,32]

accurate value of the slopes. This provides evidences of the mutual accuracy and reliability of the experiments both conducted in solutions and supersonic expansion gas phase. Similar results were obtained by Tripathy *et al.*[74] for MgTPP, where the intercept

of the plot at $f_1 = 0$ is 7984 $\pm$ 20 cm^{-1} compared with 7996 cm^{-1} obtained from supersonic jet spectroscopy.[6] In addition, the energy gap separating the electronic transition origins of the S_2 and S_1 states in ZnTBP is 8953 cm^{-1} obtained by Even *et al.*[52] in supersonic expansion, which is beautifully agreement with the intercept of 8949 $\pm$ 30 cm^{-1} obtained in this study from a similar plot of $\Delta E(S_2 - S_1)$ *vs.* f_1. All three plots together with intercepts of the plots are shown in Fig. 4.4. Thus, the value of the electronic energy gap $\Delta E(S_2 - S_1)$ of other isolated metalloporphyrins that have not been examined in supersonic expansions can be reasonably predicted from good linear correlations between $\Delta E(S_2 - S_1)$ and f_1 obtained in solution.

Does such a linear relationship between $\Delta E(S_2 - S_1)$ and f_1 apply to metalloporphyrins other than ZnTPP, MgTPP and ZnTBP? For comparison, the absorption spectra of other four metalloporphyrins, ZnP, ZnTPP(F_{20}), ZnTPP(Cl_8) and ZnOEP were also measured carefully in different solvents with wide range of solvent polarizabilities, and the corresponding values of $\Delta E(S_2 - S_1)$ were estimated by taking the difference between the maximum of the Soret bands and Q bands, though this way is not accurate as stated previously in this thesis. However, a clear trend of linear correlation between $\Delta E(S_2 - S_1)$ and f_1, with similar slope to that of ZnTPP, is obtained for ZnP, ZnTPP(F_{20}), ZnTPP(Cl_8) but not for ZnOEP, as shown in Fig.4.5. For ZnOEP, in the set of solvents employed, two well-separated lines were obtained. One is for polar solvents, and the other for nonpolar solvents. The different solvatochromic behavior of the ZnOEP from other metalloporphyrins implies that more factors other than dispersion may affect the interaction between solvent and excited solute in ZnOEP. As introduced in Chapter 1, the $\Delta E(S_2 - S_1)$ is very important in the interpretation of the different decay rates of the S_2 state of the metalloporphyrins. In addition to solvent polarizability, the $\Delta E(S_2 - S_1)$ is also affected by nature or pattern of the substituents of the porphyrin macrocycle, as will be discussed in Chapter 5.

The fact that the electronic energy gap $\Delta E(S_2 - S_1)$ of metalloporphyrins studied here is a good linear function of the solvent polarizability in solvents including both polar and nonpolar, indicates that the observed solvatochromic effects on the spectroscopic properties are due to the different polarizabilities of the S_2 and S_1 states. Effects due

to dipolar and multipolar solvent-excited solute interactions might be expected in polar solvents, however, the magnitude of these effects must either be about the same for both excited states or must be too weak to be distinguished from the total effects which are dominated by dispersive interactions between solvent and excited solute molecules. The dynamic interaction between excited solute and solvent occurs on a time scale of several 10's of picoseconds. The solvent-excited solute relaxation processes associated with reorientation of the solvent molecules are too slow to complete during the ultrafast depopulation, on a time scale of several ps to 100s of fs, of the S_2 state. However, the ns S_1 lifetime is long enough for these processes to complete. Thus such dynamic solvent-excited solute interaction can influence the spectroscopic signatures of the Q band, but not for the Soret band.

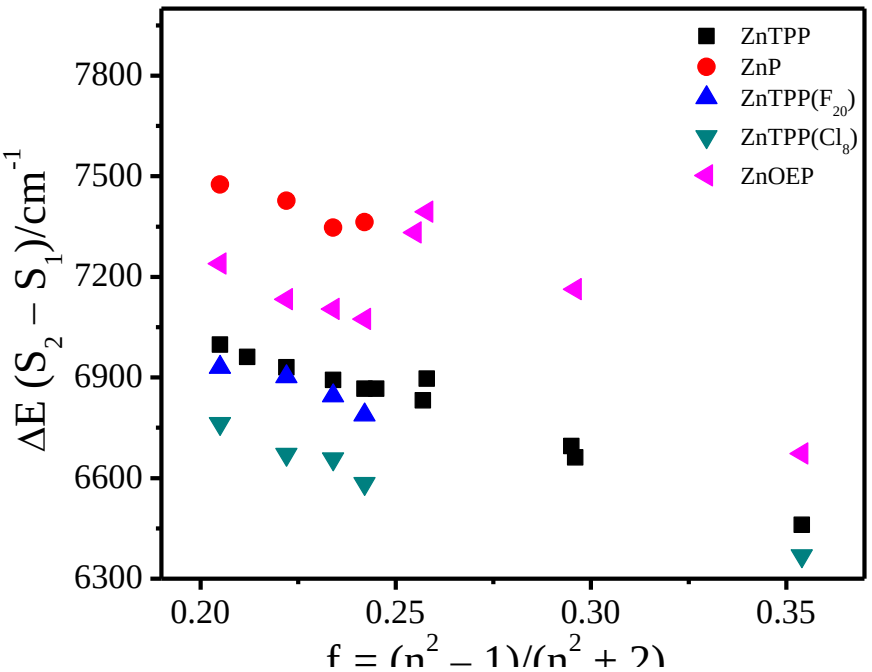

Fig. 4.5 Plot of the $\Delta E(S_2 - S_1)$ energy gap versus Lorenz-Lorentz solvent polarizability function, $f_1 = (n^2 - 1)/(n^2 + 2)$, for metalloporphyrins as shown. Data of ZnTPP are included for comparison.

Nevertheless, the similar slopes of the $\Delta E(S_2 - S_1)$ *vs.* f_1 plots for the compounds as shown in the graph, indicate that the solvation effects on each compound in solvents

employed here are, if not the same, at least similar. The common conclusion can be drawn is that the changes in $\Delta E(S_2 - S_1)$ of all the metalloporphyrins due to solvent-solute interactions are governed by dispersive interactions, which are proportional to the solvent polarizability, irrespective of whether the solvent is polar or nonpolar.

The slope of the $\Delta E(S_2 - S_1)$ *vs.* f_1 plot of ZnTPP shown in Fig. 4.4 is similar with that of MgTPP, as well as the slopes of other tetrapyrrolic metalloporphyrins shown in Fig 4.5. However, the slope of the similar plot of ZnTBP is different. It shows that the change of $\Delta E(S_2 - S_1)$ of ZnTBP is more sensitive to the change of the solvent polarizability. ZnTBP has the biggest $\Delta E(S_2 - S_1)$ among all values obtained for isolated metalloporphyrins in a supersonic expansion and in solution (refer to data in Table 5.1 and 5.2). The difference of the molecular structure between ZnTBP and other metalloporphyrins, as shown in Chart 1.1, is that ZnTBP has an extended 42 π-electron macrocycle, compared to a 26 π-electron macrocycle of ZnTPP and other metalloporphyrins. The calculations in Chapter 3 show that the extended macrocycle greatly stabilizes the 1^1E_u (S_1) state, while the effect on the 2^1E_u (S_2) state is very small, resulting in a relatively large $\Delta E(S_2 - S_1)$ energy gap. Moreover, as will be discussed in Chapter 5, the extended π-electron macrocycle increases the polarizability of the excited states, which are then more sensitive to the change of solvent polarizability.

In the following sections, the solvation effects on the lifetimes of the excited states will be discussed.

4.2.2 S_1 Lifetimes of metalloporphyrins studied in various solvents

In the present work, the S_1 fluorescence lifetimes of five metalloporphyrins in a set of undegassed solvents have been measured as described in section 2.4.1 using the TCSPC technique with a time resolution *ca.* 50 ps. Dilute solutions were used in these experiments to avoid the effects of aggregates. The absorption spectra obtained before and after the lifetime measurements were almost identical, indicating that there is no significant photodegradation during the period that the solution was exposed to laser radiation in these experiments. For all sample solutions, the excitation wavelength was set at either 495 nm or 400 nm, and the S_1 fluorescence lifetimes are independent of the

excitation wavelength, as it was reported by others.[23,57] The wavelength at which fluorescence was collected varied within the Q band of each compound to avoid Raman

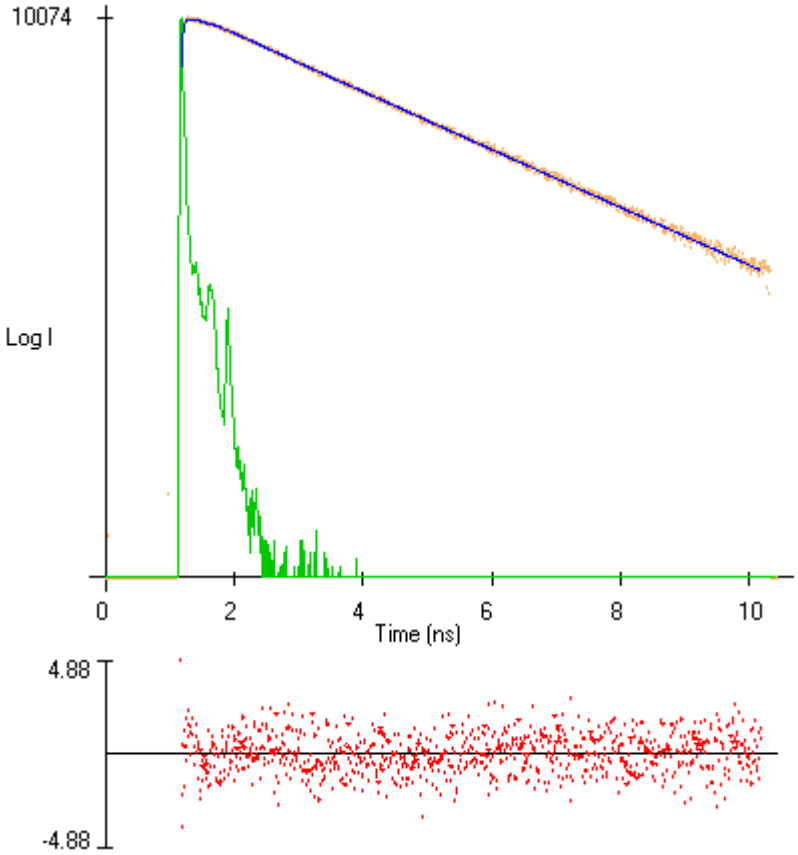

Fig. 4.6 Representative temporal S_1 fluorescence decay profile of ZnOEP in undegassed ethanol modeled with the best single exponential fit. Excited at 495 nm and observed at 585 nm. τ = 2.10 ns and $\chi_r^2 = 1.07$. The distributions of residues shown at the bottom indicate the goodness of the fitting.

scattering. Fig. 4.6 shows the representative temporal S_1 fluorescence decay profiles of ZnOEP in undegassed ethanol with excitation at 495 nm. The observed data were deconvoluted from the IRF, using the custom-developed program Psdecay 2000, following the procedures described in section 2.4. The temporal S_1 fluorescence decay profile was well-modeled by single exponential functions with a time constant of 2.10 $\pm$ 0.01 ns. The time constants obtained for the relaxation of the S_1 states of five metalloporphyrins in the set of eight solvents examined are collected in Table 4.2. It should be noted that the lifetimes of a given compound in the alcohol series solvents are almost the same

within the experimental error. However, the lifetimes obtained in CH_2Cl_2 and CS_2 are notably shorter than those obtained in other solvents except ZnTPP(Cl_8). The absence of the lifetimes for ZnP and ZnTPP(Cl_8) in c-hexane is due to their poor solubility in these solvents.

Table 4.2 S_1 lifetime of five metalloporphyrins in six solvents (λ_{ex}=495 nm).

Solvent	τ_f (ns)				
	ZnTPP	ZnP	ZnOEP	ZnTPP(F_{20})	ZnTPP(Cl_8)
Methanol	1.93	2.56	2.00	1.57	0.30
Ethanol	1.96	2.57	2.10	1.55	0.26
1-Propanol	1.94	2.57	2.05	1.56	0.29
1-Butanol	1.92	2.59	2.04	1.55	0.25
Dichloromethane	1.77	2.02	1.52	1.33	0.31
Toluene	2.02	2.09	1.76	1.37	0.33
CS_2	1.36	1.52	1.09	1.18	0.29
c-Hexane	2.06	-	1.75	1.40	-

"-" not available

It has been suggested previously that the relaxation of the S_1 state of the metalloporphyrins is dominated by $S_1 - T_1$ intersystem crossing (ISC).[57] Similar to other radiationless transitions in the weak-coupling limit,[15] intersystem crossing rates (k_{ISC}) follow the predictions of the energy gap law and follow an inverse exponential relationship with the differences in $S_1 - T_1$ energy spacing, $\Delta E(S_1 - T_1)$. Additionally, k_{ISC} is a function of the relative number of vibrational modes involved in the intersystem crossing transition, η, and the spin-orbital coupling energy, ξ^2 ($\xi \approx Z^4$, in the case of molecules containing heavy atoms with a high atomic number Z.).[128] However, TDDFT calculations presented in chapter 3 predict the presence of the T_2 state, which has an energy lower than the S_1 state but higher than the T_1 state. Both T_1 and T_2 states have the same symmetry, ^3E_u. According to the energy gap law for the weak coupling, statistical limit case, intersystem crossing $S_1 - T_2$ should be more favorable than $S_1 - T_1$ because of the smaller energy gap, $\Delta E(S_1 - T_2)$. Unfortunately, so far, no experimental evidence is available to

locate the T_2 state and to support its participation in the radiationless decay processes of the S_1 state. Nevertheless, if the T_2 state exists at energies lower than that of S_1, the fluorescence lifetime of the S_1 state would be determined by the $S_1 - T_2$ energy gap, instead of $\Delta E(S_1 - T_1)$. Thus the radiationless decay of theS_1 state will be governed by $S_1 - T_2$ ISC, followed by fast $T_2 - T_1$ IC and then very slow decay processes related to the T_1 state, which has a lifetime on the time scale of microseconds. Because of the small ($\Delta E(T_2 - T_1) \leq 0.5$ eV), it is expected that $T_2 - T_1$ IC should occur within several ps or even less, which makes it indistinguishable from the long lifetime of the T_1 state.

For a given zinc metalloporphyrin in a set of different solvents, η would be, if not same, at least similar. Thus any variation of the k_{ISC} would be attributed to the changes of $\Delta E(S_1 - T_2)$ due to solvent polarizability. In order to examine the effects of solvent polarizabilities on the relaxation dynamics of the S_1 state of the zinc metalloporphyrins studied, the radiative and nonradiative rate constants of ZnTPP were calculated, as summarized in Table 4.3. The data regarding the relaxation of the S_2 state are also included for comparison. The radiative rate constants of the S_1 state change with the variation of the solvents employed, but there is no a clear trend of these changes. The radiationless decay rate constants of the S_1 state are almost the same within experimental error even in a set of solvents with a wide range of polarizability. Because of the same electron configuration except different electron spin multiplicity, the S_1, T_1 and T_2 states all will have similar excited state polarizabilities. The effects of changing the solvent polarizability on these three states are expected to be, if not same, at least similar. Thus the changes of both $\Delta E(S_1 - T_2)$ and $\Delta E(S_1 - T_1)$ due to the variation of the solvent polarizability will be expected to be very small. As a consequence, the radiationless rate constants of the S_1 state also remain similar.

However, for different metalloporphyrins with different $\Delta E(S_1 - T_2)$ in the same solvent, it might be possible to establish the relationship of the k_{nr} of $S_1 - T_2$ ISC with the variation of the $\Delta E(S_1 - T_2)$. If an inverse exponential dependence of the k_{nr} of $S_1 - T_2$ ISC on the variation of the $\Delta E(S_1 - T_2)$ can be established, it would prove the importance of $S_1 - T_2$ ISC in the radiationless decay of the S_1 state. Unfortunately, the values of $\Delta E(S_1 - T_2)$ are not available experimentally, and the values predicted by TDDFT

Table 4.3 Photophysical properties of the S_2 and S_1 excited states of ZnTPP in several undegassed solvents at room temperature.

	S_2				S_1			
Solvent	$\phi_f/10^{-3}$	τ (ps)[a]/ (λ_{ex}=400nm)[/]	$k_r(s^{-1})$[a] $/10^8$	$\sum k_{nr}(s^{-1})$ $/10^{11}$	$\phi_f/10^{-2}$	τ (ns)/ (λ_{ex}=495nm)	$k_r(s^{-1})$ $/10^7$	$\sum k_{nr}(s^{-1})$ $/10^8$
Methanol	1.53	2.49	6.14	4.02	2.10	1.93	1.09	5.07
Acetonitrile	1.28	2.23	5.74	4.48	2.24	1.94*	1.15	5.15
Ethanol	1.42	2.34	6.07	4.27	2.26	1.96	1.15	4.99
1-propanol	1.58	2.19	7.21	4.57	2.50	1.94	1.29	5.03
1-butanol	1.64	2.01	8.16	4.98	2.60	1.92	1.35	5.07
THF	1.04	2.13	4.88	4.69	2.71	1.95*	1.52	5.47
DMF	1.5	2.15	6.98	4.65	3.42	1.92*	1.78	5.21
c-hexane	1.01	1.99	5.08	5.02	2.17	2.06	1.05	4.75
Toluene	1.14	1.34	8.51	7.46	2.93	2.02	1.45	4.81
Benzene	1.2	1.45	8.0	6.71	3.30	1.91*	1.73	5.06

* Data were provided by Dr. Kowalska and obtained at excitation wavelength = 400 nm.

calculations are not accurate enough to establish a reliable correlation between the k_{nr} of $S_1 - T_2$ ISC and the $\Delta E(S_1 - T_2)$. Thus the existence and contribution of $S_1 - T_2$ ISC to the radiationless decay of the S_1 state cannot be assessed by the methods employed in this study, and still remain open questions to date.

However, the radiationless rate constants ($\sum k_{nr}$) of the S_2 state of ZnTPP in the set of solvents employed change significantly with the variation of solvent polarizabilities. The data presented in Table 4.3 show a clear trend that the larger the solvent polarizability, the faster is the nonradiative relaxation rate. This is because, as will be discussed in later chapters, the relaxation dynamics of the S_2 state are dominated by the $S_2 - S_1$ internal conversion. As introduced in chapter 1, according to the energy gap law in the weak coupling limit of radiationless transition theory, the radiationless rate constants of

the S_2 state depend exponentially on $\Delta E(S_2 - S_1)$.[15] Different from the similarity of the polarizabilities between the S_1 and T_1 states, the polarizability of the S_2 state is different from that of the S_1 state, thus variations of solvent polarizabilities will lead to different effects on these two excited states, resulting in the changes of the $\Delta E(S_2 - S_1)$, which is account for the variation of the radiationless rate constants ($\sum k_{nr}$) of the S_2 state.

For the six zinc metalloporphyrins with different nature or pattern of the substituents of the porphyrin macrocycle, though the variation of the radiative rate constants is random, the nonradiative decay rates of the S_1 state vary in the same trend as the corresponding fluorescence lifetimes, and are of the same order of 10^8 s^{-1}, except ZnTPP(Cl_8), as shown in Table 4.4. The S_1 fluorescence lifetimes obtained in the present work show

Table 4.4 Photophysical properties of the S_1 states of six zinc porphyrins in undegassed ethanol at room temperature.

Comp.	ZnP	ZnTPP	ZnTPP(F_{20})	ZnTPP(Cl_8)	ZnTBP	ZnOEP
ϕ_f	0.80×10^{-2}	2.67×10^{-2}	0.80×10^{-2}	3.3×10^{-3}#	1.34×10^{-2}	6.77×10^{-2}
τ (ns)	2.57	1.96	1.55	0.26	1.91	2.10
$k_r(s^{-1})$	3.11×10^6	1.36×10^7	5.16×10^6	1.27×10^7	7.02×10^6	3.22×10^7
$\sum k_{nr}(s^{-1})$	3.86×10^8	4.97×10^8	6.40×10^8	3.83×10^9	5.17×10^8	4.44×10^8

Datum taken from reference 128.[128]

no difference with those reported in literatures, for example, Yang *et al.* measured the S_1 lifetimes of ZnTPP(F_{20}) is 1.4 ns and is 0.34 ns for ZnTPP(Cl_8) in toluene at room temperature,[114] compared to 1.37 ns and 0.33 ns, respectively, obtained in this thesis. The similar radiationless rate constants are due to the similar $\Delta E(S_1 - T_1)$, which is *ca.* 0.5 eV in the metalloporphyrins such as, ZnP, ZnTPP, ZnTBP and ZnOEP according to the calculations presented in chapter 3. The radiationless decay rates of the S_1 state of ZnTPP(Cl_8) is large and its S_1 fluorescence lifetime is only 0.26 ns (Fig. 4.7), which is much shorter compared to those of other metalloporphyrins studied. The electron withdraw effects of the four *meso*-substituted perfluorinated phenyl rings in ZnTPP(F_{20}) and partially chlorination in the *ortho* positions of the four *meso*-substituted phenyl rings in ZnTPP(Cl_8) may alter the electronic properties, *i.e.* $\Delta E(S_1 - T_1)$. In addition to this elec-

tronic alteration, ZnTPP(F_{20}) and ZnTPP(Cl_8) were reported to bear a nonplanar porphyrin macrocycle.[114] Previous studies have shown that the photo-physical properties of the S_1 state of porphyrins are strongly modulated by distortions of the macrocycle.[129] The S_1 fluorescence lifetimes of porphyrins with nonplanar macrocycle are significantly shortened and the quantum yields are substantially lower comparing to those of their planar analogs, because the nonradiative decay rates of both $S_1 - S_0$ internal conversion and $S_1 - T_1$ intersystem crossing can be enhanced by the perturbation of nonplanarity.

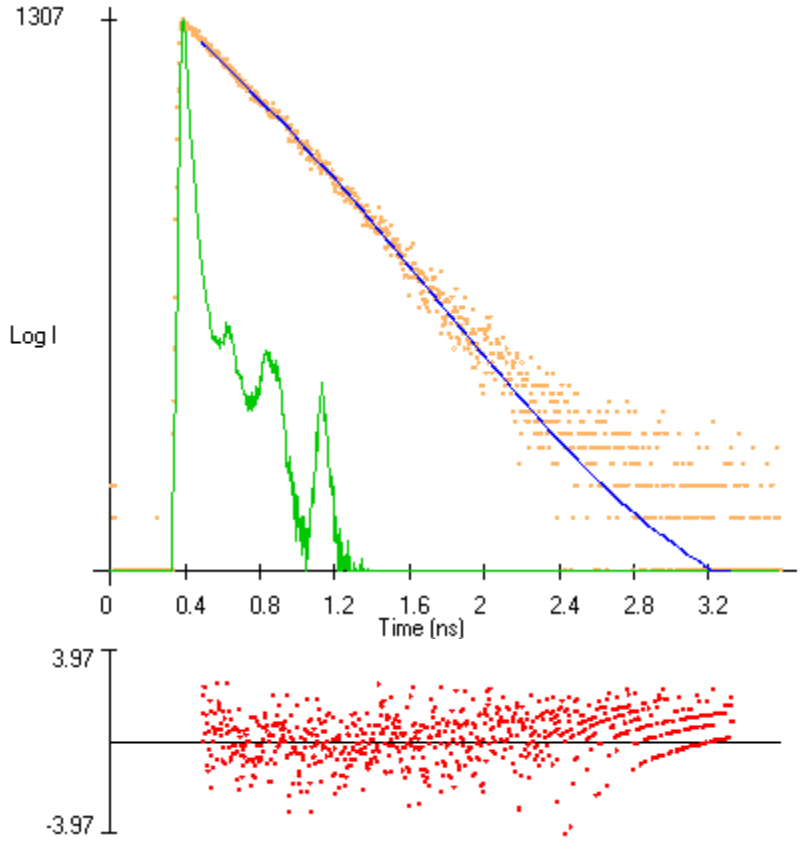

Fig. 4.7 The temporal S_1 fluorescence decay profiles of ZnTPP(Cl_8) in undegassed toluene modeled with the best single exponential fit. Excited at 495 nm and observed at 665 nm. τ = 0.33 ns and $\chi_r^2 = 1.07$. The distributions of residues shown at the bottom indicate the goodness of the fitting.

The data in Table 4.4 indicate that the effects of partially chlorination in the *ortho* positions of the four *meso*-substituted phenyl rings in ZnTPP(Cl_8) is more efficient than that of the four *meso*-substituted perfluorinated phenyl rings in ZnTPP(F_{20}). The efficiency of the halogen substituents at *ortho* positions of phenyl rings as proposed to be related

to a favorable overlap between the orbitals of the halogen atoms and those of the porphyrin core.[128]

The S_1 state can only be weakly coupled with the T_1 state because of the spin prohibition, thus the rate constants of the $S_1 - T_1$ intersystem crossing of the six zinc metalloporphyrins from ZnP to ZnOEP, follow strictly the expectations of the energy gap law of the radiationless transition theory in the weak coupling limit, though the radiationless rate constant of the S_2 state of ZnOEP is 2 orders in magnitude larger than that of ZnP as will be discussed in chapter 5.

4.2.3 S_2 lifetimes of metalloporphyrins in different solvents

The S_2 lifetimes of ZnTPP in a set of solvents have been carefully measured, with assistance of Dr. U. Tripathy, using the fluorescence upconversion method described in section 2.4. A flow sample system was used to keep the sample fresh and thus avoid photo-bleaching at the light focusing spot throughout the data acquisition period. Since the intensity of the S_2 fluorescence signal of metalloporphyrins is very weak, a high peak power laser and solutions with higher concentrations ($10^{-4} \sim 10^{-5}$M) are required to obtain a good signal to noise ratio.[35,37]

When using high porphyrin concentrations it is impossible to avoid solute aggregation effects. In order to assess the effects of the presence of aggregates, the fluorescence decay times of the S_2 state as a function of the concentration of ZnTPP in ethanol were measured. As expected, the measured decay profiles became noisy when decreasing the concentration lower than 50 μM. However, for all solutions with concentrations ranging from 50 to 300 μM, all measured decay profiles can be well-modeled by single exponential functions. No significant variations of the S_2 decay time constants due to aggregation at higher concentrations were observed. In fact, it is easy for metalloporphyrins to form aggregates even at low concentrations of the order of 10^{-6} M. Thus in those solutions used for S_2 lifetime measurements, considerable numbers of aggregates are present. However, the fact that no measurable difference of the S_2 lifetime was obtained, indicates either that the aggregates have the same lifetimes as the monomers, or, more likely, that the fluorescence quantum yields of the aggregates are too small to influence the decay rates obtained.

The high peak laser power employed is another concern which can affect the S_2 lifetime measurements.[41] In our case, no measurable variation with average laser power (300 – 480 mW) was observed for the S_2 decay profiles of ZnTPP in ethanol, indicating that sequential two-photon or multi-photon absorption is not a significant problem here. In addition, to eliminate the effects of the pump pulse, the observation wavelength was sometime varied within the Soret emission band, but no effects on the measured decay time were observed.

Typical experimental fluorescence upconversion profiles are shown in Fig. 4.8. The solid lines show the best fits of single exponential functions to the experimental data. The S_2 decay time constant of ZnTPP in methanol is 2.49 $\pm$ 0.01 ps and it is 1.31 $\pm$ 0.01 ps in toluene, with excitation at 400 nm. All experimental S_2 lifetimes and related parameters characterizing the relaxation dynamics of the S_2 state of ZnTPP are collected in Table 4.4. The S_2 lifetime of ZnTPP in ethanol, obtained in this thesis, is 2.34 ps in excellent agreement with 2.35 ps reported previously by Gurzadyan *et al.*[35] and 2.3 ps

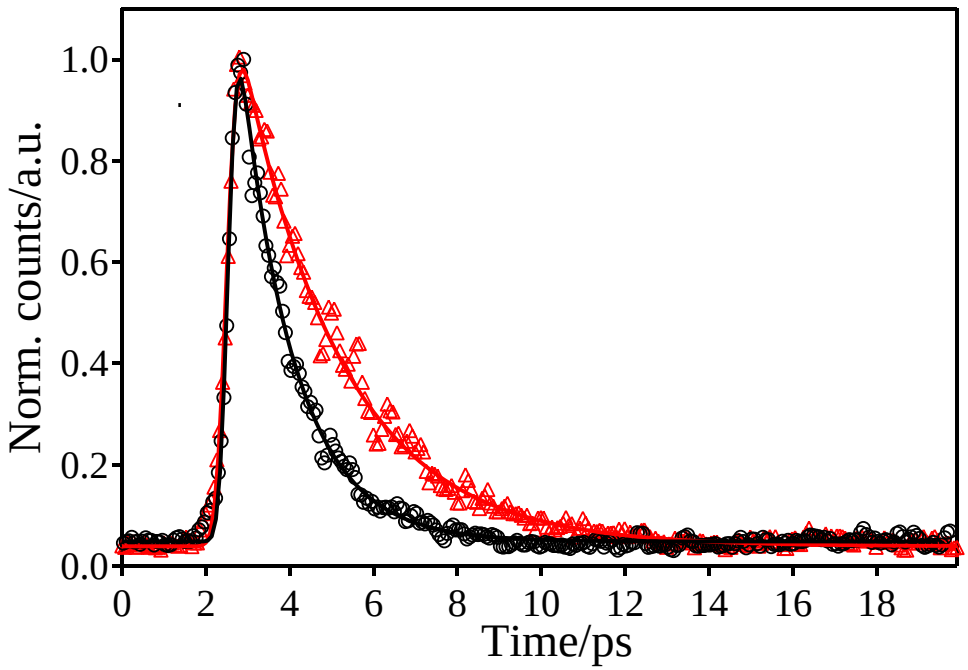

Fig. 4.8 Normalized fluorescence upconversion profiles of ZnTPP in methanol (triangular) and toluene (circle). Excitation wavelength is 400 nm and observed at 433 nm. The solid lines show the best fits of single exponential functions to the experimental data. Adapted from reference 73.[73]

obtained by Mataga *et al.*,[37] using the similar experimental techniques. For ZnTPP in benzene, an S_2 lifetime of 1.45 ps was measured, which is identical to the value published by Yu *et al.*,[41] using a similar upconversion method. In general, the results presented in Table 4.4 are in good agreement with those data, where available, reported earlier by other independent researchers. Some of them have been reviewed in Chapter 1, and that discussion will not be repeated here.

Comparison of the S_2 lifetimes of ZnTPP within the set of solvents employed shows a clear trend that the S_2 time constants decrease with increasing solvent polarizability from methanol to benzene. This is different from what is observed for the lifetimes of the S_1 state of ZnTPP in the same set of solvents, where the S_1 lifetime is not as sensitive as the S_2 lifetime with changing solvent polarizability. This difference indicates that the decay dynamics of the S_2 state is possibly different from that of the S_1 state. In order to explore the decay mechanism of the S_2 state further, the S_1 rise time of ZnTPP in different solvents were also carefully measured.

In Fig. 4.9 a pair of S_2 decay and S_1 rise fluorescence upconversion profiles of ZnTPP in ethanol at room temperature is shown, with excitation at 400 nm. Here the S_2 decay profile is fit well with a single exponential function and gives a time constant of 2.36 ps, which is identical to the single exponential S_1 fluorescence rise time of 2.35 ps. For ZnTPP in all the solvents, the deconvoluted S_1 rise fluorescence upconversion profiles were all well-modeled by multiple exponential functions as described in section 2.4.2. The S_1 rise time constants are identical to the S_2 decay time within an experimental error of *ca.* 50 fs. The results obtained in the present work are in good agreement with those reported by Mataga, *et al.*[37] that both the S_2 decay and S_1 rise times of ZnTPP in ethanol are identical with time constant of τ = 2.3 ps. A similar result was also reported by Gurzadyan *et al.*,[27] (τ_{S2} = 2.3 ps and τ_{S1}(rise) = 2.4 ps). However, Yu *et al.*,[41] reported that the S_2 decay time is 1.45 ps for ZnTPP in benzene but that S_1 rise time is shorter, 1.15 ps, when ZnTPP was excited at 397 nm by one-photon absorption. In order to interpret the difference between the S_2 decay and S_1 rise times, they proposed that the Soret band is a composite of two different electronic states. They

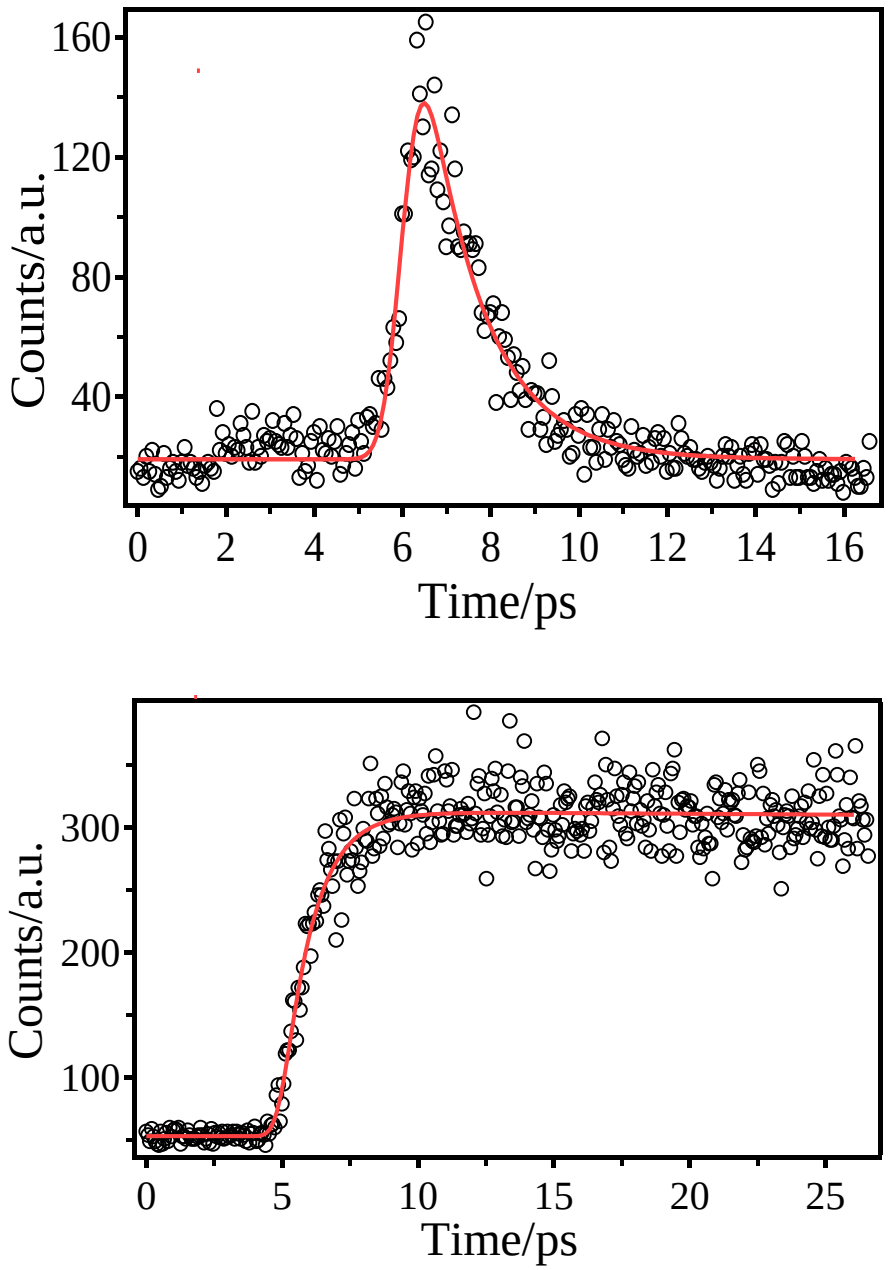

Fig. 4.9 A pair of temporal S_2 decay and S_1 rise fluorescence upconversion profiles (circles) of ZnTPP in benzene at room temperature are shown with excitation at 400 nm. The observation wavelengths are 433 nm and 604 nm, respectively. The data are modeled by S_2 decay of τ_{S2} = 1.46 ps and τ_{S1}(rise) = 1.41 ps, with the best fits shown by the solid line.

suggested that the S_2 (2^1E_u) state was accompanied by a second state labeled S_2' state by them or as a "dark" state by others.[42] No evidence of the presence of such a dark or S_2' state was found in the present work as a result of measuring both the S_2 decay and S_1

rise times of ZnTPP in a wide set of solvents. Also no such evidence was observed for the S_2 decay and S_1 rise of other metalloporphyrins studied in any of the solvents investigated in this thesis, as will be discussed in chapter 5.

However, the home-developed fluorescence upconversion system used to obtain the results presented in this thesis has a slightly poorer time resolution than that used by Yu *et al.*[41] and the S_1 rise time profiles were obtained with a lower signal to noise ratio. Therefore it is impossible to definitively refute (or support) the report that the S_1 rise time for ZnTPP in benzene is measurably faster than its S_2 decay time. It is also impossible at this time to offer some useful comments on the previous interpretation that the difference may be due to the presence of a dark S_2' state in the vicinity of the S_2 state for ZnTPP in benzene.

The radiative and the sum total nonradiative rate constants characterizing the decay dynamics of the S_2 state of ZnTPP in various solvents were calculated using eqs. 1.10 to eq. 1.12. Here, the values of $\sum k_{nr}$ can be calculated approximately by taking the inverse of the S_2 lifetimes because the values of ϕ_f are all very small. The data are collected in Table 4.3. Analysis of the values of $\sum k_{nr}$ of the S_2 state of ZnTPP obtained in different solvents shows that the values exhibit a clear trend of increasing with increasing solvent polarizability.

The relaxation dynamics of the highly excited states of azulene and its derivatives[26,27] and of the aromatic thiones[2,65] have been successfully interpreted within the framework of the energy gap law in the weak coupling limit. The energy gap law plots for the azulenes and aromatic thiones as shown in Fig. 4.10 exhibit a good linear function between the logarithm of the nonradiative rate constants of the S_2 state and the $S_2 - S_1$ energy spacing as predicted. The radiationless decay dynamics of the S_2 states of the azulenes and aromatic thiones are well understood, and are dominated by fast $S_2 - S_1$ internal conversion.

The logarithm of the sum of nonradiative rate constant $\sum k_{nr}$ of ZnTPP in all solvents examined in the present work are plotted against the energy gap $\Delta E(S_2 - S_1)$, as shown in Fig. 4.11. The plot shows a good linear correlation between $\log_{10}(\sum k_{nr})$ and $\Delta E(S_2 - S_1)$. It is interesting to note that data reported by Mataga *et al.*[37] and Yu *et al.*[41] fall perfectly on the same straight line apparently, just as predicted by the energy gap law of

weak coupling radiationless transition theory.[15] A similar correlation was also obtained previously by Gurzadyan *et al.*[36] for ZnTPP and MgTPP in a small set of solvents but with much more scattered data than that obtained in the present work. As will be shown

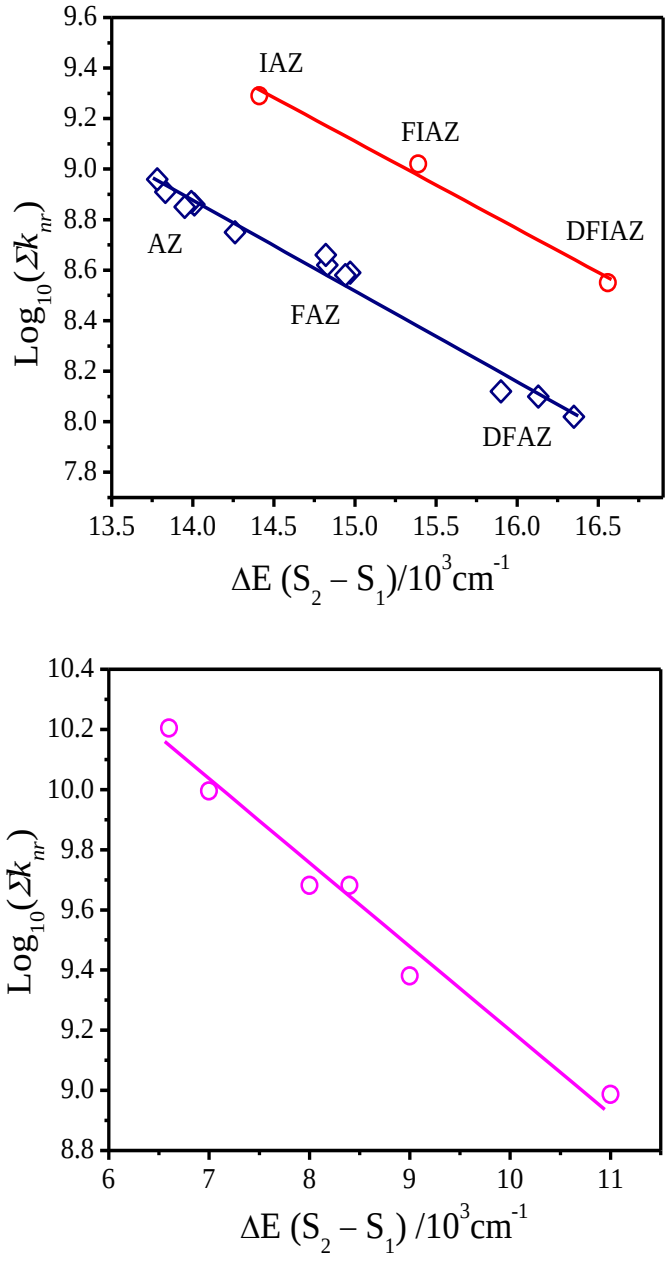

Fig. 4.10 Energy gap law plots for (upper) azulene and its derivatives in various nonpolar solvents and (lower) several rigid aromatic thiones in inert perfluoroalkane solutions. Data are taken from references 3 and 27.[3,27]

in Chapter 5, a similar energy gap law plot was also made by Tripathy *et al.*[74] for MgTPP in a wide set of solvents and shows a similar linear relationship. It is important to note that these apparent linear correlations between the nonradiative rate constants of the S_2 state and $\Delta E(S_2 - S_1)$ were obtained under the assumption that the nonradiative

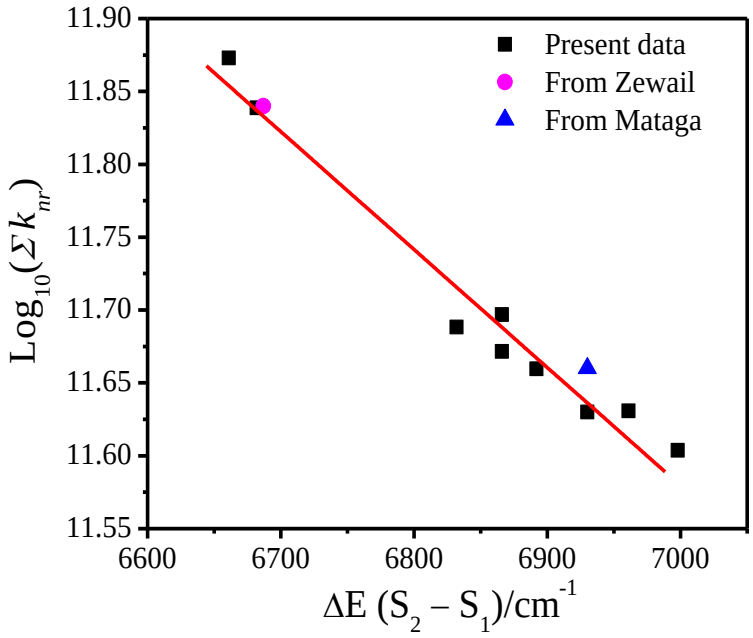

Fig. 4.11 Energy gap law plot for ZnTPP in various solvents. Data taken from references 37[37] and 41[41] are also included for comparison.

decay processes of the S_2 state is dominated by $S_2 - S_1$ internal conversion even though some other decay channels such as intersystem crossing might be competitive with it. Such an assumption is in complete accord with the interpretation of the radiationless decay of the S_2 state in both azulene and thione systems. However, the slope and intercept of the energy gap law plot for ZnTPP is distinctly different from those for MgTPP[74], the azulenes[26,27] and the aromatic thiones[3]. Two features about the radiationless decay of the azulenes and the aromatic thiones are important to note. One is that the $\Delta E(S_2 - S_1)$ is much larger than the value obtained for the metalloporphyrins so that the S_2 decays lie in the ns regions. The other is that the S_2 state and the coupled S_1 state have different symmetry in both systems. These two features result in the weak $S_2 - S_1$ coupling in the azulenes and the aromatic thiones. However, as shown in Chapter 3, the coupled S_2 and S_1 states have the same ^1E_u symmetry for the metalloporphyrins, and the

$S_2 - S_1$ energy gap is much smaller. What is the situation in the metalloporphyrins? The interaction between the coupled S_2 and S_1 states depends on the relative location and shape of the two potential energy surfaces of the S_2 and S_1 states. The above analysis of the steady-state spectroscopy shows that the Stokes shift of both the Soret and Q bands are small and that the difference of Stokes shift between the Soret and Q bands is less than 100 cm^{-1}. Are the S_2 and S_1 states of ZnTPP and other metalloporphyrins weakly coupled, as in the azulene systems?

Actually, as will be discussed in Chapter 5, much more information regarding the highly excited electronic states can be extracted from the energy gap law plot. Together with the energy gap law plots of other metalloporphyrins studied, the difference among the slopes and intercepts provide important information about $S_2 - S_1$ coupling. There the question "Does this energy gap law apply to all the metalloporphyrins studied in this thesis?" will be discussed.

4.3 Conclusions

The solvatochromic effects on the spectroscopic and photophysical relaxation properties of highly excited electronic states of the set of metalloporphyrins studied in this thesis have been investigated by carefully measuring both steady-state and time-resolved spectra in a set of solvents having a wide range of polarizabilities. For a given metalloporphyrin, the Soret band maxima of both the absorption and emission spectra are shifted toward lower energies and are more sensitive than the Q band to the change of the solvent polarizability.

A good linear function between energy gap $\Delta E(S_2 - S_1)$ and the Lorenz-Lorentz solvent polarizability function, f_1 is obtained for some of the metalloporphyrins in the set of solvents examined in the present work. The extrapolation of the straight line to $f_1 = 0$ gives the $\Delta E(S_2 - S_1)$ of the bare molecules observed in supersonic expansion conditions, which is a proof that parameter f_1 is more precise than $f_A(f_C)$ in measuring solvent polarizability. The linear correlation indicates that the interactions between the metalloporphyrins and solvents, irrespective of whether they are polar or nonpolar, are governed by dispersive solvent-excited solute interactions, the magnitude of which is proportional to the solvent polarizability. It also indicates that the solvatochromic effects

on the $\Delta E(S_2 - S_1)$ are due to the difference between the polarizabilities of the S_2 and S_1 states of the metalloporphyrins.

The results of fluorescence lifetime measurements of both S_2 and S_1 states of zinc metalloporphyrins in a set of solvents employed indicate that the S_2 lifetimes are more sensitive to the change of the solvent polarizability than the S_1 lifetimes and that the S_2 lifetimes decrease in a clear trend with increasing the solvent polarizability. Plots of the logarithm of the sum of nonradiative rate constants versus the $\Delta E(S_2 - S_1)$ shows a good linear correlation for ZnTPP in the set of solvents examined. Moreover, the identity of the S_2 decay and S_1 rise time constants of ZnTPP in the wide set of solvents examined provides no evidence for the presence of the dark or S_2' states previously proposed. One can conclude that the nonradiative decay processes of the S_2 state of the metalloporphyrins is dominated by $S_2 - S_1$ internal conversion. However, the fact that the slope and intercept of the plot for ZnTPP is different from those for MgTPP, the azulenes and the aromatic thiones indicates that the weak coupling status between the S_2 and S_1 states in metalloporphyrins other than MgTPP is questionable. This matter will be further explored in Chapter 5.

Chapter 5: Effects of the Nature and Pattern of Substituents and of Macrocycle Conformation on the Photophysics of Soret-excited Tetrapyrroles

5.1 Introduction

Tetrapyrroles and their derivatives are very important in nature, and have gained extensive applications because of their unique spectroscopic, photophysical and photochemical properties.[8,28,130-142] In order to impart some desirable properties to the tetrapyrroles, their structures can be modified by substitution some of which lead to macrocycle deformations. Previous investigations of the relationships between molecular structure and molecular photophysical and photochemical properties have been limited to the lowest singlet or triplet states of the tetrapyrroles and related compounds.[29,130,143] However, structure-property information regarding the highly excited electronic states of the tetrapyrroles and their derivatives, which are frequently involved in their photoactuated applications, is rare in the literature.[2,144]

As reviewed in Chapter 1, the photophysical properties of the higher excited states of some individual or of small sets of modified tetrapyrroles have been investigated. The results indicate that spectroscopic and photophysical properties of highly electronically excited tetrapyrroles vary with the nature of the substituents and the central metal ions, and are also greatly affected by the macrocycle substitution pattern and macrocycle conformation. The limited information available[2,35,57,144] shows that, for the same macrocycle substitution pattern, the S_2 fluorescence quantum yields do vary slightly, but not greatly, upon changing the central metal ions. However, for tetrapyrroles with different substituents and different macrocycle substitution patterns, *e.g. meso*- or β-substitutions, the S_2 fluorescence lifetimes range from tens of femtoseconds to several picoseconds.[145] The vast differences among the S_2 lifetimes imply that the effects of substituents and, perhaps, of deformation of the tetrapyrrole macrocycle framework are considerable. However, no comprehensive analysis of the variation in S_2 spectroscopic and dynamic properties of tetrapyrroles associated with different substituents, macrocycle substitution pattern, or macrocycle conformation is yet available.

Based on an analysis of the experimental results available, the following puzzling questions still remain open. (1) The $S_2 - S_0$ fluorescence quantum yields vary greatly for metalloporphyrins with different macrocycle substitution patterns, for example *meso- vs.* β-substitutions. The calculations presented in Chapter 3 do show some differences in the distribution of electron density and of net charge on the *meso*- or β-carbon atoms when their atoms are substituted by phenyl or ethyl groups. Are these changes of electron density responsible for the differences observed in spectroscopic and photophysical properties? Other than the macrocycle substitution pattern, the nature of the substituents and macrocycle conformation can also affect the spectroscopic properties of tetrapyrroles. How do these factors affect the decay dynamics of highly excited electronic states of tetrapyrroles and can the differences in dynamics be associated with these structure-related spectroscopic changes? (2) As discussed in Chapters 3 and 4, several theoretical calculations and some experimental results suggest the existence of a "dark" or S_2' state which is nearly degenerate in energy with the 2^1E_u state. It would be highly desirable if further direct experimental evidence was available to confirm the presence of this unknown state. If such a state does exist, how is it assigned? Is it a distinct third electronic state, *i.e.* 3^1E_u, or just a vibronic feature of the S_2 state (*i.e.* B(1,0))? Furthermore, if it is a distinct electronic state, how does it affect the relaxation rate of the metalloporphyrins when excited in the Soret band? (3) As mentioned in Chapter 4, the S_2 and S_1 states involved in $S_2 - S_1$ internal conversion decay were found to be weakly coupled in the azulenes and aromatic thiones. The radiationless decay behaviors of the S_2 states of these two families of compounds follow strictly the predictions of the energy gap law of radiationless transition theory in the weak coupling case. However, when the similar energy gap law plots were applied to those data obtained for MgTPP and ZnTPP in various solvents, the slope and intercept of the plot for ZnTPP are different from those of MgTPP, and are also distinctly different from those of the azulenes and aromatic thiones. What is the range of the $S_2 - S_1$ interstate coupling energies in the diamagnetic d^0 or d^{10} metalloporphyrins? Do they all belong to the weak coupling case as found in the azulenes and aromatic thiones? Or are S_2 and S_1 more strongly coupled (from intermediate to strong coupling)? Does the structure-excited state properties rela-

tionship predicted by the energy gap law apply to all tetrapyrroles and their derivatives?[75]

To answer above questions, a detailed, systematic study was undertaken of the effects of (i) substituents and central metal ions, and (ii) macrocycle substitution pattern and conformation on the S_2 relaxation rates of the tetrapyrroles and their derivatives. A set of 12 diamagnetic d^0 and d^{10} metallated tetrapyrroles substituted by different substituents in different patterns and/or different resulting macrocycle conformations were chosen as the subject of the present work. The corresponding molecular structures and their full names with abbreviations were shown in chart 1.1. Complications due to axial ligation and presence of d–d or charge transfer excited states (*i.e.* open d shell species) were avoided.[57,126,146] The structure-excited state properties relationship, if one exists, will be obtained by examining the spectroscopic and photophysical properties of their Soret-excited states.

5.2 Results and discussion

Since a great number of experimental data were obtained for the entire set of 12 compounds, the results and discussion section in this chapter will be organized in several subsections. First, the results of steady state spectroscopy experiments are analyzed in general, based on the spectroscopic measurables common to all of the compounds studied in this thesis. The differences in spectroscopic properties, together with the results of dynamics experiments related to each subset are analyzed and discussed separately. The analysis and discussion presented in each subsection focuses on several of the entire set of compounds which have common structures or properties. A global analysis of the complete set of results is presented at the end.

5.2.1 Steady-state spectroscopic properties

The steady-state absorption and emission spectra were measured following the methods and procedures described in Chapter 2. Irrespective of the presence of a “dark” or S_2' state, the conventional assumption adopted here is that the Soret band of absorption spectrum results from the $S_2 \leftarrow S_0$ radiative transition and that the corresponding emission is associated with $S_2 \rightarrow S_0$ radiative transition.[115] Both absorption and correspond-

ing emission spectra of most of twelve compounds obtained in the present work do not differ materially from those previously reported in the literature.[2,130,143,144,147-149]

As a representative, Fig. 5.1 shows the absorption spectra of ZnP, ZnTPP, ZnOEP and ZnTBP, which are plotted in molar extinction coefficient against wavenumber. As discussed in Chapter 4, spectroscopic properties of a given compound vary with solvent polarizability due to solvatochromic effects. To facilitate comparisons, all absorption spectra compared were taken using dilute solutions with concentrations in the range 1 to 3 x 10^{-6} M in ethanol at room temperature. Taking the absorption spectrum of the parent molecule ZnP as a reference, the band maxima of both the Soret and Q bands of ZnTPP,

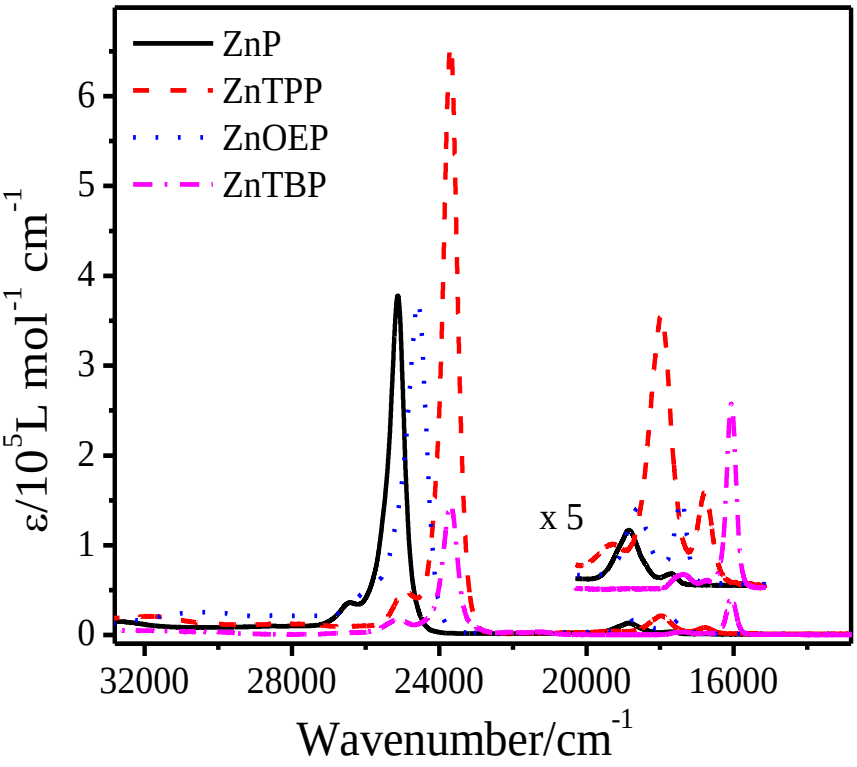

Fig. 5.1 Absorption spectra of ZnP, ZnTPP, ZnOEP and ZnTBP in ethanol. Solute concentrations are in the 1 to 3 x 10^{-6} M range.

ZnOEP and ZnTBP are all shifted to lower energies (to the red), irrespective of the nature of the substituents at either the four *meso*- (C_m) or the eight *β*- (C_β) positions. In addition to the shift of band maxima, the intensity of the molar extinction coefficient at

the band maximum of ZnP is comparable with that of ZnOEP and it is slightly increased in ZnTPP with a ratio of less than 2, but it is slightly decreased in ZnTBP by the ratio of *ca.* 2. The data of the molar extinction coefficients at the band maxima of all compounds studied are collected in Table 5.1.

The fluorescence spectra in the Soret region obtained by exciting in the Soret band are reasonable mirror images of the corresponding absorption spectra and shows a relatively small Stokes shift when both spectra were measured in the same solvent, *i.e.* ethanol except ZnOEP. The pairs of absorption and emission spectra of ZnOEP and CdTPP are shown in Fig. 5.2 as representative. However, the emission spectrum of ZnOEP was obtained by exciting at 330 nm, which initially deposits *ca.* 5733 cm^{-1} vibrational energy into the S_2 state, thus a large Stokes shift is expected, since vibrational relaxation is incomplete during the decay time of < 50 fs of the S_2 state of ZnOEP. The Stokes shift of the Soret band of ZnOEP in toluene is *ca.* 677 $\pm$ 30 cm^{-1}, which is much larger than the average (no more than 300 cm^{-1}) observed for the other metalloporphyrins studied. The bandwidths of the Soret bands of the emission spectra of ZnOEP, ZnTPP(F_{20}), ZnTPTBP and CdTPP are broader than those of the other metalloporphyrins observed in the same solvent.

The data that characterize the spectroscopic properties such as the Stokes shift and the relative intensities and widths of resolved vibrational features of both absorption and emission spectra of the set of compounds investigated are summarized in Table 5.1 and Table 5.2. To facilitate comparisons of spectroscopic properties of the entire set of compounds or subset of the compounds, all spectra were recorded under the same instrumental conditions with identical spectral bandwidths (2.0 nm). The spectra were recorded on a wavelength scale and were converted to the wavenumber scale following procedures as described in Chapter 2. Wavenumbers of the band maximum were taken directly from the spectra. To eliminate the effect of noise, the spectra were smoothed using 5 points averaging and the bandwidths were obtained from the best fits of Gaussian functions to the observed band shapes. All these analyze were done using the Origin program (version 7.5), with estimated errors of no more than 20 cm^{-1} per measurement.

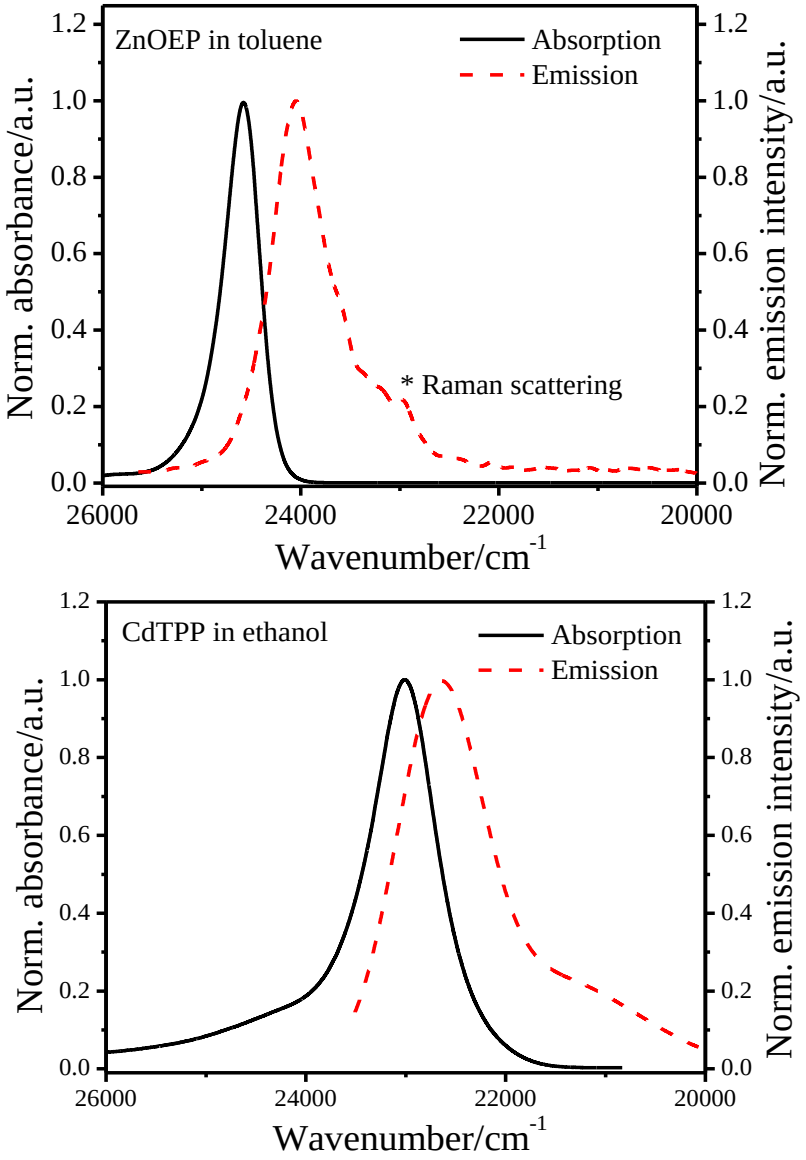

Fig. 5.2 Absorption and fluorescence spectra of ZnOEP in toluene (top) and CdTPP in ethanol (bottom), with excitation at 410 nm. The fluorescence spectrum (uncorrected for self-absorption) of ZnOEP was obtained by front-face illumination at 330 nm in a triangular cell and contains residual Raman scatter at *ca.* 23000 cm^{-1}.

Table 5.1 also contains the values of the relative intensities of the ε(0,0) and ε(1,0) vibronic features in both Q and Soret bands. The ratios of the intensities ε(1,0)/ε(0,0) or $f_Q/(f_Q + f_S)$, may be related to the extent of the interstate coupling energies between

Table 5.1 Steady state spectroscopic data of the whole set of metalloporphyrins studied in this thesis.[a]

compound /solvent	$E^{0\text{-}0}(S_2)$ (cm^{-1})	$\varepsilon_S^{max}/10^5$ ($M^{-1}cm^{-1}$)	$FWHM_S$ (cm^{-1})	$\varepsilon_{S\,(1,0)}/\varepsilon_{S\,(0,0)}$	$SS\ (S_2)$ (cm^{-1})	$E^{0\text{-}0}(S_1)$ (cm^{-1})	$\varepsilon_Q^{max}/10^4$ (cm^{-1})	$FWHM_Q$ (cm^{-1})	$SS\ (S_1)$ (cm^{-1})	$\varepsilon_{Q(1,0)}/\varepsilon_{Q(0,0)}$	$f_Q/(f_B+f_Q)$	$\Delta E(S_2–S_1)$ (cm^{-1})
MgTPP[b]												
Ethanol	23700	-	370	0.064	120	16630	-	370	80	1.59	0.083	7070
C_6H_5F	23500	-	450	0.077	190	16600	-	380	100	2.12	0.063	6900
Benzene	23420	5.36	450	0.064	160	16540	1.8	430	160	1.91	0.060	6880
Toluene	23350	5.74	540	0.074	200	16540	1.9	420	160	2.40	0.058	6910
CS_2	22830	3.90	660	0.065	-	16420	2.1	450	130	2.10	0.078	6410
ZnTPP												
Ethanol	23620	6.58	320	0.07	140	16690	2.17	400	200	2.88	0.056	6930
DMF	23470	7.29	490	0.07	120	16640	2.36	410	180	2.29	0.060	6830
Benzene	23560	5.87	690	0.07	170	16870	2.54	460	250	5.92	0.058	6695
ZnTPP-d_{28}												
Ethanol	23650	6.58	35	0.07	150	16730	2.17	360	150	2.89	0.054	6920
Benzene	23600	5.87	630	0.07	250	16890	2.54	450	290	5.86	0.061	6710
ZnTPP(F_{20})												
Ethanol	23800	5.52	500	0.106	270	16970	2.51	450	230	8.8	0.052	6830
ZnTPP(Cl_8)												
Ethanol	23450	5.70	270	0.076	190	16860	2.24	510	-	13.2	0.059	6590

Table 5.1 (cont'd)

CdTPP												
ethanol	23160	5.41	560	0.11	187	16280	2.02	420	249	1.45	0.054	6880
Benzene	22910	-	750	0.15	288	16210	-	570	684	1.75	0.059	6800
ZnP												
Ethanol	25070	3.8	440	0.094	100	17630	1.34	360	138	4.41	0.051	7440
ZnDPP												
Ethanol	24260	6.11	470	0.08	188	17130	1.99	320	170	5.95	0.057	7130
DMF	24130	-	510	0.08	217	17090	-	380	190	5.55	0.053	7040
Benzene	24150	-	-	0.08	190	-	-	-	-	-	0.057	6711
ZnTBP												
Ethanol	23640	-	390	0.12	112	16040	4.14	250	51	0.08	0.149	7600
DMF	23430	-	590	0.12	110	15980	-	260	58	0.06	0.157	7450
Pyridine	23050	-	650	0.12	-	15880	-	300	-	0.11	0.162	7170
ZnTPTBP[c]												
Ethanol	21700	3.4	840	0.12	-	15360	5.64	460	192	0.30	0.108	6190
DMF	21210	-	940	0.13	-	15160	-	480	263	0.39	0.119	6050
Benzene	21200	-	1120	0.12	-	15230	-	440	110	0.27	0.127	5970
Pyridine	20880	-	880	0.11	-	15070	-	460	304	0.43	0.124	5810
ZnOEP[c]												
Ethanol	24570	3.73	510	0.15	-	17440	2.01	350	-	0.90	0.076	7130
Toluene	24720	4.17	750	0.15	-	17560	3.94	340	-	0.55	0.078	7160

[a] wavenumbers quoted to nearest 10.
[b] Data for MgTPP adapted from reference 74.[74]
[c] Wavenumbers from the maxima of the origins of the Q and B bands in the absorption spectra, because of their noisy emission spectra.

the S_2 and S_1 states.[58] The values were calculated from the absorbance at the peak maxima in the absorption spectra. The intensity fraction $f_Q/(f_Q + f_S)$ was calculated by integration of the full Q band spectrum for f_Q, and the full Soret band spectrum for f_S. Analysis of the data regarding the resolvable vibronic features in Table 5.1 reveals that the relative intensities and widths are only a weak function of the solvent. However, they are strongly dependent on the nature of the substituents (phenyl or alkyl groups) and central metal ions (Mg, Zn or Cd), the macrocycle substitution pattern (*meso*- or *β*-) and macrocycle conformation and size (26 or 42 conjugated π electron systems).

As introduced in Chapters 1 and 3, the $S_2 \leftarrow S_0$ transition in the metalloporphyrins is fully electric dipole allowed with oscillator strength close to unity. The differences in the ε_{max} (or $\int \varepsilon(\bar{\nu})d\bar{\nu}$) are relatively small, however, the differences of the S_2 fluorescence quantum yields among the compounds examined are remarkable, as indicated by the data in Table 5.2. This fact indicates that the radiative rate constants of the S_2 states of the metalloporphyrins are similar (eq. 1.10), which is the case as indicated by the data in Table 5.2. Thus the vastly different fluorescence quantum yields among the metalloporphyrins studied result from different $k_r/(\sum k_{nr} + k_r)$ ratios, based on eq. 1.8, more accurately, are due primarily to vast differences in $\sum k_{nr}$ for the S_2 state.

Karolcazk *et al.*[42] and Lukaszewicz *et al.*[43] reported that the S_1 fluorescence quantum yields of ZnTPP in ethanol depend somewhat on the excitation wavelength when varying it from the blue to the red edge of the Soret band. To assess the excitation wavelength dependence of the fluorescence spectra, the fluorescence excitation spectra of all compounds were recorded as described in Chapter 2. The fluorescence excitation spectra were acquired, corrected and normalized before comparing with the corresponding absorption spectra. Fig. 5.3 shows a representative pair of the absorption and the corresponding emission excitation spectra of MgTPP in toluene. Similarly, for the other compounds studied, the normalized emission excitation spectra are almost identical to the corresponding absorption spectra, within experimental error. Three kinds of emission excitation spectra were acquired by fixing the observation wavelength further to the red in the Q region, while varying the excitation wavelength (i) within the Q band (ii) within the Soret region or (iii) over the whole range of the absorption spectrum. Then

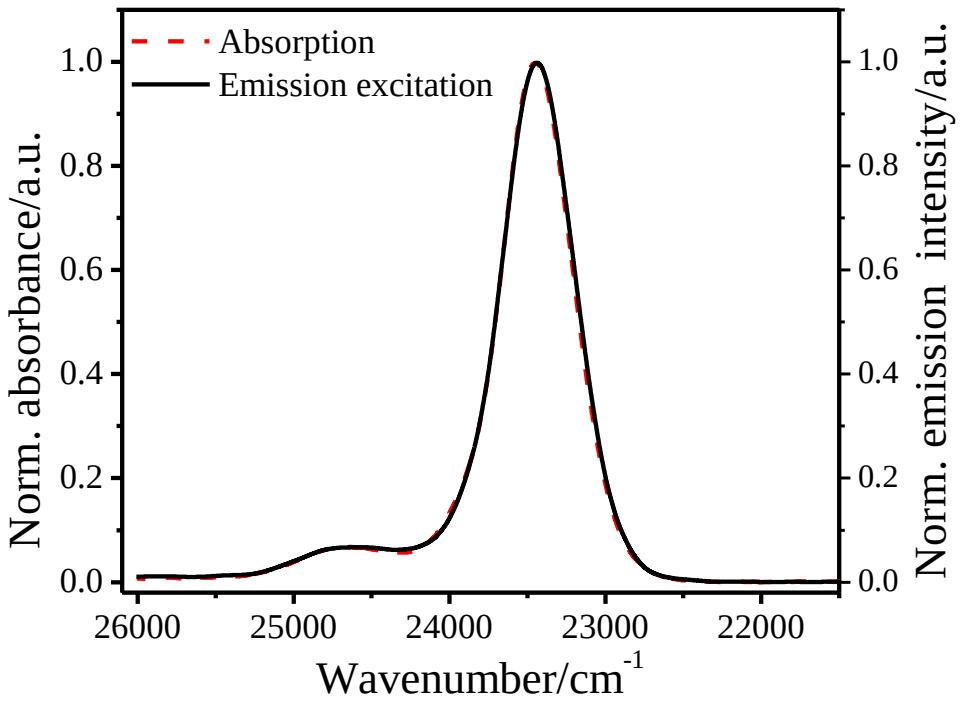

Fig. 5.3 Normalized $S_2 - S_0$ absorption spectrum and corrected emission excitation spectrum of MgTPP in toluene with concentration of 0.4 x 10^{-6}M, obtained by observing $S_1 - S_0$ emission at 663 nm. Adapted from reference 74.[74]

the corrected and normalized emission excitation spectra in each region were compared to the corresponding Soret and Q band absorption spectra, respectively, for each compound.

It is interesting to see that both the Soret band emission excitation spectrum and the Q band emission excitation spectrum reproduce the corresponding Soret and Q band absorption spectra. For the same metalloporphyrin, as the excitation wavelengths change within the Soret band from the blue side to the red side, the amount of the excess vibrational energy deposited in the S_2 state of the molecule also varies somewhat. However, the above observations also indicate that these variations have minor effects on the efficiency of the $S_2 - S_1$ internal conversion decay path. It is possible that the effects resulting from the changes of the excess vibrational energies were not significant and not revealed in the steady-state spectra.[2,144] In addition, for the whole range of the emission excitation spectrum, when normalizing only the Q band excitation spectrum with the Q band absorption spectrum, both the Soret band and the Q band match per-

fectly in the Q region, and match well in their shapes in the Soret region. They do, however, exhibit slight differences in intensities. When these differences exist, they always show that the Soret band excitation spectrum is slightly less intense by no more than 10% than the corresponding Q band excitation spectrum. These small differences of the intensities indicate that the efficiency of the $S_2 - S_1$ internal conversion $\eta(S_2 - S_1)$ must lie in the range $0.9 \leq \eta(S_2 - S_1) \leq 1.0$ in all the systems investigated here, irrespective of the vast differences in the nonradiative decay rates of this process.[74] This will be discussed in later sections of this Chapter.

5.2.2 Effects of deuteration

The absence of S_2 fluorescence in most OEP complexes and free base porphyrins such as H_2TPP has been attributed to the presence of high frequency C–H vibrations in these molecules, which act as energy accepting modes in the S_1 state during $S_2 - S_1$ internal conversion process.[57,58] However, direct experimental evidence confirming this hypothesis has not been presented. In the weak coupling limit, perdeuteration of polyatomic aromatic hydrocarbons leads to a reduction of the Franck-Condon factors of the C–H stretching vibrational modes in the S_1 state, which act as excess vibrational energy accepting modes during the $S_2 - S_1$ internal conversion. As a consequence, the $S_2 - S_1$ radiationless decay rates are slower in the perdeuterated molecule than in the perhydro counterparts. For an $\Delta E(S_2 - S_1)$ energy gap of 7000 cm^{-1}, assuming that the C–H(D) stretching vibrations are the dominant energy accepting modes, according to eq. 1.28, the effect of the perdeuteration would slow down the $S_2 - S_1$ internal conversion decay rate by a factor *ca.* 2 to 4 in a metalloporphyrin. As a consequence, the S_2 lifetime would be increased of the same factor. Such large differences of the S_2 lifetimes would be easily measurable.

In order to evaluate the contributions of the high frequency C–H vibrations to the nonradiative decay process of the S_2 state in metalloporphyrins, both the spectroscopic and dynamic properties of the Soret-excited S_2 states of the perdeuterated H_2TPP and ZnTPP (yielding TPP-d_{30} and ZnTPP-d_{28}, respectively, with isotopic purity higher than 98%) were studied. The data are summarized in either Table 5.1 or Table 5.2 and compared with those of the perhydro compounds.

Table 5.2 Dynamics data for the S_2 state of all compounds investigated and f_1 of solvents examined.

compound /solvent	f_1	$\Delta E(S_2\text{-}S_1)$ (cm^{-1})	$\phi_f/10^{-3}$	τ_{S1} rise ps	τ_{S2} ps	$k_r/10^8$ (s^{-1})	$k_{nr}/10^{11}$ (s^{-1})	β_{el} [a] (cm^{-1})
MgTPP								76
Ethanol	0.222	7103	2.4	3.25	3.28	7.3	3.05	
C_6H_5F	0.276	6910	2.4	-	2.82	8.5	3.55	
Benzene	0.295	6893	2.5	2.69	2.71	9.2	3.69	
Toluene	0.296	6880	2.3	-	2.55	9.0	3.92	
ZnTPP								81
Ethanol	0.222	6930	1.42	2.34	2.35	6.04	4.26	
DMF	0.257	6832	1.50	2.07	2.15	6.98	4.65	
Benzene	0.295	6695	1.14	1.41	1.49	7.65	6.71	
ZnTPP-d_{28}								80
Ethanol	0.222	6922	1.5	2.34	2.36	6.4	4.24	
Benzene	0.295	6713	-	1.49	1.50	-	6.67	
ZnTPP(F_{20})								183
Ethanol	0.222	6828	0.19	0.45	0.46	4.0	22	
ZnTPP(Cl_8)								98
Ethanol	0.222	6671	0.88	1.34	1.36	6.5	7.35	
CdTPP								197
Ethanol	0.222	6875	0.138	0.30	0.31	4.5	32	
Benzene	0.295	6696	0.129	0.24	0.24	5.4	42	
ZnP								173
Ethanol	0.222	7445	0.42	0.90	0.91	4.6	11.0	
ZnDPP								85
Ethanol	0.222	7129	1.61	2.31	2.30	7.00	4.35	
DMF	0.257	7033	1.50	2.00	2.01	7.46	4.98	
Benzene	0.295	6711	1.67	1.78	1.79	9.33	5.59	

Table 5.2 (cont'd)

ZnTBP								136
Ethanol	0.222	7601	-	-	1.30	-	7.69	
DMF	0.257	7447	2.37	-	2.55	9.29	3.92	
Benzene	0.295	7487	-	-	1.01	-	9.90	
Pyridine	0.300	7169	-	1.51	1.53	-	6.54	
ZnTPTBP								87
Ethanol	0.222	6189	0.79	0.93	0.93	8.5	10.8	
DMF	0.257	6047	1.22	0.74	0.75	16	13.3	
Benzene	0.295	5962	1.43	0.68	0.68	21	14.7	
Pyridine	0.300	5810	-	0.43	0.43	-	23	
ZnOEP								2000[b]
Ethanol	0.222	7133	~0.001	< 0.05	<0.05	-	>200	

[a] Calculated for data in ethanol.
[b] Best estimate based on $\tau(S_2) = 24$ fs (see text).
"-" not available

The pairs of S_2 decay and S_1 rise fluorescence upconversion profiles for ZnTPP and ZnTPP-d_{28} obtained in ethanol are shown in Fig. 5.4. The solid lines show the best fit to the experimental data. The deconvolution of the temporal profiles, using the method described in Chapter 2, gives an S_2 decay time constant of 2.36 ps and S_1 rise time of 2.34 ps for ZnTPP-d_{28} in ethanol. Note that both results are identical, within an experimental error of *ca.* 50 fs, to those values obtained for undeuterated ZnTPP in the same solvent. In addition, the S_2 fluorescence quantum yields of ZnTPP and ZnTPP-d_{28} are also similar, with a difference of only *ca.* 5% obtained under the same experimental conditions. These results indicate that deuteration of ZnTPP has no measurable effects on either lifetimes or fluorescence quantum yields of the Soret-excited S_2 state. The negligible differences between ZnTPP and ZnTPP-d_{28}, imply that C–H(D) vibrations are not directly involved in the $S_2 - S_1$ interstate coupling in ZnTPP. It is more likely that in-plane macrocycle skeletal C–C and C–N stretching modes, rather than C–H(D) vibrations, act as the most efficient energy accepting modes. If this is true, the deuteration effect would be expected to be finite due to vibrational coupling, but small and beyond the resolution accessible with this instrumentation.

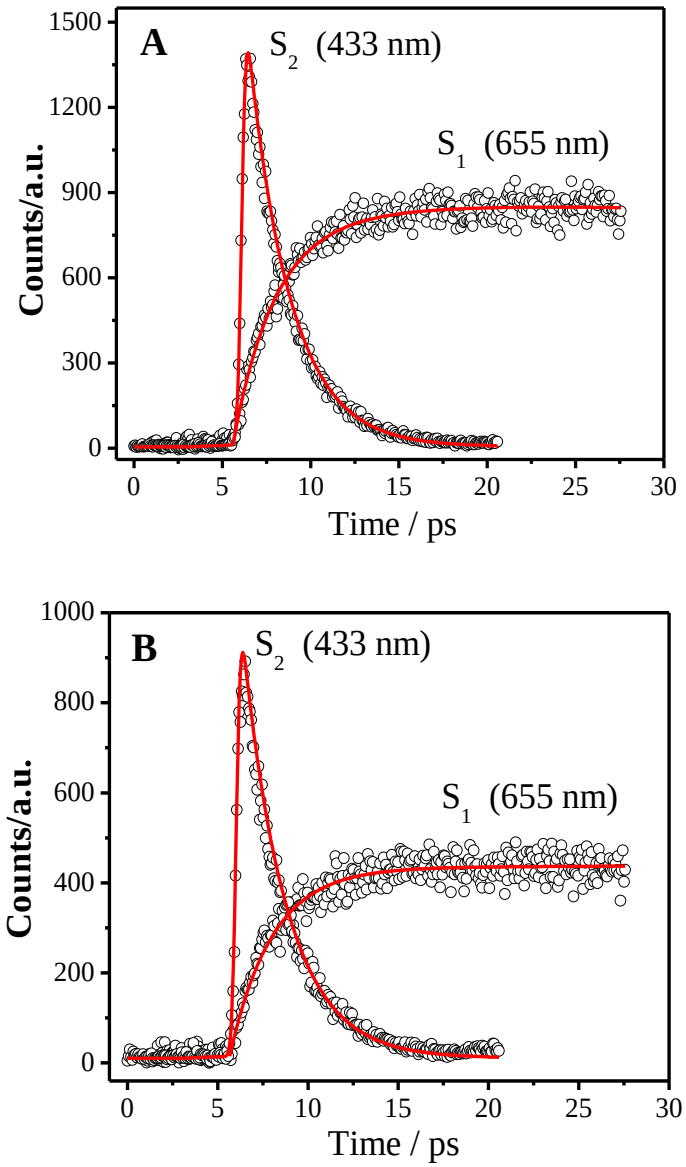

Fig. 5.4 Temporal S_2 decay and S_1 rise fluorescence upconversion profiles obtained in ethanol of (A) ZnTPP ($\tau(S_2)$ = 2.35 ps; $\tau(S_1$ rise) = 2.34 ps) and (B) ZnTPP-d_{28} ($\tau(S_2)$ = 2.36 ps; $\tau(S_1$ rise) = 2.34 ps). Excitation wavelength λ_{ex} = 400 nm and central observation wavelengths are shown for each event. The decay profiles were well modeled by single exponential decay and rise temporal profiles were deconvoluted by multiple exponential functions as described in Chapter 2. This figure was adapted from reference 75.[75]

The effect of the perdeuteration of ZnTPP on the nonradiative decay rate can also be evaluated as introduced in chapter 1. Such kind of perdeuteration would decrease the average frequency of the in-plane macrocycle skeletal C–C(N) stretching vibrations by

$\leq$ 4%, thus the expected ratio of the k_{nr}^{H}/k_{nr}^{D} will fall in the range $1.00 \leq k_{nr}^{H}/k_{nr}^{D} \leq 1.03$.[75] In fact careful measurements of the $S_2 - S_0$ fluorescence spectra of dilute solutions of ZnTPP and ZnTPP-d_{28} in ethanol, excited under exactly the same set of instrumental conditions and using the exactly same absorbance (0.05) at the same excitation wavelength (400 nm), reveals that a very slight increase (estimated to be *ca.* 3%) of the S_2 fluorescence quantum yield is obtained for ZnTPP-d_{28}. Based on the S_2 lifetime measurements, the nonradiative rate constants have been calculated, and values of 4.26 x 10^{11} s^{-1} for ZnTPP and 4.24 x 10^{11} s^{-1} for ZnTPP-d_{28} are obtained. The data are included in Table 5.2. The ratio k_{nr}^{H}/k_{nr}^{D} = 1.05 $\pm$ 0.05 is completely consistent with the above predictions, which confirms that C–H(D) vibrations are not important in the $S_2 - S_1$ interstate interactions of the metalloporphyrins examined. Together with calculations presented in Chapter 3, one can conclude that, in the metalloporphyrins, in-plane macrocycle skeletal C–C(N) stretching vibrations, not high frequency C–H vibrations, are the active energy accepting vibrational modes in the $S_2 - S_1$ radiationless transitions. As discussed earlier in this chapter, the fact that the emission spectra and the corresponding absorption spectra are good mirror images and small Stokes shift makes it reasonable to assume that the vibrational structures of the excited states are almost the same as those in the ground state. Thus the use of ground state frequencies instead of excited states ones for this analysis is reasonable.

However, the deuteration effects in the free-base tetraphenylporphyrin (*i.e.* H_2TPP) are more complicated due to the dual role of N–H(D) vibrations. On the one hand, they might act as energy accepting modes because of the high frequency associated with the larger Franck-Condon factor; in this case, deuteration will lead to the reduction of the Franck-Condon factor, and slow down the rate of $S_2 - S_1$ internal conversion. On the other hand, N–H(D) vibrations are also involved in the possible radiationless decay due to interconversion, via tunneling, between two tautomeric structures. The exchange between two tautomeric structures is associated with the motion of the H(D) atoms and involves large amplitude atom displacement. Thus the isotope effect might be considerably larger than the effects associated with the reduction of the Franck-Condon factor. Studies of the S_2 relaxation dynamics of the H_2TPP and its deuterated species (TPP-d_{30}) will explore the effects of the dual role of N–H(D) vibrations.

The S_2 lifetime of H_2TPP has previously been found to be very short, ranging from 20 fs[56] to 82 fs[150] depending on the condensed media employed. More recently, Baskin *et al.*[55] measured an S_2 lifetime of $\tau \leq 50$ fs for H_2TPP in benzene using the fluorescence upconversion technique. This lifetime is almost two orders of magnitude shorter than that of ZnTPP, which was found to be 1.45 ps in benzene.[55] What is the fundamental source(s) of this difference? Baskin *et al.*[55] determined that the $S_2 - S_1$ energy gap ($\Delta E(B - Q_y)$) of H_2TPP in benzene is only 5650 cm^{-1}. Because of such small $\Delta E(B - Q_y)$ in H_2TPP, the $S_2 - (Q_y)$ internal conversion would be expected to be much faster than those metalloporphyrins with substantially larger $S_2 - S_1$ energy gaps. They also attribute the fast nonradiative $S_2 - S_1$ internal conversion in H_2TPP to the excess vibrational energy deposited in the molecule by exciting to the blue side of the Soret band. However, as discussed in section 5.2.1, the effects of the variation in the amount of excess vibrational energy are not very important in the determination of the nonradiative decay of the S_2 state of the compounds studied at least the effects are not large enough to be revealed in the steady-state spectra.

In the present work, the S_2 lifetimes of the S_2 states of both H_2TPP and TPP-d_{30} in benzene were carefully measured using fluorescence upconversion under experimental conditions similar to those used by Baskin *et al.*[55]. When excited at 400 nm, *ca.* 1200 cm^{-1} to 1300 cm^{-1} of vibrational energy was initially deposited in the molecule. The temporal S_2 population decay profile of H_2TPP in benzene was nearly indistinguishable from the IRF but could be fit by a single exponential decay with a time constant of ≤ 50 fs. Meanwhile, the S_2 population decay time of the TPP-d_{30} in benzene was estimated to be *ca.* 100 fs. These results are in good agreement with the results reported by Baskin *et al.*[55] Based on the present results, the best estimate shows that the nonradiative decay rate of the $S_2 - S_1$ internal conversion of TPP-d_{30} in benzene was slowed down by a factor of *ca.* 2, when compared to that of H_2TPP. However, it is impossible to obtain a precise value of k_{nr}^{H}/k_{nr}^{D} ratio owing to the limited time resolution of the current experimental setup.

As discussed previously, the finite but immeasurable differences of the S_2 lifetimes between ZnTPP-d_{28} and ZnTPP indicate that perdeuteration of the four *meso*-substituted phenyl groups has a minor effect on the $S_2 - S_1$ radiationless decay rates of ZnTPP. If

this is also the case in H_2TPP and TPP-d_{30}, any decrease of the relaxation rate of $S_2 - S_1$ internal conversion in TPP-d_{30} must be due to the deuteration of the pyrrole N atoms. Due to the deduction of the Franck-Condon factor introduced by lowering the N-H(D) vibrational frequency, such deuteration is able to significantly slow the relaxation rate of the $S_1 - S_0$ internal conversion by a factor of almost 6 in TPP-d_{30}, given a large $S_1(Q_x) - S_0$ electronic energy gap of 15400 cm^{-1}.[15] However, the $\Delta E(B - Q_y)$ energy gap is only 5650 cm^{-1} for H_2TPP in benzene.[55] In this case, the changes of the Franck-Condon Factor associated with deuteration of N–H(D) have a minor effect (in a factor of less than 2) on the radiationless decay of the $S_2 - S_1$ internal conversion.

Thus the great reduction in the $B - Q_y$ radiationless relaxation rate of the S_2 state in TPP-d_{30} compared to that of H_2TPP, can only be due to the reduced rate of interconversion between two tautomeric structures, via tunneling. This interpretation is consistent with the tunneling model of radiationless transitions developed by Azenha *et al.*[128] The $B - Q_y$ interstate coupling, which can be enhanced when atom displacement is along molecular coordinates describing the tautomerization from $N_{1,3}$–H(D) to $N_{2,4}$–H(D), leads to ultrafast radiationless relaxation of the S_2 state in H_2TPP and a modest decrease in this rate on deuteration at the pyrrole N atoms.

5.2.3 Effect of a change in molecular symmetry of meso-substitution by phenyl groups

As discussed in Chapter 3, TDDFT calculations predict that the degeneracy of each excited electronic state obtained in ZnTPP(D_{4h}) is split into two closely spaced states (with $\Delta E \leq 0.02$ eV) when the symmetry is decreased in ZnDPP(D_{2h}), as displayed in Fig. 3.6 (b). The excited states with ^1E_u symmetry in ZnTPP are split into two closely lying states of $^1B_{2u}$ and $^1B_{3u}$ symmetry in ZnDPP due to the static Jahn-Teller effect. Fig. 5.5 shows the emission and corresponding absorption spectra of ZnDPP in ethanol. Compared to the spectra of ZnTPP, both the Soret and Q bands of ZnDPP are shifted slightly to the blue. However, the splitting of the excited states predicted by TDDFT calculations, results in no significant effect on the shapes or intensities of the solution phase absorption and emission spectra. The data presented in Table 5.1 show that the $S_2 - S_1$ electronic energy gap of ZnDPP is about 200 cm^{-1} larger than that of ZnTPP when

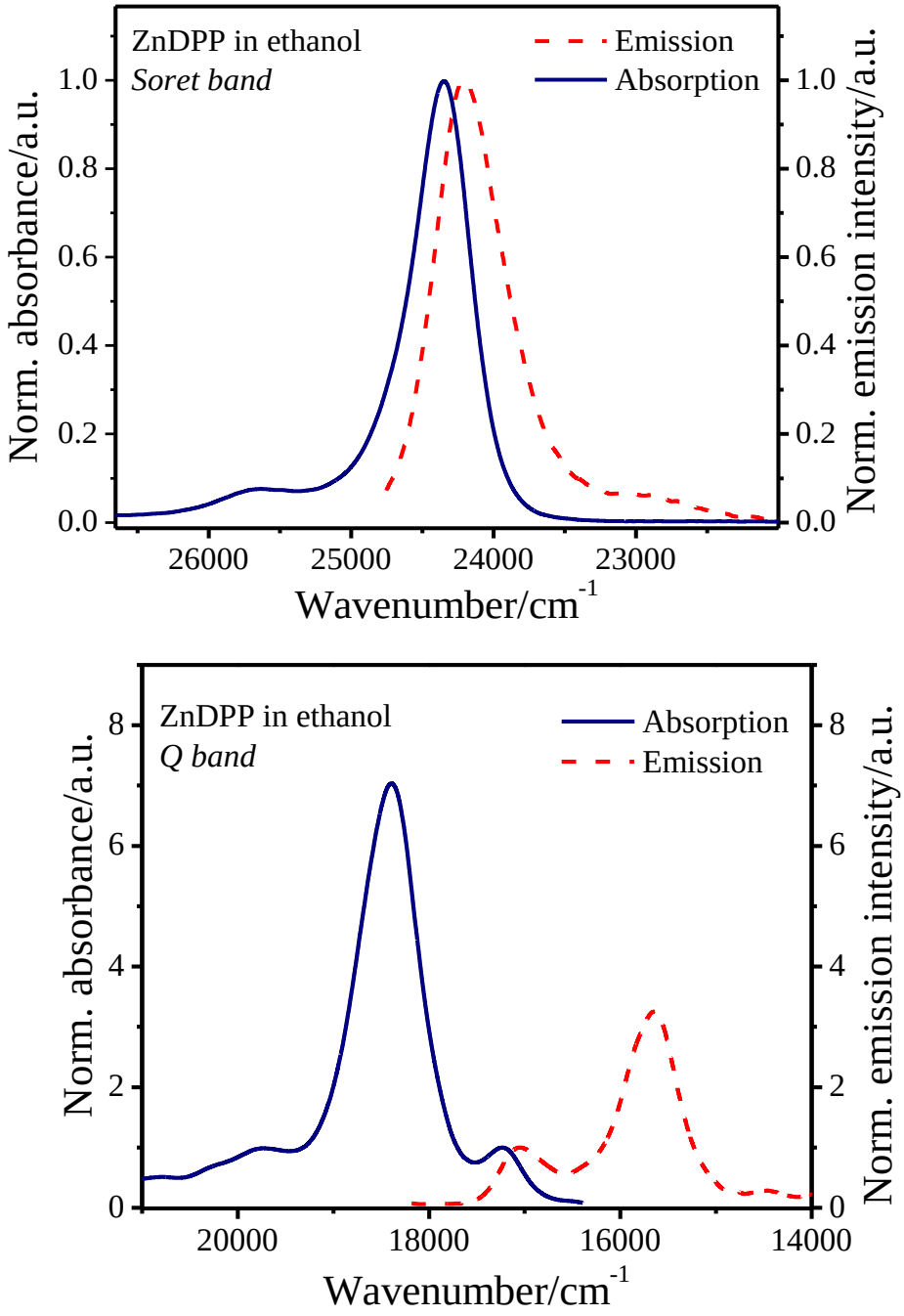

Fig. 5.5 Normalized Soret band and Q band absorption and emission spectra pair of ZnDPP in ethanol. The excitation wavelength is 400 nm.

both are measured in the same solvent, *i.e.* ethanol. However, the solvatochromic effect on the $S_2 - S_1$ energy gap of ZnDPP is similar to that of ZnTPP.

To examine the effect of the *meso*-substitution pattern on the S_2 population decay rates, both the S_2 decay and S_1 rise times of ZnTPP and ZnDPP were measured. The radiative and nonradiative rate constants characterizing the decay dynamics of the S_2 state of ZnDPP were calculated and summarized in Table 5.2. Similar to ZnTPP, the S_2 decay time of ZnDPP in ethanol is identical to its S_1 rise time. Moreover, the S_2 lifetime of ZnDPP is only 50 fs shorter and the calculated k_{nr} is just slightly larger than that of ZnTPP. The similar lifetimes and radiationless decay rates of the S_2 state in ZnDPP to those of ZnTPP indicate that static Jahn-Teller effects associated with lifting the degeneracy of the excited states, as predicted by TDDFT calculations discussed in chapter 3, is not an important determinant of the S_2 depopulation rate constants in ZnDPP.

In addition, Mataga, *et al.*[37] investigated the differences of the temporal S_2 decay and S_1 rise profiles of ZnTPP in ethanol and of zinc *meso*-diarylporphyrin in tetrahydrofuran (THF), which also has a lower symmetry than that of ZnTPP. Though in different solvents, the differences of the nonradiative rate constants of the S_2 state of two compounds are negligible. Their results strongly support the above conclusion that static Jahn-Teller effects are not important in determining the S_2 relaxation rate constants of the diamagnetic metalloporphyrins.

5.2.4 Effect of halogenations of *meso*-substituted phenyl groups

Halogenation of either β-substituents or *meso*-substituted phenyl groups is known to strongly influence the spectroscopic and photophysical properties of the lower excited states of both free-base porphyrins and their metallated derivatives.[78,108,151] As discussed in Chapter 4, the S_1 lifetime of ZnTPP(F_{20}) (1.55 ns) is shorter than that of ZnTPP (1.96 ns), but it is significantly shortened in ZnTPP(Cl_8) (0.26 ns) due to an enhanced $S_1 - T_1$ intersystem crossing. To investigate the effects of halogenations of the *meso*-substituted phenyl rings on the S_2 depopulation rates of the metallated tetraphenylporphyrins, both steady-state spectroscopic properties and dynamic population decay behaviour of Soret-excited ZnTPP(F_{20}) and ZnTPP(Cl_8) in ethanol were studied. The results are presented in Tables 5.1 and 5.2. Comparisons of the data regarding ZnTPP, ZnTPP(F_{20}) and ZnTPP(Cl_8) in Table 5.1 shows that the band maximum of the absorption of ZnTPP(F_{20}) is shifted slightly to the higher energy to that of ZnTPP, but, in ZnTPP(Cl_8), it shifted

slightly to the lower energy. Note that the $S_2 - S_1$ energy gaps of these three compounds in the same solvent are similar with a difference of no more than 200 cm^{-1}. However, the radiationless decay rates of the Soret-excited S_2 states of ZnTPP(F_{20}) are 6-fold larger in magnitude compared to that of ZnTPP, whereas, in ZnTPP(Cl_8), it is just slightly increased by a factor of less than 2. Thus the effects of perfluorination of the phenyl groups are significant, while partial chlorination of the phenyl rings has only a small effect on the S_2 radiationless decay rate. In particular, as shown in Fig. 5.10 **(**presented later in section 5.2.8), the energy gap law plots for the whole set of compounds investigated show that the datum for ZnTPP(Cl_8) falls squarely on the same straight line as for ZnTPP itself, while that of ZnTPP(F_{20}) lies well above because of its much larger k_{nr}.

Why do they behave differently? It has been reported[78,108,114,151] that perfluorination and partial chlorination of the four *meso*-substituted phenyl groups and result in a withdrawal of electron density from the conjugated macrocycle π electron systems, and leads to a ruffled macrocycle framework. The porphyrin macrocycles in ZnP and ZnTPP remain planar. However, for perfluoroalkyl porphyrinsthe nonplanarity (or ruffling) itself cannot account for the spectral shifts observed for the free base porphyrins and their metallated analogues.[108] The results of high level TDDFT calculations indicate that for these compounds,[151] saddling distortions only introduce a negligible difference on the geometry of the ground state and excitation energies of the excited states. Because both ZnTPP and ZnTPP(F_{20}) have similar energy gaps in the same solvent, the larger $S_2 - S_1$ radiationless transition rate in the perfluorinated compound compared to its planar counterpart could be ascribed to the distortion of the planarity. However, such changes in macrocycle planarity also exist in ZnTPP(Cl_8) and thus are insufficient to account for the great increase of the nonradiative decay rates of the S_2 states of ZnTPP(F_{20}). Further discussions will be presented in later sections of this Chapter.

5.2.5 Effect of the d^0 and d^{10} metal atoms in meso-substituted MTPP metalloporphyrins

As mentioned in section 5.2.4, halogenation of the four *meso*-substituted phenyl groups distorts the porphyrin macrocycle from planarity. The ground states of some

other sterically crowded *meso*-substituted tetraarylmetalloporphyrins have also been found to have either a ruffled or a saddle-shaped non-planar porphyrin framework.[78,108,109,151-155] In metallated porphyrins, when the size of the central metal ion (*e.g.* Cd^{2+}) exceeds that of the cavity provided by the tetrapyrrole ligand or when a solvent ligand such as pyridine pulls the metal ion out of the macrocyclic plane,[110,128,156,157] the metallated macrocycle is no longer planar. Such structural changes may be important in facilitating the biophysical functions of the metalloporphyrins and their derivatives. However, as discussed in section 5.2.4, structural distortion alone is insufficient to account for the spectral shifts observed for these tetrapyrroles with non-planar macrocycle.[78,108,151] Whether or not they are important in the determination of the photophysical properties of the S_2 states of the d^0 and d^{10} metalloporphyrins studied in this thesis remains an open question.

As introduced in Chapter 1, in addition to the potential distortion of the planarity of the porphyrin macrocycle, heavy metal atoms are able to enhance intramolecular $S_2 - T_n$ intersystem crossing, a process which could be involved in the radiationless decay of the S_2 state in tetrapyrroles due to the availability of several triplet states with energies close to or lower than that of S_2. To evaluate the influence of size and mass of the metal atom on the radiationless relaxation of the Soret-excited S_2 states of *meso*-substituted tetraphenylmetalloporphyrins, the photophysical behaviors of the S_2 states of MTPP (M = Mg, Zn and Cd) were investigated systematically. Here, the Mg^{2+} with d^0 and Zn^{2+}, Cd^{2+} with d^{10} valence electron configurations were chosen to eliminate the complexity associated with open shell structures. The data are collected in Tables 5.1 and 5.2. The efficiency of $S_2 - S_1$ internal conversion in these three compounds was also studied in order to evaluate the contributions of the $S_2 - T_n$ intersystem crossing to the radiationless relaxation of their S_2 states and the data are tabulated in Table 5.3 presented later in section 5.2.8. Though the $S_2 - S_0$ fluorescence quantum yield of CdTPP is extremely small, the $S_1 \rightarrow S_0$ fluorescence quantum yield is comparable to that of MgTPP and ZnTPP. Thus, it is possible to measure accurately the relative intensities of $S_1 \rightarrow S_0$ fluorescence of pairs of these three compounds.

For example, for MgTPP and ZnTPP in ethanol, the relative intensities of the $S_1 - S_0$ fluorescence were measured by exciting both solutions at the same wavelength (415

nm) in the Soret region, with an identical absorbance of 0.20 to obtain I_S, while exciting in the Q band region, the excitation wavelength was set at 559 nm with identical absorbance of 0.023 to obtain I_Q, as shown in Fig. 5.6. As a consequence, a ratio of $R_{MTPP} = I_S/I_Q$ of the $S_1 - S_0$ fluorescence intensity is obtained. The measurements were done under the identical conditions and the effects of excitation wavelength and absorbance at

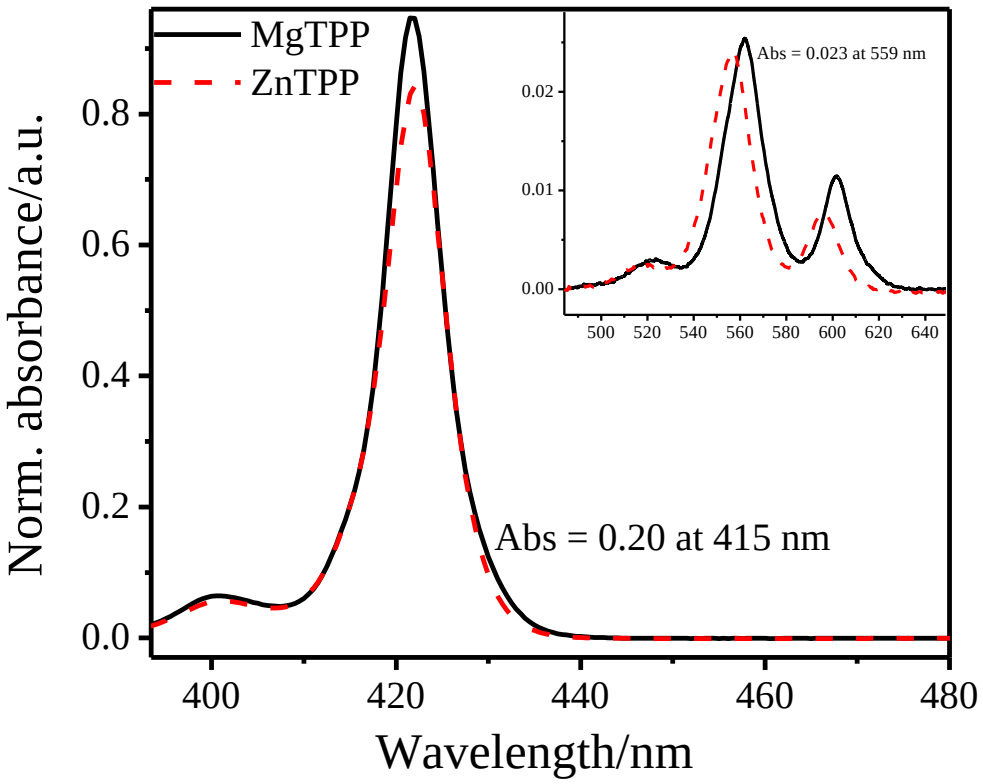

Fig. 5.6 Absorption spectra of MgTPP and ZnTPP in ethanol showing the wavelengths of overlap in the Soret and Q band regions chosen for excitation to measure the relative efficiencies of $S_2 - S_1$ internal conversion.

the excitation wavelength are eliminated. The ratio of ratio, R_{MgTPP}/R_{ZnTPP} obtained in this way for each pair compounds is equal to the ratio of their net $S_2 - S_1$ internal conversion efficiencies ($\eta(S_2\text{-}S_1)$), namely, $R_{MgTPP}/R_{ZnTPP} = \eta(S_2\text{-}S_1)(MgTPP)/\eta(S_2\text{-}S_1)(ZnTPP)$. Similar measurements and calculations were also done for the ZnTPP and CdTPP pair.

The value of $\eta(S_2\text{-}S_1)$ (ZnTPP) is slightly less than 1 for an excitation wavelength of 415 nm, which was obtained by measuring the absolute quantum yields of $S_1 - S_0$ emission as a function of excitation wavelength varying within the Soret band.[43] By taking

value of $\eta(S_2\text{-}S_1)$ (ZnTPP) as a reference, the results for three compounds were obtained as follows, $\eta(S_2\text{-}S_1)$ (MgTPP) = 1.00, $\eta(S_2\text{-}S_1)$ (ZnTPP) = 0.93 (reference) and $\eta(S_2\text{-}S_1)$ (CdTPP) = 0.69. The efficiency of $S_2 - S_1$ internal conversion in MgTPP is entirely consistent with the fact that the corrected, normalized fluorescence excitation spectrum of MgTPP is perfectly overlapped with the corresponding absorbance spectrum (*cf.* section of 5.2).

The $S_2 - S_1$ internal conversion efficiency of CdTPP is 0.69, so that other radiationless decay processes account for *ca.* 30% of S_2 decay in this compound. However, the data in Table 5.2 indicate that the $S_2 - S_1$ nonradiative decay rate has been increased in a factor of 7.5 comparing to that of ZnTPP. The 30% decrease of the $S_2 - S_1$ internal conversion efficiency could be attributed to enhanced competing $S_2 - T_n$ intersystem crossing, but its magnitude is insufficient to account for the 7.5-fold increase in the $S_2 - S_1$ nonradiative decay rate in CdTPP relative to ZnTPP at the same energy gap. In addition, the solvatochromic effect on the $S_2 - S_1$ internal conversion the decay rates of

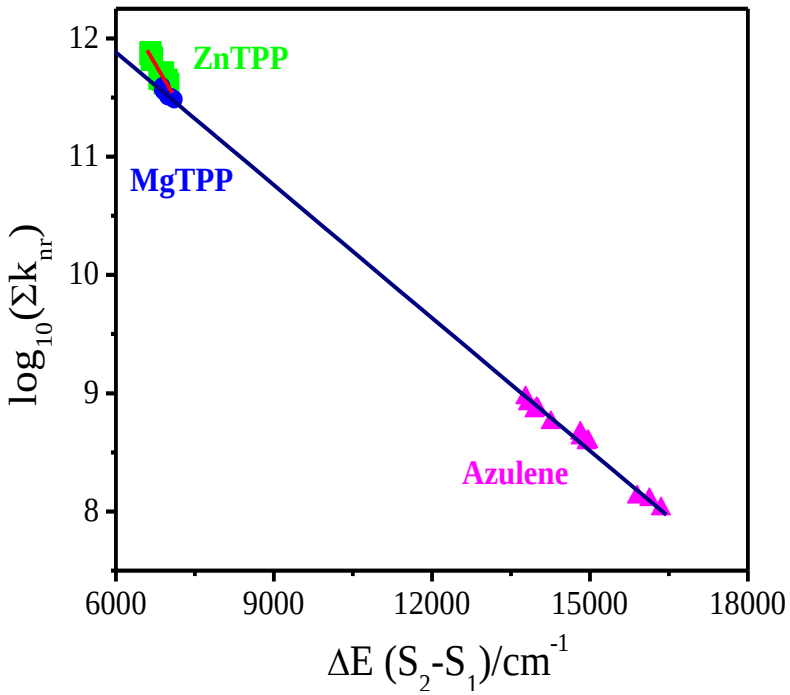

Fig. 5.7 Energy gap law plots for MgTPP and ZnTPP and the azulenes. Data for the azulenes were taken from reference 26,[26] and data for MgTPP taken from reference 74.[74]

CdTPP are qualitatively similar to those seen in ZnTPP and MgTPP. The data in Table 5.2 reveal that the S_2 decay time is very similar to the S_1 rise time for CdTPP in ethanol. Based on all these results, it is no doubt that the $S_2 - S_1$ internal conversion process is the dominant decay processes in these three MTPP metalloporphyrins, and that $S_2 - T_n$ intersystem crossing is not primarily responsible for the greatly increased S_2 radiationless decay rates in ZnTPP and especially in CdTPP.

It is very important to note that, as shown in Fig. 5.7, the energy gap law plot for MgTPP falls on the same straight line as that established for the azulenes. This result indicates that, similar to the azulenes, the $S_2 - S_1$ interstate coupling in MgTPP also belongs to the weak interstate coupling limit. However, the slope of the linear plot for ZnTPP is obviously different and the datum for CdTPP lies well above the weak coupling limit line, as shown later in Fig. 5.10 (to be discussed later in this Chapter).

5.2.6 Effect of extensions of the conjugated macrocycle structure and *meso*-tetraphenyl substitutions.

It has been reported previously that the $S_2 - S_1$ energy gap ($\Delta E(S_2 - S_1)$ in ZnTBP is 8953 cm^{-1} when measured in a supersonic expansion.[52] This is considerably larger than those of ZnTPP and other metalloporphyrins, and is close to those of some thiones. If the S_2 population decay rates of ZnTBP were to follow the predictions of the energy gap law of radiationless transition theory in the weak coupling case, its S_2 lifetime should-fall in the range from 50 to 500 ps. However, lifetimes of *ca.* 4 ps and 2.4 ps have been previously reported for ZnTBP in gas phase or in solution.[52,158]

To test the possible effects of extensions of the conjugated π-electron macrocycle and of any distortions of planarity introduced by *meso*-tetraphenyl substitution in the benzo-annulated macrocycles, both the steady state spectroscopic properties and dynamic photophysical decay rates of a subgroup of ZnP, ZnTBP and ZnTPTBP molecules were investigated in several solvents. The data are summarized in Tables 5.1 and 5.2. The results can be compared with those obtained previously for ZnTPP. The spectra obtained in the present work for ZnP and ZnTPTBP do not differ materially from those reported previously.[158-164] The spectra of ZnTBP require further comment. As men-

tioned in Chapter 2 a significant impurity, which is possibly fluorescent, with an absorption maximum near 460 nm has been reported in previous syntheses of ZnTBP.

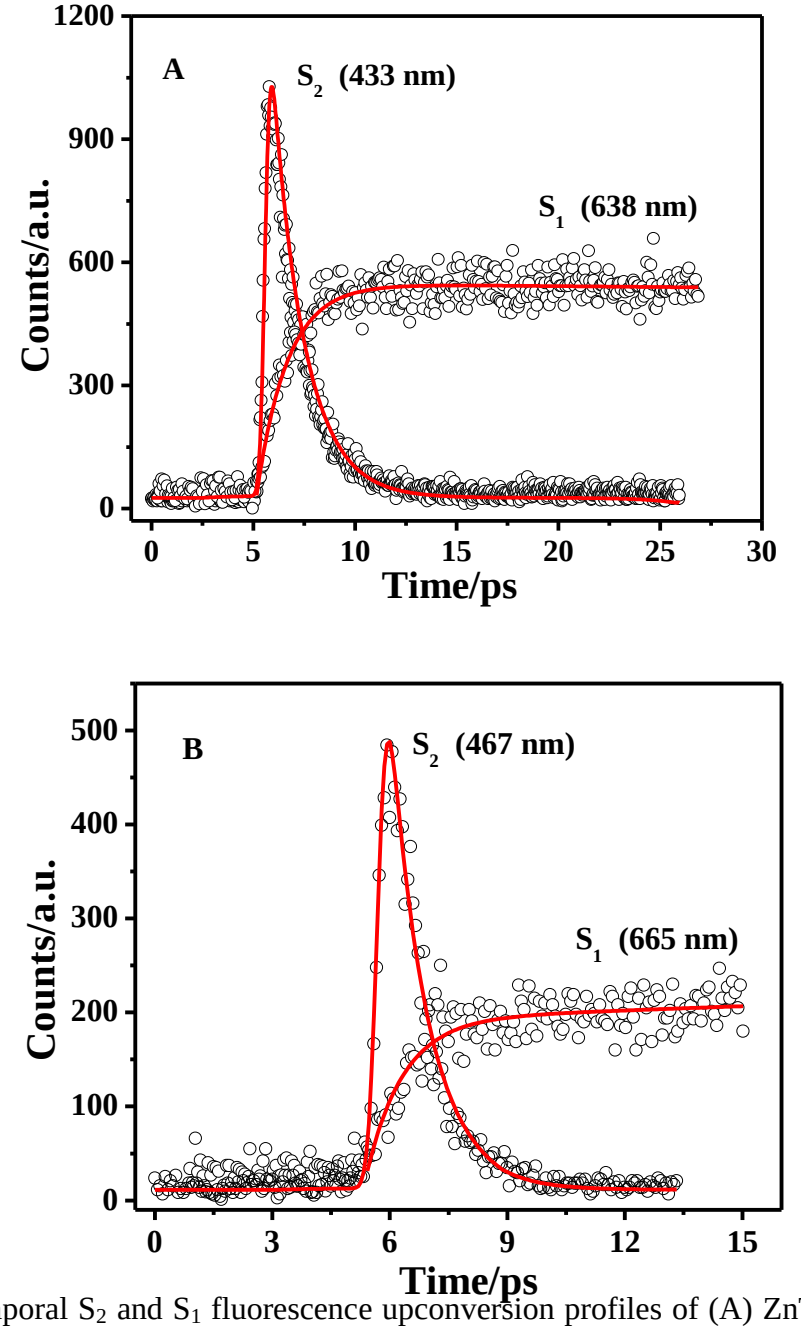

Fig. 5.8 Temporal S_2 and S_1 fluorescence upconversion profiles of (A) ZnTBP in pyridine ($\tau(S_2)$ = 1.53 ps; $\tau(S_1$ rise) = 1.51 ps) and (B) ZnTPTBP in ethanol ($\tau(S_2)$ = 930 fs; $\tau(S_1$ rise) = 933 fs). Measurements are at room temperature with λ_{ex} = 400 nm and central observation wavelength shown. The solid lines give the best fits of single exponential decay and rise functions to the measured data. Adapted from reference 75.[75]

This impurity is also present in commercially available samples. Discrepancies in previously reported $S_2 - S_0$ fluorescence quantum yields of this compound have been attributed tothis contamination.[25,26] Therefore, particular care was taken by professor S. Langford and his group in purifying and characterizing the ZnTBP used in this study. Despite careful purification, an absorption at 460 nm indicates the presence of residual impurity. However, this impurity is found to be non-fluorescent and the sample was therefore deemed suitable for investigation. Details regarding the purification of ZnTBP were given as supplementary information in reference 75.[75]

Both the absorption and emission spectra of ZnTBP and ZnTPTBP are greatly shifted to lower energies and both have relatively broader FWHM than the unannulated porphyrins. Both exhibit a larger ratio of relative intensities of the Q bands to the Soret bands, compared to those of ZnP and ZnTPP. Note particularly that ZnTBP has the largest $\Delta E(S_2 - S_1)$ value of 7601 $\pm$ 50 cm^{-1} in ethanol, consistent with previous reports.[52,162] However, the value of $\Delta E(S_2 - S_1)$ = 5810 cm^{-1} for ZnTPTBP in pyridine was the smallest of all the metalloporphyrins investigated in this thesis. An extended investigation of their solvatochromic effects was limited by the poor solubility of these larger molecules in non-coordinating solvents. Nevertheless, as shown in Fig. 4.5, despite the limited experimental data obtained, the intercept of the plot of $\Delta E(S_2 - S_1)$ versus the solvent polarizability function, f_1, for ZnTBP has almost the same value as that found for bare ZnTBP molecules (8953 cm^{-1}) in a supersonic expansion.

The pairs of temporal S_2 decay and S_1 rise profiles for ZnTBP in pyridine and ZnTPTBP in ethanol are shown in Fig. 5.8. The S_2 lifetimes of ZnTBP measured in a small set of solvents exhibit a modest dependence on the nature of solvent, and are comparable to those of ZnTPP obtained in the same solvent. This is consistent with the fact that the macrocycle with an extended conjugated π-electron network has a larger polarizability and hence is more sensitive to changes of the polarizability of the solvent. The radiationless decay constants calculated from the measured S_2 lifetimes are also comparable to those found in ZnTPP. Similar results were obtained for ZnTPTBP, but with smaller $S_2 - S_1$ energy spacings yielding slightly shorter lifetimes than those of ZnTBP. However, for ZnP, irrespective of its significantly larger energy gap ($\Delta E(S_2 -$

S_1) = 7445 cm^{-1} in ethanol, the S_2 lifetime of 0.91 ps obtained in ethanol was slightly shorter than that of ZnTPTBP. All the related data are summarized in Table 5.2.

Based on the data obtained and the analysis described above, one can conclude that the S_2 relaxation behaviors of both ZnTBP and ZnTPTBP do not follow the predictions of the energy gap law of radiationless transition theory in the weak coupling limit. Changes in neither the $S_2 - S_1$ energy gap nor the rigidity of the macrocycle framework can be used to interpret the effects on the $S_2 - S_1$ radiationless decay rate of the extension of the conjugated macrocycle from 26 to 42 π-electrons. In addition, the effect of *meso*-tetraphenyl substitution of either ZnP to give ZnTPP or of ZnTBP to give ZnTPTBP on the $S_2 - S_1$ radiationless decay rate cannot be correlated with changes in the macrocycle geometry.[75] Note also that the initial excess vibrational energy deposited in different metalloporphyrins by using the same excitation wavelength, 400 nm, varies with the different metalloporphyrins studied in solution (E_{vib} increasing from *ca.* 0 cm^{-1} in ZnP to *ca.* 3500 cm^{-1} in ZnTPTBP). However, no significant effect on the S_2 depopulation dynamics was found due to this difference in the amount of excess vibrational energy. This confirms the previous conclusions in section 5.2 which were made by comparing the emission excitation and absorption spectra of the same molecules.

5.2.7 ZnOEP and other d^0 or d^{10} metalloporphyrins without S_2 emission

For many years, it was believed that the Soret-excited (S_2) state of ZnOEP was "non-fluorescent".[33,57] However, very weak emission from the S_2 state of ZnOEP in ethanol was observed in the 400 ~ 430 nm range, when exciting at wavelengths to the blue side of the main Soret band in the present work. Details of these measurements have been described in Chapter 2. It is impossible to obtain an accurate spectrum because of the inner filter effect and the effects of scattering. Nevertheless, the $S_2 - S_0$ fluorescence quantum yield is estimated to be *ca.* 1×10^{-6}. The radiative rate constant and natural fluorescence lifetime of the S_2 state of ZnOEP in toluene were estimated based on integration of the absorption and emission spectra according to eq. 1.6. The lifetime of the S_2 state was calculated to be *ca.* 20 fs. By taking the inverse of this S_2 lifetime, a radiationless decay rate of *ca.* 5×10^{13} s^{-1} was obtained. Note particularly that this value is almost exactly the average frequency of the in-plane skeletal C–C and C–N stretching

vibrations of the porphyrin macrocycle. As discussed previously, these particular vibrations are the major energy accepting modes in the $S_2 - S_1$ radiationless decay of ZnTPP and MgTPP.

Though the S_2 fluorescence quantum yield of ZnOEP is very low, it is sufficient to obtain reliable temporal fluorescence upconversion decay profiles, although data acquisition takes a relatively long time. The reason is that the oscillator strength of the Soret transition in ZnOEP is large and comparable to those of other metalloporphyrins studied. The S_1 fluorescence rise time of ZnOEP in ethanol was also measured and compared to the S_2 decay time. Plots of the pair of temporal S_2 decay and S_1 rise fluorescence upconversion profiles of ZnOEP in ethanol are given in Fig. 5.9. The temporal S_2 decay profile is almost indistinguishable from the pure Gaussian instrument response function when both are obtained with a 3.3 fs step size during data acquisition. The deconvolution of the temporal decay profiles gives an S_2 population decay time of *ca.* 24 fs, which is entirely consistent with the S_2 lifetime of *ca.* 20 fs calculated previously based on the steady-state absorption and emission spectra of ZnOEP in toluene.

It is important to point out that the $\Delta E(S_2 - S_1)$ value of β-substituted ZnOEP in solvents such as ethanol (7445 ± 50 cm^{-1}) is slightly larger than that of *meso*-substituted ZnTPP in the same solvents (6930 ± 50 cm^{-1}) (Table 5.1). The energy gap law developed on the basis of the weak coupling case therefore cannot be used to explain the ultrafast radiationless relaxation rate of the S_2 state of ZnOEP, compared to that of ZnTPP. However, the fluorescence quantum yield of the S_1 state of ZnOEP is independent of the variation of the excitation wavelength ranging from the Q bands to the Soret bands, thus one can conclude that the efficiency of the $S_2 - S_1$ internal conversion is also close to unity, just as it is in ZnP and ZnTPP. In addition, the varying amounts of vibrational energy deposited in these metalloporphyrins cannot account for the differences in radiationless decay rates of the Soret-excited S_2 states, since, by fixing the excitation wavelength at 400 nm, *ca.* 1350 cm^{-1} of vibrational energy is deposited in ZnTPP, almost 0 cm^{-1} in ZnP and *ca.* 500 cm^{-1} in ZnOEP.

To interpret the large radiationless decay rate of the S_2 state of ZnOEP, strong $S_2 - S_1$ interstate coupling is hypothesized based on the results obtained in the present work. If strong coupling is involved, the larger S_2 radiationless decay rate can be attributed to

a much larger $S_2 - S_1$ interstate electronic coupling constant. Whether or not strong coupling exists in this system is the source of the ultrafast radiationless depopulation of the S_2 state in ZnOEP, and whether or not this strong coupling, if present, is characteristic of all β-substituted metalloporphyrins, are questions that will be discussed in the following section.

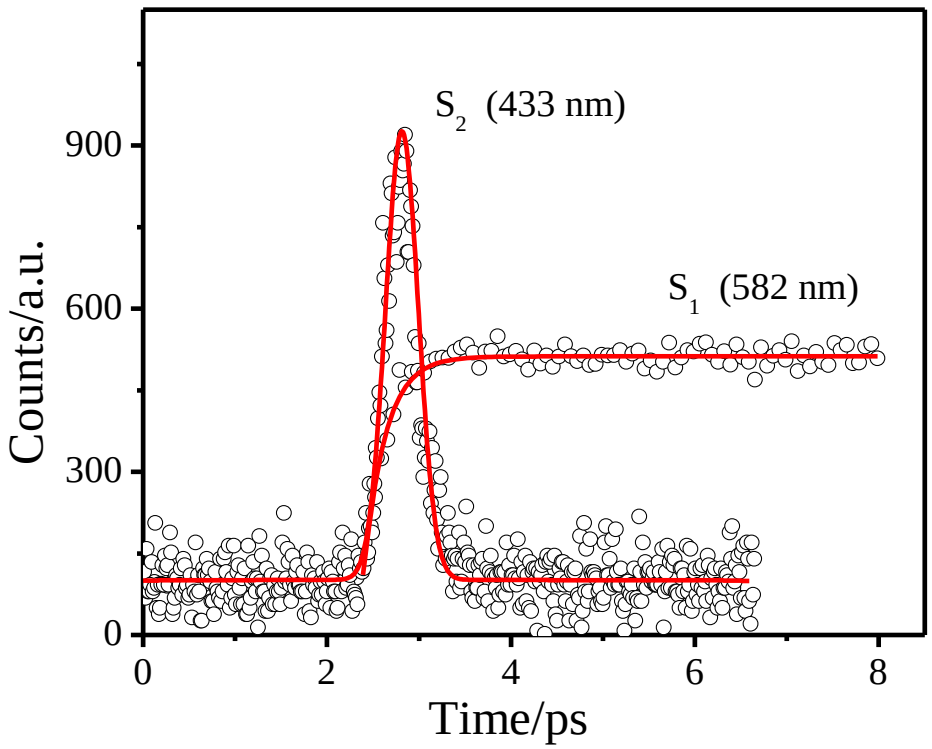

Fig. 5.9 Temporal S_2 fluorescence decay and S_1 fluorescence rise profiles of ZnOEP in ethanol at room temperature. Measurements are for λ_{ex} = 400 nm and the central observation wavelength shown. For the S_2 fluorescence upconversion signal, the solid line gives the best fit of the data to a Gaussian instrument response function with FWHM = 400 fs and S_2 population decay time, $\tau(S_2)$ = 24 fs. For the S_1 fluorescence signal, the solid line gives the best fit to an S_1 population rise time, $\tau(S_1$ rise) = 30 fs.[75] Obtained with 3.3 fs increment per data point.

5.2.8 Global Analysis of the entire set of compounds studied and Conclusions

The data presented in Table 5.2 show that the lifetimes and radiationless relaxation rates of the S_2 states of the entire set of twelve compounds studied here are strongly de-

pendent on molecular structure. The effects of the nature of the substituent and of the central metal ion, and the different macrocycle substitution patterns and macrocycle conformations have been evaluated by analysis of each of the several subsets of the entire set of compounds. Based on this analysis, several general conclusions can be drawn.

First, the superimposability of the corrected, normalized emission excitation spectra and the corresponding absorption spectra and the independence of the radiationless decay rates of the S_2 states of these molecules on the initial vibrational energy content at vibrational energies up to *ca.* 3500 cm^{-1} (in some compounds), indicate that no important excitation wavelength-dependent process is occurring in any of these metalloporphyrins investigated in solution. Second, efficiencies of $S_2 - S_1$ internal conversion are close to unity in all the systems studied in this thesis except for CdTPP (0.69). This indicates that the $S_2 - S_1$ internal conversion process is the major S_2 depopulation pathway in all the tetrapyrroles investigated, and that $S_2 - T_n$ intersystem crossing or other "dark" decay processes are not primarily responsible for the variation in the S_2 decay rates (although they could play a minor role in CdTPP).

Third, the temporal S_2 depopulation profiles obtained for all compounds studied, can be well represented by single exponential decay functions convoluted with the instrument response function. Moreover, the S_2 decay time is identical to the S_1 rise time of each compound/solvent system examined, within a measurement error of *ca.* 50 fs. These observations are in good agreement with those obtained by Mataga, *et al.*[37] and Gurzadyan, *et al.*,[35,36] but different from the measurements reported by Yu, *et al.*[41] The latter authors reported that the S_2 population decay time of ZnTPP in benzene was measurably longer than the rise time of S_1 fluorescence. Identical S_2 decay and S_1 rise times were observed for all compounds studied in this thesis, including ZnOEP, which has the shortest S_2 lifetime of *ca.* 24 fs, and CdTPP which has an $S_2 - S_1$ internal conversion efficiency of only 0.69. Based on all these observations, no obvious evidence emerges to verify the existence of any "dark' or S_2' state. However, if such a state exists and is responsible for the minor decay rate leading to the $S_2 - S_1$ internal conversion efficiency of < 1.0 in a few of the tetrapyrroles examined, it must be a parallel not a sequential relaxation process.

Fourth, as previously shown in Fig. 4.4 in Chapter 4, the $S_2 - S_1$ energy gap is a linear function of the solvent's Lorenz-Lorentz polarizability function (f_1) for the metalloporphyrins as shown in the graphs. This result is similar to that found for H_2TPP earlier by Renge.[165] The gradients of the plots of $\Delta E(S_2 - S_1)$ *vs.* f_1 were analyzed. The gradients are almost identical for the metalloporphyrins possessing the same macrocyclic framework, irrespective of the *meso*-aryl or *β*-alkyl substitution pattern, and give essentially one well-defined point on the graph (Fig. 5.9). These are 26 π electrons is in the 24-member macrocycle framework in ZnP and its derivatives, and 42 π electrons for ZnTBP and its derivatives, which have an extended 40-member macrocycle framework. The plot of the gradients of $\Delta E(S_2 - S_1)$ *vs.* f_1 plots versus the total number of π electrons in the macrocycle framework shows a good linear correlation, and passes through the origin, as shown in Fig. 5.10. Consistent with the previous interpretation in Chapter 4, the linear relationship indicates that dispersive interactions between the excited solute and solvent molecules, which is proportional to the polarizabilities of the molecules in both the S_2 and S_1 states, controls the magnitude of the solvent-induced changes of $\Delta E(S_2 - S_1)$ for the metalloporphyrins in solution studied in this thesis. This interpretation confirms the previous observation that the $\Delta E(S_2 - S_1)$ of ZnTBP is more sensitive to the changes of solvent polarizability due to its larger π system and the resultant larger polarizabilities of both its S_2 and S_1 states, compared to that of ZnP and its derivatives.

Based on the data in Tables 5.1 and 5.2, energy gap law plots of the nonradiative rate constants of the Soret-excited S_2 states versus the $\Delta E(S_2 - S_1)$ of MgTPP, ZnTPP and ZnTBP are linear in a wide set of solvents, but with different slopes. This observation confirms previous reports of linear energy gap correlations obtained for a small group of porphyrins in a small set of solvents.[4,35,36,41,55,73,74] As shown in Fig. 5.7, the energy gap plot of MgTPP in various solvents falls on the same straight line as that of azulene and its derivatives. However, the different slopes of the linear plots of ZnTPP and ZnTBP from that of MgTPP indicate that only the S_2 relaxation rate of MgTPP can be properly interpreted on the basis of the energy gap law derived from radiationless transition theory in the weak vibronic coupling case. It does not apply fully to ZnTPP, or to the other metalloporphyrins examined in this thesis as will be discussed in the following text. This indirectly confirms the previous conclusion that the magnitude of$\Delta E(S_2 - S_1)$

in some cases is only a minor controlling factor in determining the $S_2 - S_1$ internal conversion rate constant.

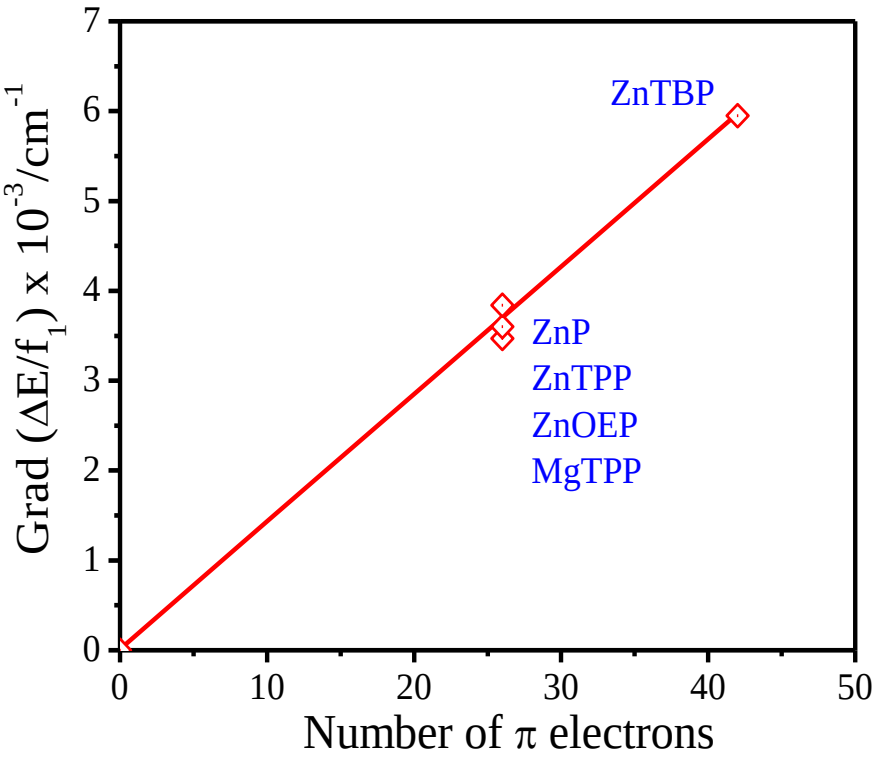

Fig. 5.10 Gradients of $\Delta E(S_2 - S_1)$ *vs.* f_1 plots (Fig. 4.4 and Fig. 4.5) *vs.* the number of π electrons in the fully conjugated macrocycle framework.[75]

As introduced in Chapter 1, the radiationless rate constants of the S_2 state is proportional to the square of the $S_2 - S_1$ interstate electronic coupling energy, β_{el}^2. According to the above results and analysis, one can conclude that when considering different d^0 and d^{10} metallated tetrapyrroles, in addition to the Franck-Condon factor, the magnitude of the β_{el}^2 is also an important determinant of the radiationless decay rate of the S_2 state. Whether weak or strong coupling[15] is involved, k_{nr} is proportional to β_{el}^2, according to eq. 1.21. To account for the >100-fold difference in radiationless decay rates of the S_2 states found for metalloporphyrins with about the same $\Delta E(S_2 - S_1)$, the values of β_{el} are thus expected to vary by a factor of about an order of magnitude.

The values of the β_{el}^2 can be calculated using eq. 1.27 if values of γ, $\hbar\omega_M$ and ΔE are known. In practice, the value of γ can be obtained from the slopes of the energy gap law plots shown in Fig. 5.7, for a given energy gap ΔE, and an assumed vibrational mode with a specific frequency $\hbar\omega_M$ and degeneracy or near-degeneracy. Together with the S_2 nonradiative decay rate k_{nr}, the strength of the $S_2 - S_1$ interstate electronic coupling energy can be calculated by substituting appropriate values of γ, ΔE and $\hbar\omega$ into eq. 1.27. To facilitate comparisons among the three MTPP compounds, the variation in the energy gap is eliminated by using the measured decay rates at the same value of ΔE = 6875 cm^{-1}. Three different assumed but realistic values of $\hbar\omega_M$ were used to evaluate the values of γ and β_{el}, 3000 cm^{-1}, 1580 cm^{-1} and 1350 cm^{-1} corresponding to a typical C–H stretch, aromatic in-plane C–C stretch and mixture of in-plane skeletal C–C and C–N stretches. The results of these calculations together with other parameters characterizing the properties of the energy gap law plots are summarized in Table 5.3. Because insufficient data were obtained to produce an accurate slope, the values for CdTPP were calculated using the same parameters obtained from the energy gap law plot as those used for ZnTPP.

Azulene is known to exhibit weak $S_2 - S_1$ coupling as is expected when the S_2 and S_1 states do not cross and are of different symmetry.[26] However, in the cases of metalloporphyrins, the S_2 and S_1 states which are of the same symmetry (^1E_u), could exhibit strong coupling. For comparison, the values of γ and β_{el} for $S_2 - S_1$ internal conversions in the azulenes were calculated using the data reported previously by Wagner *et al.*[26] These results are summarized in Table 5.3 as well. The data indicate that the slopes and intercepts of the energy gap law plots for the azulene system and for MgTPP are identical within experimental error. Both have intercept and interstate coupling energy that fall within the range predicted by the weak coupling radiationless transition theory, *i.e.* the magnitude of the intercept should be $10^{(13\pm2)}$ s^{-1}, with $\beta_{el} \leq 10^3$ cm^{-1}. However, the values of β_{el} and the intercept calculated for ZnTPP and CdTPP by using the same method are close to or even exceed the upper limits of the weak coupling case. The magnitude of values of β_{el} obtained for ZnTPP and particularly for CdTPP compared to that of MgTPP (for which $S_2 - S_1$ internal conversion is the only major radiationless

decay pathway of the Soret-excited S_2 state[74]) implies that either $S_2 - S_1$ internal conversion in ZnTPP and CdTPP involves two strongly coupled electronic states, or that there are one or more additional parallel radiationless decay processes that are competitive with the $S_2 - S_1$ internal conversion pathway. In either case, the values of β_{el} for ZnTPP and CdTPP listed in Table 5.3, which were calculated within the weak coupling framework of the energy gap law, would be incorrect.

Table 5.3 Energy gap law parameters and calculated values of γ and β_{el} for $S_2 - S_1$.[74]

system	slope (cm)	intercept	$\hbar\omega_M$ (cm^{-1})	$\Delta E(S_2\text{-}S_1)$ (cm^{-1})	$\eta(S_2–S_1)$	γ	$\beta_{el}{}^{\#}$ (cm^{-1})
azulenes	$–4.0x10^{-4}$	14.46	3000 1580	15,000	1.00	1.65 0.40	167 12
MgTPP	$–4.1x10^{-4}$	14.38	3000 1580 1350	6875	1.00	1.64 0.38 0.18	498 114 76
ZnTPP	$–7.6x10^{-4}$	16.91	1580 1350	6875	0.93	(1.65) (1.27)	(2.1×10^3) (1.4×10^3)
CdTPP*	-	-	1580 1350	6875	0.69	(1.65) (1.27)	(7.2×10^3) (4.8×10^3)

#Values in parentheses are calculated assuming (incorrectly) that $S_2 - S_1$ internal conversion in ZnTPP and CdTPP can be described by the weak coupling case (see text).
*Calculated for $k_{nr} = 5.6 \times 10^{12}\ s^{-1}$ and the energy gap law parameters for ZnTPP (see text).

In order to accurately evaluate the $S_2 – S_1$ interstate coupling energy in ZnTPP and the metalloporphyrins other than MgTPP studied in the present work, the weak coupling energy gap law dependence of $\log_{10}(\Sigma k_{nr})$ on $\Delta E(S_2 - S_1)$ for MgTPP was used as a standard.[75] For a given energy gap, any increase in the rate (k_{IC}) of the $S_2 - S_1$ internal conversion for other compounds can be attributed to the variation of the magnitude of β_{el}^2. Here $k_{IC} = \eta(S_2 - S_1)/\tau_{S_2}$, where η was taken as 1.0 for all compounds except CdTPP, for which $\eta = 0.69$ as discussed previously. The small deviations of η from 1.0 measured in some other compound were ignored to facilitate comparisons among all

compounds studied. Therefore, k_{IC} is assumed to equal k_{nr} for all compounds except CdTPP.

For MgTPP, based on the energy gap law plots shown in Fig. 5.11, an empirical linear relationship between the k_{IC}' (the ' denotes the $S_2 - S_1$ radiationless decay rate of

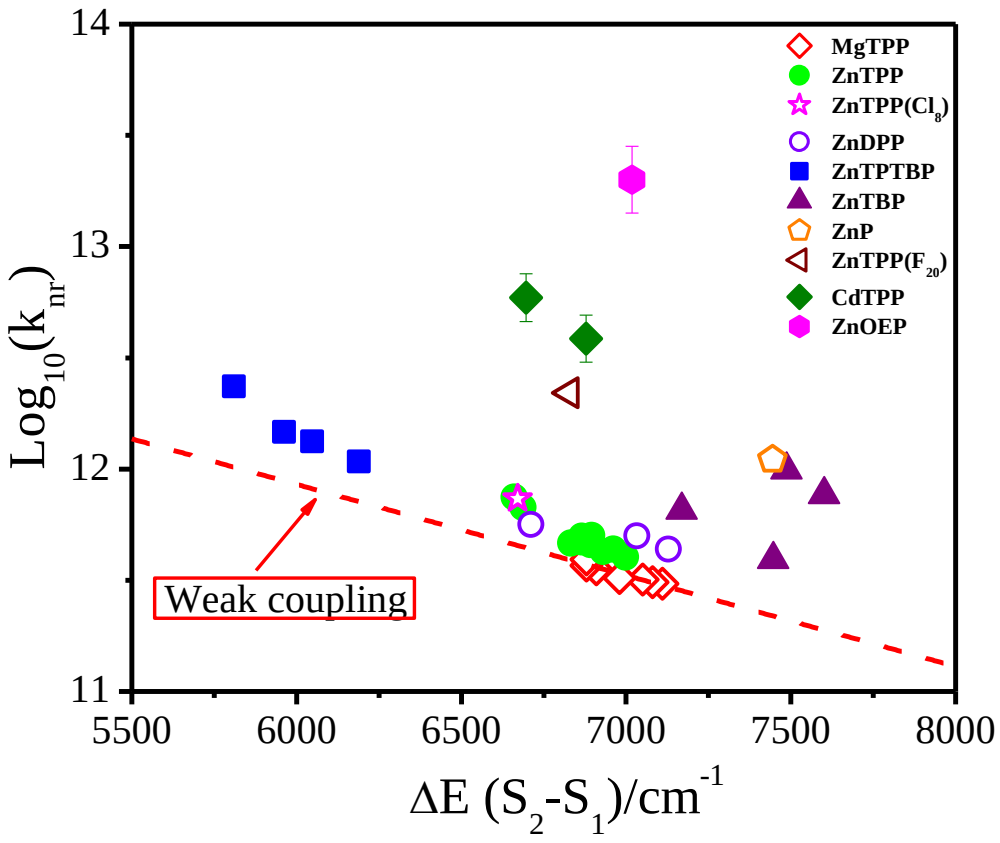

Fig. 5.11 Global analysis of factors controlling the $S_2 - S_1$ internal conversion rate in d^0 and d^{10} metalloporphyrins.[75]

MgTPP) and $\Delta E(S_2 - S_1)$ predicted by the energy gap law in the weak coupling case can be obtained graphically, as expressed in eq. 5.1 (data in Table 5.3).

$$\log_{10}(k_{IC}') = 14.38 - 4.1 \times 10^{-4}\,\Delta E \qquad (5.1)$$

where ΔE is in cm^{-1}. The values of k_{IC}' calculated this way are those that would be found if the metalloporphyrin were to exhibit the same weak vibronic coupling as

MgTPP. The value of $\beta_{el}(X)$ for each compound, X, in ethanol, is then calculated by substituting the appropriate values of $k_{IC}(X)$, $k_{IC}^{'}$ and $\beta_{el}(MgTPP)$ into eq. 5.2.

$$k_{IC}(X)/k_{IC}^{'}(MgTPP) = (\beta_{el}(X)/\beta_{el}(MgTPP))^2 \qquad (5.2)$$

where the value of $\beta_{el}(MgTPP)$ = 76 cm^{-1}, as determined previously.[74] The values of β_{el} obtained using this method are summarized in Table 5.2. Analysis of these data shows that, for ZnTPP, ZnTPP-d_{28}, ZnTPP(Cl_8), ZnDPP and ZnTPTBP, the $S_2 - S_1$ interstate electronic coupling energies are only slightly larger than that of MgTPP, and are close to those characteristics of weak interstate electronic coupling. For ZnTPP(F_{20}), CdTPP and ZnTBP, the values of β_{el} are twice that of MgTPP, indicating intermediate interstate coupling. The value of β_{el} for ZnOEP (2000 cm^{-1}) is much higher than the others, implying that the S_2 and S_1 states are strongly electronically coupled in this compound. Thus the values of β_{el} are correlated with the nonradiative decay rates of the Soret-excited S_2 states for the whole set of compounds investigated in this thesis. The importance of the $S_2 - S_1$ interstate coupling energy in determining the nonradiative decay rates of the Soret-excited S_2 states of the tetrapyrroles studied is confirmed.

What is the source of the intermediate to strong interstate electronic coupling found in most metalloporphyrins studied? Is there a measurable spectroscopic quantity that can be correlated to the interstate electronic coupling energy? In the following paragraphs, relationships between the interstate electronic coupling energy and specific measurable spectroscopic parameters that might reflect the effects of different interstate electronic coupling energies are examined and discussed.

The first spectroscopic parameter to be considered is the relative intensities of the Q(0,0) and Q(1,0) vibronic bands in the Q region of the absorption spectra of metalloporphyrins obtained in the gas-phase. Ohno, *et al.*[58] found that, for some metalloporphyrins, the ratio of the $\varepsilon_Q(0,0)/\varepsilon_Q(1,0)$, which are the relative intensities of the Q(0,0) and Q(1,0) vibronic bands in the Q region of the absorption spectra, is correlated with the vibronic $S_2 - S_1$ coupling energy, as expressed in eq. 5.3.

$$\varepsilon_Q(0,0)/\varepsilon_Q(1,0) = a(\delta E)^2 \qquad (5.3)$$

where δE is the energy difference between two ($^1a_{2u}{}^1e_g$) and ($^1a_{1u}{}^1e_g$) excited state electron configurations which are almost degenerate in energy for most metalloporphyrins with D_{4h} symmetry, and a is a constant. However, they simply considered the δE as the same as $\Delta E(S_2 - S_1)$, though it is incorrect.

Both the ratio of the $\varepsilon_Q(0,0)/\varepsilon_Q(1,0)$ and $\varepsilon_Q(1,0)/\varepsilon_Q(0,0)$ can be obtained by analysis of the steady-state absorption spectra, but here only the data of the $\varepsilon_Q(1,0)/\varepsilon_Q(0,0)$ are presented in Table 5.1 in order to compare to those of $\varepsilon_S(1,0)/\varepsilon_S(0,0)$. However, the correlation of the $\Delta E(S_2 - S_1)$ *vs.* either $\varepsilon_Q(0,0)/\varepsilon_Q(1,0)$ or $\varepsilon_Q(1,0)/\varepsilon_Q(0,0)$ were both examined. The results indicate that each ratio is only a modest function of the nature of the solvent for a given metalloporphyrin, but is strongly dependent on the nature and pattern of the substituents on the porphyrin macrocycle. However, based on the limited available data in the present work, no clear correlation between the ratio either $\varepsilon_Q(0,0)/\varepsilon_Q(1,0)$ or $\varepsilon_Q(1,0)/\varepsilon_Q(0,0)$ and the $\Delta E(S_2 - S_1)$, as well as β_{el} was obtained for the entire set of the metalloporphyrins investigated.

The second spectroscopic quantity of interest is the relative intensity of the Q − X transitions and the B − X transitions expressed as $f_Q/(f_Q + f_B)$, the oscillator strength of the Q band divided by the sum of the oscillator strengths of the Q and B bands. This quantity can also reflect the magnitude of the $S_2 - S_1$ coupling energy in different metalloporphyrins.[166,167] The data are presented in Table 5.1, and show that $f_Q/(f_Q + f_B)$ is a relatively weak function of the solvent (for at least non-coordinating solvents), but has a stronger dependence on the metalloporphyrin substitution pattern. This result is consistent with the previous discussion of the qualitative correlation between $\varepsilon_Q(0,0)/\varepsilon_Q(1,0)$ and $\Delta E(S_2 - S_1)$ of some of the set of the metalloporphyrins studied in the present work.

In order to determine the quantitative dependence of any spectroscopic quantity such as $\varepsilon_Q(0,0)/\varepsilon_Q(1,0)$ and $f_Q/(f_Q + f_B)$ on the $S_2 - S_1$ interstate electronic coupling energy, plots such as $\log_{10}(\beta_{el}(X))$ *vs.* $\log_{10}(\varepsilon_Q(0,0)/\varepsilon_Q(1,0))$ and *vs.* $\log_{10}(f_Q/(f_Q + f_B))$ were tried to determine the power dependence of $\beta_{el}(X)$ on each quantity. However, although a clear trend of $\beta_{el}(X)$ increasing with both $\varepsilon_Q(0,0)/\varepsilon_Q(1,0)$ and $f_Q/(f_Q + f_B)$ was found when applying this test to the limited set of compounds studied, both correlations were poor. And no clear trend was obtained for the entire set of compounds ex-

amined. For example, the value of β_{el}^2 of ZnTPP differs by a factor of about 100 from that of ZnOEP, whereas the values of $\varepsilon_Q(0,0)/\varepsilon_Q(1,0)$ for both compounds are almost identical and those of $f_Q/(f_Q + f_B)$ differ by no more than a factor of 5. Thus, the correlation between $\varepsilon_Q(0,0)/\varepsilon_Q(1,0)$ and $(\delta E)^2$ proposed by Ohno *et al.*[58] cannot be extended to the entire set of tetrapyrroles investigated in this thesis.

Another measurable spectroscopic quantity is the bandwidth of the Soret band, which is possibly correlated with the $S_2 - S_1$ electronic coupling energy. Hochstrasser[168] proposed that the bandwidth of the higher of two coupled electronic states is correlated with the square of the vibronic coupling energy which in turn scales the vibronic interaction between the two excited states, as expressed approximately in eq. 5.4.

$$\Delta E_{1/2} = E_v^2 \, F \, \rho \tag{5.4}$$

Here $\Delta E_{1/2}$ (in cm^{-1}) is the FWHM of the electronic absorption band, E_v is the vibronic coupling energy defined for each vibrational normal mode that has the proper symmetry to allow the upper excited state to couple with the lower excited state, F is the Franck-Condon factor and ρ is the density of vibronic accepting states in the lower excited state. As introduced in Chapter 3, in the metalloporphyrins the basic molecular symmetry is D_{4h} and the symmetries of the S_2 and S_1 excited states are both of ^1E_u. Thus only those vibrations with gerade symmetry, such as a_{1g}, a_{2g}, b_{1g}, b_{2g} can efficiently accept the electronic energy of the S_2 state. Extrapolating Hochstrasser's approach[168] to the metalloporphyrins, the FWHM of the main Soret absorption band (B(0,0)) would be correlated to the vibronic coupling energy between the S_2 and S_1 excited states. To facilitate comparisons, this consideration focuses on only those metalloporphyrins that have the same electronic macrocycle (and have about the same energy gap). F and ρ will be approximately constant under these circumstances, and the FWHM of the main Soret band would then be linearly dependent on the magnitude of E_v^2, to the extent that vibronic coupling is responsible for the spectral broadening.

However, the real situation is much more complicated due to the fact that the FWHM of the main Soret band is influenced by many factors, such as solvation and the significant thermal population of several low-lying vibrational states when the absorp-

tion spectra are taken in fluid solution at room temperature. Under such circumstances, the vibronic bands are inhomogeneously broadened and their intensity is distributed in a quasi-Gaussian, rather than a Lorentzian function, even though the later is appropriate for application of Hochstrasser's theory.[168] Extrapolating from the ideas used to obtain the relative $S_2 - S_1$ interstate electronic coupling energies in non-weak coupling cases, if vibronic coupling is the dominant mode of $S_2 - S_1$ interstate interaction, then the vibronic coupling energy should be at least proportional to the $S_2 - S_1$ interstate electronic coupling energy (β_{el}^2) calculated previously. And ratios between values of the FWHM of the Soret band of the metalloporphyrins and that of MgTPP (weak coupling) might reasonably scale the ratios of the β_{el}^2. The data in Table 5.1 show that the FWHM of the Soret band (B(0,0)) do increase with increasing β_{el}^2, but the expected quantitative correlation between the ratios of the FWHM of the B bands to the ratios of β_{el}^2 is not found. The absence of a good correlation suggests that the assumption that vibronic coupling is the dominant mode of $S_2 - S_1$ interstate interaction is not valid. By default, direct electronic interaction between the two coupled states, both of which are of ^1E_u symmetry (in D_{4h}), is indicated.

Finally, the magnitude of direct $S_2 - S_1$ interaction might be reflected by the relative magnitude of the Stokes shifts of the B and Q bands. In principle, similar Stokes shifts of the B and Q bands would imply that the two potential energy surfaces are displaced by similar amounts relative to that of the ground state, and are thus well nested within each other. Otherwise, if one potential energy surface is displaced by relatively larger amount than the other, different Stokes shifts of two absorption bands would result. As a consequence, the two upper potential energy surfaces could lie close enough to each other to result in stronger direct interaction, at vibrational energies in the S_1 state near the zero point energy of S_2 state.

The Stokes shift (SS) data of both the B and Q bands are included in Table 5.1. Because the Stokes shift is also influenced by many factors, especially when taking the data from spectra which were measured in fluid solution at room temperature, it is not a surprise to see that only a qualitative trend such as described above is observed in some of the compounds studied. Nevertheless, the data shows that the Stokes shifts of both the B and Q bands (150 cm^{-1} ~ 300 cm^{-1}) are either smaller than or comparable to the

widths of the individual bands. Moreover, the difference between the Stokes shifts of the Q band and that of the Soret band is even smaller. As can be seen that, the Stokes shifts of the B bands obtained from the steady state spectra of the weakly fluorescent (from S_2 state) molecules, such as ZnOEP, are considerably larger (*e.g.* 750 cm^{-1} in toluene). However, these big Stokes shifts are subject to much greater error, due to constrains imposed by measuring the emission spectrum as described in Chapter 2. In particular, in ZnOEP the timescale of the S_2 lifetime (*ca.* 24 fs) is comparable to the intramolecular vibrational relaxation time. Thus the B band Stokes shifts of ZnOEP will be somewhat time-dependent and only a time-averaged Stokes shift will be measured in the steady-state spectra. Nevertheless, a qualitative correlation between β_{el}^2 and the Stokes shifts estimated from the steady state solution spectra can be established for some of the metallated tetrapyrroles investigated in this thesis.

In summary, based on the above analysis and discussion there is no single solution phase spectroscopic observable that can be correlated with the magnitude of the $S_2 - S_1$ interstate coupling energies of the tetrapyrroles examined in this thesis. None of the effects discussed above can be used by themselves to explain the significant differences in the S_2 lifetimes and the radiationless decay rates obtained among the entire set of the twelve compounds studied.

Nevertheless, the following conclusions can be drawn. (1) *β*-Substitutions introduce enhanced $S_2 - S_1$ interstate coupling compared to *meso*-substitutions. In particular, *β*-octaalkyl metalloporphyrins exhibit strong $S_2 - S_1$ interstate coupling (β_{el} = 2000 cm^{-1}), resulting in ultrashort S_2 lifetimes that are comparable to macrocycle stretching frequencies. (2) Comparing ZnP with ZnTPP, the effects of *meso*-aryl substitutions are modest. They reduce both the $S_2 - S_1$ electronic energy gap and the $S_2 - S_1$ interstate coupling energy (β_{el} = 81 cm^{-1} for ZnTPP), resulting in a small net effect on the nonradiative decay rate of the S_2 state. (3) Akimoto *et al.*[60] reported that the S_2 population decay time of 150 fs was measured for *β*-tetraethyl-*meso*-diaryl-substituted zinc porphyrin. Its value of β_{el} = 315 cm^{-1} was calculated as described above using eq. 5.2. Comparing their result with the results obtained in the present work, one can conclude that when both *β*-alkyl and *meso*-aryl substitution occur together, the resultant $S_2 - S_1$ interstate electronic coupling energies fall in the range of intermediate case. (4) Though

non-planar tetrapyrroles exhibit relatively larger interstate electronic coupling energies, compared to their planar counterparts, comparison of the results of non-planar tetrapyrroles such as ZnTPP(F_{20}), CdTPP and their planar counterparts, such as ZnTPP, shows that effect of non-planarity itself may not account for the increased interstate coupling energies and the resulting relatively fast $S_2 - S_1$ radiationless decay rates. (5) Benzoannulation leading to an extended macrocycle, results in a slightly decreased $S_2 - S_1$ interstate coupling energy compared to that of ZnP. In addition, since the polarizability is proportional to the number of π electrons in the extended macrocycle, benzoannulation at four pyrrole rings increases the polarizability of the excited states leading to a greater sensitivity of the $S_2 - S_1$ spacing to solvent polarizability. (6) Only the S_2 relaxation behavior of MgTPP can be properly represented by the energy gap law within the framework of the weak coupling case. Other metalloporphyrins investigated exhibit intermediate to strong $S_2 - S_1$ interstate coupling energies and do not follow the predictions of the energy gap law in the weak coupling limit.

Chapter 6: Photophysics of Soret-excited Porphyrinoids–Aluminum and Gallium Corroles

6.1 Introduction

The corroles, porphyrinoids that are one *meso*-carbon deficient and have a contracted macrocycle cavity, constitute one of several families of tetrapyrrolic compounds.[64,169] Early studies of corroles mainly focused on the aspects of their synthesis and their coordination chemistry rather than their potential applications. However, the recent discovery of their use in catalysis, as sensors and possibly in dye-sensitized solar cells and the treatment of cancer, have prompted studies of their applications in different fields.[64] Of particular interest here is their use in the design of photon-actuated devices such as dye-sensitized solar cells, which involve energy and/or electron transfer processes from highly excited corroles to the other components.[64]

Relatively few reports have been devoted to investigating the spectroscopic and photophysical properties of the free base and metallated corroles. The limited investigations available have focused on the lowest excited singlet (S_1) and triplet (T_1) states.[170-172] Previous studies[173] show that the electronic absorption spectra of the metallated corroles, like the metalloporphyrins, are characterized by weak Q (visible) bands and intense B (Soret) bands, but that their spectroscopy is quantitatively different. For example, the spectra of the *meso*-substituted triarylcorroles are more solvent-sensitive and are somewhat red-shifted compared to the corresponding *meso*-substituted tetraarylporphyrins, and the ratios of the intensity of the Q bands to that of the Soret bands are somewhat larger than in the corresponding porphyrins. Of particular interest is the observation that the metallated corroles have larger quantum yields of $S_1 - S_0$ fluorescence compared to their metalloporphyrin counterparts, as reported by Mahammed *et al.*[174] and Bendix *et al.*[173] In addition, certain selectively substituted corroles were found to perform well and to display higher dye-sensitized solar cell efficiencies compared to those of cells composed of other tetrapyrrolic compounds.[175] These observations indicate that the corroles have some advantages superior to those of the metalloporphyrins in applications such as fluorescent probes and solar energy harvesting devices.[64] Moreover, the use of hydrophilic substituents makes the corroles easily water-soluble and

thus can extend their potential applications to the fields of photodynamic therapy and biostructural probes,[176] where water solubility is required.

For photo-actuated applications, it is important to know the photophysical properties of the photoactive species. Though a few measurements of the corroles' S_1 and T_1 photophysics have been reported,[170-172] no reports at all have been found regarding dynamics of more highly excited electronic states, such as those populated by exciting in the Soret region.[173] Thus it is worthwhile to obtain information concerning the photophysical properties of the metallated corroles. In the present work, the $S_2 - S_0$ fluorescence of the Soret-excited corroles metallated with Al and Ga (Al(tpfc)(py) and Ga(tpfc)(py), as shown in Chart 6.1), was observed for the first time using both static and dynamic methods. The photophysical properties of these corroles will be compared with those of MgTPP and ZnTPP. The $S_2 - S_1$ interstate electronic coupling status of these two corroles was also examined by comparing them to the model metalloporphyrin, MgTPP, which exhibits weak $S_2 - S_1$ interstate electronic coupling, as discussed in Chapter 5.

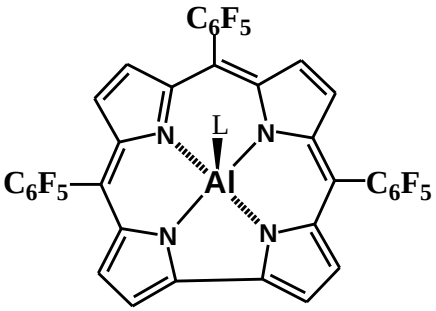

Al(tpfc)(py)

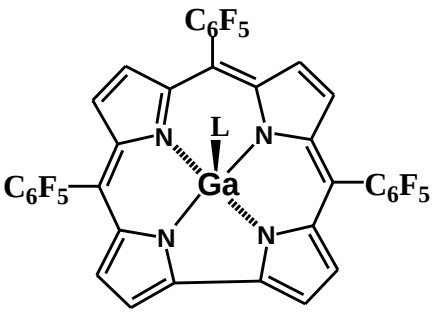

Ga(tpfc)(py)

Chart 6.1 Structures of the corroles. L = py = pyridine.

6.2 Results and discussion

The corroles (Al(tpfc)(py) and Ga(tpfc)(py) (Chart 6.1) were synthesized and provided by the group of Professor Z. Gross from Technion-Israel Institute of Technology. In the solid, these two corroles are coordinated by a pyridine ligand on the central metal ions as shown by their x-ray structure.[173] Due to this coordination, the central metal ion

is pulled out of the macrocycle plane leading to a domed pyramidal geometry in which the four individual pyrrole rings remain planar and point toward to the central metal ion. As discussed in Chapter 5, a domed porphyrin macrocycle has no significant effect of itself on the electronic spectra and the relaxation of the S_2 state of substituted metalloporphyrins. Do these structure differences influence the spectroscopic properties and relaxation dynamics of the Soret-excited electronic states of the corroles?

6.2.1 Steady state experiments

Experiments to examine solvation effects and the influence of solvent coordination on the electronic spectra were carried out in ethanol, benzene, benzene + 5% pyridine, toluene and toluene + 5% pyridine solutions at room temperature. To test the effects of oxygen quenching, the solution of Al(tpfc)(py) in benzene + 5% pyridine was degassed before measuring the emission spectra. The results indicate that degassing has negligible effects on the S_2 fluorescence spectra and yields. Thus both absorption and emission spectra were taken using air saturated solutions. In addition, no significant photodegradation of the corroles was observed during the data acquisition period while their solutions were exposed to room light, steady-state fluorometer light or laser radiation for time-resolved dynamics measurements.

The steady state absorption and emission spectra were taken using the methods described in Chapter 2. In Fig. 6.1 the electronic absorption spectra of Al(tpfc)(py) in benzene is compared with that of MgTPP, while that of Ga(tpfc)(py) is compared with ZnTPP. Relevant parameters are collected in Table 6.1. In each pair of absorption spectra, the intensities were normalized to the maximum of the Soret band to facilitate comparison. As can be seen from Fig. 6.1 (A), the Soret band of Al(tpfc)(py) is a shifted to the blue compared with that of MgTPP. Both have a similar shape and vibronic structure, except that the FWHM of the Soret band of Al(tpfc)(py) is slightly broader and has a higher B(1,0) vibronic band intensity. It is interesting to note that in the Ga(tpfc)(py)-ZnTPP pair, as shown in Fig. 6.1 (B), the normalized Soret bands of both of them are almost overlapped, except that the B(1,0) vibronic band of Ga(tpfc)(py) has relatively higher intensity compared to that of ZnTPP. Note in particular that, in both cases, the ratios of

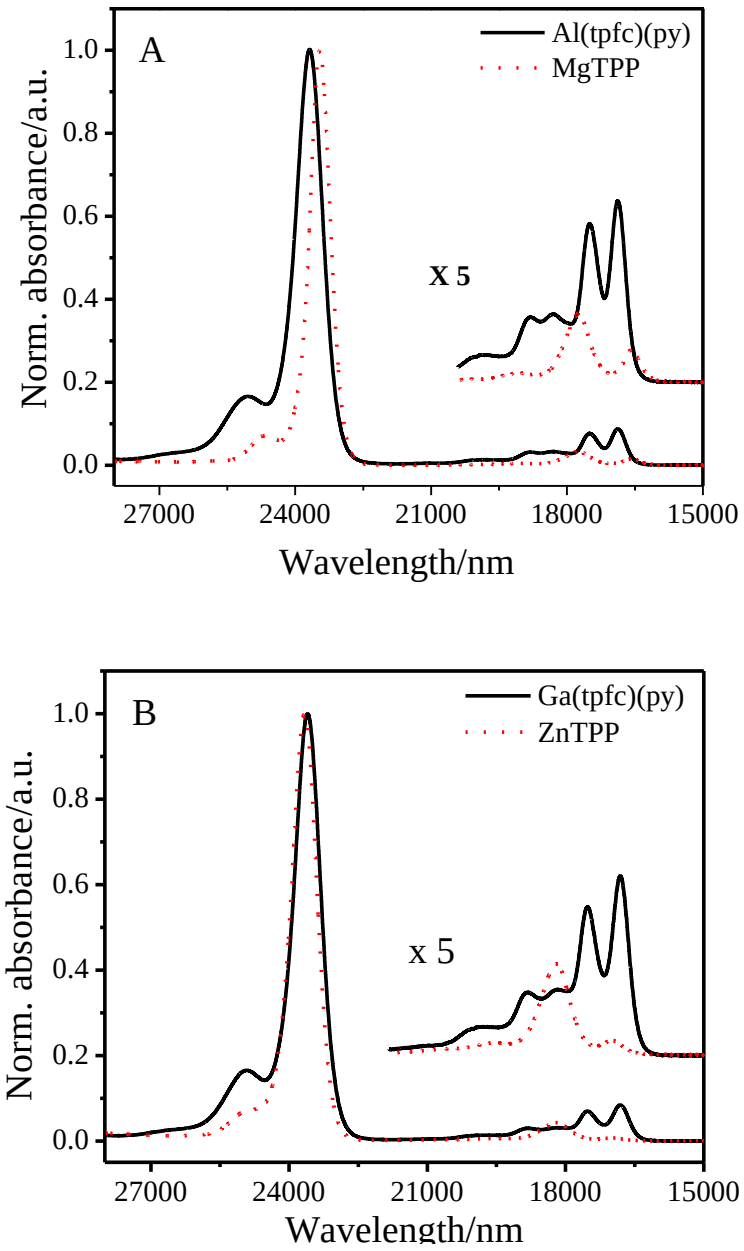

Fig. 6.1 Absorption spectra of (A) Al(tpfc)(py) compared with MgTPP and (B) Ga(tpfc)(py) compared with ZnTPP, all in benzene. In each pair of spectra the intensities have been normalized to the maxima of the Soret bands.

the relative Soret band intensities, B(1,0)/B(0,0), are higher in the corroles compared to those of MgTPP or ZnTPP.

Both Al(tpfc)(py) and Ga(tpfc)(py) show more vibronic structure in the Q region compared to MgTPP and ZnTPP. The progression of four vibrational bands observed in the $S_1 - S_0$ absorption of H_2TPP was ascribed to the lower molecular symmetry compared to D_{4h} of its metallated derivatives.[23] The Al(tpfc)(py) and Gal(tpfc)(py) do have

lower molecular symmetry because of the contracted macrocycle and pyridine ligation with the central metal ion. However, the relative intensities of the five vibrational bands progression observed in the corroles suggest that the interpretation used for H_2TPP should not be applied to the metallated corroles. Nevertheless, the vibronic features of the Q bands of the two metallated corroles do indicate the extent of the displacement between two potential energy surfaces of the S_1 state and the ground state. In addition, the Q band of Ga(tpfc)(py) is shifted to the red compared to that of ZnTPP. Comparison of the relative intensities of the Q bands for each pair shows that the ratio of the intensities of the Soret band to that of the Q band is much lower in both corroles than in MgTPP and ZnTPP.

Table 6.1 Spectroscopic parameters obtained from the absorption and emission spectra the corroles Al(tpfc)(py) and Gal(tpfc)(py) together with that of MgTPP and ZnTPP in benzene solution at room temperature*.

Compound	$\bar{\nu}_{max}(S_2)$ /cm^{-1} (ε_{max}/ M^{-1}cm^{-1})	$\bar{\nu}_{max}(S_1)$/cm^{-1} (ε_{max}/ M^{-1}cm^{-1})	$f(S_2)/f(S_1)^{\#}$	$SS^{@}(S_2)$/cm^{-1}	$SS^{@}(S_1)$ /cm^{-1}	$\phi_f(S_1)$	$\phi_f(S_2)$
MgTPP	23350 (5.5×10^5)	16470 (1.9×10^4)	29	164	163	0.12	2.3×10^{-3}
Al(tpfc)(py)	23515 (2.9×10^5)	16779 (2.4×10^4)	8.0	170	110	0.40^{+}	1.7×10^{-4}
ZnTPP	23560 (5.87×10^5)	18198 (2.54×10^4)	16.2	167	246	0.033	1.14×10^{-3}
Gal(tpfc)(py)	23487 (4.4×10^5)	16695 (3.7×10^4)	7.3	110(?)	125	0.76^{+}	1.1×10^{-4}

* All energies in cm^{-1}; subject to errors of ± 10 cm^{-1}. Values of ε_{max} in L mol^{-1} cm^{-1} in parentheses. Values for MgTPP from reference 74. [74]

Ratio of oscillator strengths.

@ Stokes shifts in cm^{-1}, subject to errors of ± 20 cm^{-1}. The value for the $S_2 - S_0$ Stokes shift of Gal(tpfc)(py) is less certain due to a smaller S/N in its emission spectrum.

+ In degassed toluene + 5% pyridine, reference 174.[174].

The emission spectra of the two corroles were also carefully measured using dilute solutions to minimize inner filter effects. A representative pair of absorption and emission spectra of Al(tpfc)(py) in benzene is shown in Fig. 6.2. The absorption and $S_1 - S_0$ emission spectra of Al(tpfc)(py) and Ga(tpfc)(py) observed in the present work are

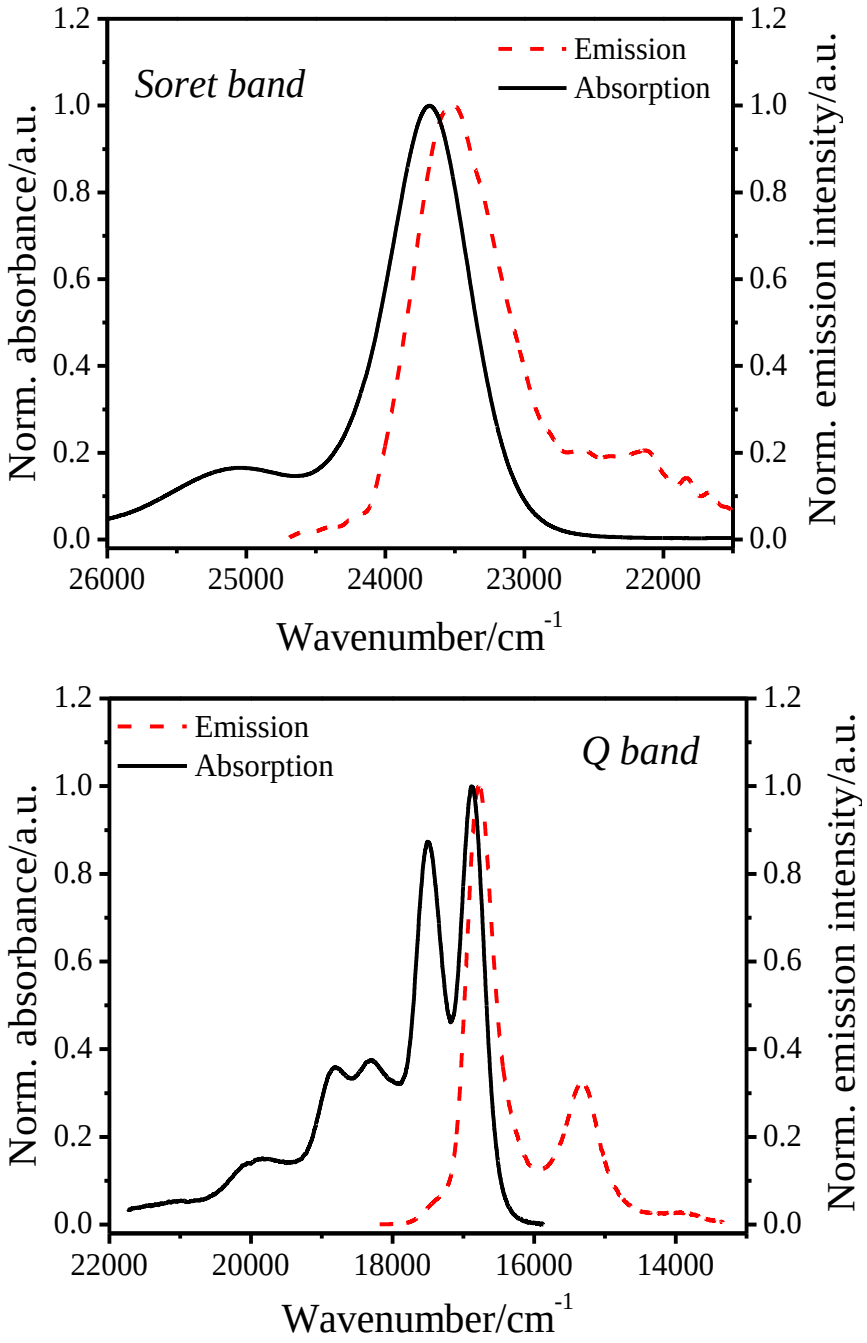

Fig. 6.2 Normalized absorption and the corresponding emission spectra of Al(tpfc)(py) in benzene.

similar to those described previously.[173,174] Only two vibronic bands accompany the "origin Q (0,0)" emission band of the corroles' $S_1 - S_0$ emission spectrum, whereas the "origin Q (0,0)" absorption band is accompanied by five vibronic bands to the blue in the Q bands of the absorption spectrum. Why a larger number of vibronic transitions are

observed in the emission spectrum remains an open question. However, the $S_2 - S_0$ emission obtained by exciting in their Soret bands has not been previously reported. The $S_2 - S_0$ emission spectrum is a reasonable mirror image of the corresponding absorption spectrum. A similar result was obtained for Ga(tpfc)(py) in benzene. The Soret bands of these emission spectra show that the strong B(0,0) band envelopes are accompanied by weaker B(0,1) vibronic band envelopes to the red similar to those previously observed in metalloporphyrins such as MgTPP and ZnTPP. However, the B(0,1) vibronic features are stronger in the Soret spectra of the corroles than in those of the metalloporphyrins, consistent with what is observed in the corresponding absorption spectra.

The effect of pyridine ligation on the absorption and Soret emission spectra of Al(tpfc)(py) was also examined. The spectra observed in pure benzene and benzene containing 5% pyridine are shown in Fig. 6.3. A comparison of these two absorption spectra shows that the entire absorption spectrum obtained in benzene containing 5% pyridine is shifted to the red. For example, the normalized Soret band emission spectra shown in Fig. 6.3 exhibit that it is shifted from λ_{max} = 426 nm in benzene to 436 nm in benzene containing 5% pyridine. In addition, the relative intensities of the Soret bands compared with the Q bands and of the vibronic bands within the Q band spectrum are also different between two spectra obtained in pure benzene and in benzene with 5% pyridine.

The differences in the molecular structures of the metallated corroles when dissolved in a non-coordinating solvent such as toluene or benzene *vs.* coordinating solvents such as pyridine are revealed by comparing their x-ray structures.[173,174] The pure compounds that are obtained by crystallization from pyridine contain coordinated pyridine. The central metal atom is at least 5-coordinate with pyramidal symmetry and pyridine in an axial position. However in coordinating solvents the metal is 6-coordinate and the energies of both the Soret and Q transitions are lower compared to that of their 5-coordinate counterparts. These structures are consistent with the observations of the present work described previously. In addition, in both solvents the Soret band fluorescence is weak ($\phi_f < 2 \times 10^{-4}$), but due to the large oscillator strength of the $S_2 - S_0$ radiative transition, the emission spectrum is readily observable (with lower signal to noise

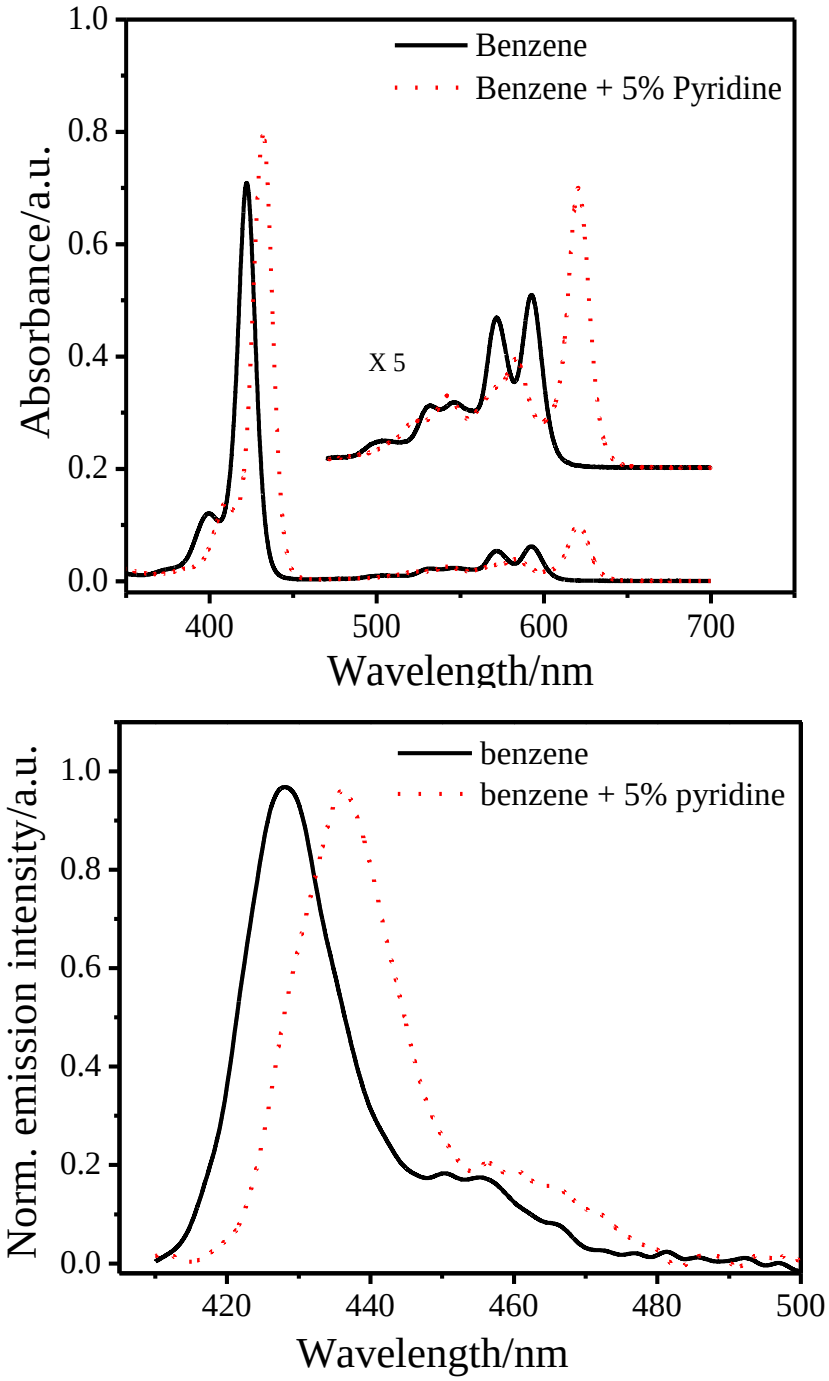

Fig. 6.3 Absorption and Soret emission spectra of Al(tpfc)(py) in benzene (5-coordinate) and benzene + 5% pyridine (6-coordinate). The emission spectra have been separately normalized to 1.00 at the band maxima.

ratio). Moreover, the Stokes shifts of both Al(tpfc)(py) and Gal(tpfc)(py) in the same solvent are similar to, or slightly smaller than those of the metalloporphyrins. The data

are summarized in Table 6.1. A similar Stokes shift was also obtained for Al(tpfc)(py) in either non-coordinating or coordinating solvents.

The quantum yields of $S_2 - S_0$ fluorescence of two corroles studied were measured relative to that of ZnTPP in ethanol ($\phi_f = 1.42 \times 10^{-3}$),[42] as described in Chapter 2. These results are also summarized in Table 6.1.

6.2.2 Dynamics experiments

The S_2 decay and S_1 rise fluorescence lifetimes were measured using the fluorescence upconversion system described in Chapter 2. Fig. 6.4 shows typical temporal S_2 decay and S_1 rise fluorescence profiles together with the best fits of the instrument response function convoluted with single exponential S_2 fluorescence decays to obtain the corresponding time constants. The temporal fluorescence profiles shown in Fig. 6.4 were recorded with an excitation wavelength of 400 nm, and the S_2 fluorescence was monitored at 433 nm, on the red side of the $S_2 - S_0$ emission spectrum. The observation wavelength was set at the maximum of the $S_1 - S_0$ emission, 626 nm, to monitor the S_1 fluorescence. The deconvolution of the temporal fluorescence upconversion profiles yielded S_2 population decay times of 0.52 ± 0.03 ps for Al(tpfc)(py) and 0.28 ± 0.03 ps for Ga(tpfc)(py), both measured in benzene, where the 5-coordinate species are predominant.

Since the S_2 fluorescence lifetimes are so short, if a considerable amount of vibrational energy is deposited in the molecule excitation, the $S_2 - S_0$ fluorescence spectra are expected to be time-dependent during the first hundreds of fs of excitation due to intramolecular vibrational redistribution (and intermolecular vibrational relaxation on a tens of ps time scale). However, in the present work, the molecule was excited at 400 nm, where only *ca.* 1350 cm^{-1} vibrational energy is deposited to the molecule, resulting in relatively small effects of intramolecular vibrational redistribution within the S_2 state. The differences in the S_2 decay times due to the variation of observation wavelengths spanning the $S_2 - S_0$ emission band are small and within the experimental error of the instrument. Attempting convolution using multiexponential decay functions also produced no significant improvement in fits and the resulting time constants at the time resolution employed in these experiments. The S_2 decay time constants and the S_2 fluo-

rescence quantum yields presented in Table 6.2 are used to calculate the radiative and non-radiative decay constants for the Soret excited S_2 states using eqs. 1.10 and 1.12 introduced in Chapter 1.

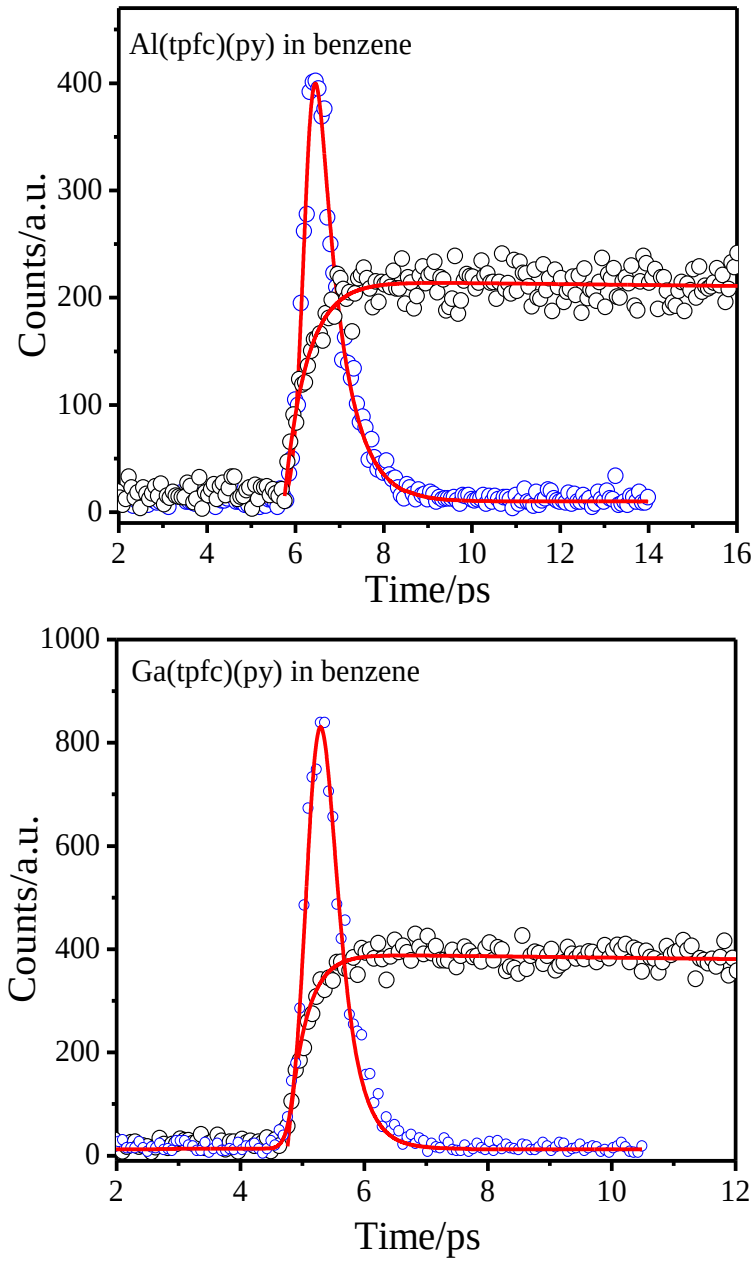

Fig. 6.4 S_2 fluorescence decay and S_1 fluorescence rise of Al(tpfc)(py) and Gal(tpfc)(py) in benzene. Excitation in the Soret band at 400 nm, with S_2 fluorescence monitored at 433 nm and S_1 fluorescence monitored at 626 nm. Convolution of the instrument response function with the exponential functions is described in the text. Data were taken in collaboration with Dr. U. Tripathy.

Table 6.2 S_2 fluorescence lifetimes, radiative and non-radiative decay constants for Al(tpfc)(py) and Ga(tpfc)(py) corroles comparing with MgTPP and ZnTPP metalloporphyrins in solutions at room temperature.

Compound	$\tau(S_2)$* (ps)	$\phi_f(S_2)$	$k_r(S_2)$ (s^{-1})	$k_{nr}(S_2)$ (s^{-1})	$\Delta E(S_2\text{-}S_1)$ (cm^{-1})
MgTPP	2.71± 0.07 (2.69)	2.5×10^{-3}	9.2×10^{8}	3.7×10^{11}	6880
Al(tpfc)(py)	0.52 ± 0.03 (0.51)	1.7×10^{-4}	$3._3 \times 10^{8}$	$1._9 \times 10^{12}$	6790
ZnTPP	1.49 ± 0.07 (1.41)	1.2×10^{-3}	8.0×10^{8}	6.71×10^{11}	6695
Ga(tpfc)(py)	0.28 ± 0.03 (0.28)	1.1×10^{-4}	$3._9 \times 10^{8}$	$3._6 \times 10^{12}$	6780

* Numbers in parentheses are S_1 rise times (see text). Data for MgTPP are taken from reference 74 .[74]

The deconvolution of the S_1 fluorescence upconversion rise profiles yielded time constants identical, within experimental error, to the decay times for S_2 fluorescence of both Al(tpfc)(py) and Ga(tpfc)(py). The identity of the S_2 decay and S_1 rise time constants indicates that $S_2 - S_1$ internal conversion occurs directly with no intervening additional decay processes.

To examine the potential presence of any S_2' or dark state lying close in energy to the S_2 state, and which might contribute to the fast S_2 relaxation in the metallated corroles, the efficiency of the $S_2 - S_1$ internal conversion was also measured. It has been found previously that, for six triaryl-substituted free-base corroles, the quantum yields of $S_1 - S_0$ fluorescence obtained by exciting in the Q bands is almost the same as that obtained when exciting in the Soret band.[172] This observation indicates that the quantum efficiency of $S_2 - S_1$ internal conversion of the free-base corroles is near unity. In the present work, the $S_2 - S_1$ internal conversion efficiencies of both Al(tpfc)(py) and Ga(tpfc)(py) were estimated by comparing their absorption and corrected fluorescence excitation spectra, as described in Chapter 5 for the metalloporphyrins. The Soret band emission excitation spectrum obtained by monitoring $S_1 \rightarrow S_0$fluorescence is identical to the corresponding Soret band absorption spectrum, and the Q band emission excita-

tion spectrum is identical to the Q band absorption spectrum. The identity of the emission excitation spectrum to the corresponding absorption spectrum indicates that no vibrational energy-dependent relaxation process is occurring.

However, when the corrected emission excitation spectrum over the entire range from the visible to the near uv regions is obtained by monitoring $S_1 \rightarrow S_0$ fluorescence and the Q band excitation spectrum is normalized to the Q band of the absorption spectrum, the Soret band excitation spectrum shows a slightly lower intensity (by *ca.* 10 to 20%) than that of the $S_2 - S_0$ absorption band. Similar results were obtained for Al(tpfc)(py) and Ga(tpfc)(py) and both of them are similar to those observed for the metalloporphyrins as discussed in Chapter 5. Thus, one can conclude that the quantum efficiency of $S_2 - S_1$ internal conversion lies in the 0.8 ~ 0.9 range in both Al(tpfc)(py) and Ga(tpfc)(py). Based on the above analysis and the fact that the S_2 decay and S_1 rise time constants of the metallated corroles are identical, one can conclude that no obvious evidence of the presence of either S_2' or other dark states was obtained.

The ground state structures of the corroles are better described as distorted pyramidal than square planar. Their $S_1 \leftarrow S_0$ absorption spectra show more extensive vibronic structure and have stronger "origin" band envelopes than the corresponding porphyrins, and their Q band emission spectra have fewer vibronic features and are not mirror images of the corresponding Q band absorption spectra. These observations imply that the vibrational levels of the S_1 state are likely different from those of the ground state, contrary to what is observed in most metalloporphyrins. In addition, the corroles have Soret vibronic (1,0) band envelopes that are rather more intense than those of the metalloporphyrins, which implies that the equilibrium coordinates of the atoms in the excited state are more displaced and the shape of the S_2 state potential energy surface is more distorted relative to that of the ground state.

The data presented in Table 6.2 and those previously reported in Table 5.2 demonstrate that the radiative $S_2 - S_0$ transition rate constants are smaller for these metallated corroles compared to those of the metalloporphyrins.[144] In addition, as previously discussed, the ratios of the relative intensities of the Q and B bands of absorption spectra of the metallated corroles are also larger than those found in the metalloporphyrins. The changes in the relative intensities of the Q and B bands in the absorption spectra of me-

talloporphyrins are attributed to changes in molecular symmetry.[177] In the two metallated corroles studied, the central metal ion is slightly out-of-plane because of the effects of axial ligation by the pyridine molecule. The contracted cavity is slightly domed and has a distorted pyramidal conformation. The symmetry of the macrocycle is reduced to C_{2v}, nominally, from D_{4h} in metallated porphyrin. As a consequence of this reduction of symmetry, the degeneracy of the e_g (in D_{4h}) unoccupied molecular orbitals is lifted in the metallated corroles. The net electric dipole transition moment for the $S_1 - S_0$ (Q band) transition in the corroles is therefore larger and that for the $S_2 - S_0$ (B, Soret band) transition is smaller, leading to a higher ratio of the intensities of the Q/B bands in the absorption spectra, relative to the metalloporphyrins.[177] As demonstrated by the data in Table 6.1, relatively larger $S_1 - S_0$ fluorescence and relatively smaller $S_2 - S_0$ fluorescence quantum yields are observed in the corroles compared with metalloporphyrins containing "nearby" metals and having similar electronic energy spacings (*e.g.* MgTPP *cf.* Al(tpfc)(py) or ZnTPP *cf.* Ga(tpfc)(py)). The data in Table 6.2 also show that the radiationless relaxation rates of the Soret-excited S_2 states of the corroles are higher than those of the Soret-excited metalloporphyrins. The shorter S_2 fluorescence lifetimes of the metallated corroles are due to larger nonradiative decay rates, which are about a factor of 5 (Al(tpfc)(py)) to 10 (Ga(tpfc)(py)) faster than that of MgTPP, as shown in Table 6.2.[74]

The spectroscopic data obtained in the present work suggest that the following characteristics are important in understanding the photophysics of the corroles. (1) The similar $\Delta E(S_2 - S_1)$ electronic energy gap in the two families of similarly-substituted tetrapyrroles would indicate that the number of vibrational modes acting as energy acceptor in the lower state of two couple electronic states (the macrocycle C–C and C–N stretches in the 1200 ~ 1600 cm^{-1} range), are similar to those of the metalloporphyrins when using the same excitation wavelength.[74] However, the more extensive vibronic features associated with the $S_1 \leftarrow S_0$ absorption suggest that a larger number of vibrations are Franck-Condon active in the S_1 state than the metalloporphyrins. (2) The tetrapyrrole framework in the metallated corroles is domed due to the pyridine ligand pulling the central metal slightly out of plane. This leads to distorted pyramidal (C_{2v}) mole-

cular symmetry, other than square planar found in metalloporphyrins with D_{4h} symmetry.

As discussed in Chapter 5, among the group of d^{10} or d^0 diamagnetic metalloporphyrins investigated in this thesis only in MgTPP the $S_2 - S_1$ internal conversion rate constants properly conform to the weak coupling case of radiationless transition theory. The S_2 fluorescence lifetime of ($\tau(S_2)$ = 2 to 4 ps in common solvents) is consistent with the predictions of the energy gap law in the weak coupling statistical limit[74] for the particular $\Delta E(S_2 - S_1)$ energy gaps obtained for MgTPP. However, the metalloporphyrins other than MgTPP exhibit $S_2 - S_1$ interstate couplings that are stronger than predicted by the weak coupling case of radiationless transition theory; CdTPP is in the intermediate range; ZnOEP exhibits the strongest $S_2 - S_1$ couplings among all the tetrapyrroles studied.[75] The data in Table 6.2 show that the $S_2 - S_1$ energy spacings of these two corroles are similar, and are also almost the same as that of MgTPP. Nevertheless, the corrole S_2 radiationless relaxation rates are distinctly larger than expected in the weak coupling case. Thus, the relaxation behavior of the Soret-excited S_2 states of metallated corroles cannot be interpreted in the basis of the energy gap law of radiationless transition theory in the weak coupling limit.

In fact, comparing the data in Table 6.2 to those of the metalloporphyrins in table 5.2, it is important to note that the S_2 radiationless rates of the metallated corroles are comparable with that of CdTPP. Thus the magnitude of the $S_2 - S_1$ coupling energies of the Al(tpfc)(py) and Ga(tpfc)(py) corroles would be expected to be similar to that of CdTPP and therefore to fall within the intermediate coupling range. In fact, energy gap law plots for both Al(tpfc)(py) and Ga(tpfc)(py) provide two data which lie close to the datum for CdTPP in the Fig. 5.11. Both strong and weak coupling models[15] predict that the rates of nonradiative excited state relaxation are proportional to β_{el}^2. By applying the same method used to estimate the values of β_{el}^2 of the metalloporphyrins the values of β_{el} of 167 cm^{-1} for Al(tpfc)(py) and 232 cm^{-1} for Ga(tpfc)(py) were obtained. Thus the interaction between the S_2 states and the S_1 state exceeds the weak coupling limit and is comparable to β_{el} = 205 $cm^{-1}$of CdTPP, falling within the intermediate coupling range.

In addition, it is interesting to note that for a given $S_2 - S_1$ electronic energy spacing of 6800 cm^{-1}, the ratios k_{nr}(Al(tpfc)(py)/k_{nr}(MgTPP) = 5 and k_{nr}(Ga(tpfc)(py)/k_{nr}(ZnTPP)

= 7 are just slightly different,[74] whereas k_{nr}(Ga(tpfc)(py)/k_{nr}(Al(tpfc)(py) = 1.9, about a factor of 2. Later difference (the approximate doubling of the radiationless transition rate of Ga(tpfc)(py) compared with Al(tpfc)(py)) might be ascribed to heavy-metal enhanced spin-orbit coupling of S_2 to the large number of triplet states that must lie at similar or lower energies, as predicted by calculations in Chapter 3 for the case of the metalloporphyrins. However, the fact that the quantum efficiencies of internal conversion for Al(tpfc)(py) and Ga(tpfc)(py) are both large ($\geq$ 0.8) and are of almost the same magnitude, provides no evidence of significant contributions to the S_2 decay from the $S_2 - T_n$ (n > 2) interstate crossing. Actually, as discussed in Chapter 5 for the limited series of metallated tetraphenylporphyrins MTPP (M = Mg, Zn, Cd), the effect of heavy metal-enhanced $S_2 - T_n$ (n > 2), intersystem crossing is small ($\eta_{isc} \leq 0.07$ for ZnTPP and $\leq$ 0.31 for CdTPP.[74] These observations thus indicate that metallation with Ga compared with Al has a similar effect on the radiationless decay rate of the triarylcorroles as does metallation of the tetraphenylporphyrin with Zn compared with Mg. As a conclusion for the metallated corroles, a dominant, very fast $S_2 - S_1$ decay path with near unit efficiency governs the relaxation of the S_2 states populated by exciting to the Soret bands, and the difference between Al(tpfc)(py) and Ga(tpfc)(py) cannot be due to the heavy-metal enhanced $S_2 - T_n$ intersystem crossing.

6.3 Conclusions

The relaxation dynamics of the Soret-excited singlet states of two metallated corroles, Al(tpfc)(py) and Ga(tpfc)(py) have been investigated by measuring both steady-state absorption and emission spectroscopy and temporal fluorescence intensity decay profiles. The Soret-excited S_2 states relax to the S_1 state on a sub-picosecond time scale and with a quantum efficiency in a range of 0.8 to 0.9, similar to that of ZnTPP. The identity of the rate constants of S_2 population decay to S_1 population rise indicates that the relaxation of the Soret-excited S_2 states of metallated corroles is also dominated by $S_2 - S_1$ internal conversion. The calculations presented in Chapter 3 show in the metalloporphyrins that some higher members of the triplet manifold or singlet states corresponding to those of gerade parity, which could be dark states, lie close in energy to the S_2 states.[178] The corroles are likely similar. Nevertheless, no evidence of either signifi-

cant heavy-atom induced $S_2 - T_n$ ($n > 2$) intersystem crossing or the participation of a dark state such as S_2' (if it exists) has been found in both corroles examined. The magnitudes of the radiative and nonradiative decay rate constants for the S_2 states of these corroles are consistent with smaller transition moments for $S_2 - S_0$ radiative decay and substantially increased $S_2 - S_1$ radiationless transition rates compared with similar metalloporphyrins. Similar to those metalloporphyrins other than MgTPP presented in Chapter 5, the magnitude of the decay rates of $S_2 - S_1$ internal conversion are also strongly influenced by direct interaction of the coupled S_2 and S_1 states. The values of the $S_2 - S_1$ interstate electronic coupling energies fall within the intermediate coupling range for both corroles investigated.

Chapter 7: Conclusions and Suggestions for Future Work

7.1 Conclusions

The photophysics of the highly excited electronic states of a wide set of d^0 and d^{10} metallated tetrapyrroles have been investigated both theoretically and experimentally. Theoretically, the ground state geometries, vibrational frequencies, electronic structures and excited states energies of a set of 10 metalloporphyrins have been calculated using DFT and TDDFT methods. The calculation results have proved to be sufficiently reliable to aid in the interpretation of experimental data presented in this thesis. Experimentally, steady-state absorption and emission spectra and time-resolved fluorescence decay profiles have been measured. A set of two porphyrinoid corroles and twelve tetrapyrrole compounds of the porphyrin family and having different peripheral substituents and central metal atoms, macrocycle substitution patterns and macrocycle conformations have been selected to explore the potential structure-property relationships governing the photophysics of their Soret-excited electronic states.

The calculations show that substitutions on the porphyrin macrocycle do not significantly change the ground state geometry. However, they do affect the electronic structures by altering the energies and orders of the frontier molecular orbitals and the energy and the rank in energy of the excited states in the metalloporphyrins studied. The calculations indicate that the energy gap $\Delta E(2^1E_u - 1^1E_u)$ between the first and second excited singlet states, (the observable $\Delta E(S_2 - S_1)$ energy gap) is very similar among all the metalloporphyrins studied, with the largest gap found in ZnTBP and the smallest in ZnTPTBP. In addition, reduction of the molecular symmetry from D_{4h} in ZnTPP to D_{2h} in ZnDPP lifts the degeneracy of the E_g and E_u states in ZnTPP due to the static Jahn-Teller effect.

Contrary to a previous report that triplet states are not located between the S_2 and S_1 states in the metalloporphyrins,[57] a number of singlet and triplets electronic states are predicted by TDDFT calculations to lie either above or between the 2^1E_u and 1^1E_u states. No experimental evidence was obtained that these dark states, or specifically the S_2'

state predicted by Yu *et al.*[41] have a significant influence on the relaxation of the S_2 state. Calculations of ground state frequencies show that the number of in-plane skeletal C–C and C–N vibrations, and their average frequency are almost the same for all the metalloporphyrins examined. These vibrations were shown to be the major energy accepting vibrations in the $S_2 - S_1$ internal conversion process.

The solvatochromic effects on the spectroscopic and photophysical relaxation properties of the highly excited electronic states of some of the entire set of the metalloporphyrins studied in this thesis have been investigated by carefully measuring both steady-state absorption and emission spectra and temporal fluorescence intensity decay profiles in a set of solvents having a wide range of polarizabilities. The results show that, for a given metalloporphyrin, the Soret band maxima of both the absorption and emission spectra are shifted to the red, and are more sensitive than the Q band to the change of solvent polarizability. A linear correlation was obtained between the $S_2 - S_1$ energy gap, $\Delta E(S_2 - S_1)$, and the Lorenz-Lorentz solvent polarizability function, f_1, for MgTPP, ZnTPP and ZnTBP in this set of solvents. Extrapolation of the straight line plots to $f_1 = 0$ yields a value of the intercept that is perfectly matched to the value of $\Delta E(S_2 - S_1)$ of the isolated bare molecule obtained in a supersonic jet. The linear correlation thus indicates that the solvatochromic interactions between the metalloporphyrins and solvents, both polar and nonpolar, are governed by dispersive solvent-excited solute interactions, the magnitude of which is proportional to the solvent polarizability. The gradients of these plots of $\Delta E(S_2 - S_1)$ *vs.* f_1 are a linear function of the total number of π-electrons present in the conjugated macrocycle. Therefore, the $\Delta E(S_2 - S_1)$ of ZnTBP with 42 π-electron is more sensitive to the change of the solvent polarizability than are the 26 π-electron porphyrins. This linear relationship also indicates that the solvatochromic effects on the spectroscopic properties are due to the different polarizabilities of the S_2 and S_1 states of the metalloporphyrins.

The results of the fluorescence lifetime measurements of both the S_2 and S_1 states of the whole set of metalloporphyrins indicate that the S_2 lifetimes are more sensitive to a change of solvent polarizability than are the S_1 lifetimes. Plots of the logarithm of the sum nonradiative rate constants of the S_2 state versus the energy gap, $\Delta E(S_2 - S_1)$, shows a good linear correlation for ZnTPP in the set of solvents examined. Similar

energy gap law plots are also obtained for several of the compounds investigated in this thesis, however, except for MgTPP, they also exhibit different slopes than expected for weak coupling. Only the S_2 relaxation behavior of MgTPP can be properly explained by the energy gap law within the framework of the weak coupling, statistical limit case, but others of the entire set of tetrapyrroles investigated can not.

The effects of the nature of the peripheral substituents and central metal ions, the macrocycle substitution pattern and the macrocycle conformation on the relaxation rates of the highly excited electronic states of the tetrapyrroles were investigated. The following conclusions were drawn. (1) *β*-Alkyl substitutions enhance the $S_2 - S_1$ interstate coupling energy compared to *meso*-substitutions. In particular, *β*-octaalkyl metalloporphyrins exhibit strong $S_2 - S_1$ interstate coupling energy (β_{el} = 2000 cm^{-1}), resulting in ultrashort S_2 lifetimes that are comparable to macrocycle ring stretching frequencies. (2) Compared to ZnP and the effects of *β*-substitutions, the effects of *meso*-aryl substitutions are modest. They reduce both the $S_2 - S_1$ electronic energy gap and the $S_2 - S_1$ interstate coupling energy (β_{el} = 81 cm^{-1} for ZnTPP), resulting in a minor net effect on the nonradiative decay rate of the S_2 state. (3) The effects of *β*-alkyl together with *meso*-aryl substitutions lead to intermediate $S_2 - S_1$ interstate coupling energies. (4) Though non-planar tetrapyrroles exhibit relatively larger interstate coupling energies compared with their planar counterparts, the results for non-planar tetrapyrroles such as ZnTPP(F_{20}) and CdTPP show that effects of non-planarity itself may not account for the increased interstate coupling energies and the relatively larger $S_2 - S_1$ radiationless decay rates. (5) The effects of benzo-annulation leading to an extended macrocycle result in a slightly decreased $S_2 - S_1$ interstate coupling energy compared to that of ZnP. In addition, the polarizability of the excited state is proportional to the number of π electrons in the extended macrocycle, so that benzo-annulation of the four pyrrole rings increases the polarizability of the excited states and specifically stabilizes the S_1 state leading to a large $S_2 - S_1$ electronic energy spacing in ZnTBP.

The S_2 decay and S_1 rise time constants of ZnTPP are equal in all solvents examined and these experiments therefore provide no evidence of the presence of either dark or S_2' states that might participate in the S_2 radiationless decays. In addition, no evidence of significant heavy-atom induced $S_2 - T_n$ ($n > 2$) intersystem crossing or of a dark or

S_2' state was found in the corroles examined. Thus the only significant decay mechanism of the Soret-excited S_2 states of the tetrapyrroles is governed by nonradiative $S_2 - S_1$ internal conversion, which decays in parallel with the much slower $S_2 - S_0$ radiative decay.

The relaxation rates of the $S_2 - S_1$ internal conversion are controlled by two factors, magnitude of the Franck-Condon factor, F, and interstate electronic coupling energy, β_{el}. For MgTPP, which meets the requirements of the weak coupling, statistical limit the change in k_{nr} with ΔE is determined exclusively by the F, which varies exponentially with ΔE, as predicted by the energy gap law for the weak coupling, statistical limit case. Because of weakly coupled of the two potential energy surfaces of the S_2 and S_1 excited states, β_{el} has only minor effect on the nonradiative decay rates of the S_2 state. However, the metallated tetrapyrroles other than MgTPP investigated in this thesis, have larger nonradiative decay rates and falls above the weak coupling limit line, as shown in Fig. 5.11, at any given $\Delta E(S_2 - S_1)$. The calculated $S_2 - S_1$ interstate electronic coupling energies of these compounds fall within the intermediate to strong coupling range. The difference of k_{nr} relative to the weak coupling limit can be rationalized by the different magnitudes of the β_{el}, and the larger of this difference, the larger is β_{el}. Thus β_{el} is the major factor in determining the radiationless depopulation rate constants of the S_2 states in the metallated tetrapyrroles which has $S_2 - S_1$ interstate electronic coupling energy exceeding the weak coupling limit.

7.2 Suggestions for future work

The spectroscopic properties and time resolved dynamic measurements presented in this thesis provide indirect evidence regarding the value of the interactions between the S_2 and S_1 states of the tetrapyrroles. Theoretical calculations using methods such as CIS and CASSCF etc.[95] can optimize the molecular geometry and predict the potential energy landscape of the upper excited states. This information would provide direct evidence of the relative displacements of two coupled potential energy surfaces. In addition, if the geometry of the excited state can be optimized and compared to the ground state, such information could also provide evidence of the changes of the relative displacement of the potential energy surfaces of the two coupled excited states.

The experiments regarding the photophysics of the corroles presented in Chapter 6 provide the first evidence of the behavior of their S_2 states. In order to make the corroles water soluble, the corrole macrocycle has been substituted with hydrophilic groups. The structures of such compounds are shown in Chart 7.1. Initial reports show that compounds 1, 2 and 3 have quite different absorption spectra, when compared to those obtained for metalloporphyrins presented in this thesis. To understand the fundamental source of the changes in their spectroscopic properties, it will be worthwhile to conduct a systematic study of a set of corroles with different substituents. As presented in Chapter 6, the Soret-excited S_2 states of the two corroles studied are short-lived with lifetimes of 100s fs. The results of direct measurements of the S_2 lifetimes of a wider range of corroles using fluorescence upconversion methods would provide information on the relaxation dynamics of their excited states. Such information on the photophysical properties of their highly excited electronic states could establish structure-property

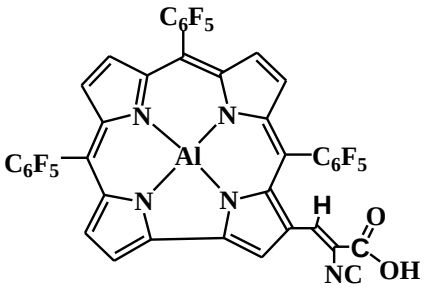

1 Al (tpfc) (CH=C(CN)(CO_2H))

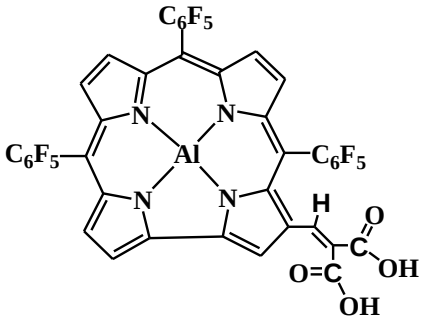

2 Al (tpfc) (CH=C(CO_2H)$_2$)

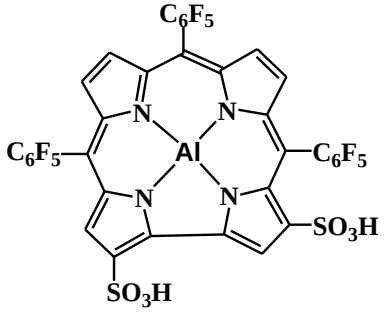

3 Al (tpfc)(SO_3H)$_2$

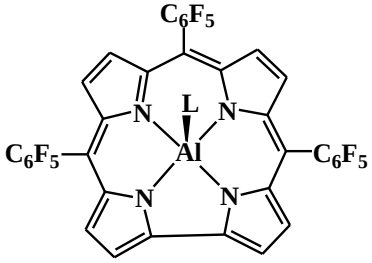

4 Al (tpfc)(py), L = py = Pyridine

Chart 7.1 Molecular structures and abbreviations of four metallated corroles.

relationships that would be valuable in improving their potential applications in many fields.[64] In particular the substituted corroles have broad absorptions in both the Soret and Q band regions. This characteristic makes them attractive for use as absorbers in dye-sensitized solar cells.[175]

The femtosecond fluorescence upconversion technique provides sufficient time resolution to permit the study of the relaxation dynamics of the ultrashort-lived Soret-excited S_2 states of the fluorescent tetrapyrroles. However, it cannot provide direct evidence of the behavior of non-fluorescence excited states. Femtosecond transient absorption spectroscopy can also provide time-resolution comparable to that of fluorescence upconversion. A striking advantage of this technique is that it can directly detect non-fluorescent excited electronic states both by measuring the transient absorption of molecules in their excited state and by measuring ground state depletion and population recovery. Since different excited states have their own unique absorption spectral features, measurement of excited state transient absorption spectra would provide valuable information of the fundamental parameters characterizing the identity and relaxation dynamics of the excited states of a much wider range of metalloporphyrins.[179] For example, using a transient absorption spectroscopy technique, Marcelli *et al.*[180] recently detected the presence of a charge transfer state and proved its participation in the relaxation dynamics of the S_2 state of the fully protonated free base porphyrin H_4P^{2+}.

Tobita *et al.*,[44] investigated the S_2 state of ZnTPP in EPA using a two-photon absorption techniques and found a large absorption cross section for the $^1A_{2g}$ (S_n) $\leftarrow$ 1^1E_u (S_1) transition. As presented in Chapter 3, TDDFT calculations predict that a number of states lie close in energy to the S_2 state. However, they are either non-fluorescent or are too short-lived to be observed by fluorescence upconversion measurements, since no evidence of their presence was obtained experimentally by analysis of the results presented in this thesis. These dark states could, in principle, be detected directly by transient absorption spectroscopy, especially those states with gerade symmetry such as $^1A_{1g}$ and $^1A_{2g}$ lying above the 1^1E_u (S_1) state, as predicted by TDDFT calculations.

In this thesis, to simplify discussion, the work focuses on the metalloporphyrins, where the central metal atom has closed shell d^0 or d^{10} electron configurations. A few reports available indicate that the dynamics of the highly excited states of those metal-

loporphyrins that possess open shell transition metal atoms, such as Ni, Fe, Ru, Co, Cu, are entirely different.[144,146] Upon excitation in their Soret bands of these transition metal porphyrins, the S_2 excited state decays rapidly to a coupled charge transfer (CT) state within 100 fs via a conical intersection of the two potential energy surfaces (PES) of the S_2 and CT states. The S_2 excited state of ZnOEP or other strong-medium coupled molecules investigated in this thesis also decays within 100s fs via internal conversion to the coupled S_1 excited state. Is there a conical intersection of two PESs of the S_2 and S_1 states promoting this ultrafast $S_2 - S_1$ internal conversion? It has been reported that the CASSCF computation method can predict the excitation energy for lower excited states and picture the PES of the excited state.[95] If the PESs of the S_2 and S_1 states in ZnOEP or other strong-to-medium coupling molecules can be sketched out, the shapes and positions of two PESs would provide direct and valuable information about whether the interstate electronic interaction (*e.g.* internal conversion) occurs via an avoided crossing minimum or a conical intersection. Such information would also provide direct proof of the extent of this interaction, whether it is strong or weak. Therefore, it would be worthwhile to conduct a detailed calculation using the CASSCF method to sketch out the PESs of the S_2 and S_1 excited states of ZnOEP and other strong-to-medium coupled molecules described in this thesis.

References

(1) K.K. Rohatgi-Mukherjee, *Fundamentals of photochemistry*, Wiley Inc.: New York, **1978**.

(2) G. Burdzinski, J. Kubicki, A. Maciejewski, R. P. Steer, S. Velate, E.K.L. Yeow. In *Organic photochemistry and photophysics*, V. Ramamurthy, K.S. Schanze, Eds., Marcel Dekker: New York, **2006**, Vol. 14.

(3) A. Maciejewski, R.P. Steer, *Chem. Rev.* **1993**, *93*, 67.

(4) Y. Kurabayashi, K. Kikuchi, H. Kokubun, Y. Kaizu, H. Kobayashi, *J. Phys. Chem.* **1984**, *88*, 1308.

(5) U. Even, J. Magen, J. Jortner, J. Friedman, *J. Chem. Phys.* **1982**, *77*, 4384.

(6) U. Even, Y. Magen, J. Jortner, H. Levanon, *J. Chem. Phys.* **1982**, *76*, 5684.

(7) F. Remacle, S. Speiser, R.D. Levine, *J. Phys. Chem. B* **2001**, *105*, 5589.

(8) E.K.L. Yeow, R.P. Steer, *Chem. Phys. Lett.* **2003**, *377*, 391.

(9) T. Hasobe, P.V. Kamat, M.A. Absalom, Y. Kashiwagi, J. Sly, M.J. Crossley, K. Hosomizu, H. Imahori, S. Fukuzumi, *J. Phys. Chem. B* **2004**, *108*, 12865.

(10) P.G. Van Patten, A.P. Shreve, J.S. Lindsey, R.J. Donohoe, *J. Phys. Chem. B* **1998**, *102*, 4209.

(11) S.A. Haque, E. Palomares, B.M. Cho, A.N.M. Green, N. Hirata, D.R. Klug, J.R. Durrant, *J. Am. Chem. Soc.* **2005**, *127*, 3456.

(12) T. Hasobe, H. Imahori, P.V. Kamat, S. Fukuzumi, *J. Am. Chem. Soc.* **2003**, *125*, 14962.

(13) N.J. Turro, *Modern molecular photochemistry*, The Benjamin/Cummings Publishing Company Inc.: California, **1978**.

(14) J.D. Graybeal, *Molecular spectroscopy*, McGraw-Hill Inc.: New York, **1988**.

(15) R. Englman, J. Jortner, *Mol. Phys.* **1970**, *18*, 145.

(16) K.F. Freed, *Acc. Chem. Res.* **1978**, *11*, 74.

(17) S.H. Lin, *Radiationless transitions*, Academic Press: New York, **1980**.

(18) S.P. McGlynn, T. Azumi, M. Kinoshita, *Molecular spectroscopy of the triplet state*, Prentice-Hall Inc.: New Jersey, **1969**.

(19) P. Atkins, R. Friedman, *Molecular quantum mechanics*, Fourth ed., University Press: Oxford, **2005**.

(20) J.R. Lakowicz, *Principles of fluorescence spectroscopy*, Second ed., Kluwer Academic/Plenum Publishers: New York, **1999**.

(21) B. Valeur, *Molecular fluorescence: principles and applications*, Wiley-VCH: Weinheim, **2002**.

(22) S.J. Strickler, R.A. Berg, *J. Chem. Phys.* **1962**, *37*, 814.

(23) D. Dolphin, *The porphyrins: physical chemistry, part A*, First Ed., Academic Press: London, **1978**, Vol. 3.

(24) M. Bixon, J. Jortner, *J. Chem. Phys.* **1968**, *48*, 715.

(25) W. Siebrand, *J. Chem. Phys.* **1967**, *46*, 440.

(26) B. Wagner, T. Tittelbach-Helmrich, R.P. Steer, *J. Phys. Chem.* **1992**, *96*, 7904.

(27) N. Tétreault, R.S. Muthyala, R.S.H. Liu, R.P. Steer, *J. Phys. Chem. A* **1999**, *103*, 2524.

(28) K.M. Kadish, K.M. Smith, R. Guilard, *The porphyrin handbook: applications: past, present, and future*, Second Ed., Academic Press: San Diego, **2000**, Vol. 6.

(29) K.M. Kadish, K.M. Smith, R. Guilard, *The porphyrin handbook: theoretical and physical characterization*, Second Ed., Academic Press: San Diego, **2000**, Vol. 7.

(30) C.A. Mirkin, M.A. Ratner, *Annu. Rev. Phys. Chem.* **1992**, *43*, 719.

(31) F. Ricchelli, S. Gobbo, *J. Photochem. Photobiol. B* **1995**, *29*, 65.

(32) U. Even, J. Magen, J. Jortner, J. Friedman, H. Levanon, *J. Chem. Phys.* **1982**, *77*, 4374.

(33) U. Even, J. Jortner, *J. Phys. Chem.* **1983**, *87*, 28.

(34) H. Chosrowjan, S. Taniguchi, T. Okada, S. Takagi, T. Arai, K. Tokuman, *Chem. Phys. Lett.* **1995**, *242*, 644.

(35) G.G. Gurzadyan, T.H. Tran-Thi, T. Gustavsson, *J. Chem. Phys.* **1998**, *108*, 385.

(36) G.G. Gurzadyan, T.H. Tran-Thi, T. Gustvsson, *Proc. SPIE-Int. Soc. Opt. Eng.* **2000**, *4060*, 96.

(37) N. Mataga, Y. Shibata, H. Chosrowjan, N. Yoshida, A. Osuka, *J. Phys. Chem. B* **2000**, *104*, 4001.

(38) Y. Shibata, H. Chosrowjan, N. Mataga, A. Osuka, *J. Lumin.* **2000**, *87-89*, 757.

(39) M. Enescu, K. Steenkeste, F. Tfibel, M.P. Fontaine-Aupart, *Phys. Chem. Chem. Phys.* **2002**, *4*, 6092.

(40) M.C. Yoon, D.H. Jeong, S. Cho, D. Kim, H. Rhee, T. Joo, *J. Chem. Phys.* **2003**, *118*, 164.

(41) H.Z. Yu, J.S. Baskin, A.H. Zewail, *J. Phys. Chem. A* **2002**, *106*, 9845.

(42) J. Karolczak, D. Kowalska, A. Lukaszewicz, A. Maciejewski, R.P. Steer, *J. Phys. Chem. A* **2004**, *108*, 4570.

(43) A. Lukaszewicz, J. Karolczak, D. Kowalska, A. Maciejewski, M. Ziolek, R.P. Steer, *Chem. Phys.* **2007**, *331*, 359.

(44) S. Tobita, Y. Kaizu, H. Kobayashi, I. Tanaka, *J. Chem. Phys.* **1984**, *81*, 2962.

(45) H. Sekino, H. Kobayashi, *J. Chem. Phys.* **1981**, *75*, 3477.

(46) E.J. Baerends, G. Ricciardi, A. Rosa, S.J.A. van Gisbergen, *Coord. Chem. Rev.* **2002**, *230*, 5.

(47) G.A. Peralta, M. Seth, T. Ziegler, *Inorg. Chem.* **2007**, *46*, 9111.

(48) K.A. Nguyen, P.N. Day, R. Pachter, S. Tretiak, V. Chernyak, S. Mukamel, *J. Phys. Chem. A* **2002**, *106*, 10285.

(49) K.A. Nguyen, R. Pachter, *J. Chem. Phys.* **2001**, *114*, 10757.

(50) A.B. Parusel, S. Grimme, *J. Porphyrins Phthalocyanines* **2001**, *5*, 225.

(51) H. Solheim, K. Ruud, S. Coriani, P. Norman, *J. Phys. Chem. A* **2008**, *112*, 9615.

(52) U. Even, J. Jortner, J. Friedman, *J. Phys. Chem.* **1982**, *86*, 2273.

(53) L. Bajema, M. Gouterman, C.B. Rose, *J. Mol. Spectrosc.* **1971**, *39*, 421.

(54) M.P. Tsvirko, G.F. Stelmakh, V. E. Pyatosin, K.N. Solovyov, T.F. Kachura, *Chem. Phys. Lett.* **1980**, *73*, 80.

(55) J.S. Baskin, H.Z. Yu, A.H. Zewail, *J. Phys. Chem. A* **2002**, *106*, 9837.

(56) Q. Zhong, Z. Wang, Y. Liu, Q. Zhu, F. Kong, *J. Chem. Phys.* **1996**, *105*, 5377.

(57) H. Kobayashi, Y. Kaizu. In *Porphyrins: excited states and dynamics*, M. Gouterman, P.M. Rentzepis, K.D. Straub, Eds., American Chemistry Society: Washington, **1986**, pp 105.

(58) O. Ohno, Y. Kaizu, H. Kobayashi, *J. Chem. Phys.* **1985**, *82*, 1779.

(59) D. LeGourriérec, M. Andersson, J. Davidsson, E. Mukhtar, L. Sun, L. Hammarstrom, *J. Phys. Chem. A* **1999**, *103*, 557.

(60) S. Akimoto, T. Yamazaki, I. Yamazaki, A. Osuka, *Chem. Phys. Lett.* **1999**, *309*, 177.

(61) N.C. Maiti, M. Ravikanth, *J. Photochem. Photobiol. A* **1996**, *101*, 7.

(62) I. Gupta, M. Ravikanth, *J. Photochem. Photobiol. A* **2006**, *177*, 156.

(63) K.M. Kadish, K.M. Smith, R. Guilard, *The porphyrin handbook: heteroporphyrins, expanded porphyrins and related macrocycles*, Academic Press: New York, **2000**, Vol. 2.

(64) I. Aviv, Z. Gross, *Chem. Commun.* **2007**, 1987.

(65) A. Maciejewski, A. Safarzadeh-Amiri, R.E. Verrall, R.P. Steer, *Chem. Phys.* **1984**, *87*, 295.

(66) H. Kobayashi, Y. Kaizu. In *Porphyrins: excited states and dynamics*, M. Gouterman, P.M. Rentzepis, K.D. Straub, Eds., American Chemical Society: Washington, **1986**, pp 105.

(67) D.E. Remy, *Tetrahedron Lett.* **1983**, *24*, 1451.

(68) P.T.I. (PTI). QuantaMaster™ UV VIS spectrofluorometer Vol. 2008.

(69) M. Kubista, R. Sjöback, S. Eriksson, B. Albinsson, *Analyst* **1994**, *119*, 417.

(70) B.C. MacDonald, S.J. Lvin, H. Patterson, *Anal. Chim. Acta* **1997**, *338*, 155.

(71) M.F. Nicol, *Applied spectroscopy reviews* **1974**, *8*, 183.

(72) D.V. O'Connor, D. Phillips, *Time correlated single photon counting*, Academic Press: London, **1984**.

(73) S. Velate, X. Liu, R.P. Steer, *Chem. Phys. Lett.* **2006**, *427*, 295.

(74) U. Tripathy, D. Kowalska, X. Liu, S. Velate, R.P. Steer, *J. Phys. Chem. A* **2008**, *112*, 5824.

(75) X. Liu, U. Tripathy, S.V. Bhosale, S.J. Langford, R.P. Steer, *J. Phys. Chem. A* **2008**, *112*, 8986.

(76) C. Lee, W. Yang, R.G. Parr, *Phys. Rev. B* **1988**, *37*, 785.

(77) A.D. Becke, *J. Chem. Phys.* **1993**, *98*, 5648.

(78) S.G. DiMagno, A.K. Wertsching, C.R. Ross, *J. Am. Chem. Soc.* **1995**, *117*, 8279.

(79) M.E. Casida, C. Jamorski, K.C. Casida, D.R. Salahub, *J. Chem. Phys.* **1998**, *108*, 4439.

(80) R. Bauernschmitt, R. Ahlrichs, *Chem. Phys. Lett.* **1996**, *256*, 454.

(81) Gaussian 03W; Version B. 05 ed.; M.J. Frisch, G.W. Trucks, H.B. Schlegel, G.E. Scuseria, M.A. Robb, J.R. Cheeseman, J.A. Montgomery, Jr.T. Vreven, K.N. Kudin,

J.C. Burant, J.M. Millam, S.S. Iyengar, J. Tomasi, V. Barone, B. Mennucci, M. Cossi, G. Scalmani, N. Rega, G.A. Petersson, H. Nakatsuji, M. Hada, M. Ehara, K. Toyota, R. Fukuda, J. Hasegawa, M. Ishida, T. Nakajima, Y. Honda, O. Kitao, H. Nakai, M. Klene, X. Li, J.E. Knox, H.P. Hratchian, J.B. Cross, C. Adamo, J. Jaramillo, R. Gomperts, R.E. Stratmann, O. Yazyev, A.J. Austin, R. Cammi, C. Pomelli, J.W. Ocheterski, P.Y. Ayala, K. Morokuma, G.A. Voth, P. Salvador, J.J. Dannenberg, V.G. Zakrzewski, S. Dapprich, A.D. Daniels, M.C. Strain, O. Farkas, D.K. Malick, A.D. Rabuck, K. Raghavachari, J.B. Foresman, J.V. Ortiz, Q. Cui, A.G. Baboul, S. Clifford, J. Cioslowski, B.B. Stefanov, G. Liu, A. Liashenko, P. Piskorz, I. Komaromi, R.L. Martin, D.J. Fox, T. Keith, M.A. Al-Laham, C.Y. Peng, A. Nanayakkara, M. Challacombe, P.M.W. Gill, B. Johnson, W. Chen, M.W. Wong, C. Gonzalez, J.A. Pople, Eds.; Gaussian Inc.: Pittsburgh PA, 2003.

(82) M.A.L. Marques, E.K.U. Gross, *Annu. Rev. Phys. Chem.* **2004**, *55*, 427.

(83) R.G. Parr, W. Yang, *Annu. Rev. Phys. Chem.* **1995**, *46*, 701.

(84) W. Koch, M.C. Holthausen, *A chemist's guide to density functional theory*, Wiley-VCH: Weinheim, **2000**.

(85) R.G. Parr, W. Yang, *Density functional theory of atoms and molecules*, Oxford University Press: New York, **1989**.

(86) W. Kohn, L.J. Sham, *Phys. Rev.* **1965**, *140*, A1133.

(87) P.J. Stephens, F.J. Devlin, C.F. Chabalowski, M.J. Frisch, *J. Phys. Chem.* **1994**, *98*, 11623.

(88) S. Grimme, M. Waletzke, *J. Chem. Phys.* **1999**, *111*, 5645.

(89) E. Runge, E.K.U. Gross, *Phys. Rev. Lett.* **1984**, *52*, 997.

(90) Y. Imamura, H. Nakai, *Chem. Phys. Lett.* **2006**, *419*, 297.

(91) M. van Faassen, K. Burke, *Chem. Phys. Lett.* **2006**, *431*, 410.

(92) R. van Leeuwen, E.J. Baerends, *Phys. Rev. A* **1994**, *49*, 2421.

(93) A. Dreuw, M. Head-Gordon, *Chem. Phys. Lett.* **2006**, *426*, 231.

(94) W. Hieringer, A. Görling, *Chem. Phys. Lett.* **2006**, *426*, 234.

(95) J.B. Foresman, Æ. Frisch, *Exploring chemistry with electronic structure methods*, Second ed., Gaussian Inc.: Pittsburgh, **1996**.

(96) A. Ghosh, *Acc. Chem. Res.* **1998**, *31*, 189.

(97) M. Gouterman, *J. Mol. Spectrosc.* **1961**, *6*, 138.

(98) C. Weiss, H. Kobayashi, M. Gouterman, *J. Mol. Spectrosc.* **1965**, *16*, 415.

(99) K.A. Nguyen, R. Pachter, *J. Chem. Phys.* **2001**, *114*, 10757.

(100) K.A. Nguyen, P.N. Day, R. Pachter, *J. Phys. Chem. A* **2000**, *104*, 4748.

(101) K.A. Nguyen, P.N. Day, R. Pachter, *J. Phys. Chem. A* **1999**, *103*, 9378.

(102) A.B.J. Parusel, T. Wondimagegn, A. Ghosh, *J. Am. Chem. Soc.* **2000**, *122*, 6371.

(103) M.-S. Liao, S. Scheiner, *J. Comput. Chem.* **2002**, *23*, 1391.

(104) T. Hashimoto, Y.K. Choe, H. Nakano, K. Hirao, *J. Phys. Chem. A* **1999**, *103*, 1894.

(105) K.A. Nguyen, R. Pachter, *J.Chem.Phys.* **2001**, *114*, 10757.

(106) V.A. Rassolov, M.A. Ratner, J.A. Pople, P.C. Redfern, L.A. Curtiss, *J. Comput. Chem.* **2001**, *22*, 976.

(107) V.A. Rassolov, J.A. Pople, M.A. Ratner, T.L. Windus, *J. Chem. Phys.* **1998**, *109*, 1223.

(108) A.K. Wertsching, A.S. Koch, S.G. DiMagno, *J. Am. Chem. Soc.* **2001**, *123*, 3932.

(109) W.R. Scheidt, J. U.Mondal, C.W. Eigenbrot, A. Alder, L.J. Radonovich, J.L. Hoard, *Inorg. Chem.* **1986**, *25*, 795.

(110) A. Hazell, *Acta Crystallographica Section C* **1986**, *42*, 296.

(111) E.R. Birnbaum, J.A. Hodge, M.W. Grinstaff, W.P. Schaefer, L. Henling, J.A. Labinger, J.E. Bercaw, H.B. Gray, *Inorg. Chem.* **1995**, *34*, 3625.

(112) P.F. Rodesiler, E.H. Griffith, P.D. Ellis, E.L. Amma, *J. Chem. Soc. Commun.* **1980**, 492.

(113) R.C. Weast, M.J. Astle, *CRC handbook of chemistry and physics*, 63rd ed. (1982-1983) ed., CRC Press: Boca Raton, **1983**.

(114) S.J. Yang, J. Seth, J.P. Strachan, S. Gentemann, D. Kim, D. Holten, J.S. Lindsey, D.F. Bocian, *J. Porphyrins Phthalocyanines* **1999**, *3*, 117.

(115) J.A. Shelnutt, V. Ortiz, *J. Phys. Chem.* **1985**, *89*, 4733.

(116) P.J. Spellane, M. Gouterman, A. Antipas, S. Kim, Y.C. Liu, *Inorg. Chem.* **1980**, *19*, 386.

(117) T. Kitagawa, Y. Ozaki, *Infrared and Raman spectra of mettaloporphyrins, structure and bonding*, Springer-Verlag Berlin Heidelberg, **1987**.

(118) J.M. Burke, J.R. Kincaid, T.G. Spiro, *J. Am. Chem. Soc.* **1978**, *100*, 6077.

(119) T.S. Rush, P.M. Kozlowski, C.A. Piffat, R. Kumble, M.Z. Zgierski, T.G. Spiro, *J. Phys. Chem. B* **2000**, *104*, 5020.

(120) L. Edwards, D.H. Dolphin, M. Gouterman, *J. Mol. Spectrosc.* **1970**, *35*, 90.

(121) J. Hasegawa, M. Hada, M. Nonoguchi, H. Nakatsuji, *Chem. Phys. Lett.* **1996**, *250*, 159.

(122) J.G. Radziszewski, J. Waluk, M. Nepraš, J. Michl, *J. Phys. Chem.* **1991**, *95*, 1963.

(123) O.E. Weigang, Jr, D.D. Wild, *J. Chem. Phys.* **1962**, *37*, 1180.

(124) C. Reichardt, *Solvents and solvent effects in organic chemistry*, Wiley-VCH: Weinheim, **2003**.

(125) Y. Zhou, E.H. Ryu, Y. Zhao, L.K. Woo, *Organometallics* **2007**, *26*, 358.

(126) M. Nappa, J.S. Valentine, *J. Am. Chem. Soc.* **1978**, *100*, 5075.

(127) C.N.R. Rao, S. Singh, V.P. Senthilnthan, *Chem. Soc. Rev.* **1976**, *5*, 297.

(128) E.G. Azenha, A.C. Serra, M. Pineiro, M.M. Pereira, J. Seixas de Melo, L.G. Arnaut, S.J. Formosinho, A.M.d.A. Rocha Gonsalves, *Chem. Phys.* **2002**, *280*, 177.

(129) S. Gentemann, N.Y. Nelson, L. Jaquinod, D.J. Nurco, S.H. Leung, C.J. Medforth, K.M. Smith, J. Fajer, D. Holten, *J. Phys. Chem. B* **1997**, *101*, 1247.

(130) S. Takagi, H. Inoue, *Molecular and superamolecular photochemistry*, Marcel Dekker: New York, **2000**, Vol. 5.

(131) W.M. Campbell, K.W. Jolley, P. Wagner, K. Wagner, P.J. Walsh, K.C. Gordon, L. Schmidt-Mende, M.K. Nazeeruddin, Q. Wang, M. Grätzel, D.L. Officer, *J. Phys. Chem. C* **2008**, *111*, 11760.

(132) R.P. Steer, *J. Appl. Phys.* **2007**, *102*, 076102.

(133) T.D.M. Bell, K.P. Ghiggino, A. Haynes, S.J. Langford, C.P. Woodward, *J. Porphyrins Phthalocyanines* **2007**, *11*, 455.

(134) M. Tanaka, S. Hayashi, S. Eu, T. Umeyama, Y. Matano, H. Imahori, *Chem. Comm.* **2007**, 2069.

(135) Q. Wang, W.M. Campbell, E.E. Bonfantani, K.W. Jolley, D.L. Officer, P.J. Walsh, K. Gordon, R. Humphry-Baker, M.K. Nazeeruddin, M. Grätzel, *J. Phys. Chem. B* **2005**, *109*, 15397.

(136) S. Mathai, T.A. Smith, K.P. Ghiggino, *Photochem. Photobiol. Sci.* **2007**, *6*, 995.

(137) E.S. Nyman, P.H. Hynninen, *J. Photochem. Photobiol. B* **2004**, *73*, 1.

(138) S.K. Pandey, A.L. Gryshuk, A. Graham, K. Ohkubo, S. Fukuzumi, M.P. Dobhal, G. Zeng, Z. Ou, R. Zhan, K.M. Kadish, A. Oseroff, S. Ranaprasad, R.K. Pandey, *Tetrahedron* **2003**, *59*, 10059.

(139) A. Gulino, S. Giuffrida, P. Mineo, M. Purrazzo, E. Scamporrino, G. Ventimiglia, M.E. van der Boom, I. Fragala, *J. Phys. Chem. B* **2006**, *111*, 16781.

(140) M.E. Köse, B.F. Carroll, K.S. Schanze, *Langmuir* **2005**, *21*, 9121.

(141) E. Pérez-Inestrosa, J.-M. Montenegro, D. Collado, R. Suau, J. Casado, *J. Phys. Chem. C* **2007**, *111*, 6904.

(142) F. Remacle, R. Weinkauf, R.D. Levine, *J. Phys. Chem. A* **2006**, *110*, 177.

(143) D. Dolphin, *The Porphyrins: Volume III Physical Chemistry, Part A*, First Ed., Academic Press Inc.: London, **1977**, Vol. III.

(144) U. Tripathy, R.P. Steer, *J. Porphyrins Phthalocyanines* **2007**, *11*, 228.

(145) X.J. Liu, Q.J. Pan, J. Meng, J.K. Feng, *J. Mol. Struct. (Theochem)* **2006**, *765*, 61.

(146) S. Sorgues, L. Poisson, K. Raffael, L. Krim, B. Soep, N. Shafizadeh, *J. Chem. Phys.* **2006**, *124*, 114302.

(147) P.D. Harvey, C. Stern, C.P. Gros, R. Guilard, *Coord. Chem. Rev.* **2007**, *251*, 401.

(148) F. Scandola, C. Chiorboli, A. Prodi, E. Iengo, E. Alessio, *Coord. Chem. Rev.* **2006**, *250*, 1471.

(149) K. Ogawa, K. Yoshiaki, *J. Photochem. Photobiol. C* **2006**, *7*, 1.

(150) M. Vacha, S. Machida, K. Horie, *J. Phys. Chem.* **1995**, *99*, 13163.

(151) H. Ryeng, A. Ghosh, *J. Am. Chem. Soc.* **2002**, *124*, 8099.

(152) W.R. Scheidt, M.E. Kastner, K. Hatano, *Inorg. Chem.* **1978**, *17*, 706.

(153) H.J. Jacobsen, P.D. Ellis, R.R. Inners, C.F. Jensen, *J. Am. Chem. Soc.* **1982**, *104*, 7442.

(154) R.J. Cheng, Y.R. Chen, E.R. Chuang, *Heterocycles* **1992**, *34*, 1.

(155) R.J. Cheng, Y.R. Chen, C.C. Chen, *Heterocycles* **1994**, *38*, 1465.

(156) P.D. Ellis, R.R. Inners, H.J. Jakobsen, *J. Phys. Chem.* **1982**, *86*, 1506.

(157) W.S. Wun, J.H. Chen, S.S. Wang, J.Y. Tung, F.L. Liao, S.L. Wang, L.P. Hwang, S. Elango, *Inorg. Chem. Comm.* **2004**, *7*, 1233.

(158) J. Aaviksoo, A. Freiberg, S. Savikhin, G.F. Stelmakh, M.P. Tsvirko, *Chem. Phys. Lett.* **1984**, *111*, 275.

(159) L. Edwards, M. Gouterman, C.B. Rose, *J. Am. Chem. Soc.* **1976**, *98*, 7638.

(160) P.E. Fielding, A.W.H. Mau, *Aust. J. Chem.* **1976**, *29*, 933.

(161) J. Aaviksoo, A. Freiberg, S. Savikhin, G.F. Stelmakh, M.P. Tsvirko, *Chem. Phys. Lett.* **1984**, *111*, 275.

(162) T.C. VanCott, M. Koralewski, D.H. Metcalf, P.N. Schatz, B.E. Williamson, *J. Phys. Chem.* **1993**, *97*, 7417.

(163) D.S. Berezin, O.V. Toldina, E.V. Kudrik, *Russ. J. Gen. Chem.* **2003**, *73*, 1309.

(164) J.E. Rogers, K.A. Nguyen, D.C. Hufnagle, D.G. McLean, W. Su, K.M. Gossett, A.R. Burke, S.A. Vinogradov, R. Pachter, P.A. Fleitz, *J. Phys. Chem. A* **2003**, *107*, 11331.

(165) I. Renge, *Chem. Phys. Lett.* **1991**, *185*, 231.

(166) W. Siebrand, *Chem. Phys. Lett.* **1971**, *9*, 157.

(167) G. Orlandi, W. Siebrand, *J. Chem. Phys.* **1973**, *58*, 4513.

(168) R.M. Hochstrasser, *Acc. Chem. Res.* **1968**, *1*, 266.

(169) Z. Gross, *J. Biol. Inorg. Chem.* **2001**, *6*, 733.

(170) R. Paolesse, F. Sagnore, A. Macagnano, T. Boschi, L. Prodi, M. Montalli, N. Zacchereni, F. Bolletta, K.M. Smith, *J. Porphyrins Phthalocyanines* **1999**, *3*, 364.

(171) T. Ding, E.A. Aleman, D.A. Modarelli, C.J. Zeigler, *J. Phys. Chem. A* **2005**, *109*, 7411.

(172) B. Ventura, A.D. Esposti, B. Koszarna, D.T. Gryko, L. Flamigni, *New J. Chem.* **2005**, *29*, 1557.

(173) J. Bendix, I.J. Dmochowski, H.B. Gray, A. Mahammad, L. Simkhovich, Z. Gross, *Angew. Chem. Int. Ed.* **2000**, *39*, 4048.

(174) A. Mahammad, Z. Gross, *J. Inorg. Biochem.* **2002**, *88*, 305.

(175) D. Walker, S. Chappel, A. Mahammed, J.J. Weaver, B.S. Brunschwig, J.R. Winkler, H.B. Gray, A. Zaban, Z. Gross, *J. Porphyrins Phthalocyanines* **2006**, *10*, 1259.

(176) J.J. Weaver, K. Sorasaenee, M. Sheikh, R. Goldschmidt, E. Tkachenko, Z. Gross, H.B. Gray, *J. Porphyrins Phthalocyanines* **2004**, *8*, 76.

(177) M. Gouterman, G.H Wagnière, L.C. Snyder, *J. Mol. Spectrosc.* **1963**, *11*, 108.

(178) O. Schalk, H. Brands, T.S. Balaban, A.-N. Unterreiner, *J. Phys. Chem. A* **2008**, *112*, 1719.

(179) K. Kalyanasundaram, *Photochemistry of polypyridine and porphyrin complexes*, Academic Press: London, **1992**.

(180) A. Marcelli, P. Foggi, L. Moroni, C. Gellini, P.R. Salvi, *J. Phys. Chem. A* **2008**, *112*, 1864.

(181) E.K.L. Yeow, R.P. Steer, *Phys. Chem. Chem. Phys.* **2003**, *5*, 97.

APPENDIX I

1. The steady-state absorption and corresponding emission spectra of metallated tetrapyrroles not shown in the text.

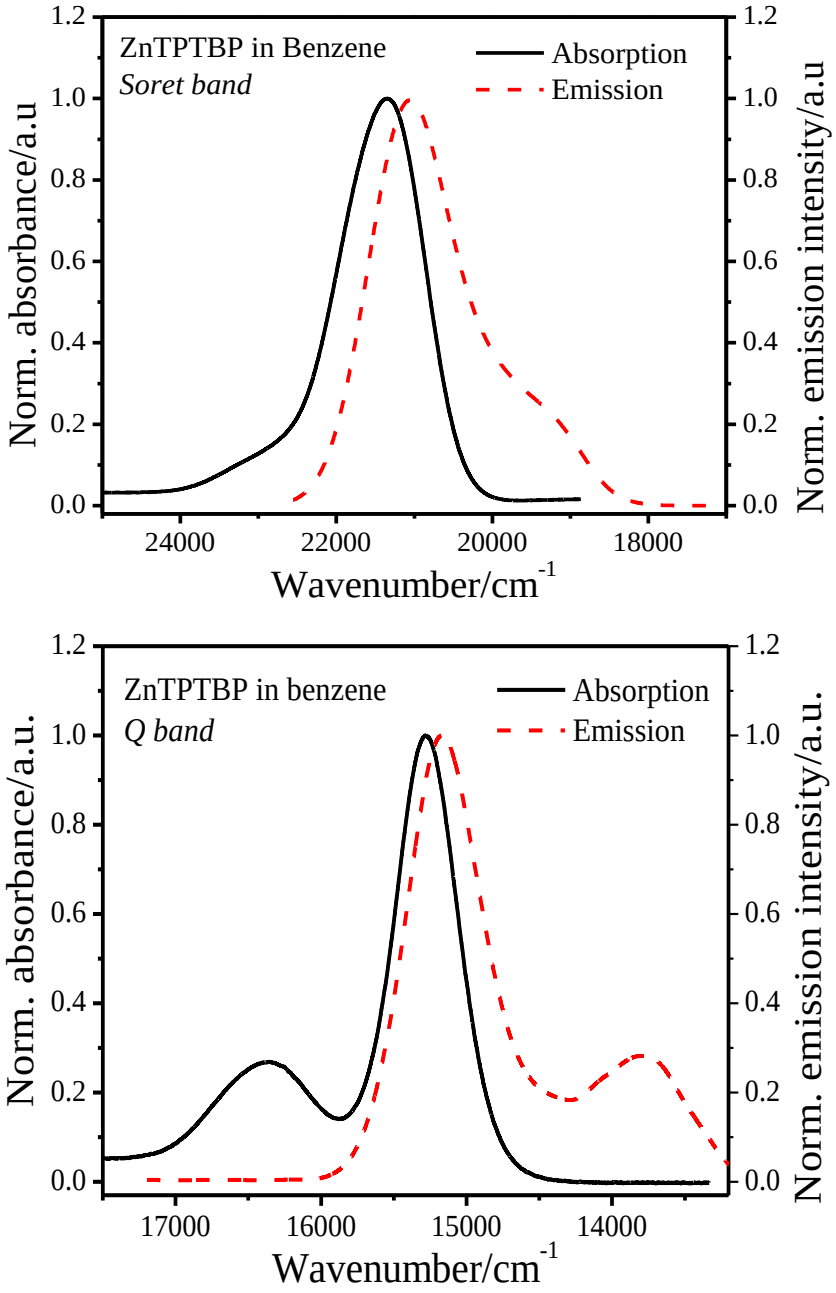

Fig. A.1 Normalized steady-state absorption and the emission spectra of ZnTPTBP obtained in benzene. The excitation wavelength is 400 nm.

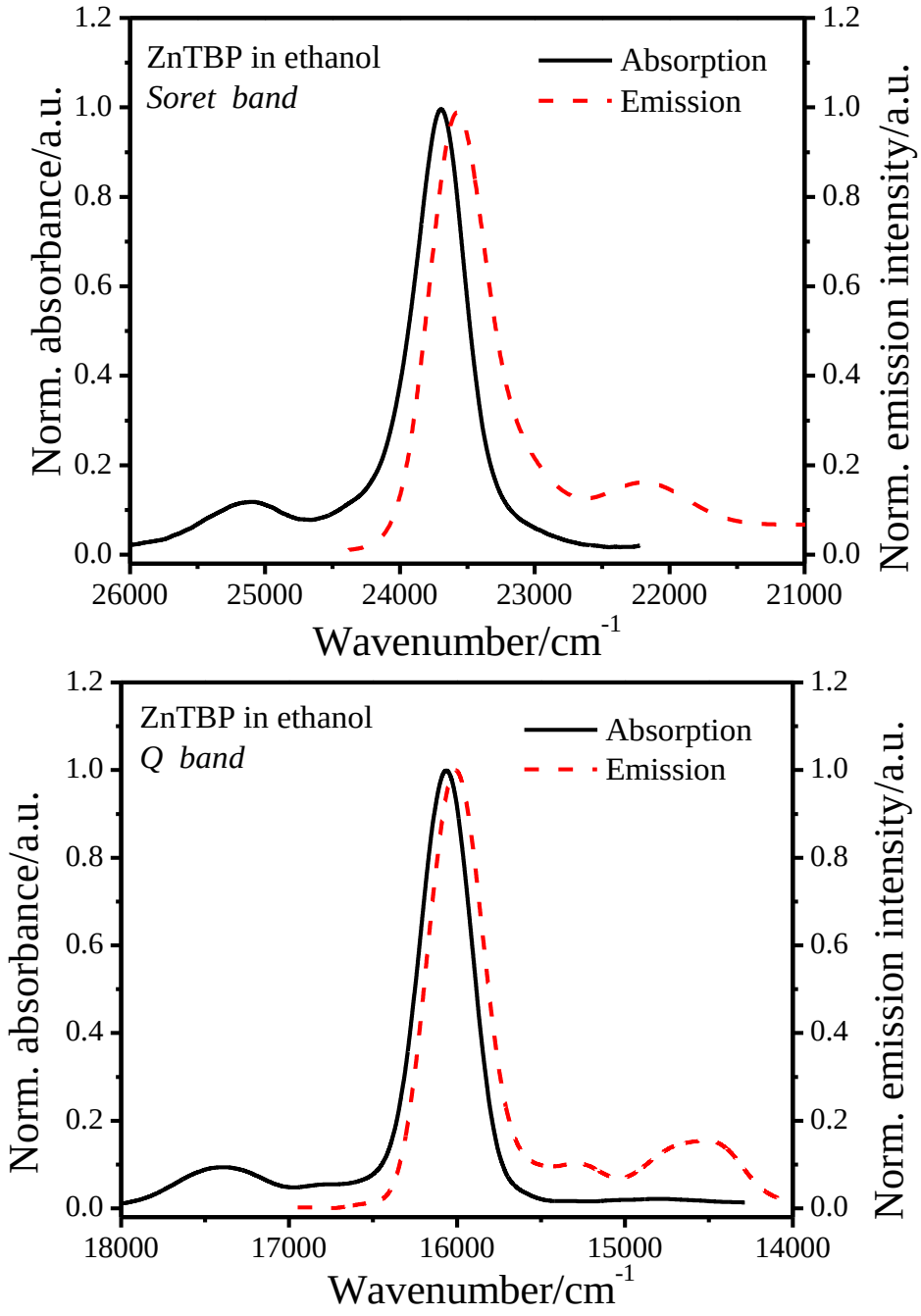

Fig. A.2 Normalized steady-state absorption and the emission spectra of ZnTBP obtained in ethanol. The excitation wavelength is 400 nm.

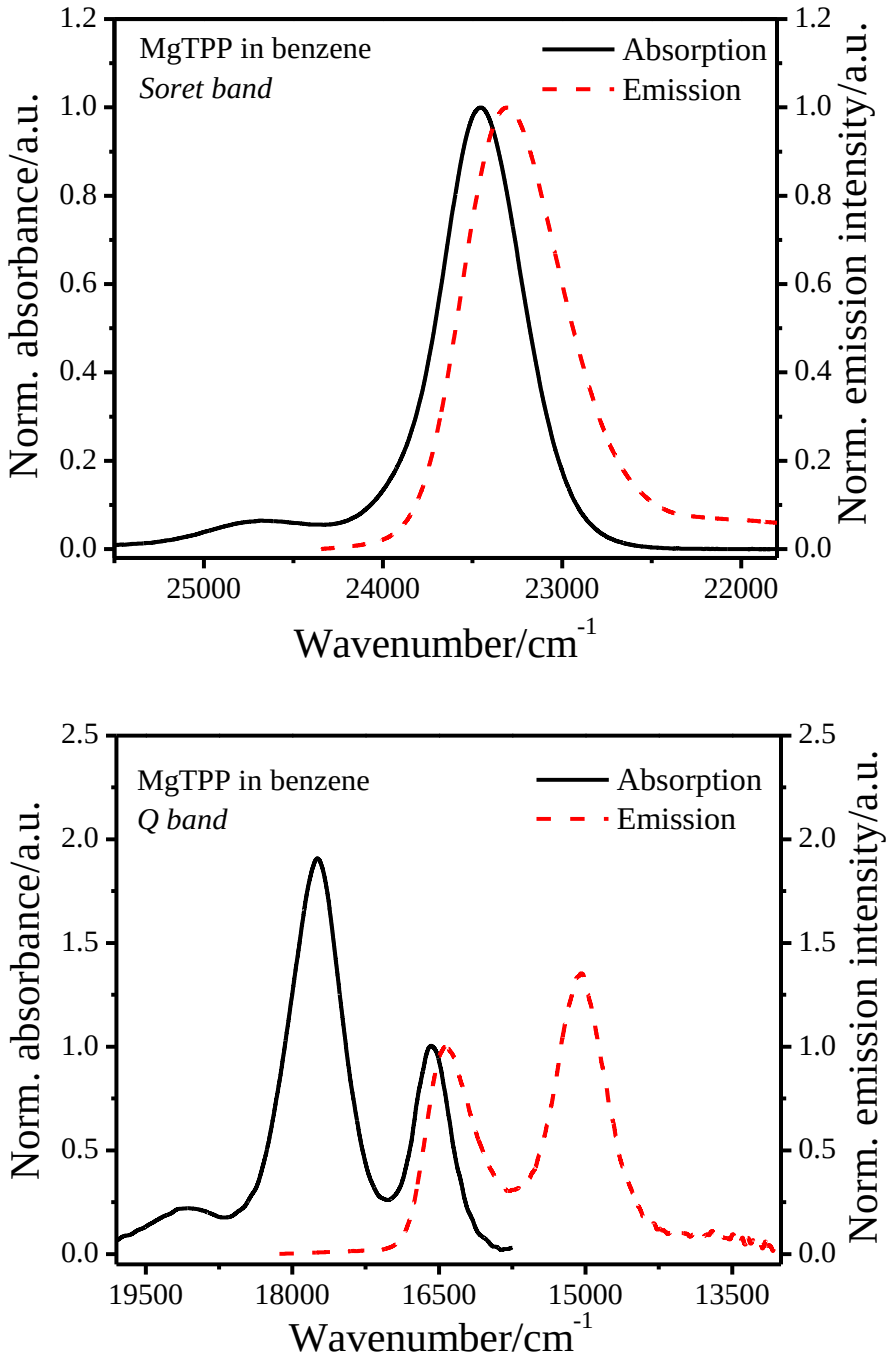

Fig. A.3 Normalized steady-state absorption and the emission spectra of MgTPP obtained in benzene. The excitation wavelength is 400 nm.

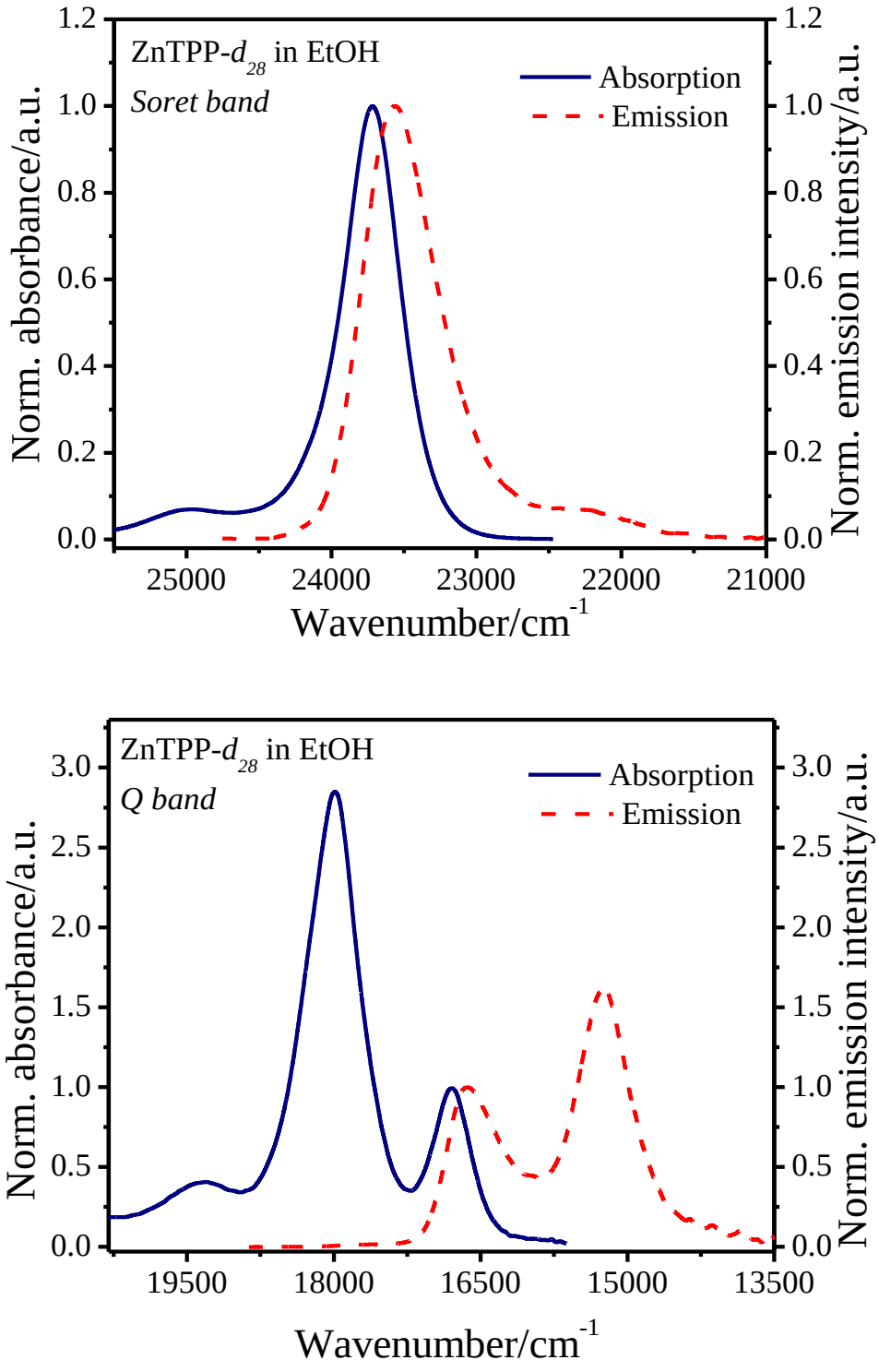

Fig. A.4 Normalized steady-state absorption and the emission spectra of ZnTPP-d_{28} obtained in ethanol. The excitation wavelength is 400 nm.

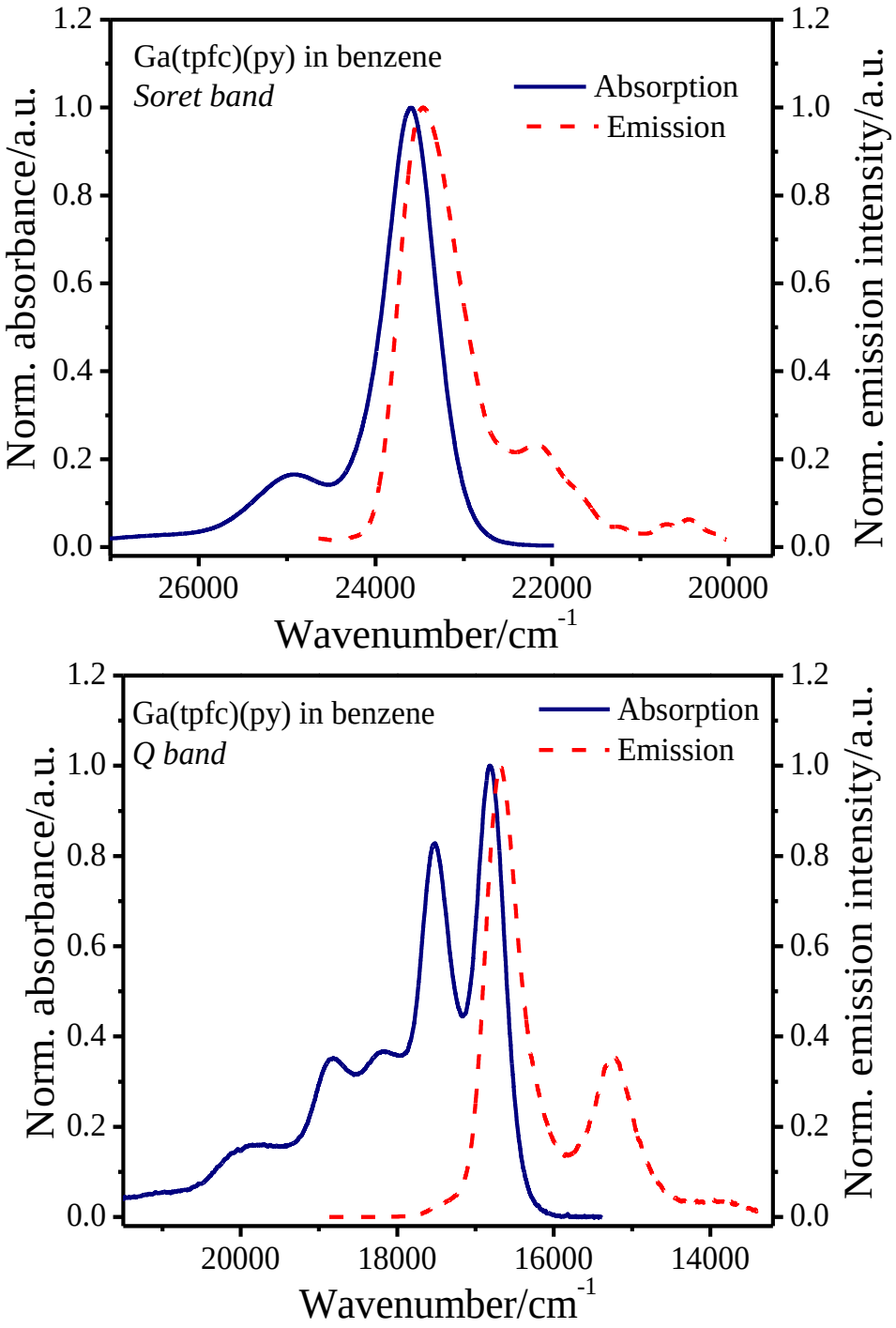

Fig. A.5 Normalized steady-state absorption and the emission spectra of Ga(tpfc)(py) obtained in benzene. The excitation wavelength is 400 nm.

2. Temporal fluorescence decay profiles of the S_1 state of those metallated tetrapyrroles not shown in the text.

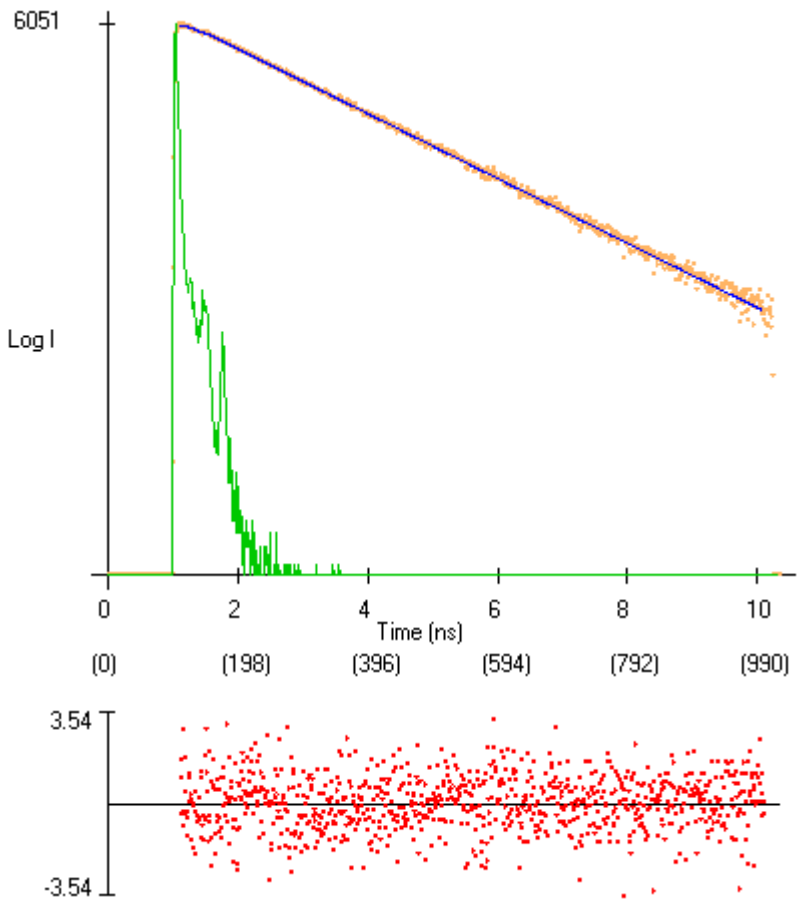

Fig. A.6 Fluorescence decay of ZnTPP in butanol modelled with the best single exponential fit. Excited at 495 nm and observed at 645 nm. τ = 1.95 ns and χ_r^2 = 1.08.

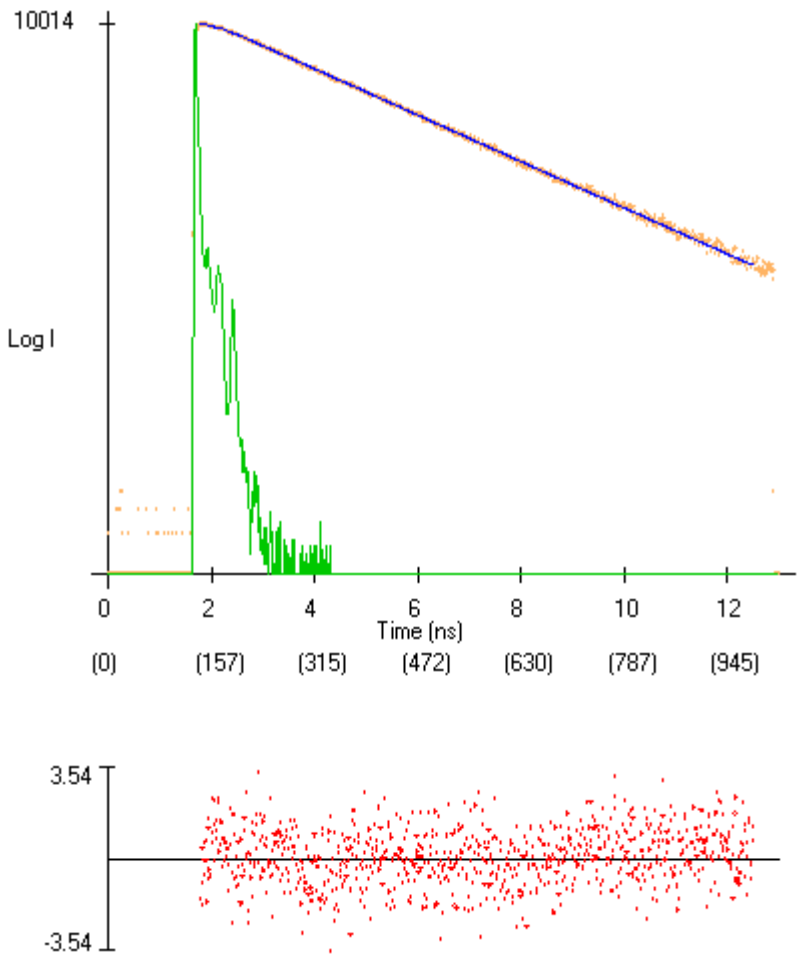

Fig. A.7 Fluorescence decay of ZnDPP in ethanol modelled with the best single exponential fit. Excited at 400 nm and observed at 640 nm. $\tau = 2.58$ ns and $\chi_r^2 = 1.13$.

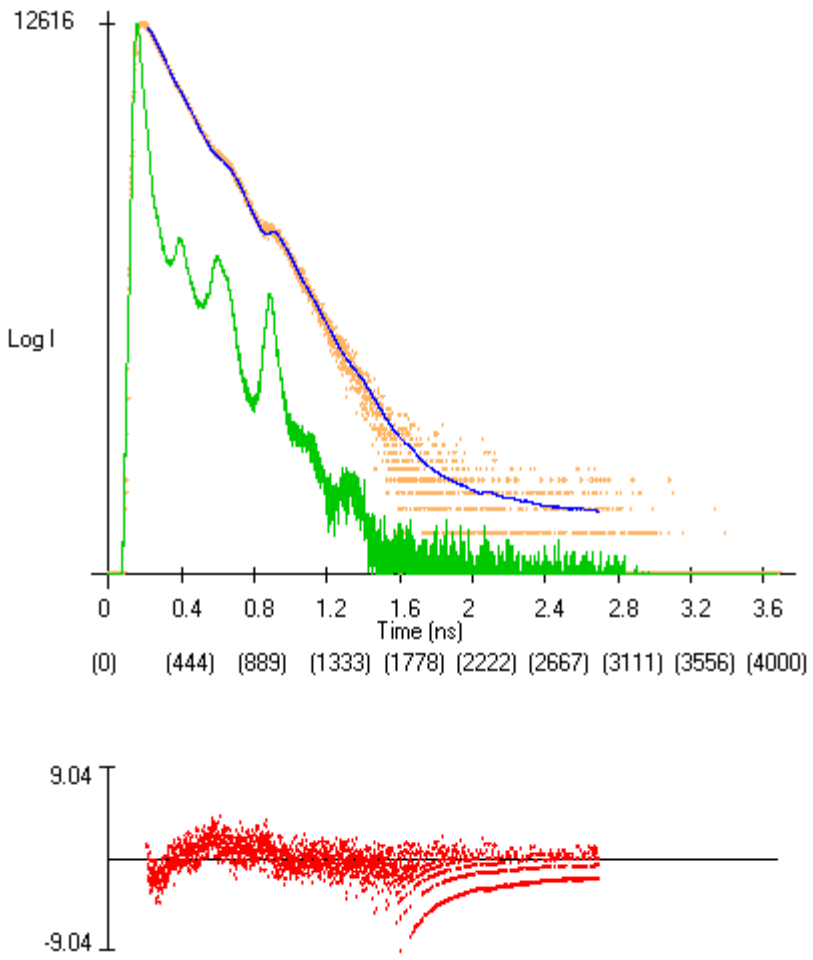

Fig. A.8 Fluorescence decay of CdTPP in ethanol modelled with the best single exponential fit. Excited at 430 nm and observed at 635 nm. $\tau = 130$ ps and $\chi_r^2 = 2.1$.

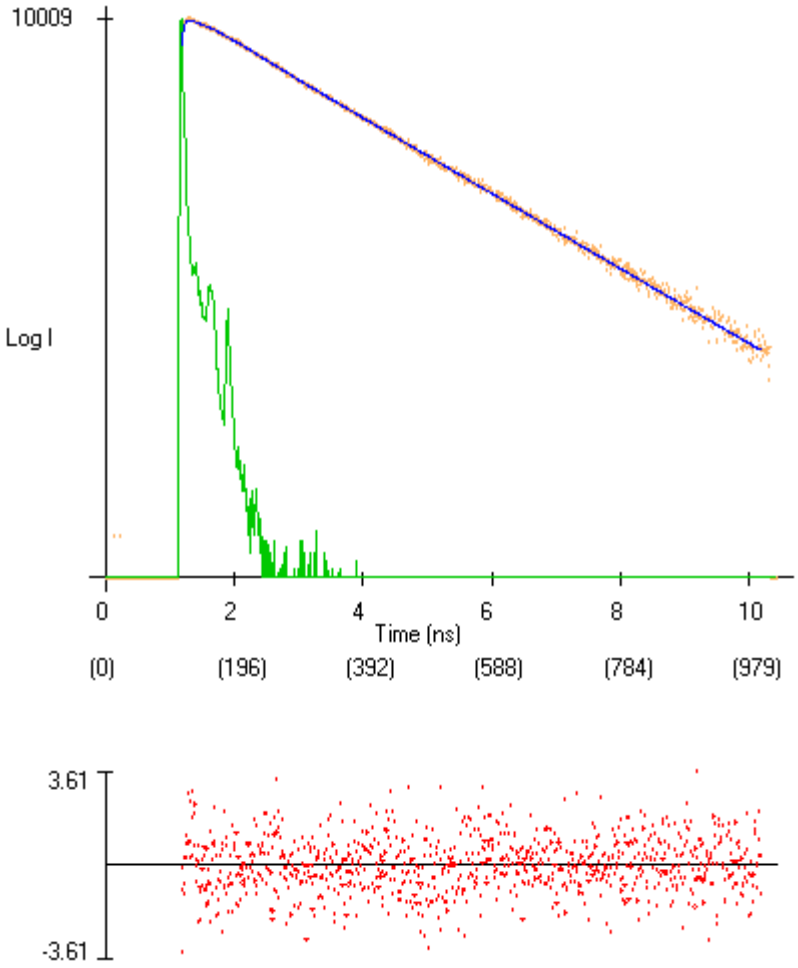

Fig. A.9 Fluorescence decay of ZnTPP(F_{20}) in ethanol modelled with the best single exponential fit. Excited at 495 nm and observed at 655 nm. τ = 1.61 ns and χ_r^2 = 1.12.

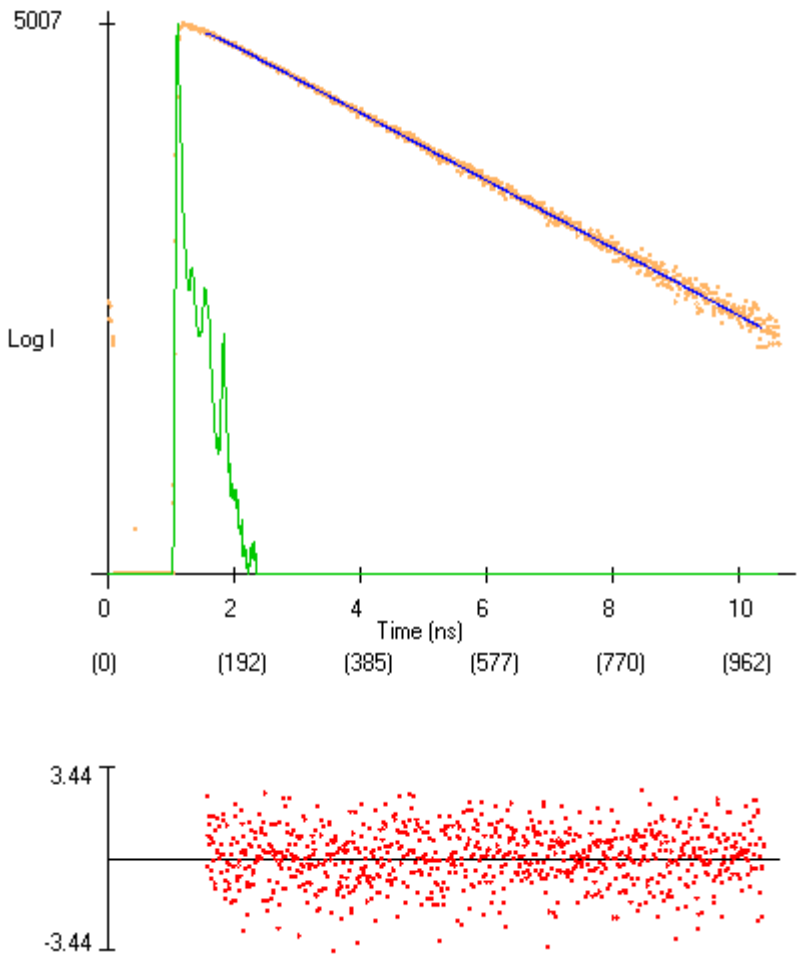

Fig. A.10 Fluorescence decay of ZnTBP in benzene modelled with the best single exponential fit. Excited at 400 nm and observed at 636 nm. $\tau = 1.91$ ns and $\chi_r^2 = 1.07$.

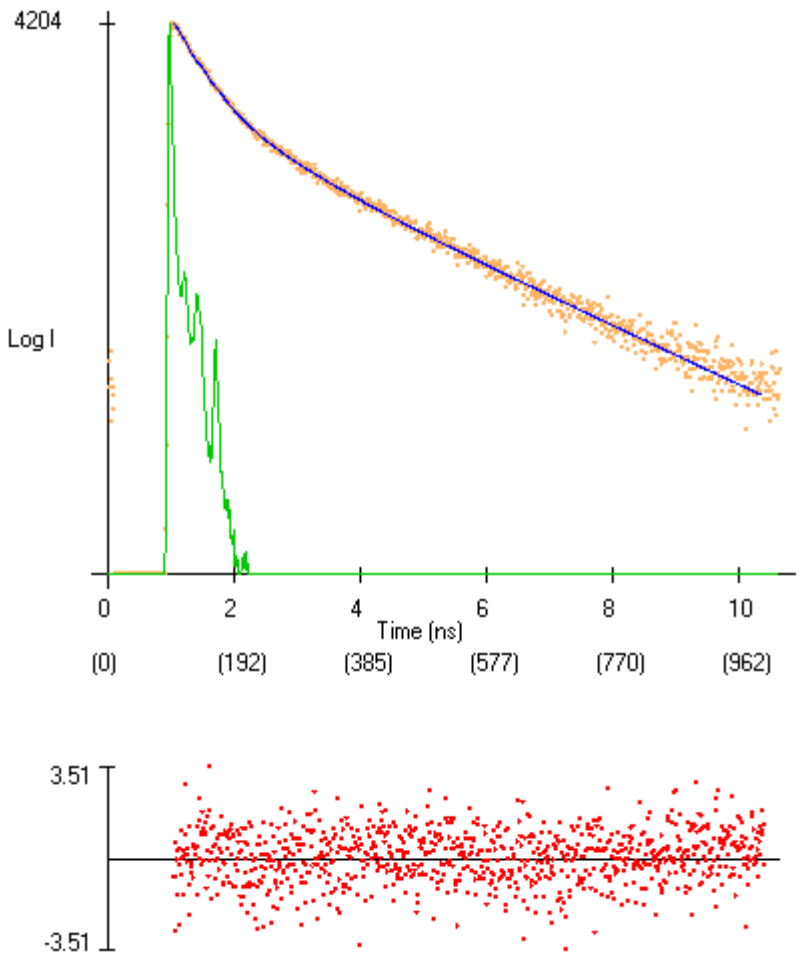

Fig. A.11 Fluorescence decays of ZnTPTBP in benzene modelled with the best multiple exponential fit. Excited at 400 nm and observed at 674 nm. $\chi_r^2 = 1.01$.

	a(n)	τ(n)/ps	F(n)
1	0.164	2235	0.52
2	0.150	862	0.18
3	0.271	385	0.15
4	0.415	251	0.15

Notes: a(n) is the coefficient of each lifetime species, τ(n) is the lifetime, F(n) is the weighted fraction of each lifetime.

3. **Temporal fluorescence decay profiles of the S_2 state of some of the set of the metallated tetrapyrroles not shown in the context**

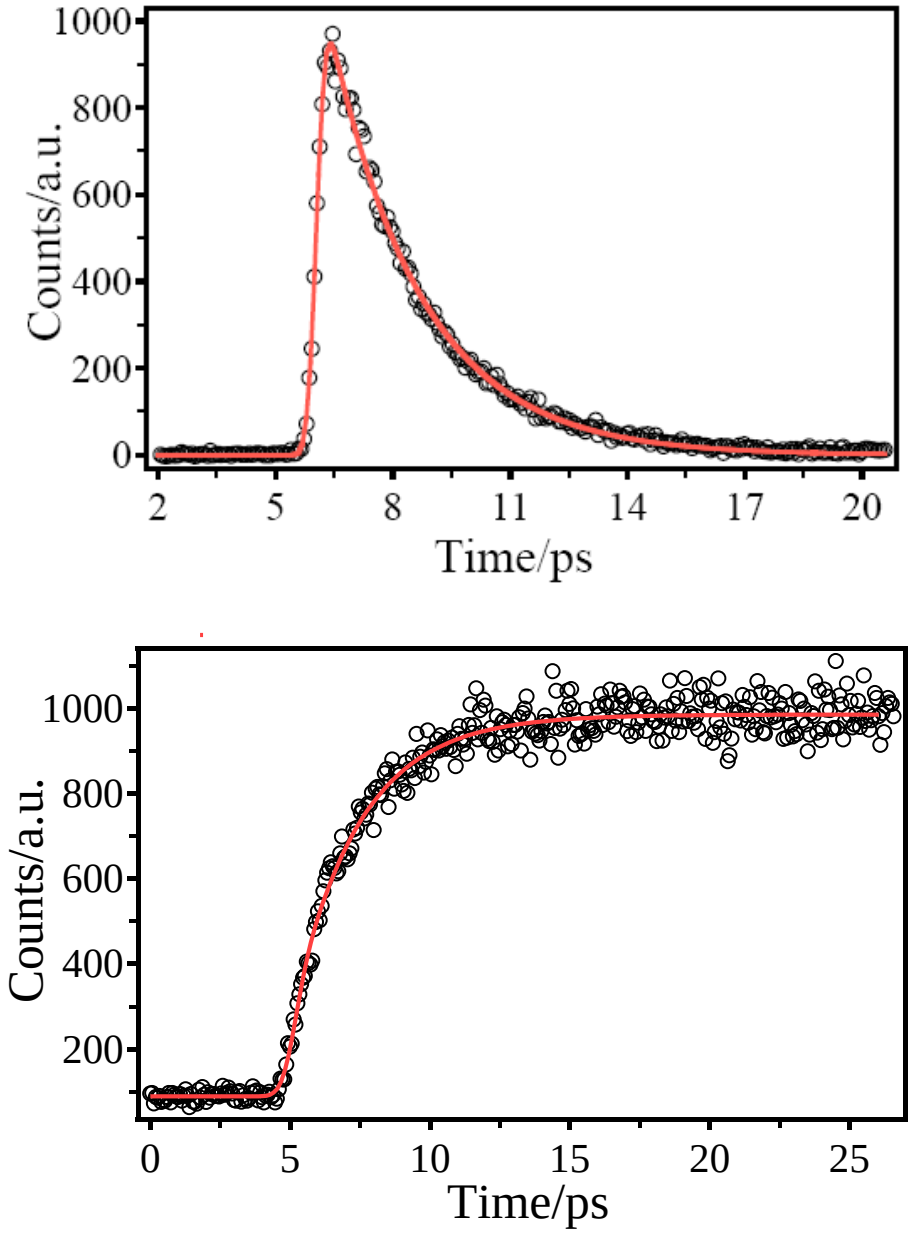

Fig. A.12 Temporal S_2 decay (top) and S_1 rise (bottom) profiles of ZnDPP in ethanol at room temperature. Measurements are at room temperature with λ_{ex} = 400 nm and central observation wavelength at 433 nm for S_2 decay and 641 nm for S_1 rise. The solid lines give the best fits of single exponential decay and rise functions to the measured data.

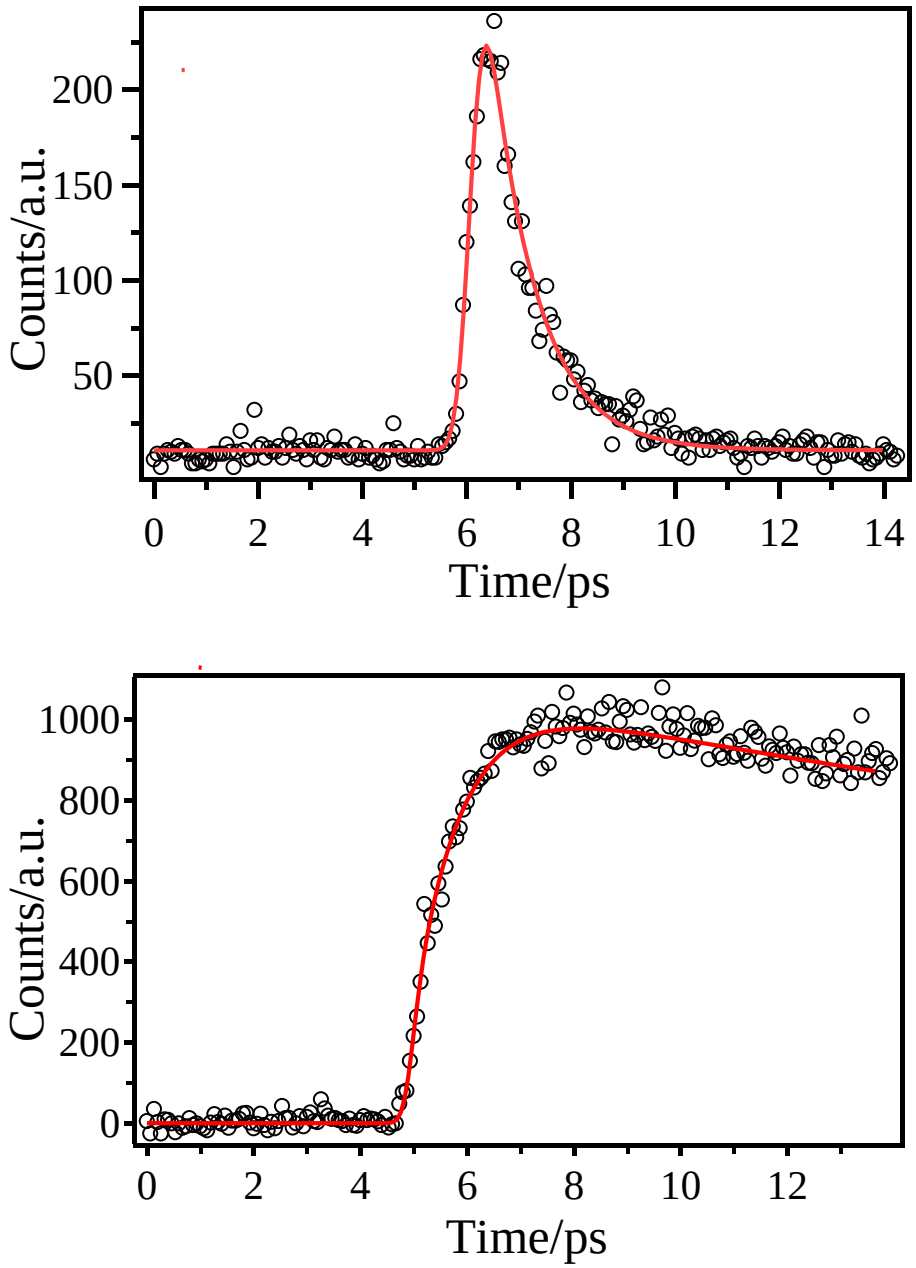

Fig. A.13 Temporal S_2 decay (top) and S_1 rise (bottom) profiles of ZnP in ethanol at room temperature. Measurements are at room temperature with λ_{ex} = 400 nm and central observation wavelength at 433 nm for S_2 decay and 635 nm for S_1 rise. The solid lines give the best fits of single exponential decay and rise functions to the measured data.

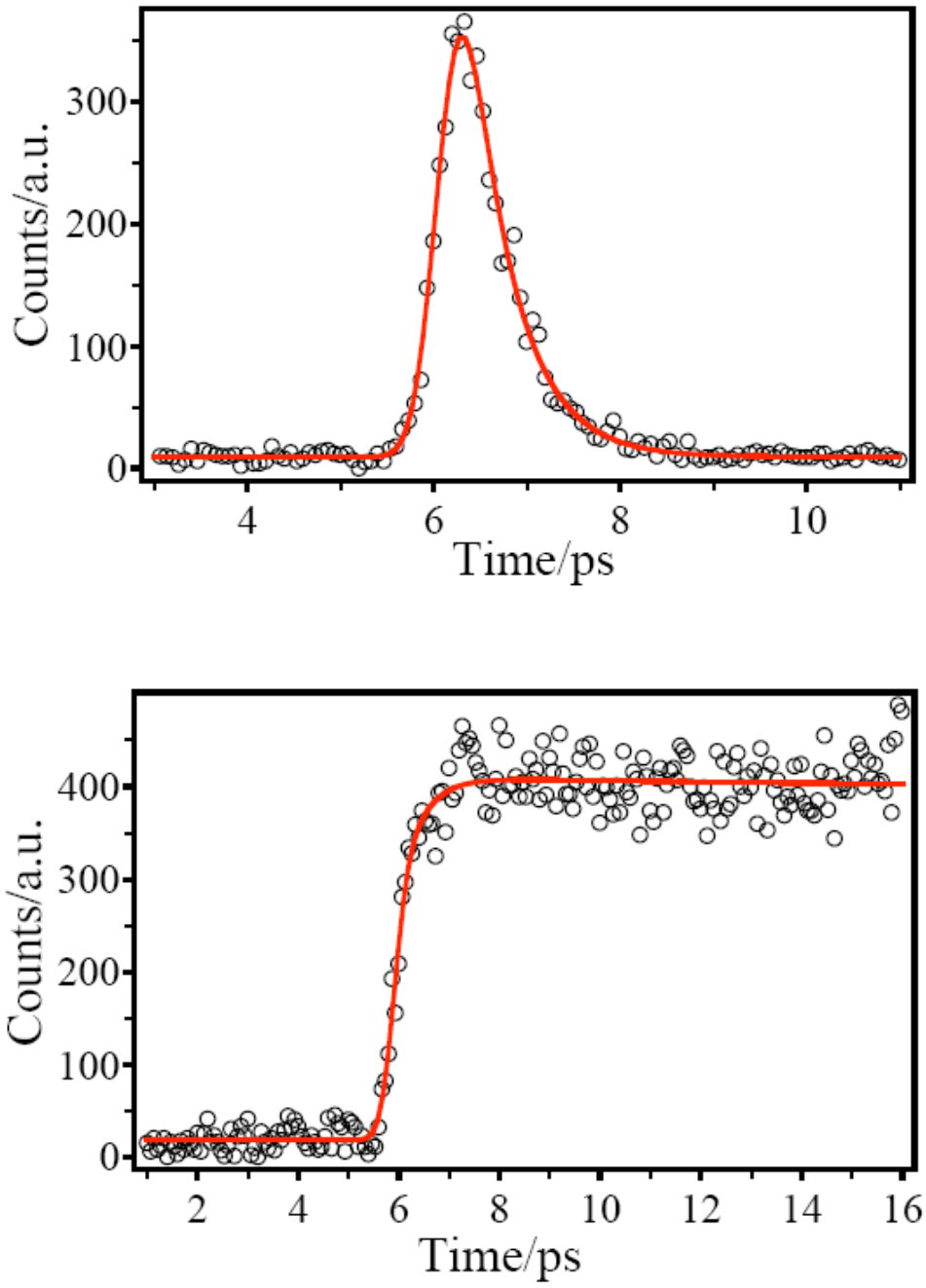

Fig. A.14 Temporal S_2 decay (top) and S_1 rise (bottom) profiles of ZnTPP(F_{20}) in ethanol at room temperature. Measurements are at room temperature with λ_{ex} = 400 nm and central observation wavelength at 433 nm for S_2 decay and 655 nm for S_1 rise. The solid lines give the best fits of single exponential decay and rise functions to the measured data.

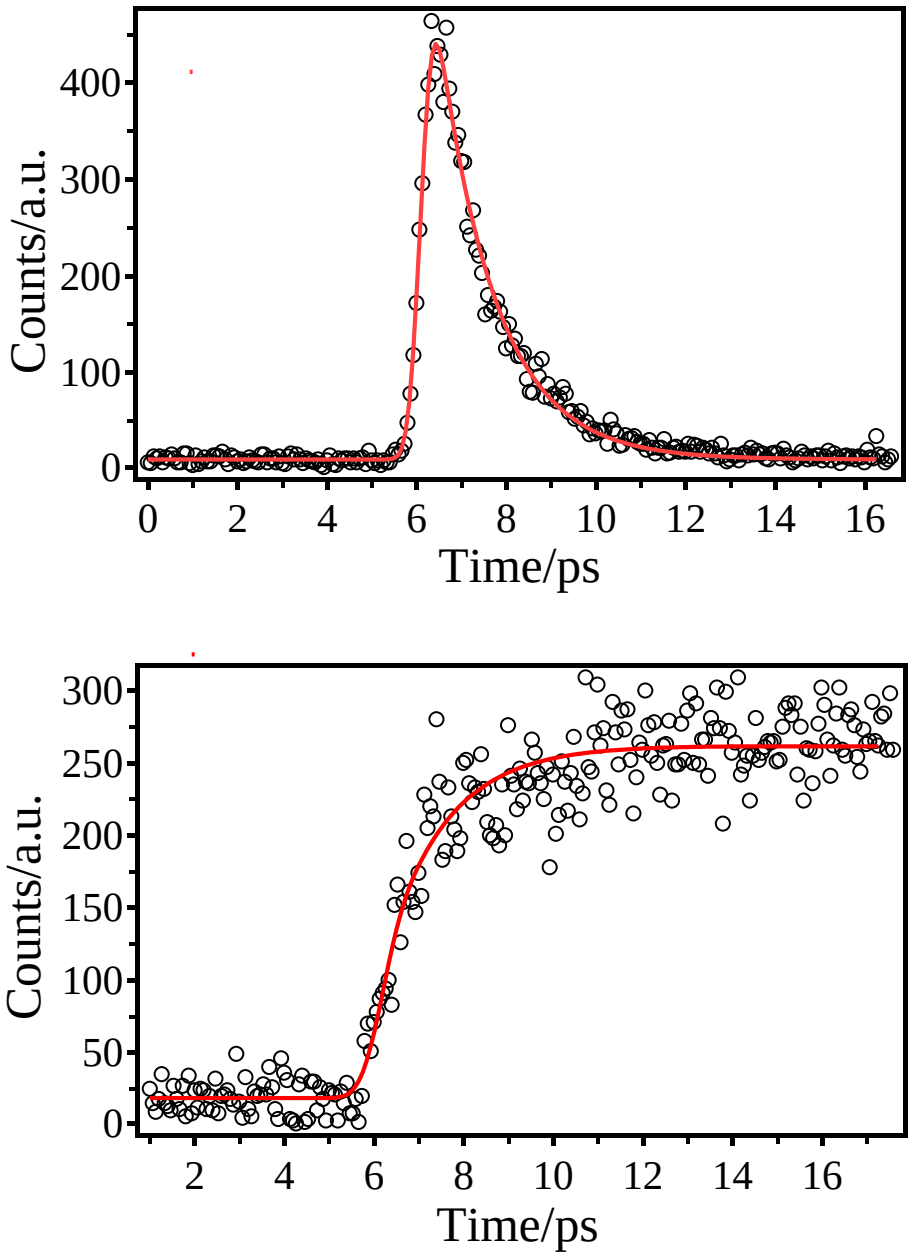

Fig. A.15 Temporal S_2 decay (top) and S_1 rise (bottom) profiles of ZnTPP(Cl_8) in ethanol at room temperature. Measurements are at room temperature with λ_{ex} = 400 nm and central observation wavelength at 433 nm for S_2 decay and 655 nm for S_1 rise. The solid lines give the best fits of single exponential decay and rise functions to the measured data.

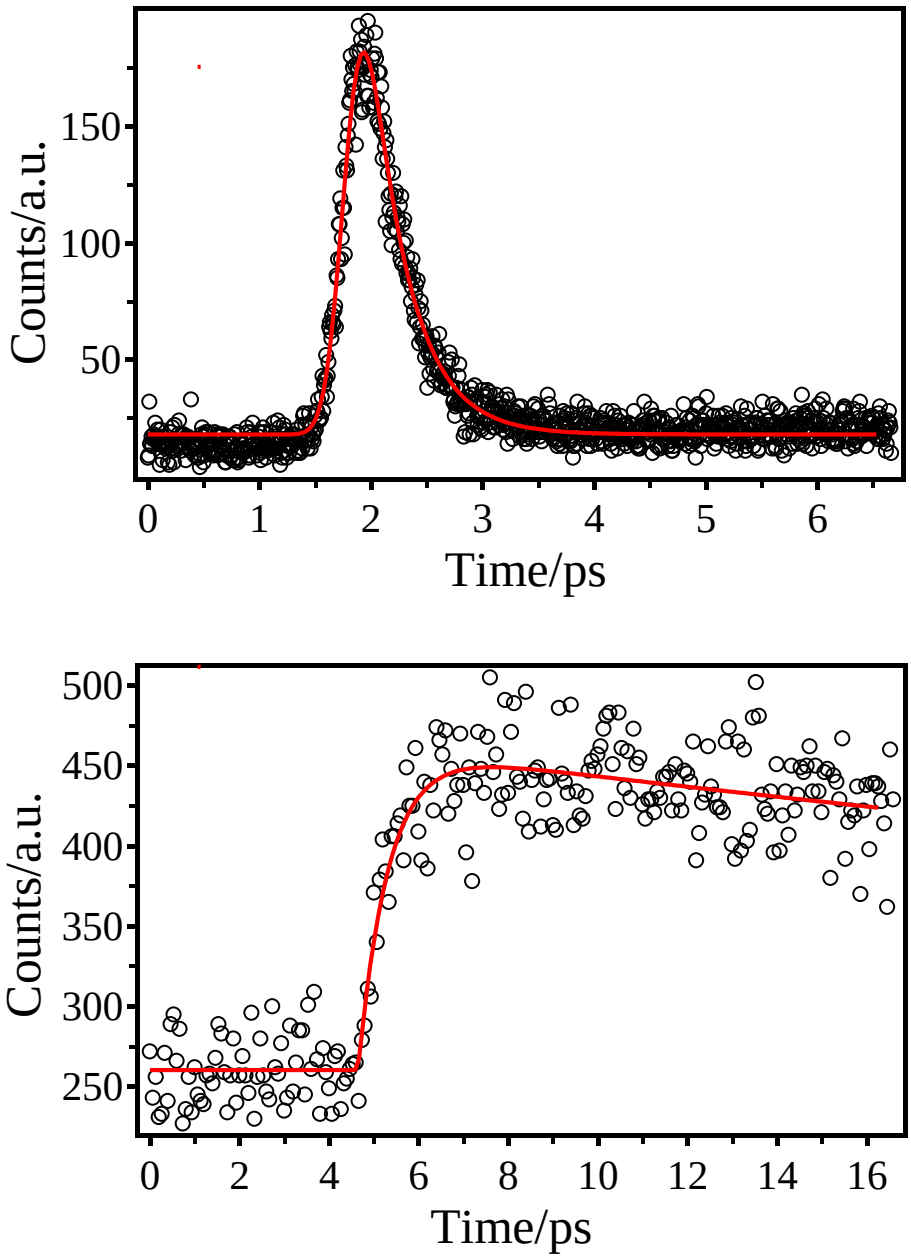

Fig. A.16 Temporal S_2 decay (top) and S_1 rise (bottom) profiles of CdTPP in benzene at room temperature. Measurements are at room temperature with λ_{ex} = 400 nm and central observation wavelength at 433 nm for S_2 decay and 655 nm for S_1 rise. The solid lines give the best fits of single exponential decay and rise functions to the measured data.

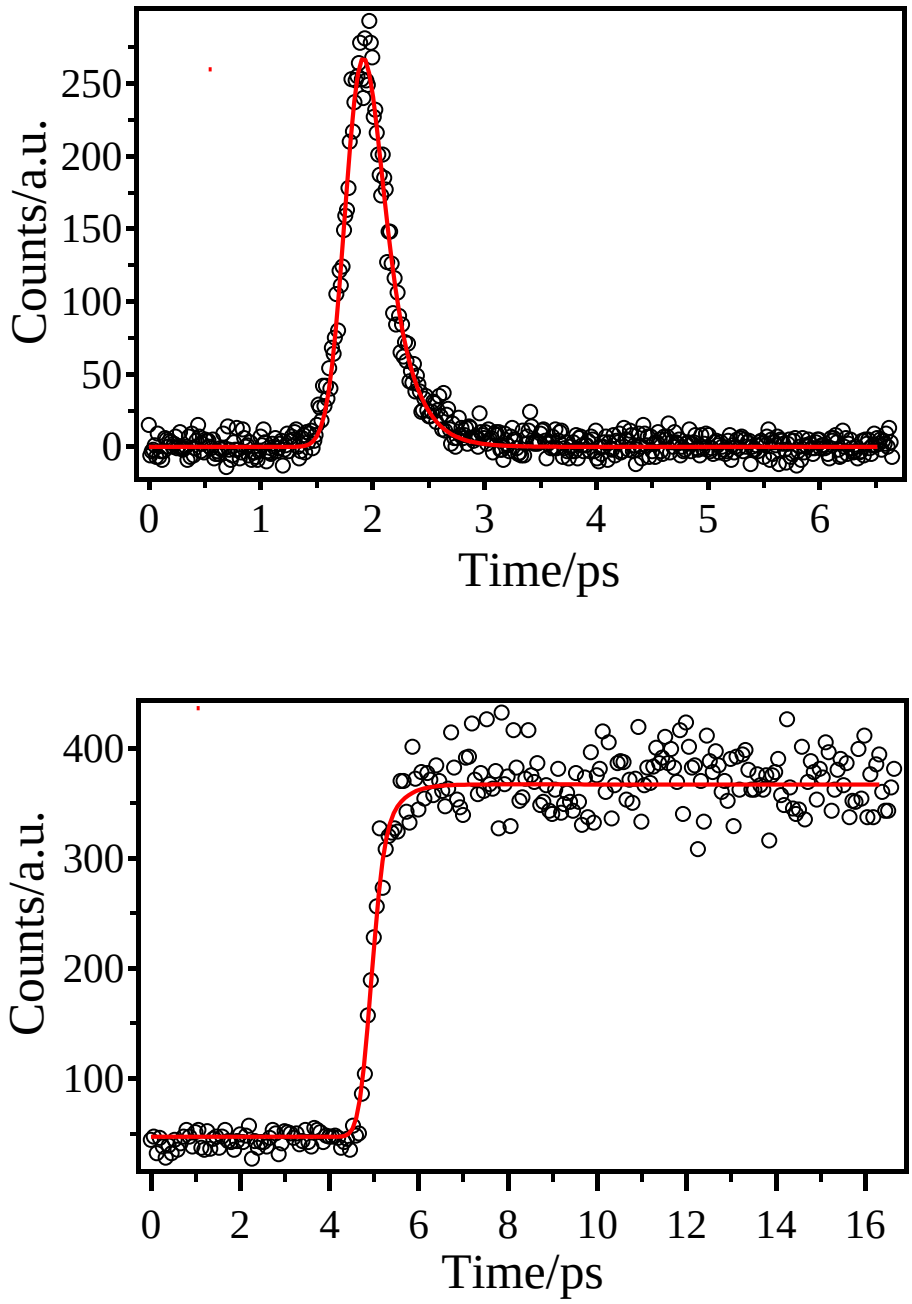

Fig. A.17 Temporal S_2 decay (top) and S_1 rise (bottom) profiles of H_2TPP in benzene at room temperature. Measurements are at room temperature with λ_{ex} = 400 nm and central observation wavelength at 433 nm for S_2 decay and 655 nm for S_1 rise. The solid lines give the best fits of single exponential decay and rise functions to the measured data.

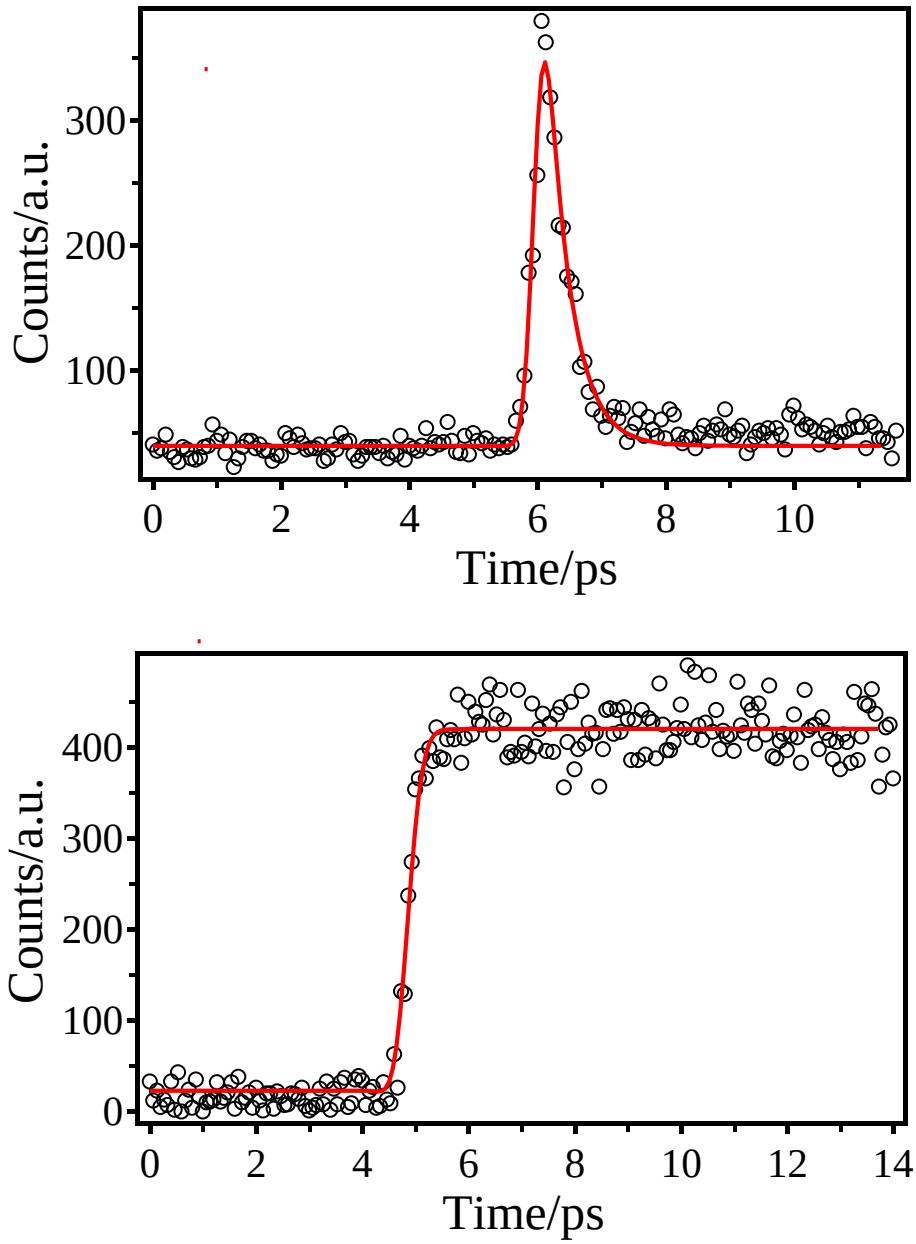

Fig. A.18 Temporal S_2 decay (top) and S_1 rise (bottom) profiles of TPP-d_{30} in benzene at room temperature. Measurements are at room temperature with λ_{ex} = 400 nm and central observation wavelength at 433 nm for S_2 decay and 655 nm for S_1 rise. The solid lines give the best fits of single exponential decay and rise functions to the measured data.

APPENDIX II

1. Derivation of equation 2.2 and the effective light length l_{em} in equation 2.1 in chapter 2.

In our experimental set-up, a 1.0 cm x 0.2 cm dimension cell instead of the square cell was used in order to decrease the reabsorption effect by shortening the emitting light path, as shown schematically in Fig. A.1. The intention of the following work is to find out the effective length l_{em} in eq. 2.2 in chapter 2 used to correct the inner filter effect on the fluorescence quantum yields measurements.

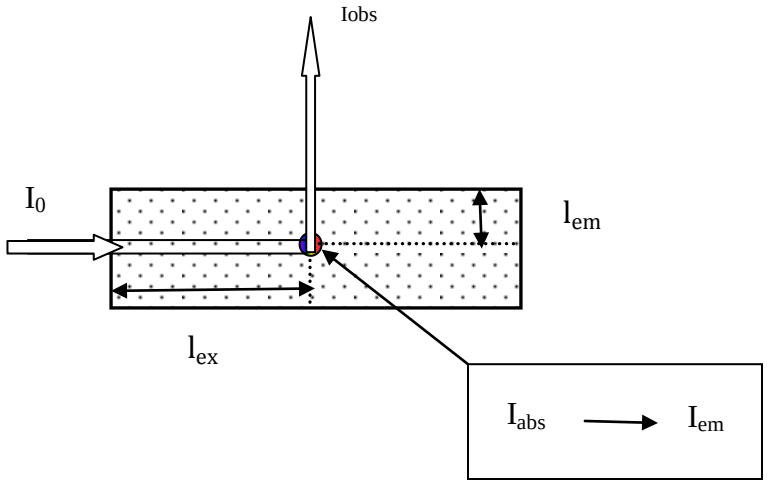

Fig. A.19 Model used to derive equations of inner filter effects correction.

I_0 is the initial excitation intensity before entering the solution; I_{abs} is the light intensity at the emitting center as a result of absorption by molecules in the ground state; I_{em} is the fluorescence intensity at the emitting center emitted initially by those molecules in the excited state; I_{obs} is the fluorescence intensity detected by the photon detector. l_{ex} is the effective light path of the excitation light and l_{em} is the effective light path of the emission light.

According to the Beer-Lambert Law,[21] eq. 1.3, the excitation light is attenuated following eq. A.1, before it reaches the point of fluorescence emission as a result of light absorption, where the light was absorbed by a number of molecules in the ground state.

The initially emitted fluorescence intensity is correlated with the excitation light intensity by multiplying a parameter, ϕ_f, the quantum yield of the compound in the solution.

$$\log\left(\frac{I_{abs}}{I_0}\right) = -A_{ex}\, l_{ex} \qquad (A.1)$$

$$I_{em} = -k\phi_f A_{ex}\, l_{ex} \qquad (A.2)$$

Here, k is a constant, and A_{ex} is the absorbance at excitation wavelength. The initially emitted fluorescence light can be reabsorbed by molecules in the ground state, thus the observed fluorescence intensity was also attenuated before exiting the solution.

$$\log\left(\frac{I_{obs}}{I_{em}}\right) = -A_{em}\, l_{em} \qquad (A.3)$$

Here A_{em} is the absorbance at emitting wavelength. Eq. A.4 is derived by submitting of eqs. A.1 and A.2 into eq. A.3.

$$\log\left(\frac{I_{obs}}{k\phi_f A_{ex}\, I_0}\right) = -(A_{ex}\, l_{ex} + A_{em}\, l_{em}) \qquad (A.4)$$

Rearrangement of eq. A.4 and introduction of one parameter R ($R = A_{em}/A_{ex}$) and one constant K ($K = k\phi_f I_0$) gives eq. A.5, which was used to obtain the effective light path length l_{em}.

$$\log\left(\frac{I_{obs}}{A_{ex}}\right) = -A_{ex}(l_{ex} + R l_{em}) + \log K \qquad (A.5)$$

The following information is given as an example to show the validity of eq. A.5 and the effective emission light path l_{em}. The data were obtained by using ZnTPP solutions with different concentrations associated with different absorbance at 400 nm (A_{400}).

The plot of $\log\left(\frac{A_{ex}}{I_{obs}}\right)$ against A_{ex} shows a good linear relationship as shown in Fig. A.20. The slope gives the total value of $l_{ex} + R l_{em}$. Since the value of l_{ex} = 0.44 cm was known,[181] and value of R can be calculated based on the absorption spectrum, the value

of l_{em} = 0.05 cm was obtained for the 1 cm x 0.2 cm cell under the experimental conditions used.

Table A.1 The observed fluorescence intensities of S_2 states of ZnTPP in ethanol with different concentrations.

Trials	A_{400}	F_{corr}	I_{obs}/a.u.
1	0.453	0.620775	2493819
2	0.3467	0.688721	2436707
3	0.283	0.734647	2303909
4	0.2376	0.77006	2143026
5	0.178	0.820271	1849290
6	0.1299	0.864151	1503414
7	0.103	0.890101	1294641
8	0.077	0.9162	994419
9	0.066	0.927555	859741
10	0.054	0.940159	721610
11	0.0437	0.951163	597482
12	0.0274	0.968933	349613

Fig. A.21 shows the difference between two plots of corrected and uncorrected emission intensity *vs.* absorbance at excitation wavelength of 400 nm. It is important to note that those points with absorbance lower than 0.05 do not need to be corrected using eq. 2.1. The deviation from the linearity of the plot between the uncorrected data and absorbance is obvious and a good linearity was obtained for the corrected data. Thus, the validity of eq. 2.1 and A.5 are verified.

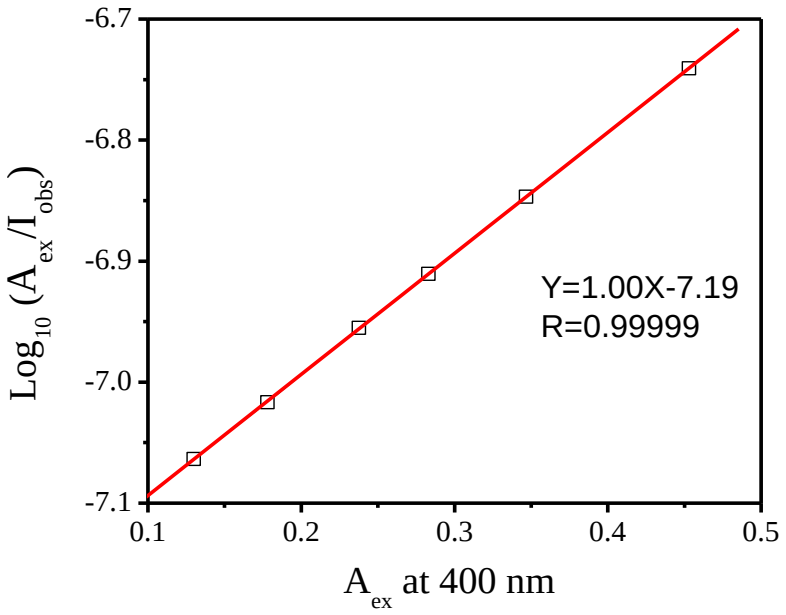

Fig. A.20 The linear plot of $\log_{10}(A_{ex}/I_{obs})$ against A_{ex} is obtained. A slope with a value of 1.00 is shown in the graph.

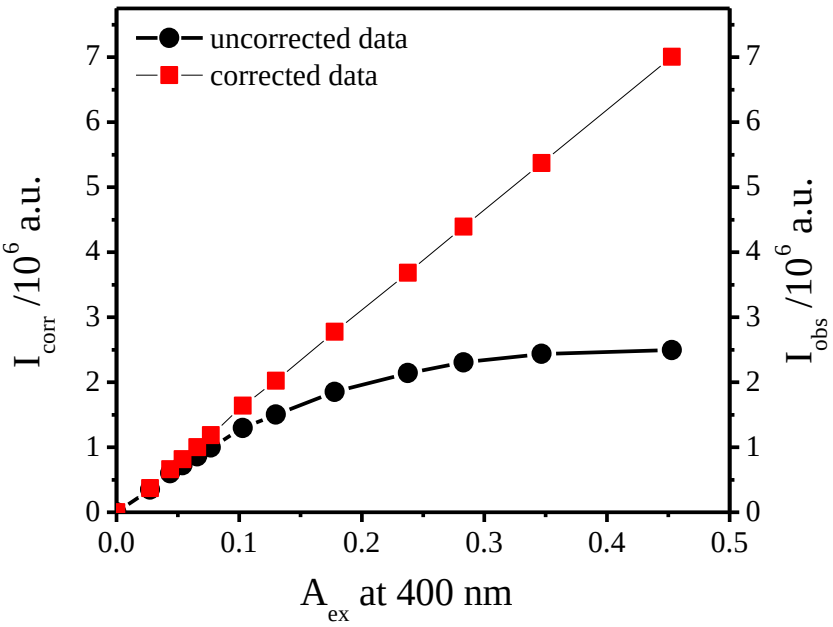

Fig. A.21 The comparison of the linear plots of the corrected and the uncorrected emission intensity against absorbance at excitation wavelength 400 nm is shown for different concentrations of ZnTPP in ethanol.